



**UNIVERSIDAD DEL PAÍS VASCO  
EUSKAL HERRIKO UNIBERSITATEA**

FACULTAD DE CIENCIA Y TECNOLOGÍA  
ZIENTZIA ETA TEKNOLOGIA FAKULTATEA

DEPARTAMENTO DE QUÍMICA INORGÁNICA  
KIMIKA EZORGANIKO SAILA

**Advanced anode materials for sodium ion batteries**

*A dissertation submitted to the University of the Basque Country in partial fulfilment of the requirements for the degree of Ph.D*

By  
**Paula Sánchez Fontecoba**

Thesis advisors:  
**Dr. Teófilo Rojo**  
**Dr. Elizabeth Castillo**

**Leioa, mayo 2017**



## ***Acknowledgements***

---

En primer lugar deseo expresar mi agradecimiento al profesor Dr. Teófilo Rojo y a la Dra. Elizabeth Castillo por haberme brindado la oportunidad de desarrollar mi actividad investigadora bajo su dirección y por haberme acompañado durante mi aprendizaje.

A la Universidad del País Vasco (UPV-EHU) por la concesión de una beca predoctoral que me ha permitido iniciarme en el campo de la investigación científica.

Al CIC Energigune y al Departamento de Química Inorgánica de la UPV-EHU por poner a mi disposición todos los medios para el desarrollo de mi investigación.

Asimismo, me gustaría expresar mi agradecimiento a los miembros del tribunal por haber leído y aceptado juzgar este trabajo.

Deseo mostrar también mi especial agradecimiento al Dr. Damien Saurel por su enorme implicación y ayuda en el desarrollo de este trabajo así como por su buena disposición siempre.

I would like to express my gratitude to Prof. Dr. Wilkening for accepting me as a visitor student during my stay in the Graz University of Technology and specially, to Dr. Ilie Hanzu for sharing his knowledge with generosity and human warmth.

I am forever grateful to Prof. Michel Armand, whose contribution is always invaluable. It has been such a privilege working with you.

Quisiera agradecer también a las personas que han contribuido a este trabajo con la realización de medidas de caracterización. A la Dra. Maribel Collado y al Dr. Juan Miguel López del Amo por las medidas de RMN. Al Dr. Damien Saurel por las medidas de SAXS. A Egoitz Martín por las medidas de XRD, al Dr. Jon Ajuria y a la Dra. Yan Zhang por las medidas de SEM, a Uxue Oteo por su ayuda con las medidas de BET. Al Dr. Aitor Eguia y al Dr. Man H. Han por su ayuda con la caracterización electroquímica en full-cell así como a los doctores Brahim Orayech, Gurpreet Singh, Javier Carretero y Maider Zarrabeitia por su ayuda en la discusión de los resultados.

Me gustaría agradecer a mis compañeros del Dpto. de Química Inorgánica por la ayuda brindada a lo largo de todos estos años, muy especialmente a Verónica, Oihane y Xabi, por infundirme ánimos en la recta final. También a mis compañeros del CIC Energigune. En especial a Amaia, Aitor, Oihane, Nerea, Jon, Nebil, Egoitz, Uxue y Esti, con los que he disfrutado de momentos inolvidables. Quiero dar las gracias también a Naiara, Sofía y Carlos por su apoyo constante.

Por último quiero expresar todo mi agradecimiento a mi familia, por su apoyo incondicional a todos los niveles. También a Edu, muy especialmente, por todo.



## Chapter 1: Introduction

<b>1.1 The need for energy storage</b> .....	<b>1</b>
<b>1.2 Energy storage for renewable energy systems</b> .....	<b>3</b>
<b>1.3 Batteries for electrochemical energy storage</b> .....	<b>6</b>
1.3.1 Li ion batteries .....	11
1.3.1.1 Cathodes for LIB.....	12
1.3.1.2 Anodes for LIB.....	13
1.3.2 Sodium ion batteries.....	14
1.3.2.1 Cathode materials for sodium ion batteries .....	18
1.3.2.2 Anode materials for sodium ion batteries .....	23
<b>1.4 Scope of this thesis</b> .....	<b>29</b>
<b>1.5 Structure of this thesis</b> .....	<b>31</b>

## Chapter 2: Biomass derived carbon anodes for sodium ion batteries

<b>2.1 Introduction</b> .....	<b>33</b>
2.1.1 Carbon materials.....	33
2.1.1.1 Structure of sp <sup>2</sup> carbons .....	33
2.1.1.2 Sodium storage mechanism of sp <sup>2</sup> carbons .....	37
2.1.1.3 Electrochemical performance of sp <sup>2</sup> carbons .....	40
2.1.2 Lignin as biomass precursor of hard carbon .....	48
<b>2.2 Experimental</b> .....	<b>49</b>
2.2.1 Synthesis of carbonaceous anodes .....	49
2.2.1.1 Lignin derived hard carbons .....	50
2.2.1.2 Sugar derived hard carbons.....	53
2.2.1.3 PVC derived soft Carbons .....	56
2.2.2 Physico-chemical characterization.....	57

2.2.3 Electrochemical characterization .....	58
<b>2.3 Results and discussion .....</b>	<b>58</b>
2.3.1 Thermogravimetric analysis (TGA) .....	59
2.3.2 X-Ray diffraction (XRD) .....	61
2.3.3 Scanning electron microscopy (SEM) .....	66
2.3.4 Raman spectroscopy .....	72
2.3.5 BET area .....	74
2.3.6 Small Angle X-Ray Scattering (SAXS) .....	76
2.3.7 Electrochemical characterization .....	81
<b>2.4 Conclusions .....</b>	<b>110</b>

## **Chapter 3: Poly Schiff bases-Poly Ethylene oxide copolymers as anodes for sodium ion batteries**

<b>3.1 Introduction .....</b>	<b>111</b>
3.1.1 Small molecules (salts) .....	115
3.1.2 Polymeric electrode materials .....	118
3.1.2.1 PolySchiff bases.....	122
3.1.3 Smart binders in lithium Ion batteries .....	122
3.1.4 Aim of the present work.....	127
<b>3.2 Experimental .....</b>	<b>129</b>
3.2.1 Synthesis of PolySchiff-PEO copolymers) .....	129
3.2.2 Electrochemical characterization) .....	133
3.2.2.1 Electrode preparation .....	134
3.2.2.2 Electrolyte preparation.....	137
3.2.2.3 Cell assembly and galvanostatic cycling parametres .....	138
3.2.2.3.1 Theoretical capacity values calculation.....	138
<b>3.3 Results and discussion .....</b>	<b>140</b>
3.3.1 Structural and morphological characterization .....	140
3.3.1.1 Attenuated total reflectance-Fourier Transform Infrared.....	140

3.3.1.2 Powder X-Ray diffraction (XRD) .....	141
3.3.1.3 Liquid <sup>1</sup> H-NMR .....	145
3.3.1.4 Solid state NMR (ss-NMR) .....	147
3.3.1.5 Scanning electron microscopy (SEM) .....	149
3.3.1.6 Thermogravimetric analysis analysis (TGA) .....	151
3.3.1.7 Solubility tests.....	152
3.3.2 Electrochemical performance .....	154
3.3.2.1 Electrochemical performance of the PSB-PEO as active material .....	154
3.3.2.2 Electrochemical performance of PSB-PEO as binder .....	173
<b>3.4 Conclusions .....</b>	<b>206</b>

## **Chapter 4: Development of Na-ion full-cells based on polySchiff-PEO and soft carbon anodes.**

<b>4.1 Introduction .....</b>	<b>209</b>
<b>4.2 Experimental .....</b>	<b>212</b>
4.2.1 Synthesis of sodium layered oxide: P2-Na <sub>0.67</sub> Fe <sub>0.5</sub> Mn <sub>0.5</sub> O <sub>2</sub> .....	213
4.2.2 Electrode preparation of sodium layered oxide: P2-Na <sub>0.67</sub> Fe <sub>0.5</sub> Mn <sub>0.5</sub> O <sub>2</sub> .....	213
4.2.3 Electrode preparation of PVC derived soft carbon and PSB-PEO .....	213
<b>4.3 Results and discussion .....</b>	<b>214</b>
4.3.1 Structural characterization of P2- Na <sub>0.67</sub> Fe <sub>0.5</sub> Mn <sub>0.5</sub> O <sub>2</sub> .....	214
4.3.2 Electrochemical characterization of P2- Na <sub>2/3</sub> Fe <sub>1/2</sub> Mn <sub>1/2</sub> O <sub>2</sub> in half cell. ....	214
4.3.3 Electrochemical performance of PSB-PEO in a full-cell .....	216
4.3.4 Electrochemical performance of PVC-derived hard carbon  P2- Na <sub>0.67</sub> Fe <sub>0.5</sub> Mn <sub>0.5</sub> O <sub>2</sub> full cell .....	222
4.3.5 Comparison of the electrochemical performance of PVC-derived hard carbon .....	226
<b>4.4 Conclusions .....</b>	<b>227</b>

## Chapter 5: Conclusions and perspectives

<b>5.1 Conclusions</b> .....	<b>229</b>
<b>5.2 Future perspectives</b> .....	<b>231</b>

## Appendix: Instrumental techniques

<b>A1. X-Ray scattering techniques</b> .....	<b>233</b>
A1.1 X-Ray powder diffraction (PXRD) .....	233
A1.2 Small Angle X-ray Scattering (SAXS) .....	235
<b>A2. Scanning Electron Microscopy (SEM)</b> .....	<b>237</b>
<b>A3. Surface area analysis (BET method)</b> .....	<b>239</b>
<b>A4. Thermal analysis</b> .....	<b>244</b>
A4.1 Thermogravimetric analysis (TGA) .....	244
A4.2 Differential Scanning Calorimetry (DSC) .....	246
<b>A5. Attenuated Fourier Transform Infrared Spectroscopy (ATR-FTIR)</b> ....	<b>247</b>
<b>A6. Nuclear Magnetic Resonance (1H-NMR)</b> .....	<b>249</b>
A6.1 Liquid state NMR .....	249
A6.2 Solid state NMR.....	251
<b>A7. Electrochemical testing</b> .....	<b>252</b>
A.7.1 Electrode preparation.....	253
A.7.2 Cell assembly .....	253
A.7.3 Galvanostatic cycling.....	255
A.7.4 Cyclic voltammetry .....	257

## ***Abstract***

---

The economic growth over the last decades has gone hand in hand with the increase of the global energy demand. The use of fossil fuels, which are nowadays the world's leading energy source, entails serious environmental issues. For that reason, in order to meet the future energy requirements, the energy systems have to gradually move from fossil fuels towards renewable energy. In this regard, electrochemical energy storage and more specifically, batteries possess desirable features for the integration of renewable energy sources. Since their commercialization, Li ion batteries have been the dominant technology in the market. However, Na ion batteries are becoming an attractive alternative to the Li ion technology for stationary applications due to their lower cost owing to sodium abundance and wider geographical distribution. Although Na presents similar chemical properties to those of Li, the Li ion technology non-fully transferable and new materials have to be developed.

On the one hand, in this work, biomass derived hard carbon materials have been developed. Given the low cost of their lignin precursor, ease of synthesis, non-toxicity and relatively high capacity, hard carbons are considered promising anode materials for sodium ion batteries. The synthesis optimization of lignin derived hard carbons focused on the improvement of the electrochemical properties though the attainment of highly disordered high purity carbons is presented. Several characterization techniques such as XRD, SEM-EDX, BET, Raman and SAXS have been used with the purpose of correlating the physico-chemical properties of the carbon materials and their electrochemical performance.

On the other hand, polySchiff bases which are low cost, non-toxic, easy to synthesize, structurally diverse and safe organic electrodes have been also prepared. The synthesis optimization oriented towards the attainment of PolySchiff-polyethylene oxide copolymers (PSB-PEO) with improved processability with respect to bare PolySchiff polymers is detailed. The evaluation of the material as anode in powder electrodes, as binder-free laminate electrodes and as binder of other active materials is shown. Finally, the electrochemical performance as anodes of a carbon material and the optimized PSB-PEO in a full-cell is evaluated.



## **Resumen**

---

El crecimiento económico de las últimas décadas ha ido de la mano del aumento de la demanda energética global. El uso de combustibles fósiles, los cuales son a día de hoy la fuente energética preponderante, conlleva serios problemas medioambientales. Por esa razón, de cara a cumplir con los requerimientos energéticos del futuro, los sistemas de energía deben orientarse paulatinamente hacia las energías renovables. En ese sentido, el almacenamiento electroquímico y, más concretamente, las baterías poseen características que las hacen adecuadas para el establecimiento de las energías renovables. Desde su comercialización, las baterías de Li-ion han sido la tecnología predominante en el mercado. Sin embargo, las baterías de Na-ion se han convertido en una alternativa a la tecnología de Li ion para aplicaciones estacionarias debido a su menor coste, a la abundancia del Na y a una distribución geográfica sea homogénea. A pesar de que el Na presenta propiedades químicas similares a las del Li, la tecnología de Li ion no es directamente transferible y por ello es necesaria la búsqueda de nuevos materiales.

Por un lado, en este trabajo se han desarrollado los materiales de "*hard carbon*" derivados de biomasa. Dado el bajo coste del precursor de lignina, de su facilidad de síntesis, no toxicidad y relativamente alta capacidad, los "*hard carbons*" se han perfilado como materiales anódicos prometedores para baterías de sodio ion. La optimización de la síntesis orientada a la mejora de las propiedades electroquímicas a través de la obtención de materiales puros altamente desordenados se presenta a lo largo del capítulo correspondiente. Varias técnicas de caracterización tales como DRX, MBE-SDE, BET, Raman y dispersión de rayos X de bajo ángulo se han empleado con objeto de correlacionar las propiedades físico-químicas de los materiales de carbón y sus propiedades electroquímicas.

Por otro lado se han preparado bases de PolySchiff las cuales son de bajo coste, fáciles de sintetizar, estructuralmente diversas y seguras. A lo largo del capítulo correspondiente se detalla la optimización de la síntesis orientada a la obtención de copolímeros de bases de polySchiff y óxido de polietileno (PSB-PEO) para mejorar las propiedades de procesabilidad con respecto a las bases de PolySchiff. El material se evalúa electroquímicamente como ánodo de baterías de sodio en electrodos en

polvo, electrodos laminados sin aglutinante, y como aglutinante con propiedades redox de otros materiales activos.

Por último, se muestra el comportamiento electroquímico de un material anódico de derivado de carbón y del polímero PSB-PEO en una celda completa.



---

# Chapter 1: Introduction

---

## 1.1 The need for energy storage

Over the past years, world economic growth has been linked to a dramatic increase of the global energy consumption (as shown in Figure 1.1a). According to British Petroleum, fuel consumption has grown in the last years from 3730 Mtoe (million tonnes of oil equivalent) to 13147 in 2015.<sup>1</sup> Despite the growth of non-fossil energy (such as nuclear, hydropower and other renewable sources), the share of fossil fuels within the world energy supply is relatively unchanged over the past four decades. In 2015 fossil fuels, including oil, natural gas and coal remained the world's leading fuel, accounting for 86.01 % of global energy consumption (Figure 1.1b)

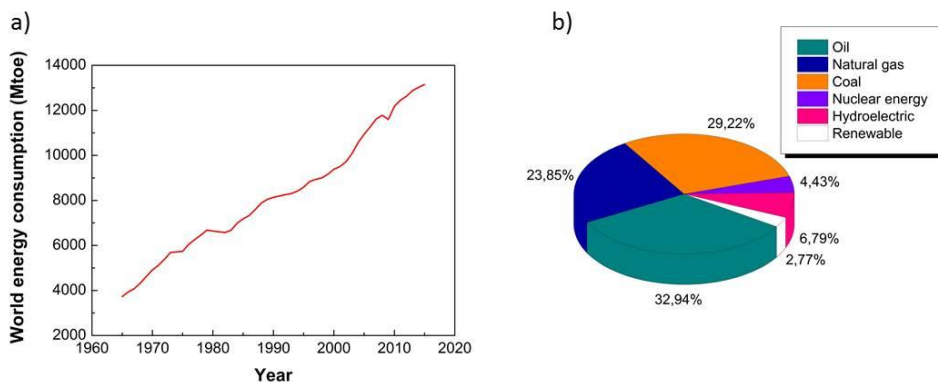


**Figure 1.1** a) World energy consumption between 1965 and 2015 and b) Primary energy consumption by fuel in 2015.

<sup>1</sup> BP-Statistical Review of World Energy, June 2016. ([bp.com/statisticalreview](http://bp.com/statisticalreview)).

In 2015, the amount of energy produced by nuclear plants reached a 4.43 %. However, transportation and storage of waste materials produced in nuclear power plants is a significant global environmental threat because the uncontrolled release of radioactive compounds is harmful to all living species. Therefore, as the use of nuclear energy has environmental, health, and security risks it is an undesirable substitute for fossil fuels, which are also responsible for air pollution and greenhouse effect.<sup>2</sup>

The International Energy Agency has reported that carbon dioxide (CO<sub>2</sub>) concentrations in the atmosphere have been increasing significantly over the past century and, even if it is at a slower rate, they will continue growing reaching 37.2 Gt by 2035.<sup>3</sup> Among the many human activities that produce greenhouse gases, the use of energy represents by far the largest source of emissions. In order to avoid dangerous climate change caused by the increase of greenhouse effect gasses in the atmosphere, some actions such as decarbonising the energy supplies of industrialised countries and shifting developing countries onto a low-carbon development path were agreed on the 21<sup>st</sup> Conference of the Parties (COP21) held in Paris in December 2015.<sup>4</sup> Thus, it is clear that the energy system has to gradually move from fossil fuels towards renewable energy sources. A variety of renewable and clean energy sources such as wind and solar power are growing quickly as low carbon energy sources. Despite the fact that nowadays they represent only the 2.77 % of the world primary energy source, their use will increase in the near future due to their advantages such as they are unlimited and environmentally friendly.<sup>4</sup> However, due to their dependence on the weather they also present a big disadvantage: the intermittency of supply, which is subjected to time, season or weather conditions. In order to solve the problem, additional stationary energy storage systems (EES) that shift electrical

---

<sup>2</sup> Michaelides, E. E. (Stathis); *Alternative Energy Sources*, Springer-Verlag Berlin Heidelberg, **2012**, 56.

<sup>3</sup> International Energy Agency (IEA), *CO<sub>2</sub> Emissions from Fuel Combustion, Highlights*, OECD/IEA, Paris, **2016**.

<sup>4</sup> International Energy Agency (IEA), *Energy and Climate Change - World Energy Outlook Special Report*, **2015**.

energy from on-peak (high demand) to off-peak (low demand) periods to reach smart grid management are extremely important.<sup>5</sup>

## 1.2 Energy storage for renewable energy systems

A number of potential Electrochemical Energy Storage technologies have been proposed for renewable energy. Suitable candidates are: mechanical systems like flywheels energy storage (FES) and pumped hydroelectric storage (PHS), pneumatic systems like compressed air energy storage (CAES), thermal energy storage systems (TES) such as sensible heat storage, latent heat storage and thermochemical storage, magnetic systems like superconducting magnetic energy storage (SMES), electrochemical energy storage systems (EES) such as fuel cells, supercapacitors and rechargeable batteries.<sup>6,7</sup>

As no single EES technology can meet all the requirements for all power system applications, a selection of technology must be carried out based on the needs of power and energy for a given application. For example, PHS and CAES show low energy density, thus they are mainly used for large-scale energy storage. A comparison of the specific power and energy of different energy storage technologies is shown in Figure 1.2. It can be seen that SMES, capacitors and supercapacitors have high specific power but low specific energy; because of their fast response time, they are more suitable for power quality applications for electric power delivery. Fuel cells and TES have high specific energy with low specific power. For acquiring a certain amount of energy, the higher the specific power and the specific energy are, the lighter the weight of the EES system will be. Thus, fuel cells and TES are suitable for large-scale storage systems. Flywheel, vanadium redox flow Battery (VRB), ZnBr redox flow battery and most conventional batteries (lead acid, NaS) are located at the middle levels in terms

---

<sup>5</sup> Pan, H.; Hu, Y.-S. and Chen, L., Room-temperature stationary sodium-ion batteries for large-scale electric energy storage, *Energy Environ. Sci.*, **2013**, 6, 8, 2338-2360.

<sup>6</sup> Zhou, Z.; Benbouzid, M.; Charpentier, J. F.; Scuiller, F.; Tang, T., A review of energy storage technologies for marine current energy systems, *Renew. Sust. Energ. Rev.*, **2013**, 18, 390-400.

<sup>7</sup> Ibrahim, H.; Ilinca, A. and Perron, J., Energy storage systems-Characteristics and comparisons, *Renew. Sust. Energ. Rev.*, **2008**, 12, 1221-1250.

of specific power and specific energy, which may serve for different small-medium size applications. Li-ion batteries can provide an outstanding performance due to both high specific energy and specific power.

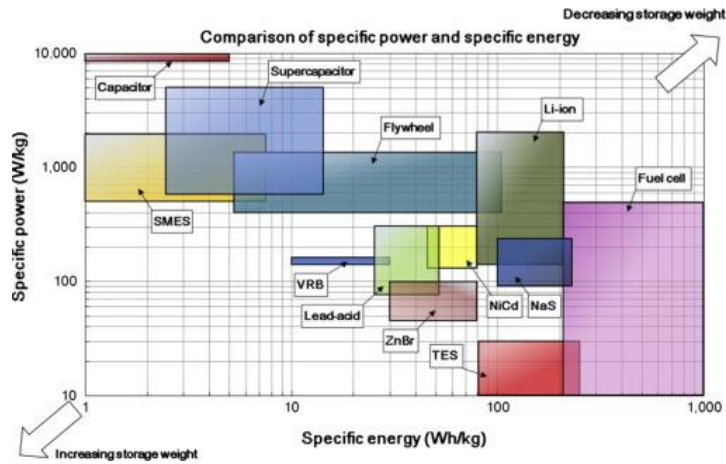


**Figure 1.2** Comparison of specific power ( $\text{W}\cdot\text{kg}^{-1}$ ) and specific energy ( $\text{W}\cdot\text{h}\cdot\text{kg}^{-1}$ ) of different energy storage technologies.<sup>8</sup>

Pumped-storage hydroelectricity are one of the oldest ESS technologies that have been employed in the electricity grid and with 127,000 MW of discharge power it represents over 99 % of total storage capacity (Figure 1.3).<sup>9</sup>

<sup>8</sup> Luo, X.; Wang, J.; Dooner, M. and Clarke, J., Overview of current development in electrical energy storage technologies and the application potential in power system operation, *Appl. Energy*, **2015**, 137, 511-536.

<sup>9</sup> EPRI. Electricity Energy Storage Technology Options, **2010**.

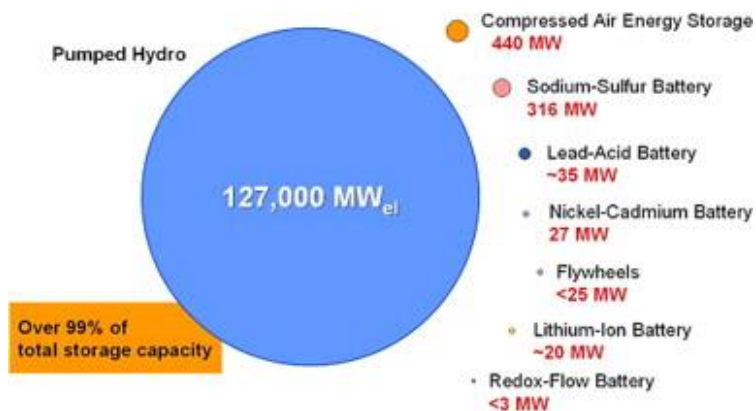


**Figure 1.3** Worldwide installed storage capacity for electrical energy.<sup>9</sup>

The energy is stored by pumping water uphill using peak-off electricity and then letting the water move downhill and driving the generator to produce electricity for power grid when needed. Advantages are the very long lifetime and practically unlimited cycle stability of the installation. However, large capital cost, highly dependent on the local topography and direct environmental damage caused by the construction of plants is the main drawback of this technology.<sup>10</sup> Compressed air storage (CAES) is a distant second worldwide storage system delivering 440 MW of discharge power. This technology uses electricity to compress air and store it in either an underground structure or an above-ground system of vessels or pipes. When needed the compressed air is mixed with natural gas, burned and expanded in a modified gas turbine. Typical underground storage options are caverns, aquifers or abandoned mines. The main advantage of CAES is its large capacity whereas disadvantages are high cost, low round-trip efficiency and geographic limitation of locations.<sup>9</sup>

Electrochemical energy storage systems possess a number of desirable features for the integration of renewable resources, including pollution-free operation, high round-trip efficiency, tunable power and energy characteristics to meet different grid functions, long cycle life, and low maintenance. Their compact size makes them especially well-suited for portable uses. Fuel cells, which are not

<sup>10</sup> Mahlia, T. M. I.; Saktisahdan, T.J.; Jannifar, A.; Hasan, M.H.; Matseelar, H. S. C., A review of available methods and development on energy storage; technology update, *Renew. Sust. Energ. Rev.*, **2014**, 33, 532-545.

rechargeable, store energy in the reactants that are externally fed to the cells. Supercapacitors offer yet a different energy storage mechanism, via a capacitive process arising from an electrochemical double layer at the electrode-electrolyte interface. Battery energy storage, which store energy within the electrode structure through charge transfer reactions, is the most widely used technology available for power system application. Different types of batteries have been developed and many of them are mature technologies available on the market.

### 1.3 Batteries for electrochemical energy storage

A battery is a device that converts the chemical energy contained in its active materials directly into electric energy by means of an electrochemical oxidation-reduction (redox) reaction. Batteries can be classified into two categories: primary batteries, which use the chemicals once only in a single discharge, and secondary batteries or “rechargeable batteries”, which can be recharged by a reversal of the process and reused again. While the term “battery” is often used, the basic electrochemical unit is the “cell.” A battery consists of one or more of these cells, connected in series or parallel, or both, depending on the desired output voltage and capacity. The cell consists of three major components: anode, cathode and electrolyte (Figure 1.4).

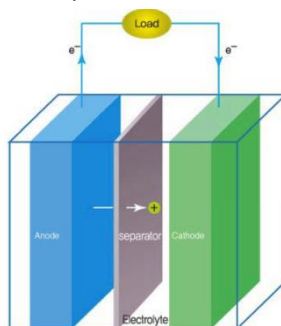


**Figure 1.4** Scheme of an electrochemical cell during discharge.<sup>11</sup>

<sup>11</sup> Park, J.-K., *Principles and applications of lithium secondary batteries*, Wiley-VCH Verlag & Co. KGaA,, Germany, **2012**, 9-11.

In a discharging battery, the process of converting chemical energy carried by the battery into electric energy takes place while electrochemical oxidation of the electrode ( $A \rightarrow A + e^-$ ) proceeds at the anode. Electrons transferred from the negative terminal through the external circuit engage in reduction ( $B^+ + e^- \rightarrow B$ ) at the positive terminal, which is known as a cathode. The electrolyte serves as an ionic conductor of the ions between the two electrodes guaranteeing the electro-neutrality. It is typically an organic solvent with dissolved salts to impart ionic conductivity although they can be also ceramic, polymeric or composite. The cell voltage depends on the potential difference between the two electrodes.<sup>11,12</sup> When voltage is applied in the reverse direction, redox reactions occur in the opposite direction leading to the conversion of electrical energy into chemical energy (charge of cell).

The amount of electrical specific energy, ( $W \cdot h \cdot kg^{-1}$ ) or volumetric energy ( $W \cdot h \cdot l^{-1}$ ), that a battery is able to deliver is a function of the cell potential (V) and capacity ( $A \cdot h \cdot kg^{-1}$ ), both of which are related to the chemistry of the system. In Figure 1.5 some of the various existing technologies on the market for EES are compared as a function of the volumetric and gravimetric energy densities they provide. The main characteristics and technical properties of different technologies are summarized in Table 1.1.

---

<sup>11</sup> Linden, D.; Reddy, T.B. *Handbook of Batteries. Third Edition.* Mac Graw-Hill. New York, **2002**, 2.1-2.3.

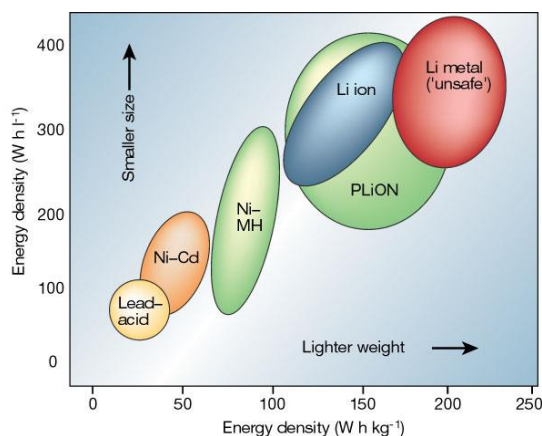


**Figure 1.5** Comparison of the volumetric and gravimetric energy densities of different rechargeable batteries for EES.<sup>13</sup>

**Lead-acid batteries** have fast response times, small daily self-discharge rates and relatively high cycle efficiencies (63-90%). However, they have limited energy density, risk of hydrogen evolution and require the use of heavy metals. Although the cost of lead-acid battery is relatively low, it is not a good option for large-scale EES applications due to its relatively short lifetime. Typical applications of lead-acid batteries include automotive power (starting engine, electric and hybrid vehicles) and standby emergency power. Although they show higher reliability in terms of specific energy, cycle life and round-trip efficiency than Pb-acid batteries, to date there have been very few commercial successes using **Ni-Cd batteries** for EES applications. The weaknesses of this technology are the use of toxic heavy metals and memory effect. They are mainly used for railroad and mass-transit installations aircraft batteries, lighting, emergency power and power stations. The metal hydride electrode of **Ni metal hydride batteries** (Ni-MH) has a higher energy density than the cadmium electrode resulting in a higher capacity or longer service life. Furthermore, as the nickel-metal hydride battery is free of cadmium, it is considered more environmentally friendly. In the portable sealed configuration, it is being used in consumer electronic devices (cellular phones, transceivers, computers, etc). In larger sizes, it is also one of the candidate for use in electric vehicles. **Sodium-sulfur battery** (Na/S) technology is commercially available for grid applications, with some 200

<sup>13</sup> Tarascon, J.-M. and Armand, M., , *Nature*, **2001**, 414, 359-367.



installations worldwide, accounting for 315 MW of discharge power capacity. However, the main drawback is that to maintain operating temperatures a heat source is required, which uses the battery's own stored energy, partially reducing the battery performance.<sup>14</sup> Redox flow batteries like **vanadium redox battery** (VRB) are especially advantageous because the power is independent of its storage capacity. It is determined by the size of the electrodes and the number of cells in the stack; whereas the storage capacity is determined by the concentration and the amount of electrolyte. They show very small self-discharge but they also show low performance resulting from non-uniform pressure drops and the reactant mass transfer limitation, relatively high manufacturing costs and more complicated system requirements compared to traditional batteries.<sup>8</sup> There are not still many commercially available redox flow battery systems at present. **Lithium ion batteries** (Li-Co and Li-FP) offer superior energy efficiency, high power density, fast charge and discharge capability, low weight and long cycle life. The main disadvantages are the high cost due to overcharging protection circuitry and risk of capacity loss or thermal runaway. Given their high energy density, they are suitable for portable applications (electronics, vehicles). That explains the share of worldwide sales for Li-ion portable batteries (63%) is much larger than those for Ni-Cd (23%), Ni-MeH (14%).<sup>13</sup> Taking into account the importance of Li ion batteries system, they will be more profoundly reviewed in the next section.

---

<sup>14</sup> Dunn, B.; Kamath, H.; Tarascon, J.-M., Electrical energy storage for the grid: a battery of choices, *Science*, **2011**, 334 (6058), 928-935.

**Table 1.1** Comparison of technicalities of different commercial secondary batteries. LAB: Pb-acid batteries; NCB: Ni-Cd batteries; Ni-MH: Ni metal hydride; Na-S: Na-S batteries; VRB: all-vanadium redox flow batteries; Li-Co : Li ion batteries having carbon anode and LiCoO<sub>2</sub> cathode; Li-FP: Li ion batteries having Li<sub>4</sub>Ti<sub>5</sub>O<sub>12</sub> anode and LiFePO<sub>4</sub> cathode.<sup>15,16,17</sup>

Battery type	Anode	Cathode	Electrolyte	OCV (V)	Specific energy (W·h·kg <sup>-1</sup> )	Operating temperature (°C)	Cycle life (cycles)	Round-trip efficiency (%)	Self-discharge (% per month)
LAB	Pb	PbO <sub>2</sub>	H <sub>2</sub> SO <sub>4</sub> (aqueous solution)	2.1	25-40	-40 - 60	1000	50-75	4-50
NCB	Cd	NiOOH	KOH (aqueous solution)	1.35	30-45	-10 - 45	2000	55-70	5-20
Ni-MH	MH	NiOOH	KOH (aqueous solution)	1.0-1.3	70-100	-20 - 50	300-600	75-80	30
Na-S	Na	S	β-alumina (solid)	2.1	150-240	300 - 350	4000	75-90	negligible
VRB	V <sup>2+</sup>	VO <sub>2</sub> <sup>+</sup>	*	1.4	10-20	10 - 40	5000	65-80	3-9
Li-Co	C	LiCoO <sub>2</sub>	Organic solvent	3-4	155	-25 - 40	1000	94-99	2
Li-FP	Li <sub>4</sub> Ti <sub>5</sub> O <sub>12</sub>	LiFePO <sub>4</sub>	Organic solvent	1.7	50-70	-25 - 40	4000	94-99	2

\*VRB stores electrical energy, typically in two soluble redox couples (VO<sub>2</sub><sup>+</sup> and V<sup>2+</sup> on the cathode and anode sides, respectively) contained in electrolyte tanks. Liquid electrolytes are pumped from storage tanks to flow-through electrode. The electrolytes flowing through the cathode and anode are often different and are referred to as anolyte and catholyte, respectively. Between the anode and cathode compartments is a membrane (or separator) that selectively allows cross-transport of nonactive species (e.g., H<sup>+</sup>, Cl<sup>-</sup>) to maintain electrical neutrality and electrolyte balance.

<sup>15</sup> Yang, Z.; Zhang, J.; Kintner-Meyer, M. C. W.; Lu, X.; Choi, D.; Lemmon, J. P. and Liu, J., Electrochemical energy storage for green grid, *Chem. Rev.*, **2011**, 111, 3577–3613.

<sup>16</sup> Kritzer, P., Separators for nickel metal hydride and nickel cadmium batteries designed to reduce self-discharge rates, *J. Power Sources*, **2004**, 137, 317-321.

<sup>17</sup> Linden, D.; Reddy, T.B. *Handbook of Batteries. Third Edition*. Mac Graw-Hill. New York, **2002**, 2.11-2.13.

### 1.3.1 Li ion batteries

The first commercial Li ion battery (LIB) was developed by Sony in the 90s and contained  $\text{LiCoO}_2$  and petroleum coke as cathode and anode, respectively.<sup>18</sup> Li ion batteries quickly became a competitive technology for portable devices thanks to their high energy and power density.

In most commercial lithium ion batteries, active materials undergo a topotactic reaction where lithium ions are reversibly removed or inserted into a host without a significant structural change to the host. They are also referred to as rocking-chair batteries as the lithium ions “rock” back and forth between the positive and negative electrodes as the cell is charged and discharged.<sup>19</sup> However, there are also alloying and conversion processes. In the latter, material undergoes a solid-state redox reaction during lithiation/delithiation, in which changes in the crystalline structure, accompanied by the breaking and recombining chemical bonds have been extensively studied. The reaction mechanisms are illustrated in Figure 1. 6.

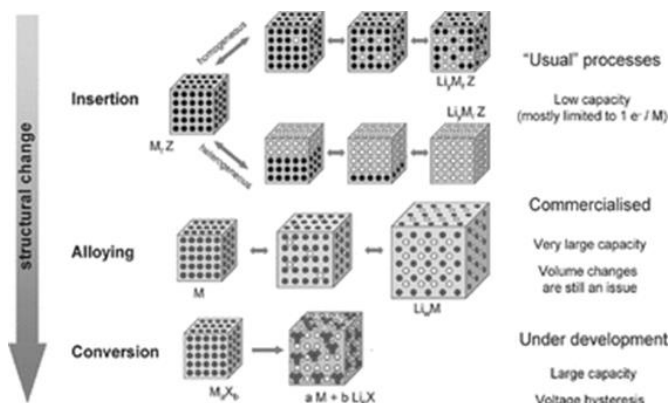


**Figure 1. 6** Schematic illustration of the reaction mechanisms of electrode materials with Li ions in lithium ion batteries.<sup>20</sup>

<sup>18</sup> Nishi; Y. , Lithium ion secondary batteries; past 10 years and the future, *J. Power Sources*, **2001**, 100, 101-106.

<sup>19</sup> Linden, D.; Reddy, T.B. *Handbook of Batteries. Third Edition*. Mac Graw-Hill. New York, **2002**, 35.1

<sup>20</sup> Kim, S.-W.; Seo, D.-H.; Ma, X.; Ceder, G. and Kang, K., Electrode materials for rechargeable sodium-ion batteries: potential alternatives to current lithium-ion batteries, *Adv. Energy Mater.*, **2012**, 2, 710-721.

Most common cathodes and anodes for LIB are represented in Figure 1.1.

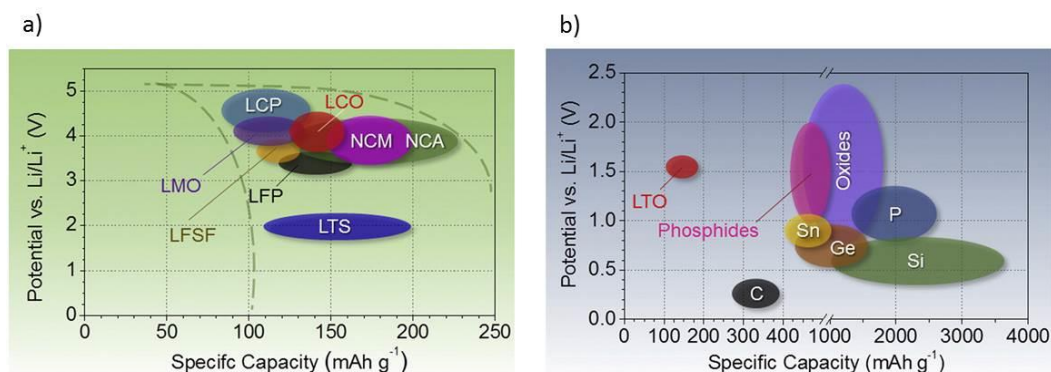


**Figure 1. 7** Approximate range of average discharge potentials and experimental specific capacity of some of the most common (a) cathodes and, (b) anodes for LIB. LCO: LiCoO<sub>2</sub>, LCP: LiCoPO<sub>4</sub>, LFP: LiFePO<sub>4</sub>, LMO: LiMn<sub>2</sub>O<sub>4</sub>, LSF: LiFeSO<sub>4</sub>F, LTS: LiTiS<sub>2</sub>, NCM: LiNi<sub>x</sub>Co<sub>y</sub>Mn<sub>z</sub>O<sub>2</sub>, NCA: LiNi<sub>0.8</sub>Co<sub>0.15</sub>Al<sub>0.05</sub>O<sub>2</sub>.<sup>21</sup>

### 1.3.1.1 Cathodes for LIB

Cathodes belong to three families of materials: layered oxides, spinel structures and polyanionic compounds. The most studied intercalation cathode materials families are layered oxides, spinel structures and polyanionic compounds.

LiCoO<sub>2</sub> (LCO) is the first and the most commercially successful form of layered transition metal oxide cathodes. It shows relatively high theoretical specific capacity of 274 mA·h·g<sup>-1</sup>, low self-discharge, high discharge voltage, and good cycling performance. The major limitations are high cost, low thermal stability, and fast capacity fade at high current rates or during deep cycling. LiNO<sub>2</sub> has a similar theoretical specific capacity of 275 mA·h·g<sup>-1</sup> and lower cost compared to Co based materials but it requires partial substitution of Ni with Co in order to avoid blocking the Li sites during synthesis and with Al in order to improve both thermal stability and electrochemical performance. The resulting LiNi<sub>0.8</sub>Co<sub>0.15</sub>Al<sub>0.05</sub>O<sub>2</sub> (NCA) cathode material has high discharge capacity (200 mA·h·g<sup>-1</sup>). LiNi<sub>0.33</sub>Co<sub>0.33</sub>Mn<sub>0.33</sub>O<sub>2</sub> (NMC) is widely used in the battery market because Mn is much cheaper and less toxic compared to Co or Ni and shows reversible specific capacity as high as 234 mA·h·g<sup>-1</sup> and good cycle stability.<sup>21</sup>

<sup>21</sup> Nitta, N.; Wu, F.; Lee, J. T. and Yushin, G., Li-ion battery materials: present and future, *Mater. Today*, **2015**, 8, 5, 252-264.

The spinel  $\text{LiMn}_2\text{O}_4$  (LMO) is interesting in terms of low cost, and environmental friendliness of Mn.  $\text{Li}^+$  can diffuse through vacant tetrahedral and octahedral interstitial sites in the three-dimensional structure leading to a moderate capacity of  $120 \text{ mA}\cdot\text{h}\cdot\text{g}^{-1}$  and an average voltage of 3.8 V vs.  $\text{Li}^+/\text{Li}$ . However, it shows insufficient long-term cyclability which is believed to be caused by irreversible side reactions with electrolyte, oxygen loss from the delithiated  $\text{LiMn}_2\text{O}_4$ , Mn dissolution, and formation of tetragonal  $\text{Li}_2\text{Mn}_2\text{O}_4$  at the surface.

$\text{LiFePO}_4$  is the most representative material of polyanionic compounds of general formula  $\text{Li}_x\text{M}_y(\text{XO}_4)$  (M=metal, X=S, P, Si, As, Mo, W).  $\text{LiFePO}_4$  is structurally and chemically stable.<sup>22</sup> It provides a capacity of  $170 \text{ mA}\cdot\text{h}\cdot\text{g}^{-1}$ ) and an average voltage of 3.5 V vs.  $\text{Li}^+/\text{Li}$ . The disadvantages of  $\text{LiFePO}_4$  are a low electron conductivity and slow diffusion of lithium ions. The electron conductivity of  $\text{LiFePO}_4$  can be improved by coating it with conducting agents such as carbon or silver nanoparticles.<sup>23</sup>

### 1.3.1.2 Anodes for LIB

Carbon based compounds are the most suitable materials among anode materials due to their low cost, high electrical conductivity and  $\text{Li}^+$  diffusivity. For the composition with  $x = 1$  ( $\text{LiC}_6$ ) in graphite, which is called the stage-one compound, the electrochemical capacity is equivalent to  $372 \text{ mA}\cdot\text{h}\cdot\text{g}^{-1}$ . Although graphite is the most widespread anode, other carbonaceous materials such as soft-carbons and hard carbons are also electrochemically active vs.  $\text{Li}$ .<sup>24,25</sup>

---

<sup>22</sup> Padhi, A. K.; Nanjundaswamy, K. S. and Goodenough, J. B., Phospho-olivines as positive-electrode materials for rechargeable lithium batteries, *J. Electrochem. Soc.*, **1997**, 144, 4, 1188-1194.

<sup>23</sup> Cheng, F.; Liang, J.; Tao, Z. and Chen, J., Functional materials for rechargeable batteries, *Adv. Mater.*, **2011**, 23, 1695-1715.

<sup>24</sup> Zaghbi, K. and Kinoshita, K., Overview of Carbon Anodes for Lithium-Ion Batteries, *New Trends in Intercalation Compounds for Energy Storage*, Volume 61 of the series NATO Science Series, 27-29.

<sup>25</sup> Stevens, D. A. and Dahn, J. R., Mechanisms of lithium and sodium insertion in carbon materials, *J. Electrochem. Soc.*, **2001**, 148, 8, A803-A811.

Among intercalation anodes, spinel lithium titanate ( $\text{Li}_4\text{Ti}_5\text{O}_{12}$ , LTO) has attracted much attention by virtue of its inherent features of zero strain and high operating potential, which results in outstanding structural stability and remarkable safety as anode materials for lithium-ion batteries. Although it delivers a moderate capacity of  $175 \text{ mA}\cdot\text{h}\cdot\text{g}^{-1}$  at 1.5 V vs.  $\text{Li}^+/\text{Li}$ , it shows a long cycle life derived from the zero strain intercalation mechanism.<sup>26</sup> Other titanium oxides like the  $\text{TiO}_2$  polymorphs can accommodate one lithium per formula unit, corresponding to a theoretical capacity of  $335 \text{ mA}\cdot\text{h}\cdot\text{g}^{-1}$  being  $\text{TiO}_2$  (B) the one providing best performance.<sup>27,28</sup>

Transition-metal oxides ( $\text{M}_x\text{O}_y$ ,  $\text{M}=\text{Fe}$ ,  $\text{Co}$ ,  $\text{Ni}$ ,  $\text{Mn}$ ,  $\text{Cu}$ , etc.) are capable of incorporating more than one Li per 3d metal, hence giving significantly higher electrochemical capacities than those of graphite anodes. Transition metal oxides are reduced to metal nanoparticles through a conversion reaction. For example, the spinel  $\text{Fe}_3\text{O}_4$  reached the theoretical reversible capacity of  $1000 \text{ mA}\cdot\text{h}\cdot\text{g}^{-1}$ . Despite the advantages of being low cost and having high capacity, one of the main drawbacks of these materials is the poor energy efficiency of the electrode related to the inherent large voltage separation between the charge and discharge profiles.<sup>23</sup>

### 1.3.2 Sodium ion batteries

For several decades, lithium ion has been successfully employed as charge carrier for secondary batteries due to its good performance derived from their small ionic size allowing fast kinetics and low atomic number leading to high theoretical specific capacity and energy density. These characteristics have made lithium ion batteries to be fully integrated into portable devices and electric vehicles. However, although there is much controversy about the extent of world

---

<sup>26</sup> Tian, Q.; Chen, P.; Zhang, Z. and Yang, L., Achievement of significantly improved lithium storage for novel clewlike  $\text{Li}_4\text{Ti}_5\text{O}_{12}$  anode assembled by ultrafine nanowires, *J. Power Sources*, **2017**, 350, 49-55.

<sup>27</sup> Subramanian, V.; Karki, A.; Gnanasekar, K.I.; Eddy, F. P. and Rambabu, B., Nanocrystalline  $\text{TiO}_2$  (anatase) for Li-ion batteries, *J. Power Sources*, **2006**, 159, 186-192.

<sup>28</sup> Liu, Z., Andreev, Y. G.; Armstrong, A. R.; Brutti, S., Ren, Y. and Bruce, P. G., Nanostructured  $\text{TiO}_2$ (B): the effect of size and shape on anode properties for Li-ion batteries, *Prog. Nat. Sci. : Materials International*, **2013**; 23 (3), 235–244.

lithium's reserves<sup>29</sup>, the large scale demand for this alkali might increase its price in the near future due to the low abundance of it on the Earth's crust.<sup>5</sup> This global situation has driven researchers to investigate new battery technologies based on abundant resources such as magnesium-sulfur, sodium ion, and magnesium ion batteries.<sup>30,31,32</sup>

Sodium ion batteries were investigated in parallel to the lithium ion batteries during the 80s.<sup>33</sup> However, lithium ion batteries drew the attention due to their higher energy density. Despite Na is chemically similar to Li, there are significant differences between them. In Table 1.2, a comparison of the characteristics of both elements is shown.

**Table 1.2** Comparison of the characteristics of Na and Li.<sup>34,5</sup>

Characteristics	Na	Li
Cation radius	1.02Å	0.76Å
Atomic weight	23 g·mol <sup>-1</sup>	6.9 g·mol <sup>-1</sup>
E <sup>0</sup> vs. SHE	-2.7 V	-3.04 V
Melting point	97.7 °C	180.5 °C
Abundance	23.6·10 <sup>3</sup> mg·kg <sup>-1</sup>	20 mg·kg <sup>-1</sup>
Distribution	Everywhere	70 % in South America
Price, carbonates	0.07-0.37 €·kg <sup>-1</sup>	4.11-4.49 €·kg <sup>-1</sup>

<sup>29</sup> Gruber, P. W.; Medina, P. A.; Keoleian, G. A.; Kesler, S. E.; Everson, M. P. and Wallington, T. J., Global lithium availability: a constraint for electric vehicles?, *J. Ind. Ecol.*, **2011**, 15, (5) 760–775.

<sup>30</sup> Tarascon, J. M., Is lithium the new gold?, *Nat. Chem.*, **2010**, 2, 510.

<sup>31</sup> Armand, M. and Tarascon, J.-M., Building better batteries, *Nature*, **2008**, 451, 652-657.

<sup>32</sup> Choi, J. W. and Aurbach, D., Promise and reality of post-lithium-ion batteries with high energy densities, *Nat. Rev. Mat.*, **2016**, 1, 16013.

<sup>33</sup> Whittingham, M. S., Chemistry of intercalation compounds: metal guests in chalcogenide hosts, *Prog. Solid St. Chem.*, **1978**, 12, 41-99.

<sup>34</sup> Palomares, V.; Serras, P.; Villaluenga, I.; Hueso, K. B. ; Carretero-González, J. and Rojo, T., Na-ion batteries, recent advances and present challenges to become low cost energy storage systems *Energy Environ. Sci.*, **2012**, 5, 5884-5901.

Na is cheaper, more abundant and it is more evenly distributed than Li, which is mostly located in South America and, as a consequence, production of LIB depends on the import of Li. Moreover, it is possible to use Al current collectors in the anode electrode instead of Cu, as happens for Li batteries, which can be translated into a decrease of the cost of the battery. However, despite Na and Li are chemically similar, the larger size of Na ions results not only in lower volumetric capacity compared to lithium but also in the lithium ion technology being non-fully transferable to sodium. On the one hand, the different size between Li and Na affects the properties in the host structure of the intercalated and deintercalated materials and, on the other hand, the existence of different surface passivation processes can lead to different electrochemical performance.

Direct anodic application of elemental alkali metals (lithium or sodium) in rechargeable alkaline ion batteries causes poor cycle performance and short-circuits because of their low melting point (180.5 °C for Li and 97.7 °C for Na), high chemical reactivity and dendritic growth during charge and discharge. Therefore, the major challenge in developing sodium ion technology lies in finding good electrode materials.<sup>35</sup> An obvious place to look for good Na electrode materials is by starting at structures and chemistries that work well for Li intercalation. This is because the open crystal structure that allows Li intercalation is often suitable for Na intercalation.<sup>20</sup>

Regarding the applications, sodium ion batteries are becoming one of the most promising alternative technologies for stationary energy storage because the weight of the device is not of primary importance, while the higher energy density makes lithium more appropriate for portable applications. For stationary applications long cycle life, low cost, and high safety are the most important parameters. Hence, abundant, nontoxic, stable and low-strain electrode materials need to be developed to ensure large-scale and long-term applications, and to decrease battery management cost.

---

<sup>35</sup> Hong, S. Y.; Kim, Y.; Park, Y.; Choi, A.; Choi, N.-S. and Lee, K. T., Charge carriers in rechargeable batteries: Na ions vs. Li ions, *Energy Environ. Sci.*, **2013**, 6, 2067-2081.



Figure 1.8 illustrates the several representative candidate materials such as cathode and anode materials reported so far.

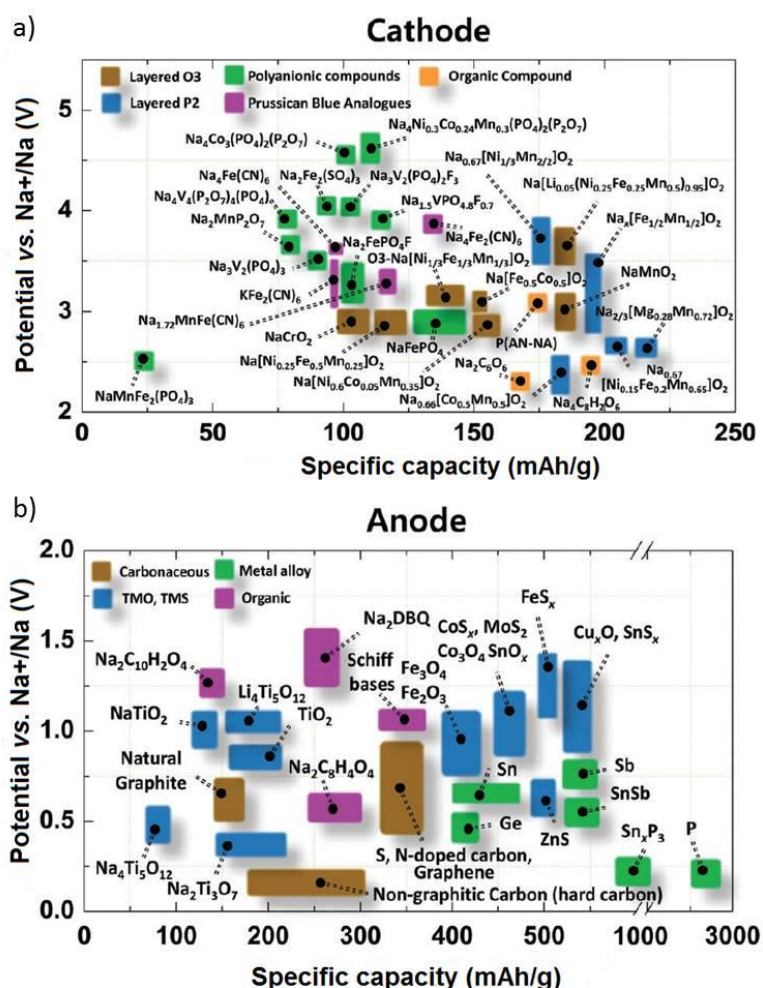


**Figure 1.8** Recent research progress in materials for sodium ion batteries: (a) cathode, (b) anode.

Recent developments in cathode materials for sodium ion batteries include layered oxides, polyanions, Prussian blue and organic compounds whereas anode materials can be categorized into carbonaceous materials, transition metal oxides or sulfides, metal alloys and organic compounds. In the next section, a short description of the main electrode materials reported for sodium ion batteries will be summarized.

### 1.3.2.1 Cathode materials for sodium ion batteries

Similar to LIBs, highly reversible cathode materials based on the intercalation reaction, which involves interstitial introduction of  $\text{Na}^+$ , are needed for high capacity and good cyclability of sodium ion batteries. These electrode materials are mainly categorized into layered oxides, polyanionic compounds, Prussian blue and its analogues and organic cathodes.

**Layered oxides** Among many cathode candidates, layered oxides ( $\text{NaT}_m\text{O}_2$ ,  $T_M = \text{Ti, V, Cr, Mn, Fe, Co, Ni}$ ) offer many advantages due to their simple structures, high theoretical capacities in the  $230\text{--}250 \text{ mA}\cdot\text{h}\cdot\text{g}^{-1}$  range, and ease of synthesis. However, the air sensitivity of most of them can be a major drawback.<sup>36</sup> They are composed of repeating sheets of  $T_M\text{O}_6$  layers with Na ions being sandwiched in between the oxide layers and they can be synthesized in different structures (O3-, P2-, and P3-, Figure 1.9). According to the notation proposed by Delmas *et al.*<sup>37</sup>, the letter indicates the environment where Na is located (O: octahedral, P: prismatic) and the number indicates the number of unique interlayers that are surrounded by different oxide layers.

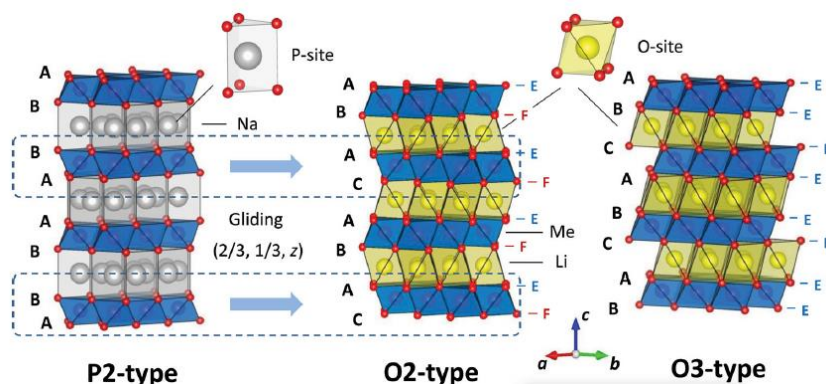


**Figure 1.9** Schematic illustrations of crystal structures for P2-, O2-, and O3-type layered oxides.<sup>38</sup>

<sup>36</sup> Han, M. H.; Gonzalo, E.; Singh, G. and Rojo, T., A comprehensive review of sodium layered oxides: powerful cathodes for Na-ion batteries, *Energy Environ. Sci.*, **2015**, 8, 81-102.

<sup>37</sup> Delmas, C.; Fouassier, C. and Hagemuller, P., Structural classification and properties of the layered oxides, *Physica B+C*, **1980**, 99, 81-85.

<sup>38</sup> Yabuuchi, N.; Hara, R.; Kajiyama, M.; Kubota, K.; Ishigaki, T.; Hoshikawa, A. and Komaba, S., New O2/P2-type Li-excess layered manganese oxides as promising multi-functional electrode materials for rechargeable Li/Na batteries, *Adv. Energy Mater.*, **2014**, 1301453.

In Figure 1.10 a comparison of the reversible capacity and operating voltage of different layered oxide phases is shown.

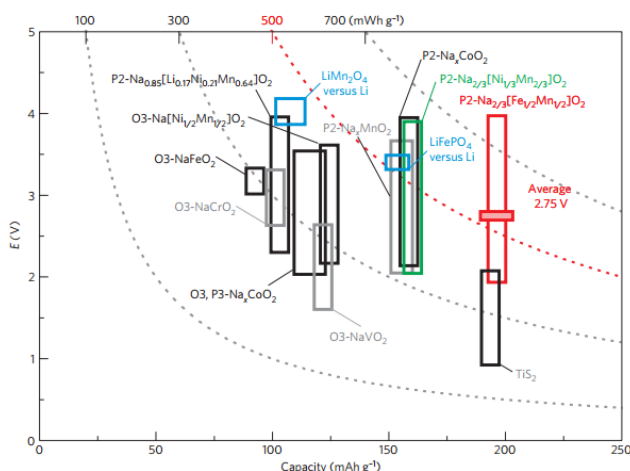


**Figure 1.10** Comparison of reversible capacity and operating voltage ranges of the layered sodium insertion materials.<sup>39</sup>

The  $\text{Na}_x\text{MnO}_2$  system and its derivatives are very interesting because of the Mn is an environmentally friendly element, costing relatively little and allowing number of different oxidation states that might allow the manipulation of products within different voltage ranges (although those most commonly used are  $3+/4+$ ).<sup>40</sup> Thin film electrodes of  $\text{P2-Na}_{0.6}\text{MnO}_2$ , which have a plateau at 2.3 V vs.  $\text{Na}^+/\text{Na}$ , can reach reversible capacity of  $120\text{--}140 \text{ mA} \cdot \text{h} \cdot \text{g}^{-1}$  for 80 cycles.<sup>41</sup> The substitution of Fe for Mn can increase the average voltage and suppress Jahn–Teller distortion leading to improved cyclability.  $\text{P2-Na}_{0.67}\text{Mn}_{0.5}\text{Fe}_{0.5}\text{O}_2$  provides  $190 \text{ mA} \cdot \text{h} \cdot \text{g}^{-1}$  with an average voltage of 2.75 V vs.  $\text{Na}^+/\text{Na}$  sodium metal.<sup>39</sup> The use of cobalt substitution to improve the performance of layered sodium manganese leads to an increase in high voltage capacity and rate capability, though this was accompanied by a less smooth voltage profile and a slight

<sup>39</sup> Yabuuchi, N.; Kajiyama, M.; Iwatate, J.; Nishikawa, H.; Hitomi, S.; Okuyama, R.; Usui, R.; Yamada, Y. and Komaba, S., P2-type  $\text{Na}_x[\text{Fe}_{1/2}\text{Mn}_{1/2}]\text{O}_2$  made from earth-abundant elements for rechargeable Na batteries, *Nat. Mater.*, **2012**, 11, 512–517.

<sup>40</sup> Ortiz-Vitoriano, N.; Drewett, N. E.; Gonzalo, E. and Rojo, T., High performance manganese-based layered oxide cathodes: overcoming the challenges of sodium ion batteries, *Energy Environ. Sci.*, **2017**, Advance Article, DOI:10.1039/C7EE00566K.

<sup>41</sup> Baggetto, L.; Carroll, K. J.; Unocic, R. R.; Bridges, C. A.; Meng, Y. S.; Veith, G. M, Sodium manganese oxide thin films as cathodes for Na-ion batteries, *ECS Transactions*, **2014**, 58 (12) 47–57.

decrease in overall capacity. P2-Na<sub>2/3</sub>Co<sub>2/3</sub>Mn<sub>1/3</sub>O<sub>2</sub> shows one plateau in the 3.5 V to 4.0 V and is able to intercalate 0.5 Na-ion per formula unit between 1.25 V and 4 V vs.

Na<sup>+</sup>/Na leading to a discharge capacity of 119 mA·h·g<sup>-1</sup> at C/100.<sup>42</sup>

**Prussian blue.** There has been also much interest in Prussian blue and its analogues (which possess the general formula A<sub>x</sub>M[D(CN)<sub>6</sub>]<sub>y</sub>·nH<sub>2</sub>O, where A is an alkali metal ion, M is a N-coordinated transition metal cation and D is a C-coordinated transition metal cation as alternative cathode materials to the conventional layered compounds. The reason is their large alkali-ion channels, which enable fast Na de/intercalation without lattice distortion as well as low element cost, toxicity, and easy synthesis at room temperature.<sup>43</sup> As an example, iron based compounds like Na<sub>1-x</sub>Fe<sup>III</sup><sub>1+(x/3)</sub>[Fe<sup>II</sup>(CN)<sub>6</sub>]<sub>y</sub>·H<sub>2</sub>O<sup>44</sup> exhibit a reversible specific charge capacity of 130 mA·h·g<sup>-1</sup>, with good coulombic efficiency and cycling stability whereas sodium manganese hexacyanomanganate (Na<sub>2</sub>Mn<sup>II</sup>[Mn<sup>II</sup>(CN)<sub>6</sub>]) can reach a charge capacity of up to 209 mA·h·g<sup>-1</sup> and a discharge capacity of 57 mA·h·g<sup>-1</sup>.<sup>40</sup>

**Polyanionic compounds.** Polyanion-type electrode materials are a type of compounds that contain a series of tetrahedron anion units (XO<sub>4</sub>)<sup>n-</sup> or their derivatives (X<sub>m</sub>O<sub>3m+1</sub>)<sup>n-</sup> (X = S, P, Si, As, Mo, or W) with strong covalent-bonded MO<sub>x</sub> polyhedra (M=transition metal).<sup>45</sup> Compared to layered oxide compounds, the strong X-O bonding in polyanion-type compounds can introduce ionicity in M-O bonding, leading to a higher redox potential by inductive effect. Furthermore, the strong X-O covalent bonds greatly improve the stability of O in

<sup>42</sup> Carlier, D.; Cheng, J. H.; Berthelot, R.; Guignard, M.; Yoncheva, M.; Stoyanova, R.; Hwang B. J and Delmas, C., 9312 The P2-Na<sub>2/3</sub>Co<sub>2/3</sub>Mn<sub>1/3</sub>O<sub>2</sub> phase: structure, physical properties and electrochemical behavior as positive electrode in sodium battery *Dalton Trans.*, **2011**, 40, 9306-9312.

<sup>43</sup> Kim, H.; Kim, H.; Ding, Z.; Hwan Lee, M.; Lim, K.; Yoon, G. and Kang, K., Recent progress in electrode materials for sodium-ion batteries, *Adv. Energy Mater.*, **2016**, 1600943, DOI: 10.1002/aenm.201600943.

<sup>44</sup> Piernas-Muñoz, M. J.; Castillo-Martínez, E.; Gomez-Cámer, J.L.; Rojo, T., Optimizing the electrolyte and binder composition for sodium prussian blue, Na<sub>1-x</sub>Fe<sub>x+(1/3)</sub>(CN)<sub>6</sub>·yH<sub>2</sub>O, as cathode in sodium ion batteries, *Electrochim. Acta*, **2016**, 200, 123-130.

<sup>45</sup> Ni, Q.; Bai, Y.; Wu, F. and Wu, C., Polyanion-type electrode materials for sodium-ion batteries, *Adv. Sci.*, **2017**, 4, 1600275.

the lattice, thus increasing the safety of such materials.<sup>43</sup> To date, phosphate-, fluorophosphate-, pyrophosphate, sulfate-, and mixed polyanion-based materials have been extensively studied as important groups of potential electrodes.

*Phosphates.* NaFePO<sub>4</sub> (NFP) is the most studied species because it shows highest theoretical capacity (154 mA·h·g<sup>-1</sup>) among phosphate polyanion cathode materials.<sup>46</sup> Electrode performance is dependent on the crystal structure. Olivine (Figure 1.11b) NFP shows a relatively high operating voltage of 2.8 V vs. Na<sup>+</sup>/Na and delivers 120 mA·h·g<sup>-1</sup> whereas maricite (Figure 1.11 a), which is a more thermodynamically stable phase can provide 142 mA·h·g<sup>-1</sup> with good rate performances and negligible capacity decay up to 200 cycles (95% retention).<sup>47,48</sup>

*NASICON-type phosphates.* NASICON (NA Super Ionic CONductor) compounds with general formula A<sub>x</sub>MM'(XO<sub>4</sub>)<sub>3</sub> (M, M'=transition metal ; X=Si, P, S, Mo) have been intensively investigated because of their open framework structure enabling the fast Na ionic conduction. Na<sub>3</sub>V<sub>2</sub>(PO<sub>4</sub>)<sub>3</sub> (Figure 1.11 c) can insert approximately two Na ions (117 mA·h·g<sup>-1</sup>) at 3.6 V with a redox reaction of V<sup>3+</sup>/V<sup>4+</sup>.<sup>49</sup>

*Fluorophosphates.* The introduction of highly electronegative fluorine ions in phosphate-based structures with a general formula of Na<sub>2</sub>MPO<sub>4</sub>F (Me = Fe, Mn, Co, and Ni) increases the operating voltage of the electrodes. Bare Na<sub>2</sub>FePO<sub>4</sub>F delivers almost no capacity but carbon coated material can provide 110 mA·h·g<sup>-1</sup> of reversible capacity, which corresponds to 90% of the theoretical capacity, with

---

<sup>46</sup> Palomares, V.; Casas-Cabanas, M.; Castillo-Martínez, E.; Han, M. H. and Rojo, T., Update on Na-based battery materials. A growing research path, *Energy Environ. Sci.*, **2013**, 6, 2312-2337.

<sup>47</sup> Kim, J.; Seo, D.-H.; Kim, H.; Park, I.; Yoo, J.-K.; Jung, S.-K.; Park, Y.-U.; Goddard III, W. A. and Kang, K., Unexpected discovery of low-cost maricite NaFePO<sub>4</sub> as a high-performance electrode for Na-ion batteries, *Energy Environ. Sci.*, **2015**, 8, 540-545.

<sup>48</sup> Moreau, P.; Guyomard, D.; Gaubicher, J. and Boucher, F., Structure and stability of sodium intercalated phases in olivine FePO<sub>4</sub>, *Chem. Mater.*, **2010**, 22, 4126-4128.

<sup>49</sup> Uebou, Y.; Kiyabu, T.; Okada, S.; Yamaki, J.-i., Electrochemical sodium insertion into the 3D-framework of Na<sub>3</sub>M<sub>2</sub>(PO<sub>4</sub>)<sub>3</sub> M=Fe,V, *Rep. Inst. Adv. Mater. Study, Kyushu Univ.*, **2002**, 16, 1-5.

small polarization and high operating voltage (3.0 V vs.  $\text{Na}^+/\text{Na}$ ).<sup>50</sup> V-based fluorophosphate compounds have also attracted much attention due to the high operating voltage and stable cycle. The  $\text{NaVPO}_4\text{F}$  electrode delivers a discharge capacity of  $82 \text{ mA}\cdot\text{h}\cdot\text{g}^{-1}$  with an average voltage of 3.7 V. Recent works revealed that  $\text{Na}_3\text{V}_2(\text{PO}_4)_2\text{F}_3$  (Figure 1.11d) can reversibly de/intercalate 2  $\text{Na}^+$  into the structure delivering  $128.2 \text{ mA}\cdot\text{h}\cdot\text{g}^{-1}$  through two distinct voltage plateaus at 3.7 and 4.2 V vs.  $\text{Na}^+/\text{Na}$ .<sup>43</sup>

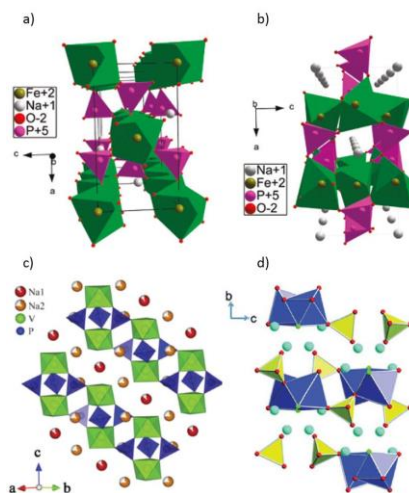


**Figure 1.11** Structure of (a) maricite  $\text{NaFePO}_4$ , (b) olivine  $\text{NaFePO}_4$ <sup>47</sup> (c)  $\text{Na}_3\text{V}_2(\text{PO}_4)_3$ <sup>51</sup> and (d)  $\text{Na}_2\text{FePO}_4\text{F}$ <sup>Error! Marcador no definido.</sup>.

**Organic-based cathode materials** are emerging candidates as alternatives to conventional inorganic electrode materials because of their abundance, safety, environmental friendliness, and high theoretical capacity. Since the aim of this work is the development of organic electrodes, they will be further described in detail in chapter 3.

<sup>50</sup> Kawabe, Y.; Yabuuchi, N.; Kajiyama, M.; Fukuhara, N.; Inamasu, T.; Okuyama, R.; Nakai, I.; Komaba, S., Synthesis and electrode performance of carbon coated  $\text{Na}_2\text{FePO}_4\text{F}$  for rechargeable Na batteries, *Electrochem. Commun.*, **2011**, 13, 1225-1228.

<sup>51</sup> Hwang, J.-Y.; Myung, S.-T. and Sun, Y.-K. , Sodium-ion batteries: present and future, *Chem. Soc. Rev.*, **2017**, Advance article, 10.1039/C6CS00776G

### 1.3.2.2 Anode materials for sodium ion batteries

Several families of compounds such as transition metal based compounds, alloys, carbonaceous materials and organics have been studied as anode materials for sodium ion batteries.

#### Transition metal based compounds

*Ti-based compounds.* Ti-based compounds are the most studied transition metal compounds due to its low cost, abundance and low toxicity.<sup>52</sup> They undergo intercalation reactions between +5 and +2 oxidation states. Several TiO<sub>2</sub> polymorphs can insert Na<sup>+</sup> reversibly. The first structural polymorph reported to insert Na<sup>+</sup> ions was anatase. Despite the mechanism is still controversial, anatase TiO<sub>2</sub> nanoparticles can deliver a capacity of 100 mA·h·g<sup>-1</sup> with good rate capabilities (86 mA·h·g<sup>-1</sup> at 5.5 C).<sup>53</sup> Amorphous nanotubes of TiO<sub>2</sub> can also achieve good capacity (150 mA·h·g<sup>-1</sup>) when cycled between 2.5 and 0.9 V vs. Na<sup>+</sup>/Na. Rutile<sup>54</sup> and monoclinic TiO<sub>2</sub> (B)<sup>55</sup> reach 100 mA·h·g<sup>-1</sup> and 87 mA·h·g<sup>-1</sup> of reversible capacity in the 0.005-3 V and in the 0.005-3 V vs. Na<sup>+</sup>/Na voltage range, respectively. However, the latter shows a lower initial coulombic efficiency due to the irreversible capture of sodium in the first cycle on the surface and inside the interlayer of TiO<sub>2</sub>(B) nanotube. Hollandite, which shows a more open structure than anatase can also reversibly insert Na ions through a structural transition to slightly distorted monoclinic structure. It delivers 85 mA·h·g<sup>-1</sup>.<sup>56</sup> The structures of the TiO<sub>2</sub> polymorphs are shown in Figure 1.12 a, b, c and d.

---

<sup>52</sup> Muñoz-Márquez, M. A.; Saurel, D.; Gómez-Cámer, J. L.; Casas-Cabanas, M.; Castillo-Martínez, E. and Rojo, T.; Na-ion batteries for large scale applications: a review on anode materials and solid electrolyte interphase formation, *Adv. Energy. Mat.*, **2017**.

<sup>53</sup> Wu, L.; Buchholz, D.; Bresser, D.; Gomes Chagas, L.; Passerini, S., TiO<sub>2</sub> nanoparticles for high power sodium-ion anodes, *J. Power Sources*, **2014**, 251, 379-385.

<sup>54</sup> Usui, H.; Yoshioka, S.; Wasada, K.; Shimizu, M.; Sakaguchi, H., Nb-Doped Rutile TiO<sub>2</sub>: a Potential anode material for Na-ion battery, *ACS Appl. Mater. Interfaces*, **2015**, 7, 6567-6573.

<sup>55</sup> Huang, J. P.; Yuan, D. D.; Zhang, H. Z.; Cao, Y. L.; Li, G. R.; Yang, H. X.; Gao, X. P.; Electrochemical sodium storage of TiO<sub>2</sub>(B) nanotubes for sodium ion batteries, *RSC Adv.*, **2013**, 3, 12593-12597.

<sup>56</sup> Perez-Flores, J. C.; Baehtz, C.; Kuhna, A. and García -Alvarado, F., Hollandite-type TiO<sub>2</sub>: a new negative electrode material for sodium-ion batteries, *J. Mater. Chem. A*, **2014**, 2, 1825-1833.

Among ternary titanium oxides,  $\text{Na}_2\text{TiO}_3$  is by far the most studied compound since it is able to intercalate reversibly two sodium ions at relatively low voltage (0.3 V vs.  $\text{Na}^+/\text{Na}$ ). This material has a theoretical capacity of  $177 \text{ mA}\cdot\text{h}\cdot\text{g}^{-1}$  and it is able to achieve capacities close to the theoretical at current rate of  $C/10$ .<sup>57</sup> The structure is shown in Figure 1.12 e.

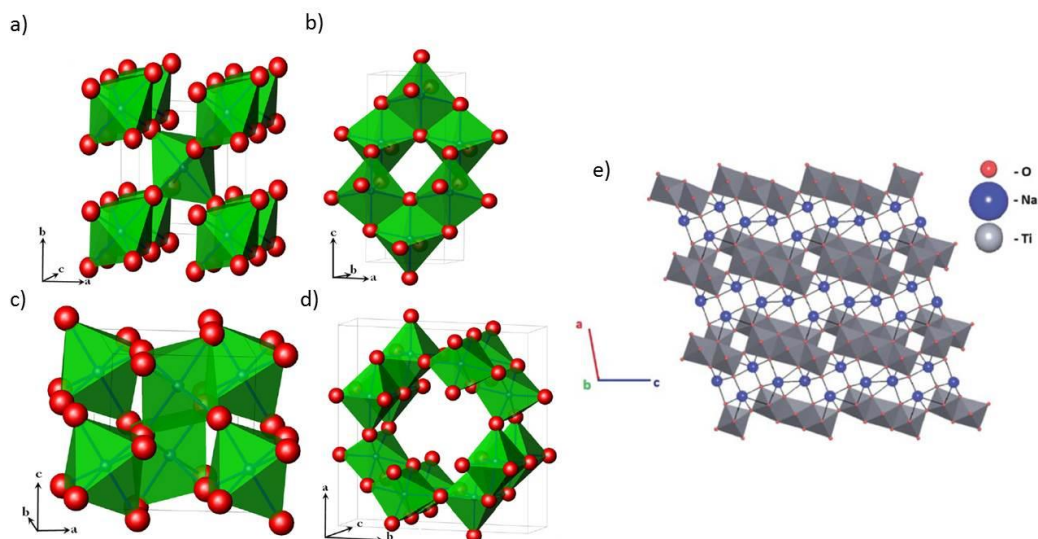


**Figure 1.12** Structure of a)  $\text{TiO}_2$  rutile, b)  $\text{TiO}_2$  anatase, c)  $\text{TiO}_2$  (B), d) hollandite and e)  $\text{Na}_2\text{Ti}_2\text{O}_7$ .<sup>57,58</sup>

*Conversion materials.* Some kinds of transition metal oxide (TMO), transition metal sulfide (TMS) and transition metal phosphides (TMP) have been considered as potential anode materials for SIBs due to their high theoretical specific capacities. However, these compounds react with  $\text{Na}^+$  ions through conversion reactions involving large volume expansion/contraction upon the sodiation–desodiation process which usually leads to the loss of electrical contact and subsequently capacity fade. Moreover, poor mobility of  $\text{Na}^+$  ions due to the large ionic size is still a challenge to fully utilize their theoretical capacity.<sup>51</sup> Some of the conversion materials investigated as anode materials include  $\text{Fe}_2\text{O}_3$ ,  $\text{Co}_3\text{O}_4$ ,  $\text{CuO}$ , sulfides such as  $\text{FeS}_2$ ,  $\text{CoS}_2$ ,  $\text{SnS}_2$  and  $\text{MoS}_2$ .<sup>51</sup>

<sup>57</sup> Rudola, A.; Saravanan, K.; Mason C. W. and Balaya, P.,  $\text{Na}_2\text{Ti}_3\text{O}_7$ : an intercalation based anode for sodium-ion battery applications, *J. Mater. Chem. A*, **2013**, 1, 2653–2262.

<sup>58</sup> Aravindan, V.; Lee, Y.-S.; Yazami, R. and Madhavi, S.,  $\text{TiO}_2$  polymorphs in ‘rocking-chair’ Li-ion batteries, *Mater. Today*, **2015**, 18, (6), 345–351. .



$\text{Fe}_2\text{O}_3$  (Figure 1.13 a) has been considered to be a promising electrode material due to its excellent chemical stability, high capacity, easy fabrication, low cost and nontoxicity. It delivers  $386 \text{ mA}\cdot\text{h}\cdot\text{g}^{-1}$  at  $100 \text{ mA}\cdot\text{g}^{-1}$  for over 200 cycles.<sup>59</sup> However, it shows high voltage hysteresis of roughly 0.75–1.0 V vs.  $\text{Na}^+/\text{Na}$ . Cu-based oxides, like other metal oxides are hindered by a large volume change during cycling but nano-structuration can improve the electrochemical performance as for CuO/C spheres, which deliver  $402 \text{ mA}\cdot\text{h}\cdot\text{g}^{-1}$  for 600 cycles (at a current density of  $200 \text{ mA}\cdot\text{g}^{-1}$ ).<sup>60</sup>  $\text{Co}_3\text{O}_4$  exhibits also high reversible capacity ( $447 \text{ mA}\cdot\text{h}\cdot\text{g}^{-1}$ ) in the voltage window of 0.01–3.0 V vs.  $\text{Na}^+/\text{Na}$  with an 86 % of capacity retention after 50 cycles.<sup>61</sup>

Sulfides have great advantages during the sodiation/desodiation process because their M–S bonds are weaker than the corresponding M–O bonds in metal oxides, which can be kinetically favorable for conversion reactions with  $\text{Na}^+$  ions.  $\text{MoS}_2$ , which has received much attention, can store  $\text{Na}^+$  ions through both intercalation and/or conversion reactions depending on the operation voltage window. It is typically combined with other materials like graphene in order to overcome low conductivity. A capacity of  $240 \text{ mA}\cdot\text{h}\cdot\text{g}^{-1}$  can be obtained for a  $\text{MoS}_2$  in reduced graphene oxide.<sup>62</sup>

Despite phosphides show continuous pulverization during sodiation and desodiation, a tin-phosphorous compound ( $\text{Sn}_4\text{P}_3$ ) delivering  $718 \text{ mA}\cdot\text{h}\cdot\text{g}^{-1}$  for 100 cycles has been successfully synthesized.<sup>63</sup> In Figure 1.13 b, a scheme of the conversion reaction of  $\text{Sn}_4\text{P}_3$  is shown.

---

<sup>59</sup> Jiang, Y.; Hu, M.; Zhang, D.; Yuan, T.; Sun, W.; Xu, B. and Yan, M., Transition metal oxides for high performance sodium ion battery anodes, *Nano Energy*, **2014**, 5, 60-66.

<sup>60</sup> Lu, Y.; Zhang, N.; Zhao, Q.; Liang, J. and Chen, J., Micro-nanostructured CuO/C spheres as high-performance anode materials for Na-ion batteries, *Nanoscale*, **2015**, 7, 2770-2776.

<sup>61</sup> Rahman, M. M.; Glushenkov, A. M.; Ramireddy, T. and Chen, Y., Electrochemical investigation of sodium reactivity with nanostructured  $\text{Co}_3\text{O}_4$  for sodium-ion batteries, *Chem. Commun.*, **2014**, **50**, 5057-5060.

<sup>62</sup> David, L.; Bhandavat, R. and Singh, G.,  $\text{MoS}_2$ /Graphene Composite paper for sodium-Ion battery electrodes, *ACS Nano*, **2014**, 8 (2), 1759-1770.

<sup>63</sup> Kim, Y.; Kim, Y.; Choi, A.; Woo, S.; Mok, D.; Choi, N. S.; Jung, Y. S.; Ryu, J. H.; Oh S. M and Lee, K. T., Tin phosphide as a promising anode material for Na-ion batteries, *Adv. Mater.*, **2014**, 26, 4139-4144.

*Transition metal carbodiimides.* They are metalorganic compounds where transition metals (TM = Mn, Fe, Co, Ni) are bonded to the carbodiimide ( $-N=C=N-)^{2-}$  group. This group has many similarities with the oxide group ( $O^{2-}$ ) as both have the same charge (2-) and similar electronegativity. However, transition metal carbodiimides improve the energy density and efficiency in comparison with oxides due to the lower voltage where the conversion reaction occurs. FeNCN (Figure 1.13 c), which delivers  $400 \text{ mA}\cdot\text{h}\cdot\text{g}^{-1}$  of reversible capacity, shows a low voltage plateau (0.3 V vs.  $\text{Na}^+ / \text{Na}$ ) with small first cycle irreversible capacity ( $220 \text{ mA}\cdot\text{h}\cdot\text{g}^{-1}$ ).<sup>64</sup>

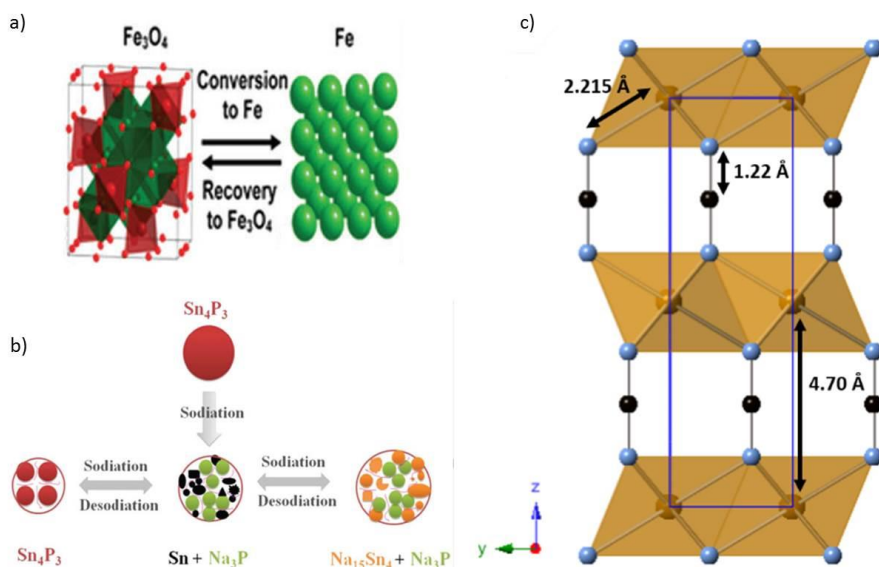


**Figure 1.13** a) Structure of  $\text{Fe}_3\text{O}_4$ <sup>51</sup> b) conversion reaction for the  $\text{Sn}_4\text{P}_3$  anode<sup>51</sup> c) structure of FeNCN<sup>64</sup>.

**Alloys.** Alloying reaction materials can store a large number of sodium ions in the host structure with a relatively low operating potential (below 1.0 V) Metals (Sn, Bi), metalloids (Si, Ge, As, Sb) and polyatomic nonmetal compounds (P) in group 14 or 15 elements in the periodic table have been widely studied as potential anode materials for SIBs. However, depending on the host materials and electrochemical sodiation levels, volume changes upon cycling give rise to mechanical stresses in active particles, leading to pulverization of the electrode.<sup>51</sup>

<sup>64</sup> Eguia-Barrio, A.; Castillo-Martínez, E.; Liu, X.; Dronskowski, R.; Lezama, L.; Armand, M. and Rojo, T. Advanced anode materials for sodium ion batteries: carbodiimides, *MRS Advances*, **2017**,

In order to overcome the pulverization problem, several strategies such as the use of nanosized particles or nanostructures that accommodate the strain, the use of carbon coating or as a matrix where metals can be embedded, and the design of intermetallics by alloying the active element, have been reported.<sup>52</sup>

Given the fact that the abundance of Ge is very low in the Earth's crust, it is not suitable for low cost applications. Sn, on the contrary, has been regarded as one of the most promising anode materials owing to its high abundance along with high theoretical specific capacity of  $(847 \text{ mA}\cdot\text{h}\cdot\text{g}^{-1})$  for the fully sodiated phase  $\text{Na}_{15}\text{Sn}_4$ ). Experimentally, capacities of about  $600 \text{ mA}\cdot\text{h}\cdot\text{g}^{-1}$  (C/10) can be obtained for a few cycles using a conductive binder.<sup>65</sup>

Antimony delivers a theoretical capacity of  $660 \text{ mA}\cdot\text{h}\cdot\text{g}^{-1}$  according to formation of  $\text{Na}_3\text{Sb}$ . However, it also suffers from drastic volume changes of about 390% during the Na alloying/dealloying process. The use of carbon composites partially solves the problem of pulverization allowing a large reversible capacity of  $631 \text{ mA}\cdot\text{h}\cdot\text{g}^{-1}$  at (C/15) for over 400 cycles although they usually show structural instability originated from the weak interaction between the active component and the carbon matrix.<sup>66</sup>

*Phosphorous.* Phosphorus reacts electrochemically with sodium to form  $\text{Na}_3\text{P}$  at 0.4 V vs.  $\text{Na}^+/\text{Na}$ , with a very high theoretical capacity of  $2596 \text{ mA}\cdot\text{h}\cdot\text{g}^{-1}$  derived from its light atomic weight. Among the three allotropes of white phosphorous, red phosphorus (red-P) is usually amorphous in nature and is widely commercially available (Figure 1.14). Experimentally, it delivers almost 2000

---

DOI:10.1557/adv.201.267.

<sup>65</sup> Dai, K.; Zhao, H.; Wang, Z.; Song, X.; Battaglia, V.; Liu, G., Toward high specific capacity and high cycling stability of pure tin nanoparticles with conductive polymer binder for sodium ion batteries, *J. Power Sources*, **2014**, 263, 276-279.

<sup>66</sup> Wu, L.; Hu, X.; Qian, J.; Pei, F.; Wu, F.; Mao, R.; Ai, X.; Yang H. and Cao Y., Sb-C nanofibers with long cycle life as an anode material for high-performance sodium-ion batteries, *Energy Environ. Sci.*, **2014**, 7, 323-328.

$\text{mA}\cdot\text{h}\cdot\text{g}^{-1}$  with stable capacity for 30 cycles.<sup>67</sup> However, its toxicity can prevent its use in commercial devices.

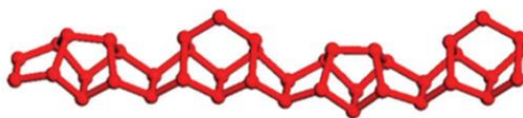


**Figure 1.14** Structure of red phosphorus.

**Carbon based materials.** For practical utilization of sodium ion batteries, low-cost anode materials similar to graphite anodes in lithium ion batteries are also needed. As pristine graphite shows negligible electrochemical activity with Na, other carbon-based materials such as disordered carbon will be the dominant player for the anodes of NIBs.<sup>!Error! Marcador no definido.</sup> In this thesis, the synthesis of carbonaceous materials will be carried out. For that reason, carbon-based anode materials will be reviewed in chapter 2.

**Organic compounds** have received much less attention as potential anodes for sodium ion batteries because of the success of inorganic materials in commercial applications. However, new requirements in secondary batteries such as flexibility accompanied by low production costs and environmental friendliness, reach the limit of inorganic electrode materials. In this respect, organic compounds have several advantages, including their chemical diversity, tunable redox property, lightweight, mechanical flexibility and cost-effective aspects, thus offering a wide selection of applications for use in batteries.<sup>51,68</sup> Being the scope of this thesis, the development of organic anodes, a summary of the most relevant compounds will be presented in chapter 3.

Under the drive of searching a feasible substitute for lithium ion batteries, the studies of sodium ion batteries have increased rapidly. However, the lack of suitable electrode materials has prevented their commercialization. Given the fact that rechargeable battery systems utilizing Na as a guest ion have been

---

<sup>67</sup> Kim, Y.; Park, Y.; Choi, A.; Choi, N. S.; Kim, J.; Lee, J.; Ryu, J.H.; Oh, S. M. and Lee, K. T., An amorphous red phosphorus/carbon composite as a promising anode material for sodium ion batteries, *Adv. Mater.*, **2013**, 25, 3045-3049.

<sup>68</sup> Song, Z. and Zhou, H.; Towards sustainable and versatile energy storage devices: an overview of organic electrode materials, *Energy Environ. Sci.*, **2013**, 2280- 2301.

extensively studied in order to develop less expensive and sustainable energy storage systems based on the abundance and easy accessibility of Na, it seems reasonable the search for low cost electrode materials.

**Motivation to further investigate organics and carbons as negative electrodes in Na-Ion batteries.** Organic electrodes and biomass derived carbons which are subject of study in this thesis are interesting candidates due to the low cost of their precursors compared to the traditional transition metal based electrodes which might imply resource limitations, environmental pollution and large energy consumption in both synthesis and recycling. Organic electrode materials could be ideally extracted directly or eventually synthesized from biomass and easily recycled. Likewise, biomass derived carbons can be synthesized from organic wastes, providing an added value to them. Moreover, although in recent years most interest has been focused on research on inorganic compounds, **organic electrodes** have many distinct merits over them in terms of reaction kinetics, structure diversity flexibility and processability. **Carbons** are considered the most promising anode material for sodium ion batteries because of their non-toxicity, high capacity and safety. For these reasons, poly-Schiff base based polymers and lignin derived hard carbons will be studied in this work.

### 1.4 Scope of this thesis

The main objective of this thesis is the search of new low cost anode materials based on abundant precursors such as organic molecules or natural polymers byproducts from industry that can enable non-expensive and sustainable energy storage systems such as sodium ion batteries.

On that basis, the following aspects have been addressed:

- 1) Development of **hard carbons** using as precursor **lignin isolated from an industrial waste**, which are competitive anode materials in Na-ion batteries. This involves:
  - Synthesis optimization and structural and morphological characterization of lignin derived hard carbons.
  - Electrochemical characterization of lignin derived hard carbons as anodes in sodium ion half cells.
  - Comparison of the structural, morphological and electrochemical properties of lignin derived hard carbons with those of carbonaceous materials synthesized from other precursors (sugar, polyvinyl chloride) and with a commercially available carbon black.
  - Study of the electrochemical performance of a soft carbon in a full-cell.
  
- 2) Development of a **double-rolled** organic material based on **polySchiff-bases-PEO copolymer** that keeps the redox activity of polySchiff bases and add the binding properties of the PEO units. This involves:
  - Synthesis of polySchiff base- polyethylene oxide copolymers (PSB-PEO) with improved processability with respect to bare polySchiff bases.
  - Structural, morphological and physico-chemical characterization of polySchiff base-polyethylene oxide copolymers.
  - Study of the electrochemical performance of polySchiff base-polyethylene oxide copolymers as binder free anode materials in powder and film form in sodium ion half cells.
  - Study of the electrochemical performance of polySchiff base-polyethylene oxide copolymers as binder of other active materials in sodium ion half cells.
  - Study of the optimized polySchiff base-polyethylene oxide copolymer as anode material in a full-cell.

## 1.5 Structure of this thesis

The thesis is divided into five chapters and one annex. First chapter is an introduction to the energy storage. In the second, third and fourth chapters, the experiments, results and discussions are presented. The fifth chapter is a brief summary of the most relevant conclusions. In the annex, the characterization techniques are explained in detail.

Hereafter, an overview of each chapter is presented:

**Chapter 1.** In this chapter the **need for the electrochemical energy** storage is introduced along with a brief review of the different **existing electrode materials** for sodium ion batteries and the **motivation** towards the selection of the materials that will be further studied.

**Chapter 2.** In this chapter, the experimental details conducting to the attainment of **lignin-derived hard carbons** together with other carbonaceous anodes are presented along with their structural, morphological and electrochemical characterization.

**Chapter 3.** In this section, the synthesis and characterization of **polySchiff base -polyethylene oxide copolymer** is detailed. The electrochemical performance of the material is initially studied in powder form as a base for synthesis optimization and further tested as binder-free anodes in order to achieve the aim of getting a redox active binder material.

**Chapter 4.** In this part, the behavior of one of each type of the studied materials (PVC derived soft carbon and optimized polySchiff-polyethylene oxide copolymer) are evaluated as anodes in a **full-cell system**.

**Chapter 5.** The most relevant **conclusions** are described in this section.

**Annex.** The appendix is devoted to the explanation of the **theoretical bases** of the different characterization techniques employed in this work.





---

# Chapter 2. Biomass derived carbon anodes for sodium ion batteries

---

## 2.1 Introduction

### 2.1.1 Carbon materials

There are several carbon allotropes, for example, graphite with a  $sp^2$  hybrid orbital, diamond with a  $sp^3$  hybrid orbital, and carbene with a  $sp$  hybrid orbital. Among them,  $sp^2$  carbons have been extensively studied as electrode material candidates for sodium rocking chair batteries because they are capable of undergoing reversible intercalation/deintercalation of sodium.

#### 2.1.1.1 Structure of $sp^2$ carbons

*Graphite.* In graphite, graphene layers are formed by carbon atoms of the  $sp^2$  hybrid orbital layered along a hexagonal plane. Delocalized  $\pi$  electrons have Van der Waals bondings between graphene layers. Since  $\pi$  electrons have freedom to move between graphene layers, graphite has a good electronic conductivity.<sup>1</sup>

---

<sup>1</sup> Park, J.-K., *Principles and applications of lithium secondary batteries*, 2012, Wiley-VCH Verlag, Weinheim, Germany, 92-93.



graphitizable carbons because they can be graphitized under heat treatment. In general, the graphitization process includes the expansion and stacking of graphitic planes, in a three-dimensional manner. During graphitization, carbon undergoes an increase in density and crystallite sizes ( $L_a$  and  $L_c$ ), respectively and a decrease in (002) interplanar spacing. (Figure 2.2) The turbostratic disorder is removed and strain in the material, relieved.

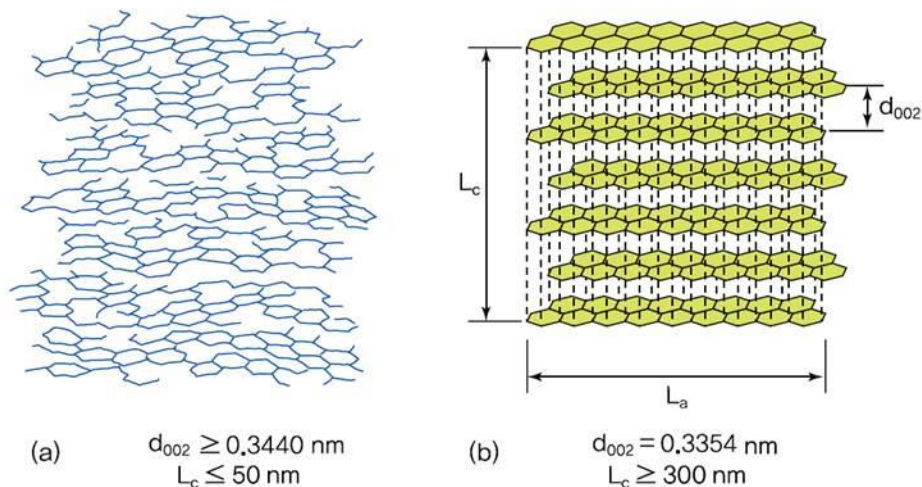


**Figure 2.2** Comparison of the structure of (a) a disordered carbon with turbostratic disorder and (b) 3D graphite lattice.

In soft carbons, the crosslinking between the layers is weak due to Van der Waals bonding, so layers are mobile enough upon further heat-treatment at high temperatures to form graphite-like crystallites. In contrast, strong cross-linking will immobilize graphene layers avoiding graphitization by heat treatment and increasing their mechanical strength leading to “hard” or non-graphitizable carbons.<sup>4</sup>

Whether the final product after pyrolysis will be hard or soft carbon depends mainly on the nature of the precursor. Oxygen-rich precursors tend to form hard carbon whereas hydrogen rich precursors usually lead to soft-carbons.

<sup>4</sup> Franklin, R., The structure of graphitic carbons, *Acta Cryst.*, **1951**, 4, 253-261.

Disordered carbons are produced by means of pyrolysis of organic precursors at temperatures exceeding 500 °C and the ability to graphitize is related to the ordering and texture of the organic precursor.<sup>5</sup> The presence of large content of oxygen and low content of hydrogen in the precursor facilitates the formation of hard carbons.<sup>6</sup> Therefore, hard carbons are typically prepared from polymers such as polyvinylpyrrolidone,(PVP),<sup>7</sup> wood,<sup>8</sup> oak leaves,<sup>9</sup> wool,<sup>10</sup> resorcinol-formaldehyde,<sup>11</sup> cotton,<sup>12</sup> pomelo peels,<sup>13</sup> sugar,<sup>14</sup> apple wastes,<sup>15</sup> corn cob,<sup>16</sup> mangosteen shells,<sup>17</sup> peanut shell<sup>18</sup> and okara<sup>19</sup>.

- 
- <sup>5</sup> Franklin, R., Crystallite growth in graphitizing and non-graphitizing carbons, *Proc. R. Soc. Lond. A*, **1951**, 209, 196-218.
- <sup>6</sup> Muñoz-Márquez, M. A.; Saurel, D.; Gómez-Cámer, J. L.; Casas Cabanas, M.; Castillo- Martínez, E. and Rojo, T., Na-ion batteries for large scale applications: a review on anode materials and solid electrolyte interphase formation, *Adv. Energy Mater.*, **2017**.
- <sup>7</sup> Bai, Y.; Liu, Y.; Li, Y.; Ling, L.; Wu, F. and Wu, C., Mille-feuille shaped hard carbons derived from polyvinylpyrrolidone via environmentally friendly electrostatic spinning for sodium ion battery anodes, *RSC Adv.*, **2017**, 7, 5519-5527.
- <sup>8</sup> Shen, F.; Luo, W.; Dai, J.; Yao, Y.; Zhu, M.; Hitz, E.; Tang, Y.; Chen, Y.; Sprenkle, Vincent L.; Li, X. and Hu, L., Ultra-thick, low-tortuosity, and mesoporous wood carbon anode for high-performance sodium-ion batteries, *Adv. Energy Mater.*, **2016**, 6, 1600377.
- <sup>9</sup> Li, H.; Shen, F.; Luo, W.; Dai, J.; Han, X.; Chen, Y.; Yao, Y.; Zhu, H.; Fu, K.; Hitz, E. and Hu, L., Carbonized-leaf membrane with anisotropic surfaces for sodium-ion battery, *ACS Appl. Mater. Interfaces*, **2016**, 8, 2204-2210.
- <sup>10</sup> Zhu, X.; Li, Q.; Qiu, S.; Liu, X.; Xiao, L.; Ai, X.; Yang, H. and Cao, Y., Hard carbon fibers pyrolyzed from wool as high-performance anode for sodium-ion batteries *JOM*, **2016**, 68, 10, 2579- 2584.
- <sup>11</sup> Hasegawa, G.; Kanamori, K.; Kannari, N.; Ozaki, J.; Nakanishi, K. and Abe, T., Studies on electrochemical sodium storage into hard carbons with binder-free monolithic electrodes, *J. Power Sources*, **2016**, 318, 41-48.
- <sup>12</sup> Li, Y.; Hu, Y.-S.; Titirici, M. M.; Chen, L.; Huang, X., Hard Carbon Microtubes Made from Renewable Cotton as High-Performance Anode Material for Sodium-Ion Batteries, *Adv. Energy Mater.*, **2016**, 6, 1600659.
- <sup>13</sup> Hong, K.-I.; Qie, L.; Zeng, R.; Yi, Z.-q.; Zhang, W.; Wang, D.; Yin, W.; Wu, C.; Fan, Q.-J. Zhang, W.-X. and Huang, Y.-H., Biomass derived hard carbon used as a high performance anode material for sodium ion batteries, *J. Mater. Chem. A*, **2014**, 2, 12733-12738.
- <sup>14</sup> Ponrouch, A.; Goñi, A.R. and Palacín, M. R., High capacity hard carbon anodes for sodium ion batteries in additive free electrolyte, *Electrochem. Commun.*, **2013**, 27, 85-88.
- <sup>15</sup> Wu, L.; Buchholz, D.; Vaalma, C.; Giffin, G. A.; Passerini S., Apple-biowaste-derived hard carbon as a powerful anode material for Na-ion batteries, *ChemElectroChem*, **2016**, 3, 292-298.

Soft carbons are usually obtained from highly condensed aromatic hydrocarbon precursors such as mesophase pitch,<sup>20</sup> coal tar pitch,<sup>21</sup> phosphorous doped pitch,<sup>22</sup> 3,4,9,10-perylene-tetracarboxylicacid-dianhydride (PTCDA)<sup>23</sup> or from petroleum or coal refinement or plastics with low oxygen content.

### 2.1.1.2 Sodium storage mechanism of $sp^2$ carbons

**Graphite.** Graphite is the most common anode material for commercialized LIBs, which can exhibit a capacity of  $372 \text{ mA}\cdot\text{h}\cdot\text{g}^{-1}$ , corresponding to the formation of graphite intercalation compound ( $\text{LiC}_6$ ).<sup>24</sup> However, the conventional graphite cannot be applied as efficient anode material for SIBs in the usual way since the sodium intercalation into graphite is limited to the formation of  $\text{NaC}_{70}$  equivalent to a poor capacity of  $31 \text{ mA}\cdot\text{h}\cdot\text{g}^{-1}$ .<sup>25</sup> To realize the sodium storage of graphite,

---

<sup>16</sup> Liu, P.; Li, Y.; Hu, Y.-S.; Li, H.; Chen, L. and Huang, X., A waste biomass derived hard carbon as a high performance anode material for sodium-ion batteries, *J. Mater. Chem. A*, **2016**, 4, 13046-13052.

<sup>17</sup> Wang, K.; Jin, Y.; Sun, S.; Huang, Y.; Peng, J.; Luo, J.; Zhang, Q.; Qiu, Y.; Fang, C. and Han, J., Low-cost and high-performance hard carbon anode materials for sodium-ion batteries, *ACS Omega*, **2017**, 2, 1687-1695.

<sup>18</sup> Lv, W.; Wen, F.; Xiang, J.; Zhao, J.; Li, L.; Wang, L.; Liu, Z. and Tian, Y., Peanut shell derived hard carbon as ultralong cycling anodes for lithium and sodium batteries, *Electrochim. Acta*, **2015**, 176, 533-541.

<sup>19</sup> Yang, T.; Qian, T.; Wang, M.; Shen, X.; Xu, N.; Sun, Z. and Yan, C., A sustainable route from biomass byproduct okara to high content Nitrogen-doped carbon sheets for efficient sodium ion batteries, *Adv. Mater.*, **2016**, 28, 539-545.

<sup>20</sup> Cao, B.; Liu, H.; Xu, B.; Lei, Y.; Chen, X. and Song, H., Mesoporous soft carbon as anode material for sodium ion batteries with superior rate and cycling performance, *J. Mater. Chem. A*, **2016**, 4, 6472-6478.

<sup>21</sup> Song, L.-J.; Liu, S.-S.; Yu, B.-J.; Wang, C.-Y. and Li, M.-W., Anode performance of mesocarbon microbeads for sodium-ion batteries, *Carbon*, **2015**, 95, 972-977.

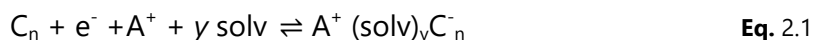
<sup>22</sup> Miao, Y.; Zong, J. and Liu, X., Phosphorus-doped pitch-derived softcarbon as an anode material for sodiumion batteries, *Mater. Lett.*, **2017**, 188, 355-358.

<sup>23</sup> Luo, W.; Jian, Z.; Xing, Z.; Wang, W.; Bommier, C.; Lerner, M. M. and Ji, X., Electrochemically expandable soft carbon as anodes for Na-ion Batteries, *ACS Cent. Sci.*, **2015**, 1, 516-522.

<sup>24</sup> Winter, M.; Besenhard, J. O.; Spahr, M. E. and Novák, P., Insertion Electrode materials for rechargeable lithium batteries, *Adv. Mater.*, **1998**, 10, 725-763.

<sup>25</sup> Doeff, M. M.; Ma, Y.; Visco, S. J. and De Jonghe, L. C., Electrochemical insertion of sodium into carbon, *J. Electrochem. Soc.*, **1993**, 140, (12), L169-L170.

some special treatments have to be undertaken. One approach is based on the use of graphite oxide and expanded graphite which, due to the enlargement of the interlayer spacing, can effectively store  $\text{Na}^+$  through intercalation.<sup>26</sup> However, intercalation is not just matter of diameter of the intercalating alkali metal as the insertion through the co-intercalation of  $\text{Na}^+$  and solvent molecules has been reported to happen according to the reaction in Eq. 2.1.<sup>27</sup>



**Disordered carbons.** Due to their good conductivity, non-toxicity, electrochemical activity at low voltages and potential low cost, disordered hard and soft carbons are the main candidates to become anode materials in commercial sodium ion batteries. The nature of the reaction mechanism of sodium insertion in disordered carbons is controversial. The existing proposed mechanisms are summarized below.

- *Insertion-Adsorption mechanism*

Until recently, it has been accepted the “house of cards” (Figure 2. 3 a) mechanism proposed by Dahn *et al.* in 2000.<sup>28,29</sup> According to it, in disordered carbons, the turbostratic disorder between graphene layers creates interlayer insertion sites for sodium ions with a range of chemical environments, giving rise to a range of potentials, thus a sloping voltage on the electrochemical profile below 1V vs.  $\text{Na}^+/\text{Na}$ . Additionally, hard carbons show a low voltage plateau which can be ascribed to the filling of the micro-pores of the voids between randomly stacked layers.

---

<sup>26</sup> Wen, Yang; He, Kai; Zhu, Yujie; Han, Fudong; Xu, Yunhua; Matsuda, Isamu; Ishii, Yoshitaka; Cumings, John; Wang, Chunsheng, Expanded graphite as superior anode for sodium-ion batteries, *Nature Commun.*, **2014**, 5:4033.

<sup>27</sup> Jache B. and Adelhelm P., Use of graphite as a highly reversible electrode with superior cycle life for sodium-ion batteries by making use of co-intercalation phenomena, *Angew. Chem. Int. Ed.*, **2014**, 53, 10169-10173.

<sup>28</sup> Stevens, D. A. and Dahn, J. R., High capacity anode materials for rechargeable sodium-ion batteries, *J. Electrochem. Soc.*, **2000**, 147 (4), 1271-1273.

<sup>29</sup> Stevens, D. A. and Dahn, J. R.; The mechanisms of lithium and sodium insertion in carbon materials, *J. Electrochem. Soc.*, **2001**, 148 (8), A803-A811.

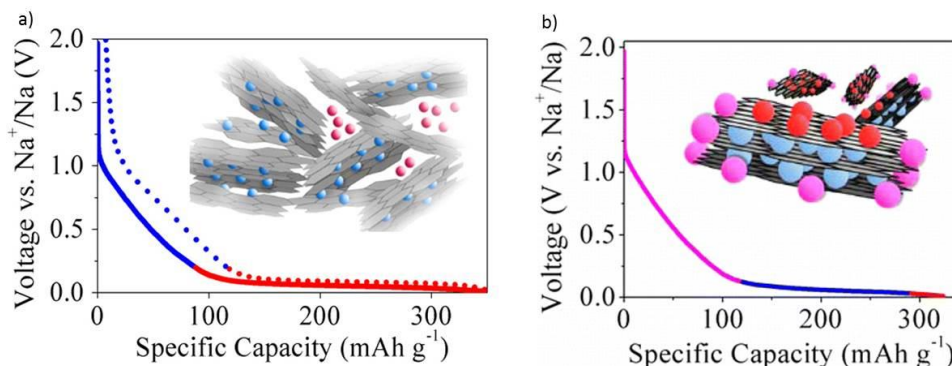


**Figure 2. 3** Visual representation of a) the house of cards model for the sodium/lithium storage in hard carbon showing two distinct parts in the voltage profile: intercalation inside the turbostratic nanodomains (blue) and pore filling (red). b) Three-step mechanism proposed by Bommier *et al.* showing three distinct binding sites.<sup>31</sup>

Although some experimental results have confirmed this mechanism, researchers have also found that it cannot be used to explain several experimental phenomena. For the same precursor, there are lots of micropores in the hard carbon pyrolyzed in low temperature, but low plateau capacity is exhibited. Besides although the micropore volume of carbon decreases with the increase of pyrolytic temperature, the plateau capacity gradually increases.<sup>30</sup>

- *Adsorption- Insertion mechanism.*

Bommier *et al.*<sup>31</sup> found that the slope capacity plotted against defect concentration lead to a linear relationship evidencing that defected carbon sites are responsible for the slope capacity rather than turbostratic nanodomains. Those defects (monovacancies, stone-wales defects, extreme curvature in graphene sheets and presence of sp<sup>3</sup> linking carbons that connect neighbouring turbostratic nanodomains, etc) might have its own sodiation voltage leading to a sloping voltage. They also observed expansion and contraction of d-spacing at the plateau region suggesting that intercalation occurs at low voltages. Based on these results above, it was concluded that the slope region is related to the

<sup>30</sup> Hou, H.; Qiu, X.; Wei, W.; Zhang, Y. and Ji, X., Carbon anode materials for advanced sodium-ion batteries, *Adv. Energy Mater.*, **2017**, 1602898.

<sup>31</sup> Bommier, C.; Wesley Surta, T.; Dolgos, M. and Ji, X., New mechanistic insights on Na-ion storage in non-graphitizable Carbon, *Nano Lett.*, **2015**, 15 (9), 5888–5892.

sodium storage on edges and surface defects of carbon, rather than micropores, and the low potential plateau region corresponds to the insertion of Na<sup>+</sup> into carbon interlayers and minor Na<sup>+</sup> adsorption on pore surfaces (Figure 2. 3b).

The mechanism proposed by Dahn *et al.* was supported by the experiments showing that the interlayer distance varies during the sloping region.<sup>32</sup> Ex-situ nuclear magnetic resonance (NMR) performed in hard carbons also demonstrated that low voltage plateau is related to sodium insertion of sodium ions forming quasimetallic clusters in closed nanopores of hard carbon.<sup>33</sup>

The existence of contradiction between results might be indicative of both mechanisms taking place at the same time. Further studies would be required in order to fully understand these mechanisms.<sup>6</sup>

### 2.1.1.3 Electrochemical performance of sp<sup>2</sup> carbons

**Graphite.** Prepared through a process of oxidation and partial reduction on graphite, expanded graphite has an enlarged interlayer lattice distance of 4.3 Å yet retains an analogous long-range-ordered layered structure to graphite and provides capacities close to 290 mA·h·g<sup>-1</sup>.<sup>26</sup>

When the diglyme was used as the solvent with commercial graphite leading to an intercalation compound with an estimated stoichiometry of Na(diglyme)<sub>2</sub>C<sub>20</sub>, a reversible capacity of 100 mA·h·g<sup>-1</sup> was delivered with excellent capacity retention for 1000 cycles.<sup>27</sup>

The use of graphite as anode for sodium ion batteries, however, still entails some problems. Firstly, the intercalation of solvent molecules would lead to the consumption of electrolyte solvent, inducing the increase of resistance and demand of excess electrolyte. Secondly, the low specific capacity and high

---

<sup>32</sup> Komaba, S.; Murata, W.; Ishikawa, T.; Yabuuchi, N.; Ozeki, T.; Nakayama, T.; Ogata, A.; Gotoh, K.; and Fujiwara, K., Electrochemical Na insertion and solid electrolyte interphase for hard-carbon electrodes and application to Na-ion batteries, *Adv. Funct. Mater.*, **2011**, 21, 3859-3867.

<sup>33</sup> Gotoh, K.; Ishikawa, T.; Shimadzu, S.; Yabuuchi, N.; Komaba, S.; Takeda, K.; Goto, A.; Deguchi, K.; Ohki, S.; Hashi, K.; Shimizu, T. and Ishida, H., NMR study for electrochemically inserted Na in hard carbon electrode of sodium ion battery, *J. Power Sources*, **2013**, 225, 137-140.



intercalation voltage would cause the decrease of energy density in the full battery system.<sup>30</sup> Additionally, the large volume expansion ( $\approx 350\%$ ) originating from the co-intercalation behavior would result in the pulverization of graphite particles in the repeated charge-discharge cycles, leading to the degradation of cycling performance.<sup>34</sup>

**Disordered carbons.** A variety of amorphous carbon materials, especially hard carbon materials, have been employed as anode materials for SIBs with a number of micro/nanostructures. Due to fact that their kinetics are favourable for the transportation of ion and electron, some structures such as hollow nanostructured hard carbon materials,<sup>35</sup> nanocellular carbon foams,<sup>36</sup> templated carbon,<sup>37</sup> carbon microspheres,<sup>38</sup> hierarchically porous carbon/graphene composite materials,<sup>39</sup> carbon nanofibers,<sup>40</sup> carbon nanotubes,<sup>41</sup> carbon

---

<sup>34</sup> Haegyeom, K.; Jihyun, H.; Gabin, Y.; Hyunchul, K.; Park, K.-Y.; Park, M.-S.; Yoon, W.-S. and Kang, K., Sodium intercalation chemistry in graphite, *Energy Environ. Sci.*, **2015**, 8, 2963-2969.

<sup>35</sup> Cao, Y.; Xiao, L.; Sushko, M. L.; Wang, W.; Schwenzler, B.; Xiao, J.; Nie, Z.; Saraf, L. V.; Yang, Z. and Liu, J., Sodium ion insertion in hollow carbon nanowires for battery applications, *Nano Lett.*, **2012**, 12, 3783–3787.

<sup>36</sup> Shao, Y.; Xiao, J.; Wang, W.; Engelhard, M.; Chen, X.; Nie, Z.; Gu, M.; Saraf, L. V.; Exarhos, G.; Zhang, J.-G. and Liu, J., Surface-Driven Sodium Ion Energy Storage in nanocellular carbon foams, *Nano Lett.*, **2013**, 13, 3909-3914.

<sup>37</sup> Wenzel, S.; Hara, T.; Janek, J. and Adelhelm, P., Room-temperature sodium-ion batteries: Improving the rate capability of carbon anode materials by templating strategies, *Energy Environ. Sci.*, **2011**, 4, 3342-3345.

<sup>38</sup> Yan, D.; Yu, C.; Zhang, X.; Qin, W.; Lu, T.; Hu, B.; Li, H. and Pan, L., Nitrogen-doped carbon microspheres derived from oatmeal as high capacity and superior long life anode material for sodium ion battery, *Electrochim. Acta*, **2016**, 191, 385-391.

<sup>39</sup> Yan, Y.; Yin, Y.-X.; Guo, Y.-G. and Wan, L.-Ju, A sandwich-like hierarchically porous carbon/graphene composite as a high-performance anode material for sodium-ion batteries, *Adv. Energy Mater.*, **2014**, 4, 1301584.

<sup>40</sup> Wang, Z.; Qie, L.; Yuan, L.; Zhang, W.; Hu, X. and Huang, Y., Functionalized N-doped interconnected carbon nanofibers as an anode material for sodium-ion storage with excellent performance, *Carbon*, **2013**, 55, 328-334.

<sup>41</sup> Luo, X.-F.; Yang, C.-H.; Peng, Y.-Y.; Pu, N.-W.; Ger, M.-D.; Hsieh, C.-T. and Chang, J.-K., Graphene nanosheets, carbon nanotubes, graphite, and activated carbon as anode materials for sodium-ion batteries *J. Mater. Chem A*, **2015**, 3, 10320-10326.

nanoparticles,<sup>42</sup> and carbon nanosheets<sup>43</sup> have been evaluated as anode materials.

The introduction of heteroatoms (e.g., B, N, S, and P) has been considered as a quite promising approach to enhance the capacity, surface wettability, and electronic conductivity, which can promote the charge transfer and electrode/electrolyte interactions.<sup>30</sup> Thus, a variety of heteroatom-doped carbonaceous materials with several morphologies has been widely explored as anode materials for SIB. For example, N-doped bamboo-like carbon nanotubes produced from pyrolysis of a mixture of dicyandiamide (DCD) and  $\text{CoCl}_2$  can deliver  $270 \text{ mA}\cdot\text{h}\cdot\text{g}^{-1}$  at  $50 \text{ mA}\cdot\text{g}^{-1}$  and good rate capability attributed to short  $\text{Na}^+$  diffusion distance and a large electrode/electrolyte contact.<sup>44</sup> Likewise, N-doped carbon nanofibers obtained by pyrolysis of polypyrrol, deliver  $172 \text{ mA}\cdot\text{h}\cdot\text{g}^{-1}$  of reversible capacity.<sup>40</sup> However, the low initial coulombic efficiency (~30-40 %) of this kind of nanostructured materials is the main limiting factor for real applications.

*Soft carbons.* Sodium can be reversibly inserted in amorphous and non-porous carbon black, a highly pure elemental carbon in the form of colloidal particles that are produced by incomplete combustion or thermal decomposition of gaseous or liquid hydrocarbons. Carbon black provides a reversible capacity close to  $200 \text{ mA}\cdot\text{h}\cdot\text{g}^{-1}$ . However, large irreversible capacity arising from the high surface area is also observed.<sup>45</sup> Other soft carbons such as mesoporous carbon

---

<sup>42</sup> Gaddam, R. R.; Yang, D.; Narayan, R.; Raju, KVS N.; Kumar, N. A.; Zhao, X.S., Biomass derived carbon nanoparticle as anodes for high performance sodium and lithium ion batteries, *Nano Energy*, **2016**, 26, 346–352.

<sup>43</sup> Yang, F.; Zhang Z.; Du, K.; Zhao, X.; Chen, W.; Lai, Y. and Li, J., Dopamine derived nitrogen doped carbon sheets as anode materials for high-performance sodium ion batteries, *Carbon*, **2015**, 91, 88-95.

<sup>44</sup> Li, D.; Zhang, L.; Chen, H.; Ding, L.-X.; Wang, S. and Wang, H., Nitrogen-doped bamboo-like carbon nanotubes: promising anode materials for sodium-ion batteries, *Chem. Commun.*, **2015**, 51, 16045-16048.

<sup>45</sup> Alcántara, R.; Jiménez-Mateos, J. M.; Lavela, P. and Tirado, J. L., Carbon black: a promising electrode material for sodium ion batteries, *Electrochem. Commun.*, **2001**, 639-642.

derived from mesophase pitch<sup>20</sup> or cellulose<sup>46</sup> deliver reversible capacities as high as 331 mA·h·g<sup>-1</sup> (0.08 C) and 375 mA·h·g<sup>-1</sup> (0.05 C), respectively. Pyrolysis of coal tar pitch also provides soft carbons with increased layer spacing and defects thanks to phosphorus doping which leads to good electrochemical performance (251 mA·h·g<sup>-1</sup> at 0.27 C).<sup>22</sup>

Apart from the aforesaid contents there are many soft carbon materials which have been studied as anode materials for sodium ion batteries. Their electrochemical performances as anodes of SIBs are summarized in Table 2.1.

---

<sup>46</sup> Zhu, H.; Shen, F.; Luo, W.; Zhu, S.; Zhao, M.; Natarajan, B.; Dai, J.; Zhou, L.; Ji, X.; Yassar, R. S.; Li, T. and Hu, L., Low temperature carbonization of cellulose nanocrystals for high performance carbon anode of sodium-ion batteries *Nano Energy*, **2017**, 33, 37-44.

**Table 2.1** Electrochemical parameters of carbon anodes for sodium ion batteries. When the precursor is subjected to pyrolysis, the temperature of pyrolysis leading to best performance T(°C) is shown.  $Q_{rev}$  is the reversible capacity (1<sup>st</sup> cycle);  $C_d$  is the current density, c.e. is the 1<sup>st</sup> cycle coulombic efficiency. The charge rate for the current densities based on a theoretical capacity of 372 mA·h·g<sup>-1</sup> for NaC<sub>6</sub> formation are approximately the following: 100 mA·g<sup>-1</sup> ~0.3 C; 90 mA·g<sup>-1</sup> ~ 0.25 C; 75 mA·g<sup>-1</sup> ~ 0.2 C; 50 mA·g<sup>-1</sup> ~ 0.13 C; 30 mA·g<sup>-1</sup> ~ 0.08 C, 20 mA·g<sup>-1</sup> ~ 0.05 C ; 15 mA·g<sup>-1</sup> ~ 0.04 C; 5 mA·g<sup>-1</sup> ~ 0.01 C.

Material	Precursor	T (°)	$Q_{rev}$ (mA·h·g <sup>-1</sup> )	$C_d$ (mA·g <sup>-1</sup> )	1 <sup>st</sup> ce	Ref.
Templated carbon	Mesophase pitch	-	100	75	20	37
Soft mesocarbon microbeads (MCMB)	Coal tar pitch	700	208	15	67	21
Mesoporous soft carbon	Mesophase pitch	800	331	30	45	20
P-doped pitch-derived soft carbon	P- doped pitch	900	251	100	68	22
Soft carbon with rodlike morphology	PTCDA (C <sub>24</sub> H <sub>8</sub> O <sub>6</sub> )*	700	233	20	63	23
Soft carbon spheres	mesitylene (C <sub>9</sub> H <sub>12</sub> )	700	150	15	62	47
Carbon black (Repsol)	-	-	121	5	41	45

\*PTCDA: 3,4,9,10-perylene-tetracarboxylic acid-dianhydride

*Hard carbons.* One of the most employed anodes for NIBs is hard carbon whose electrochemical performance depends on the synthesis conditions such as carbon source and carbonization temperature. First hard carbons as anodes of sodium ion batteries were reported in 2000 by Stevens and Dahn<sup>28</sup>, who obtained a high reversible capacity of  $300 \text{ mA}\cdot\text{h}\cdot\text{g}^{-1}$  by carbonization of glucose at  $1000 \text{ }^\circ\text{C}$ . At present there exist commercially available pitch derived hard carbons (Carbotron P of Kureha Corporation). It delivers a reversible capacity of  $200 \text{ mA}\cdot\text{h}\cdot\text{g}^{-1}$  corresponding to a stoichiometry of  $\text{NaC}_{11}$  with a first cycle coulombic efficiency of 69 % (at C/25).<sup>47</sup>

The regulation of nanoparticle morphology and the introduction of nanoporosity are common strategies to accomplish highly reversible  $\text{Na}^+$  storage via artificially tailored nanopores. For example, sugar derived nanoporous hard carbon provides  $324 \text{ mA}\cdot\text{h}\cdot\text{g}^{-1}$  of reversible capacity with 76 % of initial coulombic efficiency.<sup>48</sup> Compared to bulk sugar derived hard carbon, these nanostructured materials show, as usually, slightly improved capacity at high cycling rates but similar reversible capacities compared with pristine hard carbon at low rates.<sup>14</sup>

The pyrolysis of polymers such as polyvinyl chloride (PVC) or polyvinylpyrrolidone (PVP) or resins like resorcinol-formaldehyde (R-F) leads to the obtention of hard carbons. The use of PVC nanofibers as hard carbon precursor leads to  $256 \text{ mA}\cdot\text{h}\cdot\text{g}^{-1}$  of reversible capacity with 66 % of first cycle coulombic efficiency and a retention of  $215 \text{ mA}\cdot\text{h}\cdot\text{g}^{-1}$  after 120 cycles at 0.03 C.<sup>49</sup> The former provides better reversible capacity ( $271 \text{ mA}\cdot\text{h}\cdot\text{g}^{-1}$  at 0.05 C) but lower first cycle irreversible capacity (48 %).<sup>7</sup> The pyrolysis of R-F leads to the attainment of binder-free monoliths with macroporous structure that provides large capacities close to 350

---

<sup>47</sup> Pol, V. G.; Lee, E.; Zhou, D.; Dogana, F.; Calderon-Moreno, J. M. M. and Johnson, C. S., Spherical carbon as a new high-rate anode for sodium-ion batteries, *Electrochim. Acta*, **2014**, 127, 61–67.

<sup>48</sup> Prabakar, S. J. R.; Jeong, J. and Pyo, M., Nanoporous hard carbon anodes for improved electrochemical performance in sodium ion batteries, *Electrochim. Acta*, **2015**, 161, 23-31.

<sup>49</sup> Bai, Y.; Wang, Z.; Wu, C.; Xu, R.; Wu, F.; Liu, Y.; Li, H.; Li, Y.; Lu, J. and Amine, K., Hard carbon originated from polyvinyl chloride nanofibers as high-performance anode material for Na-ion battery, *ACS Appl. Mater. Interfaces*, **2015**, 7, 5598-5604.

$\text{mA}\cdot\text{h}\cdot\text{g}^{-1}$  at C/20 with high first cycle coulombic efficiency (92 %).<sup>11</sup> However, high temperatures of pyrolysis are required (1600 °C).

Many hard carbons have been reported to be obtained through pyrolysis biomass precursors, which are renewable, abundant and eco-friendly. The wide range of biomass precursors having different microstructures and chemical compositions that can directly determine the structure/morphology of the derived carbon materials, opens infinite possibilities to the synthesis of hard carbons with different properties. Besides, the biomass materials often contain some heteroatoms (*e.g.*, O, N, S and P), thus the derived carbon materials doped with these heteroatoms can be directly obtained by carbonizing treatment. It is of particular interest the use of non-edible wastes as carbon precursors such as pomelo peels, corn cobs, peanut shells, etc.<sup>30</sup> For instance, shaddock peels, which have highly cross-linked and non-crystalline hemicellulose can form non-graphitic carbon that delivers up to  $430 \text{ mA}\cdot\text{h}\cdot\text{g}^{-1}$  of reversible capacity (at  $30 \text{ mA}\cdot\text{g}^{-1}$ ) with 69 % of first cycle coulombic efficiency and good rate performance.<sup>50</sup> Peanut shells which are lignin based and therefore, also have a cross-linked structure can be transformed into hard carbons delivering a capacity of  $298 \text{ mA}\cdot\text{h}\cdot\text{g}^{-1}$  with high capacity retention (98% after 300 cycles at a low current rate of 0.1 C).<sup>51</sup> Other precursors such as wood, leaves, wool, cotton, etc. have been also reported. Their electrochemical performance is summarized in Table 2.2.

---

<sup>50</sup> Sun, N.; Liu, H. and Xu, B., Facile synthesis of high performance hard carbon anode materials for sodium ion batteries, *J. Mater. Chem. A*, **2015**, 3, 20560-20566.

<sup>51</sup> Dou, X.; Hasa, I.; Hekmatfar, M.; Diemant, T.; Juergen, B. R.; Buchholz, D. and Passerini, S., Pectin, hemicellulose, or lignin? Impact of the biowaste source on the performance of hard carbons for sodium- ion batteries, *ChemSusChem*, **2017**, 10, 1-10.

**Table 2.2** Electrochemical parameters of hard carbons derived from pyrolysis different precursors tested in sodium half-cells. T(°C) is the temperature of pyrolysis leading to best performance;  $Q_{rev}$  is the reversible capacity (1<sup>st</sup> cycle);  $C_d$  is the current density, c.e. is the 1<sup>st</sup> cycle coulombic efficiency. The charge rate for the current densities based on a theoretical capacity of  $372 \text{ mA}\cdot\text{h}\cdot\text{g}^{-1}$  for  $\text{NaC}_6$  formation are the following:  $50 \text{ mA}\cdot\text{g}^{-1} \sim 0.13 \text{ C}$ ;  $40 \text{ mA}\cdot\text{g}^{-1} \sim 0.1 \text{ C}$ ;  $30 \text{ mA}\cdot\text{g}^{-1} \sim 0.08 \text{ C}$ ,  $20 \text{ mA}\cdot\text{g}^{-1} \sim 0.05 \text{ C}$ ;  $10 \text{ mA}\cdot\text{g}^{-1} \sim 0.03 \text{ C}$ .

Precursor	T (°)	Morphology	$Q_{rev}$ ( $\text{mA}\cdot\text{h}\cdot\text{g}^{-1}$ )	$C_d$ ( $\text{mA}\cdot\text{g}^{-1}$ )	1 <sup>st</sup> ce	Ref.
Wood	1000	mesoporous	270	10	70	8
Oak leaves	1000	porous carbon membrane	270	40	75	9
Wool	1100	fibers	303	10	63	10
Cotton	1300	microtube	314	40	80	12
Pomelo peels	700	micronized sheets	314	50	27	13
Sugar	1100	10-100 $\mu\text{m}$	326	40	60	14
Apple waste	1100	1-100 $\mu\text{m}$	245	20	61	15
Corn cobs	1300	5-10 $\mu\text{m}$ irregular granular	298	40	86	16
Mangosteen shell	1500	irregular shapes, smooth surfaces	330	20	83	17
Peanut shell	600	3D-porous structure	190	250	32	18
Okara	900	N-doped C sheets	292	50	-	19
Oatmeal	500	Nitrogen-doped carbon microspheres	320	50	40	38

From an economic viewpoint, the biomass (especially the biowaste) derived carbon materials would be ideal electrode materials for SIBs. Besides, they show relatively high capacities  $190\text{--}330\text{ mA}\cdot\text{h}\cdot\text{g}^{-1}$ .

### 2.1.2 Lignin as biomass precursor of hard carbon

Within the framework of the 2009/28/EC1 directive released by the European Commission with the objective of regulating the competition between bioenergy and food sector and the impact they might have on food prices and food security, the large scale use of a food supply like sugar or oatmeal as hard carbon precursor might lead to limitations in its commercial use within the European Union. Given the good prospects of carbonaceous materials as anodes for sodium ion batteries, it is necessary to look for alternative carbon precursors. For that purpose, lignin was considered as biomass precursor of hard carbon due to its highly cross-linked nature, which might avoid graphitization under high temperature heat treatments.

Lignin is one of the important chemical constituents of lignocellulosic materials in wood and it is the second most abundant biopolymers in nature after cellulose. It has a three dimensional complex branched structure based on three basic monomeric units: *p*-hydroxyphenyl (H), guaiacyl (G) and syringyl (S) (Figure 2. 4). The relative distribution of these units and the degree of cross linking in any lignin sample depend primarily on the plant source.<sup>52</sup>

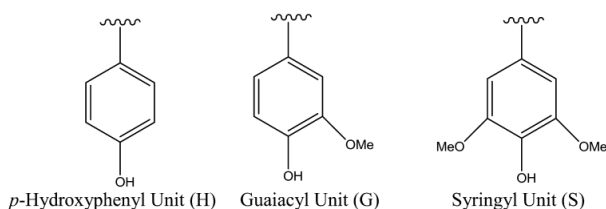


**Figure 2. 4** Lignin monomeric units.

The physical properties and the chemical characteristics of lignin vary not only between different wood species, but also according to the method of isolation. Different plant sources, chemical processing and pulping techniques yield



different types of lignin, such as Alcell lignin, Kraft lignin and lignosulfonate which are generated from the Alcell, Kraft and sulfite pulping process, respectively.

Lignin is considered a waste component of biomass and mostly consumed as a low grade energy source in combustion.<sup>53</sup> However, the advent of biorefineries that convert cellulosic biomass into liquid transportation fuels is expected to generate substantially more lignin than necessary to power the operation, and therefore it is worth studying how to transform it to value-added products.<sup>54</sup> Moreover, lignin is one of the cheapest polymers that can be extracted from biomass.<sup>55</sup>

All the above mentioned characteristics of low-cost, abundance, non-edible and appropriate chemical structure of lignin make it suitable as a carbon precursor. Therefore, the aim of this work is the development of lignin derived hard carbon as anodes for sodium ion batteries.

## 2.2 Experimental

### 2.2.1 Synthesis of carbonaceous anodes

In this section, the synthesis of natural lignin derived hard carbons will be presented. Besides, the synthesis of other carbonaceous materials such as sugar derived hard carbons and polyvinyl chloride (PVC) derived soft carbons will be

---

<sup>52</sup> Chatterjee, S.; Saito, T.; Rios, O. and Johs, A., Lignin based carbon materials for energy storage applications, *Green Technologies for the Environment*, **2014**, Chapter 11, 203-218.

<sup>53</sup> Jin, J.; Yu, B. J.; Shi, Z. Q.; Wang, C. Y. and Chong, C. B., Lignin-based electrospun carbon nanofibrous webs as free-standing and binder-free electrodes for sodium ion batteries, *J. Power Sources*, **2014**, 272, 800-807.

<sup>54</sup> Ragauskas, A. J.; Beckham, G. T.; Bidy, M. J.; Chandra, R.; Chen, F.; Davis, M. F.; Davison, B. H.; Dixon, R. A.; Gilna, P.; Keller, M.; Langan, P.; Naskar, A. K.; Saddler, J. N.; Tschaplinski, T. J.; Tuskan, G. A. and Wyman, C. E., Lignin valorization: improving lignin processing in the biorefinery, *Science*, **2014**, 344, 1246843.

<sup>55</sup> Stevens J. and Gardner, D. J., Enhancing the fuel value of wood pellets with the addition of lignin, *Wood Fiber Sci.*, **2010**, 42(4), 439-443.

carried out for comparative purposes. A commercial carbon black will be also used.

### 2.2.1.1 Lignin derived hard carbons

Lignin is a biopolymer that acts as precursor of hard carbon and is isolated from black liquor, a by-product of the paper industry. It contains a between 3-80 % of solids being 30-55 % organic compounds and 45-70 % inorganics. Inorganic compounds such as sodium hydroxide ( $\text{NaOH}$ ,  $5\text{-}6\text{ g}\cdot\text{L}^{-1}$ ), sodium sulphide ( $\text{Na}_2\text{S}$ ,  $14\text{-}16\text{ g}\cdot\text{L}^{-1}$ ) and sodium carbonate ( $\text{Na}_2\text{CO}_3$ ,  $25\text{-}30\text{ g}\cdot\text{L}^{-1}$ ) are added during the Kraft process in order to separate cellulose from lignin.<sup>56</sup>

Natural lignin was first isolated from black liquor according to the methodology reported by A. M. Navarro-Suárez *et. al.*<sup>57</sup> The extraction of natural lignin consisted of a two-step process: precipitation in acid media by addition of 250 mL of 1M sulphuric acid ( $\text{H}_2\text{SO}_4$ , Sigma-Aldrich, ACS reagent, 95-98 %) to 40 mL of black liquor (provided by Smurfit Kappa Nervion, S. A.) and further separation of the precipitate by centrifugation. The precipitate was rinsed with distilled water several times before being dried at 80 °C. The final amount of lignin per volume of black liquor was  $120\text{ g}\cdot\text{L}^{-1}$ .

Then, lignin powder (0.5 g approximately) was ground in an agate mortar, placed into a crucible and pyrolyzed according to the synthesis conditions summarized in Table 2.3.

---

<sup>56</sup> Spent liquor from alkaline pulping and bleaching containing spent inorganic process chemicals and dissolved organic substances originating from the cellulosic raw material.<https://echa.europa.eu/registration-dossier/-/registered-dossier/15523/1>.

<sup>57</sup> Navarro-Suárez, A. M.; Carretero-González, J.; Roddatis, V.; Goikolea, E.; Ségalini, J.; Redondo, E.; Rojo, T. and Mysyk, R., Nanoporous carbons from natural lignin: study of structural-textural properties and application to organic-based supercapacitors, *RSC Adv.*, **2014**, 4, 48336-48343.

**Table 2.3** Summary of the lignin derived hard carbons synthesized and the corresponding synthetic conditions: age and type of lignin precursor (old/fresh natural lignin or commercial lignin), furnace’s tube material (SST: stainless steel or quartz), crucible material (Inconel or alumina), Ar flow rate during pyrolysis, grinding of the lignin precursor, heating rate (H. Rate) dwell time at a temperature of synthesis ( $t_{\text{dwell}}$ ), maximum temperature reached in the first and second step ( $T_{\text{max}}$ ).

Synthesis conditions	Sample	Lignin precursor	Tube	Crucible	Ar flow (mL/min)	Grinding	1 <sup>st</sup> step			2 <sup>nd</sup> step		
							H. Rate (°C/min)	$t_{\text{dwell}}$ (h)	$T_{\text{max}}$ (°C)	H. Rate (°C/min)	$t_{\text{dwell}}$ (h)	$T_{\text{max}}$ (°C)
A	HC-L900-01	Fresh	SST	Inconel	100	Yes	10	1	110	1	1	900
	HC-L1000-02	Fresh	SST	Inconel	100	Yes	10	1	110	1	1	1000
	HC-L1100-03	Fresh	SST	Inconel	100	Yes	10	1	110	1	1	1100
	HC-CL900-04	Commercial	SST	Inconel	100	Yes	10	1	110	1	1	900
B	HC-L700-05	Fresh	SST	Inconel	100	Yes	5	2	700	-	-	-
	HC-L800-06	Fresh	SST	Inconel	100	Yes	5	2	800	-	-	-
	HC-L900-07	Fresh	SST	Inconel	100	Yes	5	2	900	-	-	-
	HC-L1000-08	Fresh	SST	Inconel	100	Yes	5	2	1000	-	-	-
C	HC-L900-09	Old	Quartz	Alumina	100	Yes	5	2	900	-	-	-
	HC-L900-10	Old	Quartz	Alumina	180	Yes	5	2	900	-	-	-
	HC-L900-11	Fresh	Quartz	Alumina	180	Yes	5	2	900	-	-	-
	HC-L900-12	Fresh	Quartz	Alumina	180	No	5	2	900	-	-	-
	HC-L1000-13	Fresh	Quartz	Alumina	180	Yes	5	2	1000	-	-	-
	HC-L900-14	Fresh	Quartz	Alumina	180	Yes	5	4	900	-	-	-

The synthesis was optimized in 3 series under different conditions: series A, series B and series C.

- **Series A**

Initially, pyrolysis of natural (isolated from black liquor) lignin and commercial lignin (Alkali, Sigma-Aldrich) was performed using an Inconel® crucible (Alfa Aesar, Ni:Cr:Fe 77:15.5:7.5 wt. %) and a stainless steel (SST) tube which was within a horizontal tubular furnace (Carbolite HST 12/200) under an Ar flow of 100 mL·min<sup>-1</sup> (Praxair, 99.9% purity). Samples were heated up to the final pyrolysis temperature (900, 1000 or 1100 °C) at a heating rate of (1 °C·min<sup>-1</sup>) according to the methodology reported by Stevens<sup>28</sup> for glucose derived hard carbons. Just as Stevens, who reported a dewatering step of sugar prior to pyrolysis, in order to improve the air and water removal, an intermediate heating step at 110 °C for 1 hour prior to heating to the maximum temperature was included. Considering that our approach is based on obtaining a low cost material, a temperature of 1100 °C was the highest tried not to increase the synthesis cost. The aim of using a low heating rate was to ensure that the heat treatment was long enough to allow the microstructural changes, which occur slowly above 700 °C and because in general, pyrolysis with lower heating rate results in lower volatilization and higher yield.<sup>58</sup> After reaching the maximum temperature, samples were kept at that temperature for 1 hour and left to cool down naturally. Finally, carbon samples were manually ground in an agate mortar for 10 minutes and stored in air under normal conditions before electrode preparation.

- **Series B**

Once the feasibility of the production of hard carbon as of natural lignin was proven, a second series of synthesis involving heating at a faster rate (5 °C·min<sup>-1</sup>) and a lower final pyrolysis temperature was performed. The aim was to reduce costs by decreasing the maximum heating temperature. In this regard, a temperature of 1000 °C was the highest tried whereas 700 °C was established as

---

<sup>58</sup> Mackay, D. M and Roberts, P. V., The influence of pyrolysis conditions on yield and microporosity of lignocellulosic chars, *Carbon*, **1982**, 20, 2, 95-104.

the lowest temperature enabling carbonization. In every case, prior to carbonization, the sample was left under Ar flow for at least 30 minutes inside the furnace to ensure air removal. After pyrolysis, samples were manually ground in an agate mortar for 10 minutes and stored in air under normal conditions before electrode preparation.

The existence of cross contamination in the samples produced as of A or B methods derived from the use of the same tubular stainless steel furnace for other purposes such as activation of carbons with hydroxides, made necessary to replace the tube and the crucible.

- **Series C**

The third series of samples was produced in a new quartz tube with a new alumina boat in a Carbolite tubular furnace. The use of this furnace enabled the use of a faster Ar flow, which avoids undesired reactions between the carbon and any of the released gases during pyrolysis (CO, CO<sub>2</sub>, H<sub>2</sub>O, CH<sub>4</sub>, H<sub>2</sub>, etc.).<sup>59</sup> Apart from Ar flow, other synthetic parameters such as lignin age, grinding of the precursor and dwell time at the maximum temperature were optimized as summarized in Table 2.3.

Hereafter, samples will be named according to the carbon type (hard carbon abbreviated as HC), carbon precursor (L for lignin, CL for commercial lignin), the maximum temperature reached during pyrolysis and the number of sample. As an example: HC-L900-01, means that the sample is composed by a hard carbon derived from natural lignin synthesized at a maximum temperature of 900 °C according to the synthesis conditions summarized in Table 2.3 corresponding to the sample number 01.

### 2.2.1.2 Sugar derived hard carbons

Prior to pyrolysis, a dehydration process of the hard carbon precursor (sucrose) was performed in order to avoid massive foaming inside the furnace tube

---

<sup>59</sup> Xing, W. Xue, J. S. and Dahn, J. R., Optimizing pyrolysis of sugar carbons for use as anode materials in lithium-ion batteries, *J. Power Sources*, **1996**,143, 10, 3046-3052.

derived from its melting.<sup>60</sup> For sample named as "HC-SA", oxidation was carried out by heating sugar in air for 16 hours. Sucrose was also dewatered by placing it into concentrated sulfuric acid for 16 hours leading to HC-SAW. Prior to pyrolysis, the brownish resulting solids were ground for at least 10 minutes using an agate mortar. Both sugar precursors were pyrolyzed in a quartz tubular furnace (Carbolite) under Ar atmosphere ( $180 \text{ mL}\cdot\text{min}^{-1}$ ) according to the two pyrolysis programs summarized in Table 2.4. Although Stevens reported an optimum temperature of  $1100 \text{ }^\circ\text{C}$ , a slightly lower maximum temperature of pyrolysis ( $1050 \text{ }^\circ\text{C}$ ) was selected in order to avoid reducing too much the life time of the quartz tube.<sup>59</sup>

---

<sup>60</sup> Stevens, D. A.; Mechanisms for sodium insertion in carbón materials, Thesis, Dalhousie University, **2000**, 68.

## Chapter 2 – Biomass derived carbon anodes for sodium ion batteries

**Table 2.4** Summary of the synthesis conditions of other hard and soft carbons synthesized and the corresponding synthetic conditions: type precursor (sugar or PVC), furnace's tube material (SST: stainless steel or quartz), crucible material (Inconel or alumina), Ar flow rate during pyrolysis, grinding of the lignin precursor, heating rate (H. Rate) dwell time at a temperature of synthesis ( $t_{\text{dwell}}$ ), maximum temperature reached in the first and second step ( $T_{\text{max}}$ ).

Name	Precursor	Tube	Crucible	1 <sup>st</sup> step				2 <sup>nd</sup> step			3 <sup>rd</sup> step		
				Ar flow (mL/min)	H. Rate (°C/min)	$t_{\text{dwell}}$ (h)	$T_{\text{max}}$ (°C)	H. Rate (°C/min)	$t_{\text{dwell}}$ (h)	$T_{\text{max}}$ (°C)	H. Rate (°C/min)	$t_{\text{dwell}}$ (h)	$T_{\text{max}}$ (°C)
SC_PVCLM	PVC (low M.W.)	Quartz	Alumina	180	10	60	110	1	1	800	-	-	-
SC_PVCR	PVC Recycled	SST	Inconel	100	10	60	110	1	1	800	-	-	-
SC_PVCHM	PVC (high M.W.)	Quartz	Inconel	100	10	60	110	1	1	800	-	-	-
HC_SA	Sugar (heated in air)	Quartz	Alumina	180	10	150	30	0,5	0,5	500	10	0,5	1050
HC_SAW	Sugar (acid washed)	Quartz	Alumina	180	10	150	30	0,5	0,5	500	10	0,5	1050

After pyrolysis, the resulting hard carbons were powdered by hand grinding in an agate mortar for 10 minutes. Hard carbon derived from oxidized sucrose obtained via carbonization in  $\text{H}_2\text{SO}_4$  (HC-SAW) was synthesized and provided by S. Clarke. The final carbonaceous materials were kept in air under normal conditions before electrode preparation.

### 2.2.1.3 PVC derived soft Carbons

Soft carbons were synthesized according to the protocol proposed by Stevens and Dahn, who tested the electrochemical performance of polyvinyl chloride (PVC) pyrolyzed at temperatures ranging from 600 °C to 1700 °C.<sup>60</sup> A temperature of 800 °C was chosen as they found a trade-off between low irreversible and high reversible capacities.

Before undergoing the pyrolysis program summarized in Table 2.4, PVC powder was crushed in an agate mortar and placed in an alumina crucible. Commercial PVC of high and low molecular weight (Sigma-Aldrich) and recycled PVC from Bilboplastik S. L., respectively were used as soft carbon precursors. Synthesis was carried out in a quartz tube in a Carbolite HST 12/200 furnace under Ar flow (180 mL·min<sup>-1</sup>). All the PVC precursors were pyrolyzed after an intermediate step at 110 °C for 1 hour, at a heating rate of 1 °C·min<sup>-1</sup> up to a temperature of 800 °C under an Ar atmosphere (180 mL/min).

Acetylene black (99.9%), a high purity form of carbon black made from the thermal decomposition of acetylene gas was purchased from Cymit and used as received.

Hereafter, samples will be named according to the carbon type (hard carbon/Soft carbon abbreviated as HC or SC respectively), carbon precursor (PVCHM and PVCLM for polyvinyl chloride of high and low molecular weight respectively, PVCRC for the recycled one, and SA for sugar heated in air and SAW for sugar acid washed, respectively), the maximum temperature reached during pyrolysis and the number of sample.



### 2.2.2 Physico-chemical characterization

Scanning electron microscopy (SEM) images were obtained in a Quanta 200 FEG (FEI) microscope.

The carbonization process of the natural lignin was studied by thermogravimetric analysis in a NETZSCH STA 449F3 Jupiter thermal analyzer coupled with a TGA/STA-QMS 403D Aëolos® quadrupole mass spectrometer under Ar stream (Praxair, purity 99 %) at a heating rate of 5 °C·min<sup>-1</sup> up to 900 °C. Prior to analysis, lignin sample was dried overnight at 80 °C under vacuum.

Textural properties of the carbons prepared from natural lignin were studied using a Micromeritics (ASAP 2020) surface analyzer by adsorption/desorption of N<sub>2</sub> gas at 77 K. Before the analysis, the samples were degassed for at least 8 hours at 400 °C.

Small Angle X-ray Scattering (SAXS) measurements were performed using a Nanostar U (Bruker) equipped with microfocus Cu source, evacuated beam path and Vantec 2000 detector, using 107 cm, 26 cm and 5 cm sample-detector distances. The incident beam has been carefully calibrated in order to obtain absolute intensities in cm<sup>-1</sup> with a perfect overlap of the measurements made at the three distances. Intensities were then normalized in cm<sup>2</sup>·g<sup>-1</sup> by the macroscopic density of the powder samples.

Powder X-ray Diffraction (PXRD) data was recorded using two diffractometers with Cu radiation. On the one hand, a dichromatic Bruker Advance D8 with  $\lambda_{\text{Cu}}K\alpha_1=1.5406$  and  $\lambda_{\text{Cu}}K\alpha_2=1.5444$  Å and on the other hand, a monochromatic Bruker D8 Discover  $\lambda_{\text{Cu}}K\alpha_1=1.54056$  Å

Raman measurements were carried out using a Renishaw inVia Raman Microscope equipped with a Renishaw RL532 AFM green laser at 532nm wavelength. Spectra were recorded in the range of 3200-100 cm<sup>-1</sup>, with a relative laser intensity of 1% for a duration of 30 seconds.

### 2.2.3 Electrochemical characterization

In order to test the electrochemical performance in a sodium ion half-cell, laminates were prepared by casting slurries containing 90 wt. % of lignin, sugar, PVC derived carbon or acetylene black, 5 wt. % carbon C-Nergy Super C65 (Timcal) and 5 wt. % polyvinylidene difluoride (Solef PVDF, Solvay) in 1-methyl-2-pyrrolidone (NMP, Sigma Aldrich, anhydrous, 99.5 % purity) onto copper foil (Hohsen, 18  $\mu\text{m}$  thickness). 11 mm diameter electrodes were punched and pressed (1 tons) for a few seconds and dried under vacuum in a Büchi oven at 120 °C overnight before storing them in a glove box. Coin cells (Hohsen 2032) were assembled using sodium foil (Panreac) as counter electrode, and glass fiber (Whatman GFB/55) as separator. As electrolyte, sodium perchlorate (1 M  $\text{NaClO}_4$ , Sigma Aldrich, 98 % purity) in ethylcarbonate (EC, Sigma-Aldrich, Anhydrous, 99 % purity) and propylenecarbonate (PC, Sigma-Aldrich, Reagent Plus, 99 % purity) 50 wt. % was used. The cells were galvanostatically cycled between 0.002 and 2 V vs.  $\text{Na}^+/\text{Na}$  in a Maccor Battery Tester (Model 4000). The currents applied were calculated on the basis of the  $\text{NaC}_6$  formation according to the theoretical capacity of graphite ( $372 \text{ mAh.g}^{-1}$ ).

## 2.3 Results and discussion

### Lignin after extraction from black liquor

In Figure 2. 5 SEM images (secondary electron mode) of the particles of natural lignin after isolation from the black liquor suspension by using  $\text{H}_2\text{SO}_4$  with its corresponding EDX analysis are shown. According to EDX lignin contains approximately a 69 at. % of C and 25 at. % of O. It also revealed the presence of sodium and sulphur impurities (4 % and 1 %, respectively) coming from the “white liquor” ( $\text{NaOH}$  and  $\text{Na}_2\text{S}$ ) that is added during the Kraft process in the paper industry to the wooden chips in order to separate cellulose from lignin. The final amount of lignin per volume of black liquor was found to be approximately  $120 \text{ g.L}^{-1}$ .

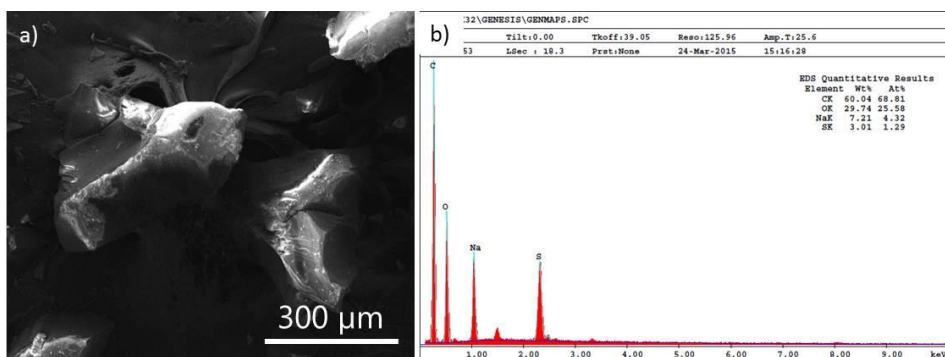


Figure 2. 5 SEM image of lignin particles and (b) EDX analysis from SEM.

## Carbon after Pyrolysis of lignin

### 2.3.1 Thermogravimetric analysis (TGA)

The mechanism of carbonization is a complex process in which the chemical composition of the precursor changes while hydrogen and oxygen content decreases allowing the establishment of the carbon microstructure in terms of porosity, size and shape.<sup>61</sup> According to R. Franklin, the development of fine structure microporosity is intimately related to the chemical composition of the carbon precursor.<sup>5</sup> For carbohydrate precursors like sugar, quick water release during pyrolysis leads to the formation of a low density disordered carbon with fine structure microporosity due to cross-linking of the graphene layers (hard carbon). Hydrocarbon precursors like PVC lead to the formation of a viscous liquid during a large temperature range promoting a progressive densification of the char structure until all hydrogen is released, leading to a soft carbon without fine structure microporosity. Lignin, contrary to other biomass molecules such as sugars and cellulose, is a very large cross-linked molecule that is more difficult to dehydrate but it also contains an excess of hydrogen (H/O atomic ratio in the order of 3 : 1), which adds up to the microstructural complexity of the carbonization products.

<sup>61</sup> Rand, B. and McEnaney, B., Carbon binders from polymeric resins and pitch. Part I - pyrolysis behavior and structure of the carbons, *Ceram. Trans. J.*, **1985**, 84, 157-165.

In order to understand the chemical phenomena occurring during pyrolysis of lignin, thermal gravimetric analysis coupled with mass spectrometry was performed. In Figure 2.6 the thermal analysis of natural lignin sample isolated from black liquor is shown.

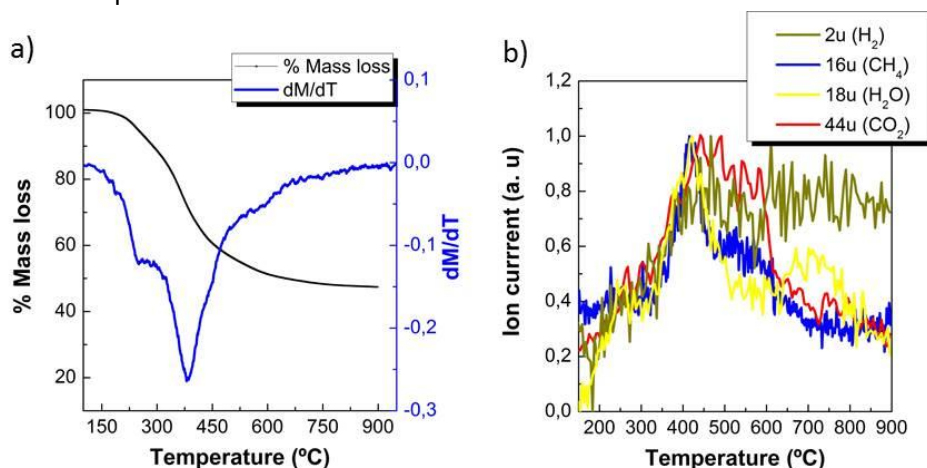


**Figure 2.6** Thermogravimetric analysis of natural lignin under argon flow ( $60 \text{ mL}\cdot\text{min}^{-1}$ ) at a heating rate of  $5 \text{ }^\circ\text{C}\cdot\text{min}^{-1}$  until  $900 \text{ }^\circ\text{C}$  followed by an isothermal step for 2 hours.

Lignin thermally decomposes over a broad temperature range, because various oxygen functional groups from its structure have different thermal stabilities and, as a consequence, their scission occurs at different temperatures.<sup>62</sup> The degradation study under argon flow showed loss mass starting at relatively low temperatures (above  $200 \text{ }^\circ\text{C}$ ) and two main mass losses at  $240 \text{ }^\circ\text{C}$  and  $367 \text{ }^\circ\text{C}$ . The former mass loss corresponds to the release of mainly volatiles such as water ( $m/z=18$ ) and  $\text{CO}_2$  ( $m/z=44$ ) as can be observed in Figure 2.6 b.  $\text{CH}_4$  ( $m/z=16$ ) starts evolving above  $200 \text{ }^\circ\text{C}$  and gradually increases up to about  $420 \text{ }^\circ\text{C}$ . Likewise, at that temperature  $\text{H}_2$ ,  $\text{H}_2\text{O}$  and  $\text{CO}_2$  are released.  $\text{CO}_2$ ,  $\text{CH}_4$  and  $\text{H}_2\text{O}$  are mainly released from the carboxyl, methoxy and hydroxyl groups, respectively whereas  $\text{H}_2$  is produced from the aliphatic and methoxy groups along with rearrangement and condensation of the aromatic rings in the lignin structural units. At temperatures above  $600 \text{ }^\circ\text{C}$  the mass loss is less pronounced and it is related to the elimination of heteroatoms with the formation of aromatic

<sup>62</sup> Brebu, M. and Vasile, C., Thermal degradation of lignin, a review, *Cellulose Chem. Technol.*, **2010**, 44 (9), 353.

hydrocarbons, phenolics, hydroxyphenolics and guaiacyl-/syringyl-type compounds, most products having phenolic hydroxyl groups. This is consistent with the mass spectrum showing H<sub>2</sub>O release at 700 °C. Above 750 °C the mass loss can be considered negligible, indicating that the basic structure of the carbon has already been formed. In consequence, release of H<sub>2</sub> from breakage and rearrangement of aromatic rings is observed. Finally after 2 hours at 900 °C the remaining carbon content was approximately 47 wt. % which can be considered a relatively high yield of pyrolysis.

### 2.3.2 X-Ray diffraction (XRD)

- **Lignin derived carbons**

The XRD pattern of natural lignin is shown in Figure 2. 7. It is observed that natural lignin contains sulphur (S<sub>8</sub>) impurities as a consequence of Kraft process. In that process the complex lignin polymer structure is partially decomposed by introducing many sulfur species (Na<sub>2</sub>S, Na<sub>2</sub>SO<sub>4</sub>) that are present in the end-product both covalently linked to the polymer chain and in the inorganic residue.<sup>63</sup> However, as it will be further determined, sulfur content after pyrolysis is almost negligible.

---

<sup>63</sup> Dondi, D.; Zeffiro, A.; Speltini, A.; Tomasi, C.; Vadiel, D.; Buttafava, A., The role of inorganic sulfur compounds in the pyrolysis of Kraft lignin, *J. Anal. Appl. Pyrolysis*, **2014**, 107, 53-58.

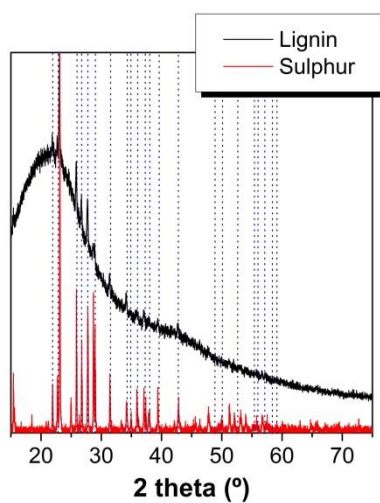


**Figure 2. 7** Comparison of the XRD pattern of natural lignin and sulfur.

The XRD patterns of the lignin derived carbons synthesized under different conditions are shown in Figure 2.8.

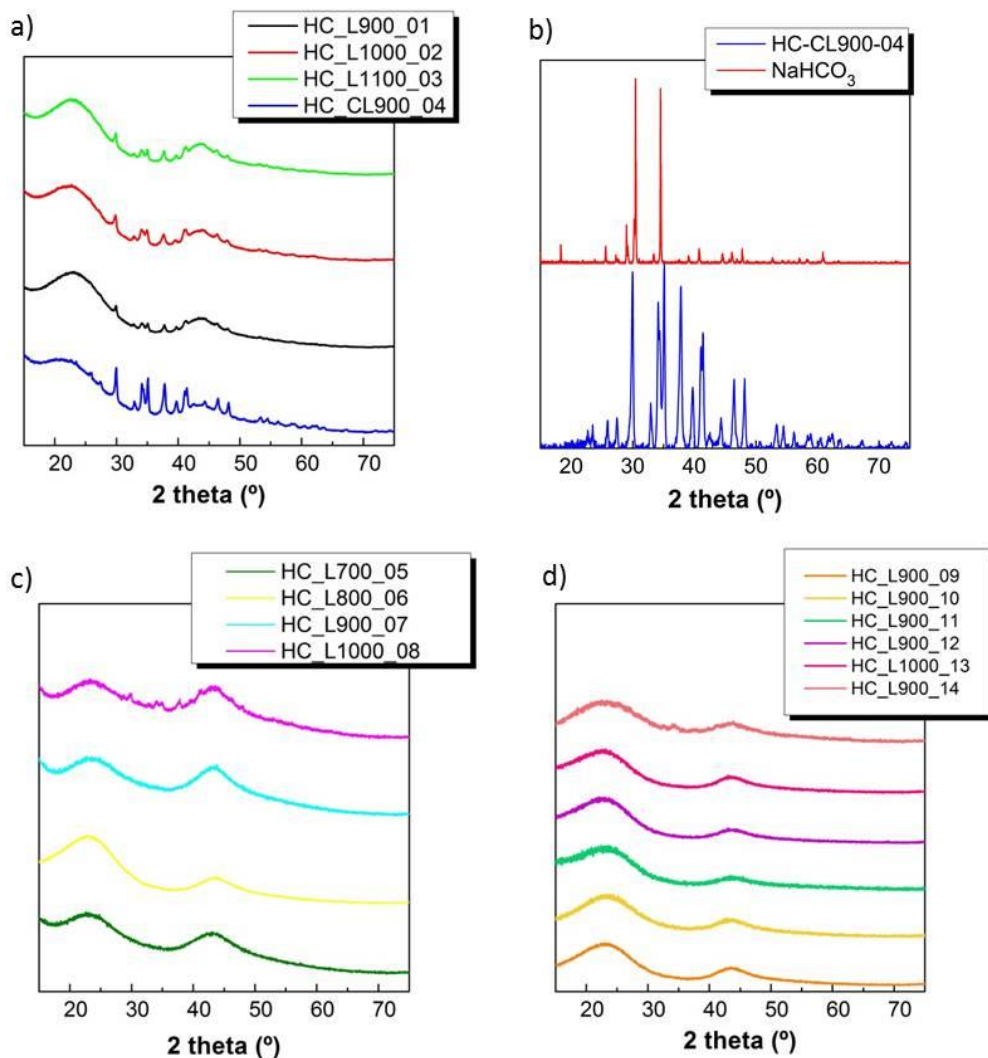


**Figure 2.8** XRD patterns for lignin derived hard carbons a) first series of synthesis (method A involving pyrolysis at a heating rate of  $1^{\circ}\text{C}\cdot\text{min}^{-1}$  up to the maximum temperature and 1 hour at that temperature), b) comparison of the XRD pattern of  $\text{NaHCO}_3$  and the HC-CL900-04 sample. Note that the background has been removed from the pattern of HC-CL900-04 so that the peaks are more visible c) second series of synthesis (method B involving pyrolysis at a heating rate of  $5^{\circ}\text{C}\cdot\text{min}^{-1}$  up to the maximum temperature and a dwell time of 2 hours at that temperature) and d) third series of synthesis under different conditions.

Generally, hard carbons are highly disordered so the intensity is low and the peaks are broad. The structure of hard carbons cannot be easily described by standard crystallographic terminology because there is no regularly repeating unit cell nor they can be considered fully amorphous. When describing disordered  $\text{sp}^2$  carbon structures, it is common to use the crystallographic

properties of 2H-graphite as reference. As a first approximation, carbon atoms form structural units based on that of graphite. Pure graphite contains  $sp^2$  hybridized carbons arranged as defect free graphene sheets stacked parallel. The main features are:

- 1) The peak located around 20-26 ° in the diffraction pattern is normally referred to as the 002 peak, in reference to the 002 interlayer spacing peak of 2H-graphite having the AB-AB-AB layer sequence and provides the  $d_{002}$  (interlayer distance).
- 2) Although it is quite broad and asymmetric, unless the material is highly graphitic because it is generated by atoms in two dimensional sheets, the 100 peak (around 44°) can be also used to estimate the lateral extent of the graphene sheets.<sup>64</sup> This peak broadening is usually ascribed to crystallite size meaning that the broader the peak, the smaller the crystallite domain. The broadening also includes contributions from strain within the graphene layers, although the strain can hardly be separated from the grain size effects. The interlayer peaks (101 and 012) of 2H and 3R graphite are not observed at the vicinity of the 100 peak, denoting a lack of layer-layer crystalline coherency probably due to a high degree of turbostratic and stacking disorder.

The presence of crystalline peaks in the XRD patterns of the first series of samples (Figure 2.8) evidences the contamination of the samples. This contamination, which will be further related with a deterioration of the electrochemical performance in section 2. 4, probably arises from the fact that the pyrolysis was performed in the same tubular furnace where pyrolysis and activation with NaOH of other materials was carried out. The fact that the contaminants are also present in carbons derived from other precursors like PVC suggested that the compounds present in black liquor prior to lignin extraction are not the source of contamination but the tube of the furnace.  $NaHCO_3$ , was

---

<sup>64</sup> Ruland, W.; *Chemistry of Physics and Carbon*; Walker Jr., P. L., Ed.; Marcel Dekker: New York, **1968**; Vol 4, 1-84.



identified as a contaminant in the XRD of commercial lignin derived hard carbon as shown in Figure 2.8.

Since impurities, which were detrimental to the electrochemical performance, were also present in the second series of samples (Figure 2.8 c) it was necessary the replacement of the tubular furnace in order to get a clean environment for the pyrolysis. After replacing the contaminated tube, purer samples were obtained in series C, as it can be observed in Figure 2.8 d.

- **Other carbonaceous materials**

In Figure 2.9 a, the XRD pattern of the recycled PVC derived soft carbon is shown. The presence of unidentified impurities in the sample, which was synthesized in the same stainless steel tube as the contaminated lignin derived carbon samples corroborated that the tube of the furnace was the source of contamination. The rest of the carbon materials were synthesized in the new quartz tube. Therefore, the XRD patterns showed no presence of impurities, as can be observed in Figure 2.9 b. PXRD patterns of sugar derived hard carbons (HC-SAW and HC-SA), natural lignin derived hard carbon (HC-L900-11), PVC derived soft carbons (SC-PVCLM, SCPVC-HM and SC-PVCR), carbon black (AB) and graphite are shown in Figure 2.9 a.

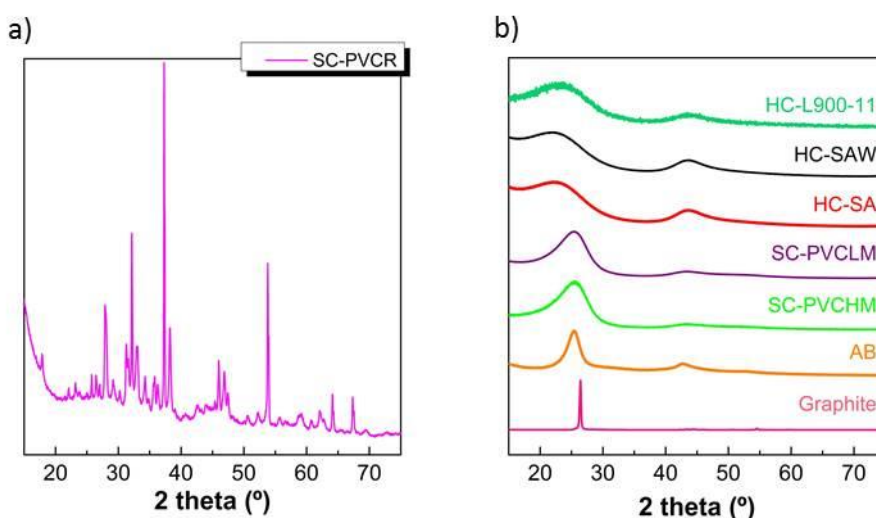


**Figure 2.9** a) PXRD profiles of various carbons with increasing disorder from bottom to top. b) PXRD pattern of soft carbon derived from recycled PVC containing impurities (SC-PVCR).

Graphite, due to its high degree of crystallinity gives rise to very well defined peak around  $26^\circ$  corresponding to the 002 reflection. Hard carbons, regardless of their precursor, lead to very wide 002 peaks due to their highly disordered structure. Moreover, the peak corresponding to the 002 reflection is shifted towards lower  $2\theta$  angles (around  $22^\circ$ ) indicating larger interlayer distance according to Bragg's law. This is known to be the fact of the "house of cards" arrangement which is induced by strong tilt disorder of graphene layers which point towards each other rather than stacking in the parallel way configuration observed in graphitic carbons.<sup>65</sup> Acetylene black and PVC derived soft carbons show an XRD profile that lies on the average between highly ordered graphite and highly disordered hard carbon. Therefore they show various degrees of disorder and interlayer distances.

### 2.3.3 Scanning electron microscopy (SEM)

- **Lignin derived carbons**

The SEM images of hard carbons obtained according to the three different methodologies A, B and C are shown in Figure 2.10, Figure 2.11 and Figure 2.12, respectively.

#### **Series A**

In the first series of samples, (Figure 2.10) there were no noticeable changes in the morphology of the samples depending on the temperature of synthesis and precursor. Due to the manual grinding, size distribution is quite broad for all samples, with particle sizes ranging from 10-150  $\mu\text{m}$ .

---

<sup>65</sup> Gupta, A. and Harrison, R.; small-angle X-ray scattering (SAXS) in carbonized phenolic resins, *Carbon*, **1994**, 32, 953-960.

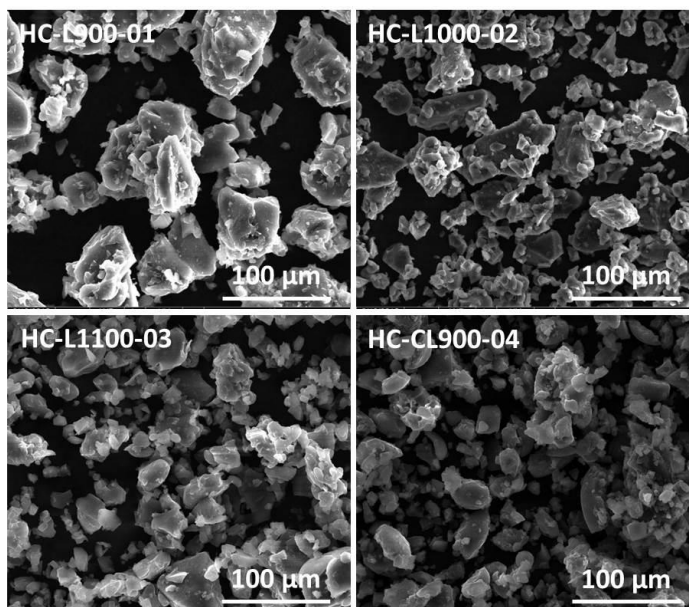


**Figure 2.10** SEM images of lignin derived hard carbons synthesized according to the synthesis conditions (A) involving pyrolysis at a heating rate of  $1^{\circ}\text{C}\cdot\text{min}^{-1}$  up to the maximum temperature (see caption in the picture) and a dwell time of 1 hour at that temperature.

### Series B

In Figure 2.11 the SEM images of the second series of synthesis are shown. Except for the sample pyrolyzed at  $700^{\circ}\text{C}$  (HC-L700-05) which shows larger particle size, there are no morphological differences among the samples. The larger size of HC-L700-05 cannot be ascribed to the temperature of pyrolysis but to the manual grinding.

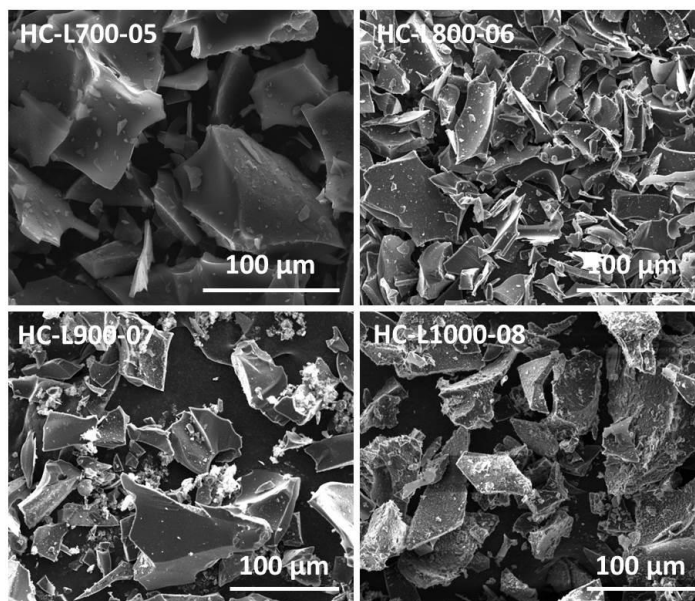


**Figure 2.11** SEM images of lignin derived hard carbons synthesized according to the synthesis conditions (B) involving pyrolysis at a heating rate of  $5^{\circ}\text{C}\cdot\text{min}^{-1}$  up to the maximum temperature (see caption in the picture) and a dwell time of 2 hours at that temperature.

### Series C

In Figure 2.12, the SEM images of samples prepared according to the different synthetic conditions summarized in Table 2.3 are shown. The variation of synthetic parameters such as lignin ageing by comparison of HC-L900-10 and HC-L900-11, Ar flow rate (HC-L900-09 and HC-L900-10), grinding of the precursor (HC-L900-11 and HC-L900-12), dwell time at the temperature of pyrolysis (HC-L900-11 and HC-L900-14) and temperature of pyrolysis (HC-L900-11 and HC-L900-13) did not provide any noticeable difference in the resulting morphology.

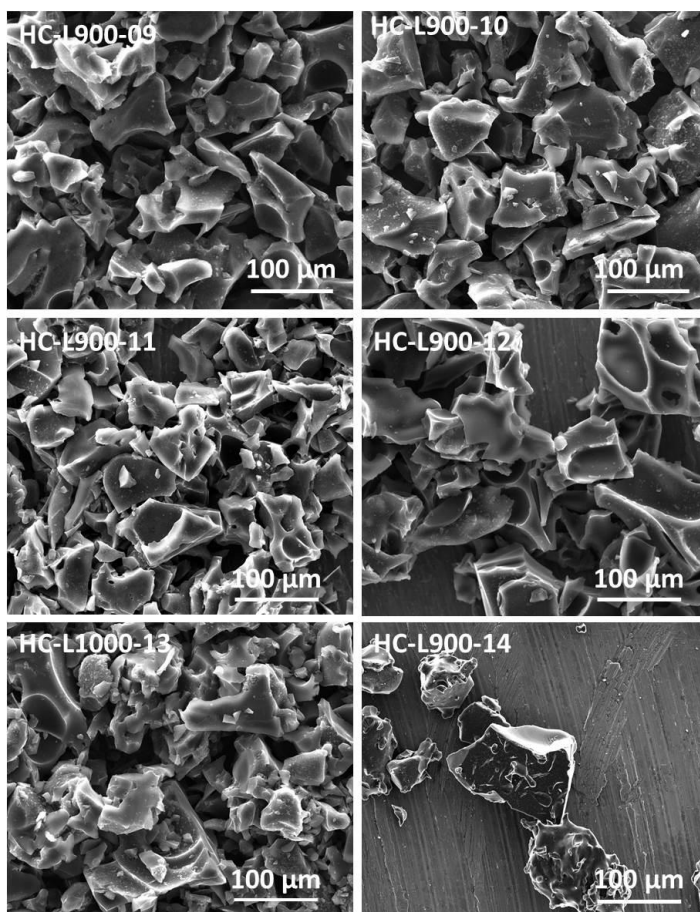


**Figure 2.12** SEM images of lignin derived hard carbons synthesized according to different synthesis conditions (C).

### **Energy-dispersive X-ray spectroscopy (EDX)**

In order to determine the composition of the carbons, energy-dispersive X-ray spectroscopy (EDX) was performed. In Figure 2.13, a comparison of average of atomic percentage content of several measurements of the three series of synthesis is shown.

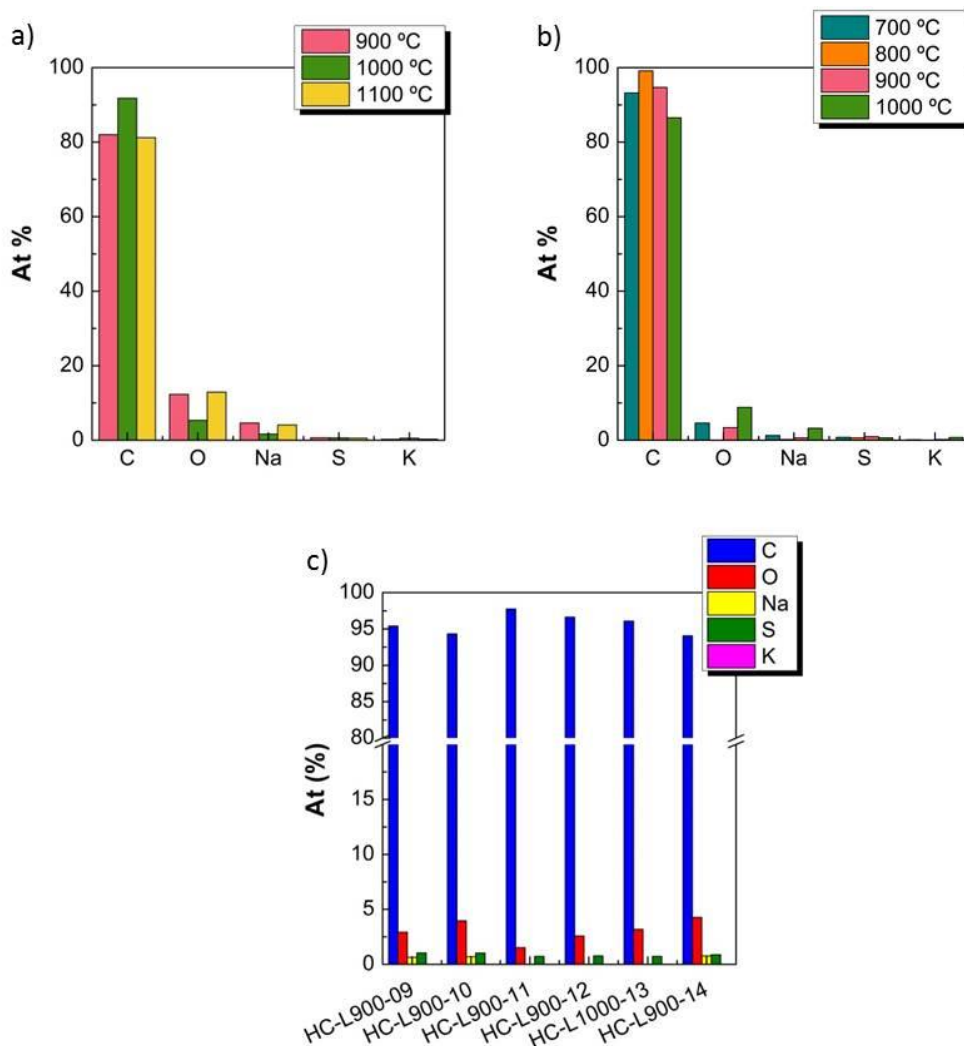


**Figure 2.13** Comparison of the composition (atomic percentage) determined by EDX of lignin derived carbons of the a) A series of synthesis synthesized at different temperatures (see legend), b) B series of synthesis synthesized at different temperatures (see legend) and c) C series of synthesis.

The purity of carbons was improved from series A to C as a consequence of the gradual elimination of the cross-contamination arising from the tube where pyrolysis was performed. Despite higher purity might be expected from the use of higher temperatures of pyrolysis, that tendency was not observed. However, a decrease of the oxygen content, which is known to affect the electrochemical performance of the materials, was observed when the heating rate was increased

from  $1\text{ }^{\circ}\text{C}\cdot\text{min}^{-1}$  (corresponding to series A, Figure 2.13 a) to  $5\text{ }^{\circ}\text{C}\cdot\text{min}^{-1}$  (series B and C, Figure 2.13 b and c).

- **Other carbonaceous materials**

The SEM pictures of commercial acetylene black and commercial PVC derived soft carbons of high (SC-PVCHM) and low (SC-PVCLM) molecular weight, of recycled PVC (SC-PVCR) and sugar derived hard carbons heated in air (HC-SA) and acid washed (HC-SAW) are shown in Figure 2.14.

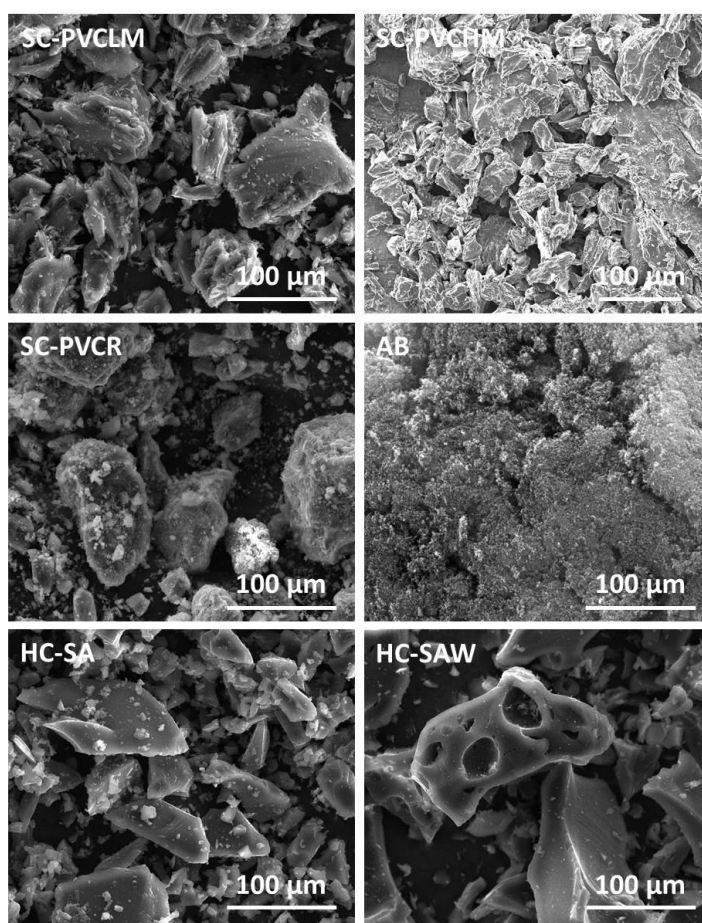


**Figure 2.14** SEM images of PVC derived soft carbons, sugar derived hard carbons and commercial acetylene black.

Except for the AB, which is commercial and shows very low particle size ( $0.042\text{ }\mu\text{m}$ ), all the hard and soft carbon samples showed quite similar features. They

present a large variety of particle sizes ranging from less than 10  $\mu\text{m}$  to more than 100  $\mu\text{m}$  and sharp edges that indicate that they are hard materials.

### 2.3.4 Raman spectroscopy

The structural properties of L-HC and H-HC have been studied by Raman spectroscopy. Raman spectra of carbon materials show double peaks at around  $1355\text{ cm}^{-1}$  (D peak) and  $1580\text{ cm}^{-1}$  (G peak).<sup>66</sup> The G peak is due to the C=C bond stretching of all pairs of  $\text{sp}^2$  atoms in rings or chains. However, the interpretation of D peak has undergone a debate because it may have various origins. In diamond or  $\text{sp}^3$  containing carbons it corresponds to the vibration modes of the  $\text{sp}^3$  C-C bonds. In disordered carbons it has been considered to be due to the breathing modes of  $\text{sp}^2$  atoms in rings so that it can be related to defects within layers (clustering of the  $\text{sp}^2$  phase, bond disorder, etc) or to the  $\text{sp}^2/\text{sp}^3$  ratio.<sup>67</sup> D mode strength is proportional to the probability of finding a sixfold ring in the cluster. Thus, in amorphous carbons the development of a D peak indicates ordering. From the G peak, information of the degree of disorder can also be extracted as its width is related to inter-planar defect density, or basal plan disorder.<sup>66</sup>

In Figure 2.15a, the Raman spectrum of lignin derived hard carbon is compared to those of sugar derived hard carbon and PVC soft carbon. In order to compare different samples, it is necessary to compare relative signals of the two peaks rather than absolute signals, as the intensities are dependent upon other factors including surface roughness and reflectance.<sup>66</sup>

The ratio of the areas of the D peak over the G peak, which can be correlated to the distance between defects, was calculated for lignin derived hard carbon, sugar derived hard carbon and PVC derived soft carbon.

---

<sup>66</sup> Tanabe, T.; Niwase, K.; Tsukuda, N. and Kuramoto, E., On the characterization of graphite, *J. Nucl. Mater.*, **1992**, 191-194, 330-334.

<sup>67</sup> Ferrari, A. C., Raman spectroscopy of graphene and graphite: Disorder, electron-phonon coupling, doping and nonadiabatic effects, *Solid State Commun.*, **2007**, 143, 47-57.



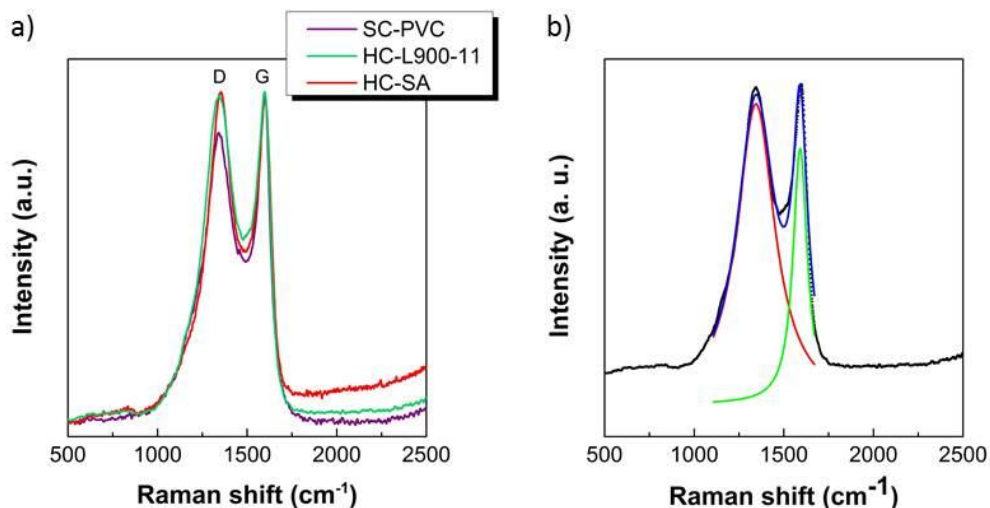


**Figure 2.15** a) Raman spectra obtained after normalization and b) Raman spectrum obtained for HC-L900-11 and the mathematical peak fitting obtained.

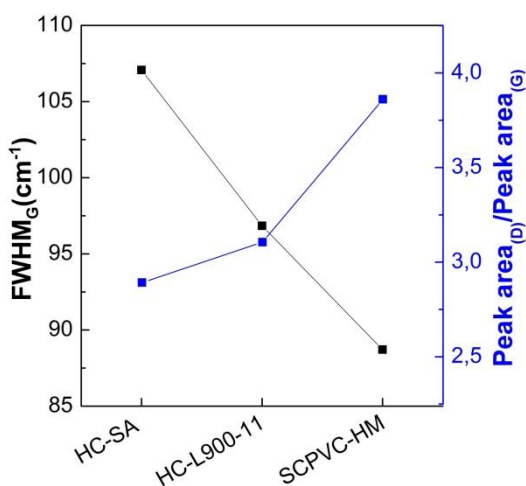
The areas together with the peak position and full width at half maximum of the G peak ( $FWHM_G$ ) were obtained after mathematical fitting of the two peaks using the sum of two pseudo-Voigt equations with Origin Lab 9.1 software. An example of the mathematical peak fitting is shown in Figure 2.15b.

Table 2.5 contains the values obtained after each spectra was fitted, including the position of the two peaks, the relative intensity and  $FWHM_G$ .

**Table 2.5** D and G peak positions, the full width at half maximum of the peak ( $FWHM_{(G)}$ ) corresponding to the G peak, and ratio between D and G peak areas ( $A_{(D)}/A_{(G)}$ ) obtained from mathematical fits of Raman spectra of the carbons.

Sample	D peak position ( $cm^{-1}$ )	G peak position ( $cm^{-1}$ )	$FWHM_{(G)}$	$A_{(D)}/A_{(G)}$
HC-SA	1352,5	1594,1	107,1	2,892
HC-L900-11	1344,7	1591,3	96,8	3,106
SC-PVCHM	1347,7	1593,3	88,7	3,861

In Figure 2.16 the  $FWHM$  of the G band is represented vs. the ratio between D and G peaks area.



**Figure 2.16** FWHM<sub>G</sub> vs. ratio between D and G peaks area.

The FWHM<sub>G</sub> gives insight into how graphitized the carbon is and decreases as the inter-planar disorder increases. The increase of the ratio between peak area of D and G bands is correlated with the decrease of the distance between defects thus, higher disorder. From Figure 2.16 it can be concluded that the degree of disorder of lignin derived hard carbon (HC-L900-11) lies on the average between sugar hard carbon (HC-SA) which is the most ordered and PVC soft carbon (SCPVC-HM), which is the less ordered. However, this tendency could be more related to the fact that an increasing temperature of pyrolysis results in larger ordering rather than to the nature of the precursor as HC-SA, HC-L900-11 and SC-PVCHM were obtained at 1050 °C, 900 °C and 800 °C, respectively.

### 2.3.5 BET area

The determination of surface area of carbonaceous electrode materials is of high importance because a large surface area provides more room for the electrolyte to decompose at the surface and react with Na to form Na-containing compounds where Na<sup>+</sup> cannot be removed thus resulting in large irreversible capacity.

Surface area analysis was performed on three hard carbons (sugar derived HC-SAW, lignin derived HC-L900-12, commercial lignin derived HC-CL900-04), on one soft carbon (SC-PVCLM) and carbon black (acetylene black). In Figure 2.17 the isotherms of the carbon materials are shown.

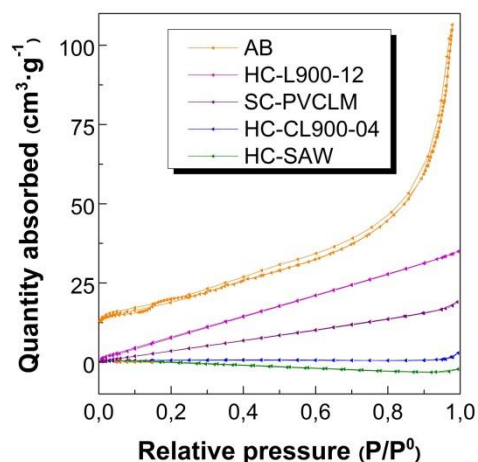


**Figure 2.17** Isotherms ( $N_2$  adsorption, 77K) of natural lignin, commercial lignin and sugar (acid washed) derived hard carbons as well as on commercial PVC derived soft carbon and acetylene black.

The specific surface area values according to the Brunauer-Emmett-Teller method are summarized in Table 2. 6.

**Table 2. 6** Specific surface areas deduced from the Brunauer-Emmett-Teller (BET) method, mass of sample used for each experiment and the total measured area.

Sample	SSA <sub>BET</sub> (m <sup>2</sup> /g)	Mass (mg)	Measured surface area (m <sup>2</sup> )
AB	65	100.1	6.5
HC-SAW	0.51	308.3	0.2
SC-PVCLM	22	338.6	7
HC-CL900-04	2	138.2	0.3
HC-L900-12	18	136.6	2

As for sugar derived hard carbon and commercial lignin derived hard carbon the values of total measured area are below 1m<sup>2</sup>, which is, according to the manufacturer, the detection limit of the apparatus, the obtained values were not

accurate. However, it can be concluded that hard carbons have very low surface area and of the same order of magnitude as PVC soft carbons.

### 2.3.6 Small Angle X-Ray Scattering (SAXS)

The representation of the intensity recorded during a SAXS experiment against the scattering vector ( $q^2$ ) after proper corrections and background subtraction as presented in the annex (A1.2) gives the SAXS profile of the samples. In Figure 2.18 a, the SAXS profiles of the lignin derived hard carbons synthesized according to the second synthetic methodology are shown. This series of samples was chosen because the range of temperatures of pyrolysis used (700-1000 °C) allows the study of the evolution of the porosity with the temperature. Figure 2.18 b shows the comparison of the SAXS profile of the lignin derived hard carbon sample showing best electrochemical performance among the samples synthesized through methodology B (as will be further discussed) and a sugar derived hard carbon (HC-SA) and a soft carbon synthesized from PVC (SC-PVCHM).

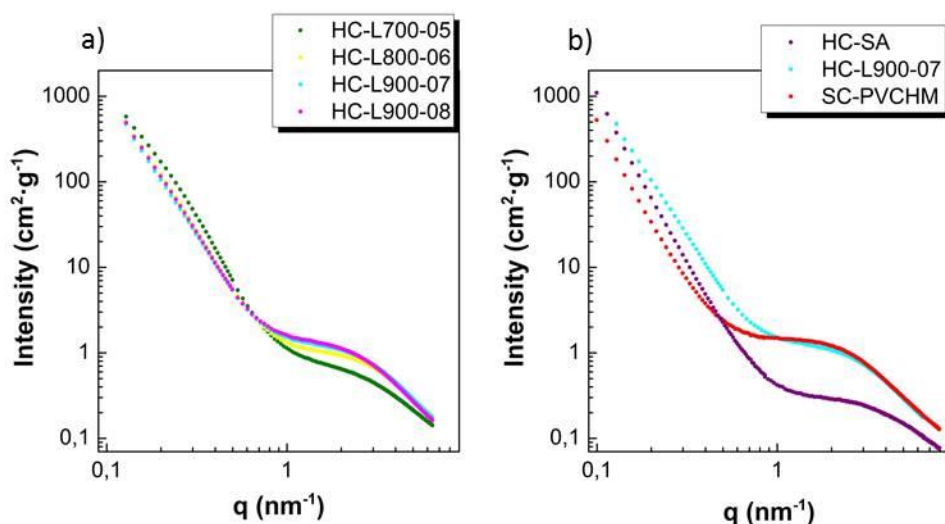


**Figure 2.18** a)  $I$  vs.  $Q$  profiles of lignin derived carbons synthesized through method B, b) comparison of the  $I$  vs.  $Q$  profiles of lignin derived hard carbon synthesized at 900 °C (HC-L900-07), of sugar derived hard carbon (HC-SA) and PVC-derived soft carbon (SC-PVCHM).

All the samples show an intensity profile typical of porous materials with a large intensity at low  $q$  decaying as  $q^{-4}$ .

Intensity (I) can be defined by as follows:

$$I(Q) = (\Delta\rho)^2 \sum_i n_i V_{pi}^2 P_i(Q) \text{ (a.u.)} \quad \text{Eq.2.2}$$

The intensity  $I(Q)$  is a sum of all the contributions of the objects (particles or pores).  $\Delta\rho$  is the contrast of scattering length between carbon and vacuum,  $n_i$  is the amount of particles,  $V_{pi}$  their volume, and  $P_i(Q)$  is the form factor which depends on the shape and size of the particles and whose value is normalized to 1 at low  $Q$  and decreases as  $Q$  increases. The form factor  $P_i(Q)$  can be approximated by a Gaussian curve at small angles. According to Guinier<sup>68</sup>, the curvature of this Gaussian is due to the overall size of the particles so that:

$$P(Q) \approx a_0 \exp(-R_G^2 \frac{q^2}{3}) \quad \text{Eq.2.3}$$

$R_G$  is the radius of gyration and can be used to calculate particle dimensions. Assuming that the particles are spherical with an equal density, the average radius can be calculated by

$$R = \sqrt{5/3} R_G \quad \text{Eq.2.4}$$

The parameter  $a_0$  is the extrapolated zero-angle intensity. In the equation above  $a_0=1$  because  $P(0)=1$  by definition, but if  $\Delta I(q)$  is used instead, then  $a_0=\Delta I(0)$ , which can be used to represent the Guinier plot. In the Guinier plot, the logarithm of the intensity is plotted vs. the square of the length of the scattering vector ( $q^2$ ).

$$\ln[\Delta I(q)] = \ln[a_0] - \frac{R_G^2}{3} q^2 \quad \text{Eq.2.5}$$

The  $R_G$  and  $a_0$  are determined by straight-line fitting from the slope ( $-R_G^2/3$ ) and from the intercept ( $\ln(a_0)$ ) as shown in Figure 2. 19.

---

<sup>68</sup> Schnablegger, H. and Sing, Y., The SAXS guide: getting acquainted with the principles, **2011**, Anton Paar, Austria.

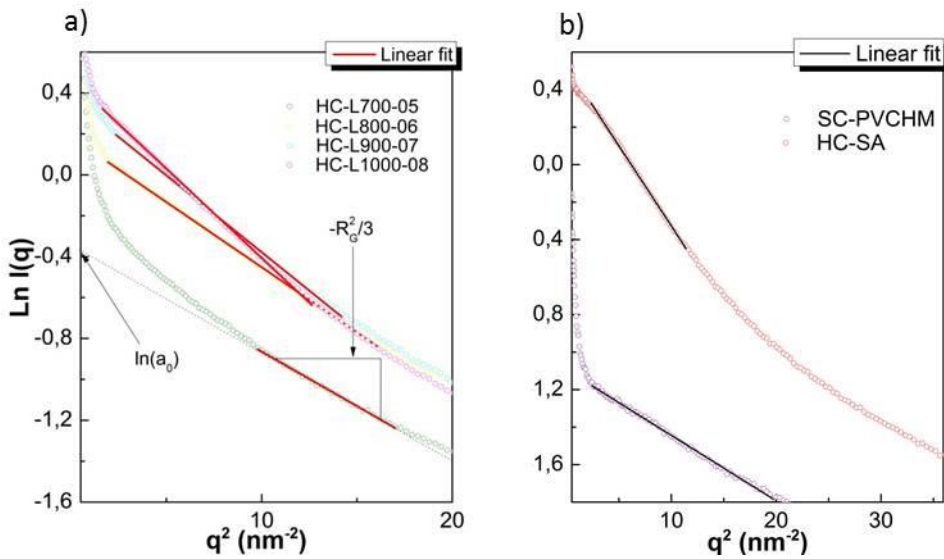


**Figure 2. 19** Linear fit of the Guinier plots of lignin derived carbons synthesized through method B (a) and PVC derived soft carbon (SC-PVCHM) and sugar hard carbon (HC-SA)

The determination of  $R_G$  allows the calculation of the radius of the pores. Although both carbon particles and pores give rise to SAXS intensity, it happens at different  $Q$  ranges since particles are typically micrometric while pores can be as small as a fraction of nanometers. SAXS does not make any distinction if the pores are open or buried and thus inaccessible from the surface by a gas or an electrolyte.

The scattering contrast ( $\Delta\rho$ ) between carbon and vacuum has been calculated on the basis of a scattering length of  $8,504 \cdot 10^{10} \text{ cm} \cdot \text{g}^{-1}$  for carbon<sup>69</sup> multiplied by the density of the carbons.

$$\Delta\rho (\text{cm}^{-2}) = \rho (\text{cm} \cdot \text{g}^{-1}) \cdot d (\text{g} \cdot \text{cm}^{-3}) \quad \text{Eq. 2.6}$$

The density of the carbons ( $d_{\text{carbon}}$ ) was calculated considering the density of graphite ( $d_{\text{graphite}} = 2.2676 \text{ g} \cdot \text{cm}^3$ ), the interplanar distance of graphite ( $d_{002\text{graphite}}$ ) and interplanar distance of carbons ( $d_{002\text{carbon}}$ )

<sup>69</sup> <https://www.ncnr.nist.gov/resources/activation/>

$$d_{carbon}(g \cdot cm^3) = \frac{d_{graphite}(g \cdot cm^{-3}) \cdot d_{002\ graphite}}{d_{002\ carbon}} \quad \text{Eq. 2.7}$$

The interplanar distance of carbons ( $d_{002carbon}$ ) was calculated by obtaining the position of the 002 peak in the XRD patterns through mathematical fitting using a pseudo-Voigt function (Figure 2.20).

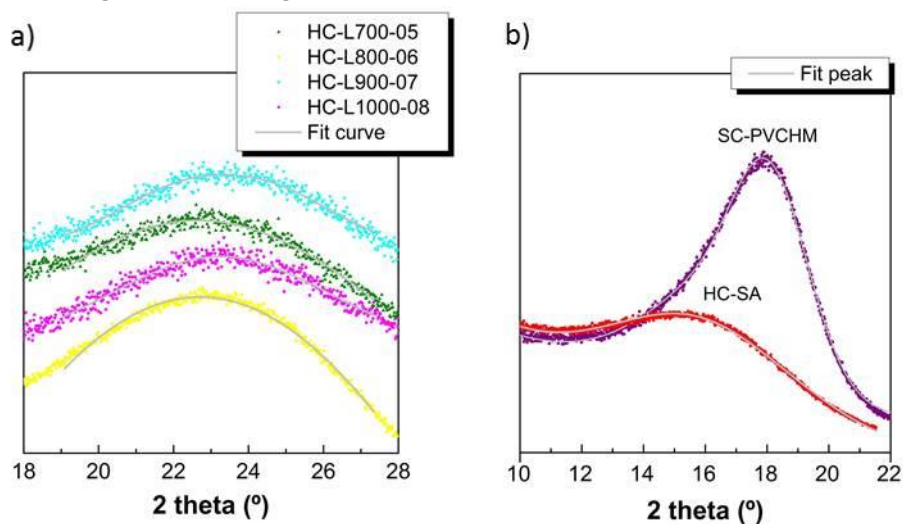


**Figure 2.20** Fitting of the XRD patterns of lignin derived hard carbons (a) and sugar hard carbon and PVC soft carbon (b) with a pseudo-Voigt function.

The porous volume ( $V_p$ ) can be calculated from the following equation considering the scattering contrast ( $\Delta\rho$ ), the zero-angle intensity ( $I_0$ ) and the average pore radius ( $R$ ).

$$V_p(cm^3 \cdot g^{-1}) = \frac{I_0(cm^2 \cdot g^{-1})}{(\Delta\rho)^2(cm^{-4}) \cdot \frac{4}{3}\pi R^3(cm)} \quad \text{Eq. 2.8}$$

In Figure 2.21, the average pore diameter and pore volume of lignin derived hard carbons synthesized through B methodology are represented vs. the temperature of pyrolysis together with sugar derived hard carbon (HC-SA) and PVC derived soft carbon.

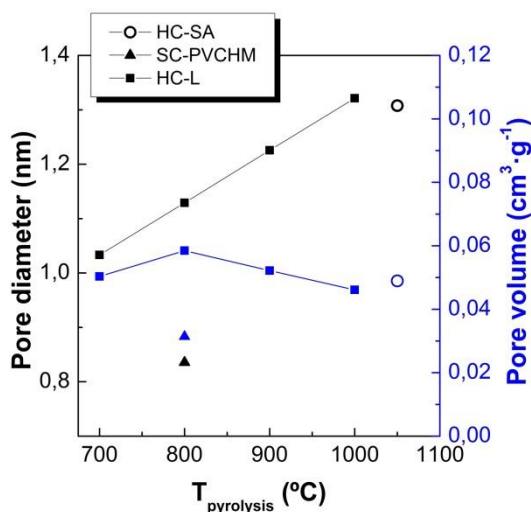


**Figure 2.21** Average pore diameter and pore volume vs. temperature of pyrolysis of lignin derived hard carbons synthesized following B methodology at different temperatures (squares), of sugar derived hard carbon (HS-SA, circles) and PVC derived soft carbon (SC-PVCHM, triangles).

It is observed that for lignin derived hard carbons the pore diameter increases with the temperature of pyrolysis. This is consistent with the “falling cards model” (Figure 2.22) proposed by Buiel *et al.*<sup>70</sup> According to this model, micropores separated by a single graphene sheet coalesce when a single layer becomes mobile at high temperature and aligns with neighboring layers in a process similar to graphitization on a very small scale.

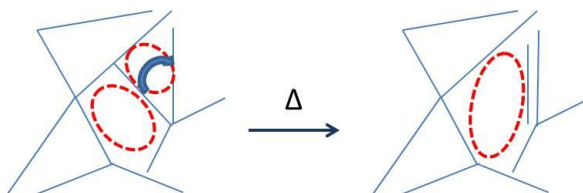


**Figure 2.22** The “falling card model” for hard carbon. Solid lines represent graphene sheets.

The fact that pore volume remains more or less constant with increasing temperature of pyrolysis while the pore diameter increases, suggests that no new microporosity is created upon heating at higher temperatures.

<sup>70</sup> Buiel, E.; George, A. E. and Dahn, J. R.; On the reduction of lithium insertion capacity in hard carbon anode materials with increasing heat-treatment temperature, *J. Electrochem. Soc.*, **1998**, 145 (7), 2252-2257.



The average pore volume is similar to that of sugar derived hard carbons at high temperatures of pyrolysis whereas it is more similar to that of PVC- soft carbons at low temperatures. These similarities in the pore diameter of carbons that have been synthesized at similar temperatures may indicate that the temperature of pyrolysis has a stronger effect on the development of the porosity than the nature of the precursor.

### 2.3.7 Electrochemical characterization

- **Carbons prepared through method A (two-step heating at  $1^{\circ}\text{C}\cdot\text{min}^{-1}$  up to the temperature of pyrolysis)**

The electrochemical performance of the lignin derived carbons was studied in order to prove the feasibility of the synthetic procedure to search for an optimum pyrolyzing temperature which would result in the largest reversible capacity for sodium insertion. Measurements were performed in a 2 electrode Na-ion cell vs. metallic sodium and deploying  $\text{NaClO}_4$  EC : PC as electrolyte.

In Figure 2.23 (a, c and e) the voltage vs. capacity of lignin derived hard carbons is shown during the first 2 cycles at a cycling rate of C/15 (equivalent to a  $25 \text{ mA}\cdot\text{g}^{-1}$  current density considering a theoretical capacity of  $372 \text{ mA}\cdot\text{h}\cdot\text{g}^{-1}$  for  $\text{NaC}_6$  formation) in the 0.002-2V vs.  $\text{Na}^+/\text{Na}$  voltage window.

As the SEM of the particles revealed sharp edges indicating that the carbons were likely to be hard carbons, a cut-off voltage as low as 0.002 V vs.  $\text{Na}^+/\text{Na}$  was chosen. The aim was to get the most out of the capacity of the material considering that a hard carbon would show a low voltage plateau close to 0 V vs.  $\text{Na}^+/\text{Na}$ , while avoiding sodium plating on the surface of the electrode that might arise from reaching 0 V vs.  $\text{Na}^+/\text{Na}$ .

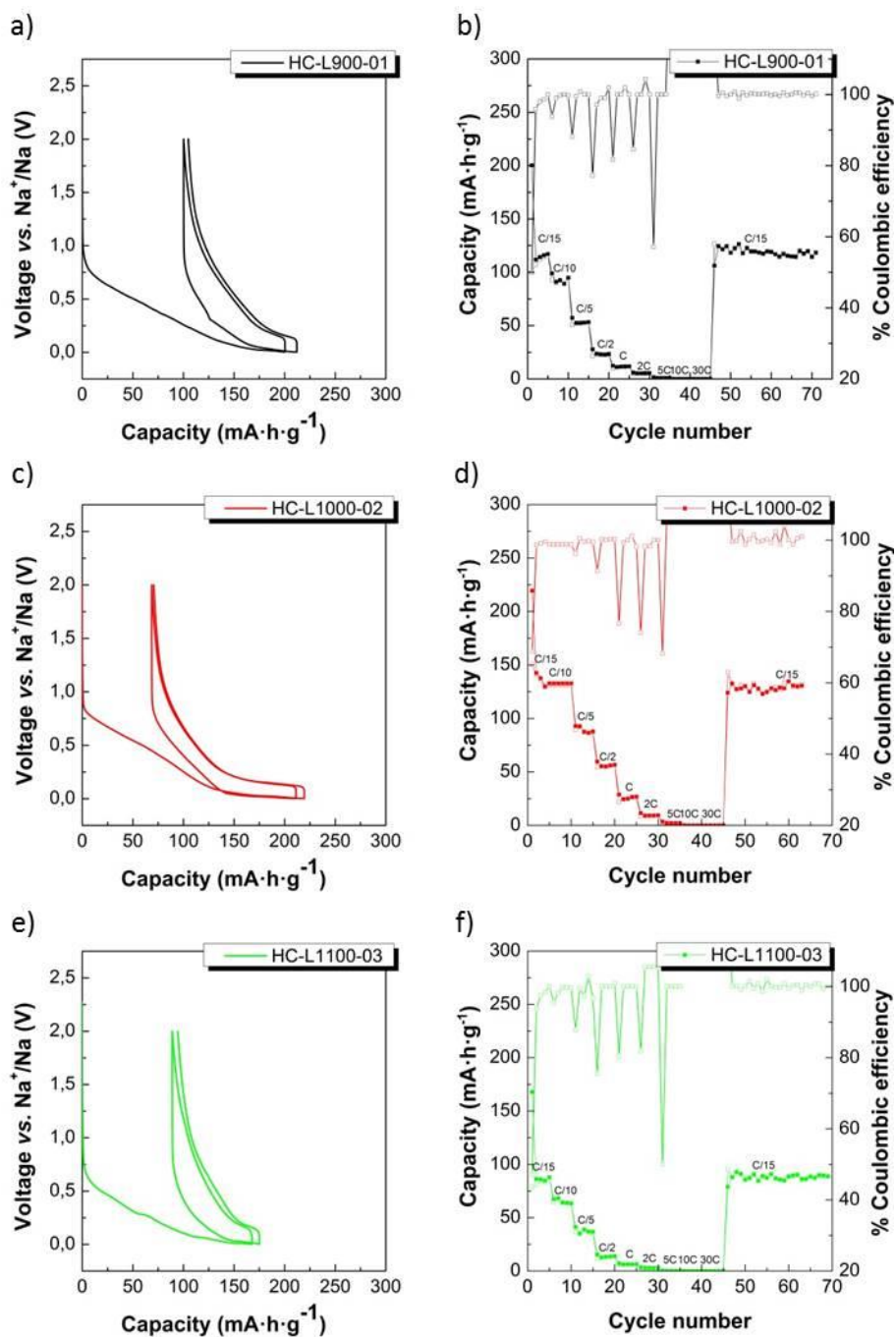


**Figure 2.23** a) c) and e) Voltage profile of the first and second cycle (C/15 rate) and b) d) and f) rate capability of lignin derived hard carbons synthesized by method A (at a heating rate of 1°C·min<sup>-1</sup> and a dwell time of 1 hour at the maximum temperature with an intermediate step of 1 hour at 110 °C).

Hard carbon materials can be represented by a series of graphene sheets arranged like a house of cards comprising two or three stacked layers and significant quantities of nanoscale porosity.<sup>71</sup> The layers are randomly rotated and shifted relative to each other, producing turbostratic disorder.<sup>72</sup> As this disorder might create interlayer sodium insertion sites with a range of chemical environments, the capacity develops over a range of potentials, giving a slope on the voltage profile. However, recent work found the slope region to be mostly related to the storage of sodium at defect sites (heteroatoms like oxygen, nitrogen) present at the surface of the crystallites as opposed to intercalation between graphene sheets.<sup>31</sup> In addition to this slope capacity, hard carbons also exhibit extensive capacity at a potential close to that of the metal itself along the low voltage plateau resulting from the insertion of sodium into the nanopores in a process analogous to adsorption.<sup>73</sup> This has been further confirmed by a recent in-situ NMR study,<sup>74</sup> while recent reports demonstrate that interlayer intercalation is also present in this voltage range.<sup>31</sup>

From the voltage profile it could be confirmed that the carbon materials are hard carbon-type because of the presence of a typical slope region in the curve below 1 V vs. Na<sup>+</sup>/Na followed by a plateau close to 0 V vs. Na<sup>+</sup>/Na.

In the voltage profile three different features can be observed: reversible capacity, irreversible capacity and hysteresis between charge and discharge. The reversible capacity ( $Q_{\text{rev}}$ ) is calculated as the charge capacity of the first cycle. It can be separated into two contributions: a slope from 1V to about 0.2 V vs.

---

<sup>71</sup> Dahn, J. R.; Xing, W. and Gao, Y., The "falling cards model" for the structure of microporous carbons, *Carbon*, **1997**, 35, 6, 825-830.

<sup>72</sup> Zheng, T. Reimers, J. N. and Dahn, J. R.; Effect of turbostratic disorder in graphitic carbon hosts on the intercalation of lithium, *Phys. Rev. B*, **1995**, 51, 734-741.

<sup>73</sup> Stevens, D. A. and Dahn, J. R.; An in situ small-angle X-ray scattering study of sodium insertion into a nanoporous carbon anode material within an operating electrochemical cell, *J. Electrochem. Soc.*, **2000**, 147 (12), 4428-4431.

<sup>74</sup> Stratford, J. M.; Allan, P. K.; Pecher, O.; Chater, P. A. and Grey, C. P., Mechanistic insights into sodium storage in hard carbon anodes using local structure probes, *Chem. Commun.*, **2016**, 52, 12430-12433.

Na<sup>+</sup>/Na and a plateau region from 0.2 to 0.002 V vs. Na<sup>+</sup>/Na. Figure 2.24 shows an example of how the different contributions to the capacity can be determined graphically and the numerical values are summarized in Table 2.7.

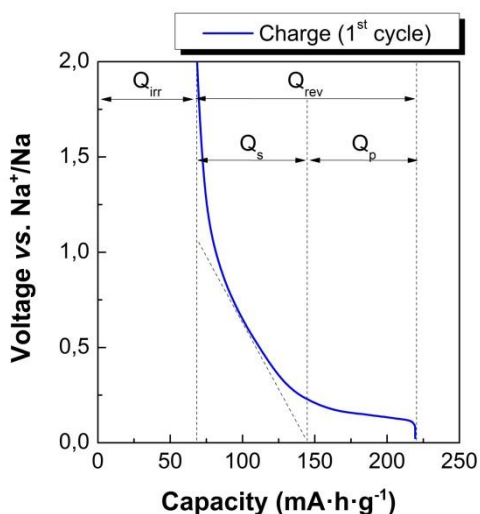


**Figure 2.24** Graphical calculation of the reversible capacity ( $Q_{rev}$ ), the sloping capacity ( $Q_s$ ), the plateau capacity ( $Q_p$ ) and the irreversible capacity ( $Q_{irr}$ ).

**Table 2.7** Reversible and irreversible capacity values of lignin derived hard carbon during the first cycle.

Sample	$Q_{rev}$ ( $\text{mA}\cdot\text{h}\cdot\text{g}^{-1}$ )			$Q_{irr}$ ( $\text{mA}\cdot\text{h}\cdot\text{g}^{-1}$ )
	$Q_s$	$Q_p$	$Q_t$	$Q_{irr}$
HC-L900-01	79	21	100	100
HC-L1000-02	98	53	151	68
HC-L1100-03	61	18	79	89

**Analysis of hysteresis.** Hysteretic behaviour meaning that the voltage of deintercalation is much higher than that of intercalation is undesirable in applications where high voltage is needed. The potential difference between charge and discharge will cause a reduction of the voltage when the battery is discharged.

The smallest hysteresis was observed for the synthesis performed at 1000 °C (HC-LC1000-02). In general, a reduction of the hysteresis would be expected for a material that has been pyrolyzed to a higher temperature, thereby removing

more functional groups.<sup>70</sup> However, the existence of cross-contamination from the tube of the furnace during pyrolysis made impossible to distinguish the source of impurities between the non-completion of the functional groups removal during pyrolysis and the incorporation of unknown chemicals to the final pyrolysis products. The presence of oxides on the carbon surface has been reported to be responsible for an increase of the hysteresis.<sup>77</sup> As discussed in section 2.3.3, EDX revealed that sample synthesized at 1000 °C (HC-LC1000-02) contained fewer impurities (mostly oxygen) than the other samples synthesized at 1100 and 900 °C. For that reason, the HC-LC1000-02 sample showed small hysteresis. Likewise, the hysteresis of hard carbons tested in lithium ion batteries has been correlated to residual hydrogen content (<0.5 % by mass). The hysteresis is caused by rehybridization of the carbon-carbon bond from  $sp^2$  to  $sp^3$  when lithium atoms bind on hydrogen-terminated edges of hexagonal carbon fragments, which has a large activation barrier that causes the potential for removal of lithium from these sites to shift to higher voltages.<sup>29</sup> The fact that little amount of sample remained after processing so as to get electrodes hampered the possibility of performing elemental analysis so as to know the hydrogen and oxygen content on the samples. For that reason, EDX was alternatively performed.

Other polarization losses can result in hysteretic behavior. For example, for charge transfer processes related to electrode reactions occurring at different rates, the slowest transfer becomes the rate-limiting process leading to an increase on the polarization. Another important source is the  $iR$  drop associated with the electrolyte, which increases proportionally to current density. Activation polarization is an inherent property of active materials and it is strongly influenced by temperature. Concentration polarization results from the concentration gradient of reactants at the surface of active materials. However, these different types of polarization are difficult to isolate and might require a deep study of the cell impedance, which is beyond the scope of this work.<sup>75</sup>

---

<sup>75</sup> Park, J.-K., Principles and applications of lithium secondary batteries, **2012**, Wiley-VCH Verlag, Weinheim, Germany, 14-15.

**Reversible capacity.** The maximum value of reversible capacity ( $151 \text{ mA}\cdot\text{h}\cdot\text{g}^{-1}$ ) was observed for the sample synthesized at  $1000 \text{ }^\circ\text{C}$  whereas lower capacities were observed for those prepared at  $900^\circ\text{C}$  and  $1100^\circ\text{C}$  ( $100$  and  $79 \text{ mA}\cdot\text{h}\cdot\text{g}^{-1}$ , respectively). Considering that the purity of the samples is independent of the temperature of pyrolysis, the different electrochemical performance cannot be ascribed to the heat treatment temperature but to the purity of the sample. In this regard, although no linear correlation was found between the reversible capacity and the impurities content (Figure 2.25a) it was observed that a large content of impurities (17 %) resulted in poor reversible capacities for samples synthesized at  $900$  (HC\_L900\_01) and  $1100 \text{ }^\circ\text{C}$  (HC\_L1100\_03). As expected, the sample providing largest capacity (HC\_L1000\_02) was the one having smallest impurity content (8 %).

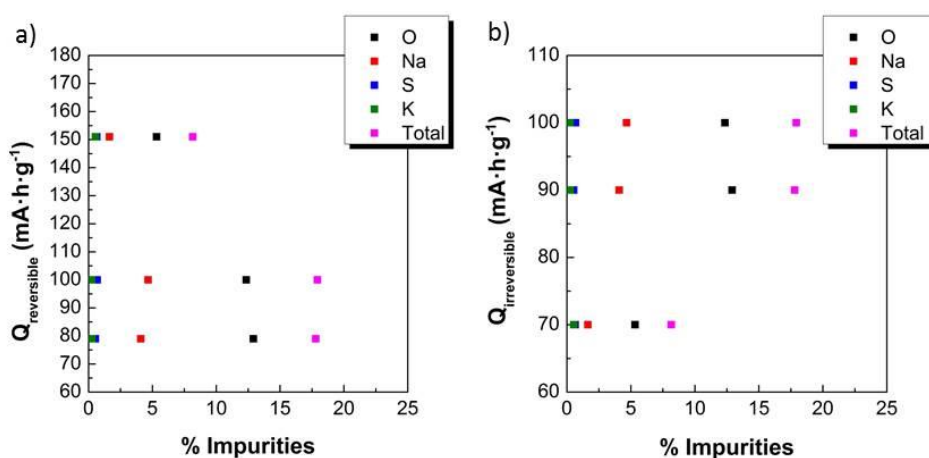


**Figure 2.25** First cycle reversible (a) and irreversible capacity (b) vs. % impurities content determined by EDX.

**Analysis of irreversible capacity.** The difference in capacity between the first discharge and the first charge gives the irreversible capacity ( $Q_{\text{irr}}$ ). Irreversible capacity is undesirable because  $\text{Na}^+$  ions consumed in the first discharge cannot be reversibly recovered. This leads to a reduction of useful capacity due to limited supply of Na ions in a real device. It is particularly important for low voltage anodes like carbons which have an insertion voltage below the voltage stability of the electrolyte which induces electrolyte degradation reactions. This electrolyte decomposition leads to the formation of a layer on the surface of the

electrode known as solid-electrolyte interphase (SEI).<sup>76</sup> Therefore, the irreversible capacity and the formation of SEI layer are known to depend on the amount and reactivity of the external specific surface. It would have been expected that the BET-specific surface area decreases as the heat treatment temperature increases because of the closing of micropores within particles or at the surface upon exposure to high temperatures.<sup>70</sup> However, the  $SSA_{\text{BET}}$  values observed (Table 2.6) were in the order of the measurement error, evidencing that the surface is barely porous and that the irreversible capacity cannot be attributed to it. Apart from the formation of SEI layer, other factors that may contribute to irreversible reactions are reduction reactions of impurities such as surface functional groups containing oxygen as reported by Xue *et al.* for lithium ion batteries.<sup>77</sup> Despite no linear correlation between the irreversible capacity and the presence of different impurities in the carbon such as O, Na, S or K was observed (Figure 2.25b) the sample showing lowest irreversible capacity (HC-L1000-02,  $68 \text{ mA}\cdot\text{h}\cdot\text{g}^{-1}$ ) was the one containing lowest percentage of total impurities (7%) and oxygen (5%). Lignin derived hard carbons prepared at  $900 \text{ }^\circ\text{C}$  (HC-L900-01) and  $1100 \text{ }^\circ\text{C}$  (HC-L1100-03) provided an irreversible capacity of 100 and  $89 \text{ mA}\cdot\text{h}\cdot\text{g}^{-1}$  with an oxygen content of 12.3 % and 12.9 %, respectively.

**Analysis of rate capability.** In Figure 2.23 b, d and e, the rate capability of the materials is shown. Despite having poor surface area might be detrimental because faster migration of ions would be expected from the presence of surface pores, the materials still exhibit some capacity at high rates up to C/5.<sup>78</sup> (Table 2.8)

---

<sup>76</sup> Peled, E., The electrochemical behavior of alkali and alkaline earth metals in nonaqueous battery systems-The solid electrolyte interphase mode *J. Electrochem. Soc.*, **1979**, 126 (12), 2047-2051.

<sup>77</sup> Xue, J. S. and Dahn, J. R.; Dramatic effect of oxidation on lithium insertion in carbons made from epoxy resins, *J. Electrochem. Soc.*, **1995**, 142, 11, 3668-3677.

<sup>78</sup> Park, J.-K., Principles and applications of lithium secondary batteries, **2012**, Wiley-VCH Verlag, Weinheim, Germany, 107.

**Table 2.8** Capacity values of lignin derived hard carbons cycled at different rates.

	C/15	C/10	C/5	C/2	C	2C	5C	10C	30C	C/15
L900-01	100	93	50	21	10	5	0	0	0	127
L1000-02	151	131	89	54	22	8	2	0	0	143
L1100-03	79	64	36	12	6	3	0	0	0	95

Very poor or even no capacity can be observed at faster rates than C/5. The hard carbon obtained at 1000 °C retained a 95 % of the initial reversible capacity after having cycled at different rates for 45 cycles. It is clear that the purity of the sample needs to be improved before going further in the performance assessment of lignin derived carbons.

- **Carbons prepared through method B ( $5^{\circ}\text{C}\cdot\text{min}^{-1}$  up to the temperature of pyrolysis)**

Once the feasibility of the production of hard carbon as of natural lignin was proven, a second series of synthesis involving heating at a faster rate ( $5^{\circ}\text{C}/\text{min}$ ) and a lower final pyrolysis temperature was performed. The aim was to reduce synthesis costs by decreasing the maximum heating temperature up to 1000 °C and to observe the effect of increasing the heating rate. In general, at temperatures below 700 °C changes regarding chemical composition leading to the so-called pyrolysis process occur. At higher temperatures materials already have very high carbon content and the composition only varies slightly.<sup>79</sup>

In Figure 2.3 the voltage vs. capacity during the first cycle at a cycling rate of C/15 (equivalent to a  $25 \text{ mA}\cdot\text{g}^{-1}$  constant current density considering a theoretical capacity of  $372 \text{ mA}\cdot\text{h}\cdot\text{g}^{-1}$  for  $\text{NaC}_6$  formation) of lignin derived hard carbons is shown. All the samples present the characteristic slope and low voltage plateau of hard carbon.

<sup>79</sup> Byrne, J. F.; Marsh, H. Introductory overview in porosity in carbons, characterization and applications, Ed. Patrick J. W. Arnold, London, **1995**.



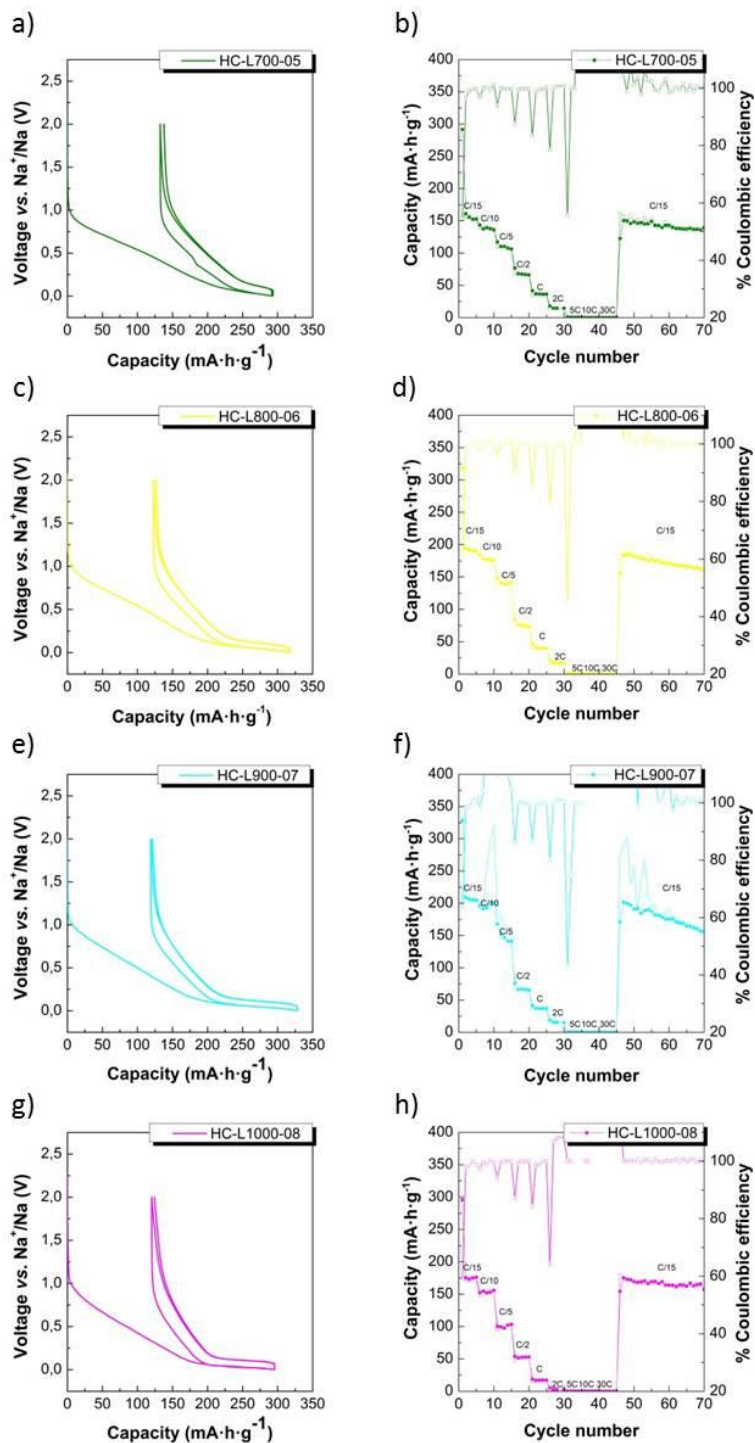


**Figure 2.26** a), c), e) and g) Voltage profile of the first and second cycle (C/15 rate) and b), d), f) and h) rate capability of lignin derived hard carbons synthesized by method B (at a heating rate of 5°C·min<sup>-1</sup> and a dwell time of 2 hour at the maximum temperature).

**Hysteresis.** For the previous series of synthesis, the amount of impurities reached 17 % but in this case, except for the sample synthesized at 1000 °C, which has a 13 % of impurities content, the rest of the samples had between 1-5 % of impurities content. Probably due to the presence of fewer remaining functional groups in the carbon, the voltage profile showed less polarization.

**Reversible and irreversible capacity.** The low voltage plateau, which provides additional capacity is enlarged compared to previous syntheses at the same temperature. Therefore, an overall increase of the reversible capacity is observed except for the sample synthesized at 1000 °C, which has low purity. Except for this sample, a decrease of the capacity ascribed to the slope and an increase of the capacity of the low voltage plateau with increasing temperature can be noticed (Table 2.9) which is in accordance with the tendency reported for sugar hard carbons.<sup>60</sup> Hence, the largest reversible capacity (209 mA·h·g<sup>-1</sup>) and lowest irreversible capacity (119 mA·h·g<sup>-1</sup>) was observed for the sample synthesized at 900 °C (HC-L900-07).

**Table 2.9** Reversible and irreversible capacity values of lignin derived hard carbon during the first cycle.

Sample	Q <sub>rev</sub> (mA·h·g <sup>-1</sup> )			Q <sub>irr</sub> (mA·h·g <sup>-1</sup> )	
	Q <sub>s</sub>	Q <sub>p</sub>	Q <sub>t</sub>	Q <sub>irr</sub>	
HC-L700-05	151	8	159	132	
HC-L800-06	140	55	195	123	
HC-L900-07	121	88	209	119	
HC-L1000-08	109	66	175	121	

**Rate capability.** In Figure 2.26 (b, d, f and h) the rate capability of the materials is shown. Regarding the cycling performance of the samples at different charge rates, they all showed good rate capability at high C rates up to C/2. In Table 2.10, the reversible capacity at different rates is shown. Hard carbons synthesized at 900 °C (HC-L900-07) provided 193, 184 and 66 mA·h·g<sup>-1</sup> when cycled at C/10, C/5 and C/2, respectively.

**Table 2.10** Capacity values of lignin derived hard carbons cycled at different rates.

	C/15	C/10	C/5	C/2	C	2C	5C	10C	30C	C/15
HC-L700-05	159	139	110	67	35	14	0	0	0	161
HC-L800-06	195	190	143	76	40	17	0	0	0	185
<b>HC-L900-07</b>	<b>209</b>	<b>193</b>	<b>184</b>	<b>66</b>	<b>36</b>	<b>15</b>	<b>0</b>	<b>0</b>	<b>0</b>	<b>271*</b>
HC-L1000-08	175	148	95	47	21	3	0	0	0	179

(\*) Extremely high capacity due to trailing plateau during charge.

The appearance of an extremely high capacity can be observed during charge in the 10<sup>th</sup> cycle of the sample synthesized at 900 °C (HC-L900-07). This is related to the presence of a large plateau during charge whose source remains unclear but seems not to be related to the carbon sample but rather to other cell components as this so-called called “trailing plateau” was also observed for organic anodes (PolySchiff bases). This will be discussed in more detail in chapter 3 of this thesis. The fact that it was randomly observed when cycling cells with different electrolytes (NaFSI MeTHF and NaClO<sub>4</sub> EC:PC) in voltage windows reaching very low voltages (0.002 or 0.005 V vs. Na<sup>+</sup>/Na) suggested that the process might related to reaching very low voltages during the reduction due to sodium plating leading to micro short-circuits or to the presence of any other electrochemically active species derived from cross-contamination when assembling the cell in the glove box.

- **Carbons prepared through method C. Optimization of the synthesis.**

As described in the experimental section, after an optimal temperature of pyrolysis was determined (900 °C), experiments were designed to search for the optimum pyrolysis conditions. In order to avoid the contamination of the samples during pyrolysis because of the presence of unknown compounds on the tubular furnace, presumably as a result of activation processes with KOH carried out in the same tube with other purposes, new quartz tube and alumina boat were used. In Table 2.11 the synthesized samples according to their synthesis conditions are summarized.

**Table 2.11** Summary of the conditions used to study the effect of the synthetic parameters on the electrochemical performance of lignin derived hard carbons.

Sample	Tube	Age	Ar flow (mL/min)	Grinding	t <sub>dwell</sub> (h)	T <sub>pyr</sub> (°C)	Q <sub>rev</sub> (mAh/g)	Q <sub>irrev</sub> (mAh/g)
<b>Reproducibility</b>								
HC_L900_07	<b>Steel</b>	Fresh	100	Yes	2h	900	209	119
HC_L900_09	<b>Quartz</b>	Old	100	Yes	2h	900	188	135
<b>Lignin ageing</b>								
HC_L900_10	Quartz	<b>Old</b>	180	Yes	2h	900	207	153
HC_L900_11	Quartz	<b>Fresh</b>	180	Yes	2h	900	254	137
<b>Ar flow rate</b>								
HC_L900_09	Quartz	Old	<b>100</b>	Yes	2h	900	188	135
HC_L900_10	Quartz	Old	<b>180</b>	Yes	2h	900	207	152
<b>Grinding</b>								
HC_L900_11	Quartz	Fresh	180	<b>Yes</b>	2h	900	254	138
HC_L900_12	Quartz	Fresh	180	<b>No</b>	2h	900	238	134
<b>Dwell time</b>								
HC_L900_11	Quartz	Fresh	180	Yes	<b>2h</b>	900	254	138
HC_L900_14	Quartz	Fresh	180	Yes	<b>4h</b>	900	155	126
<b>T<sub>pyr</sub></b>								
HC_L900_11	Quartz	Fresh	180	Yes	2h	<b>900</b>	254	138
HC_L1000_13	Quartz	Fresh	180	Yes	2h	<b>1000</b>	226	126

In Figure 2.27, voltage profiles of the first and second cycles of the lignin derived carbons are shown. All the samples exhibited the characteristic voltage profile of hard carbon.

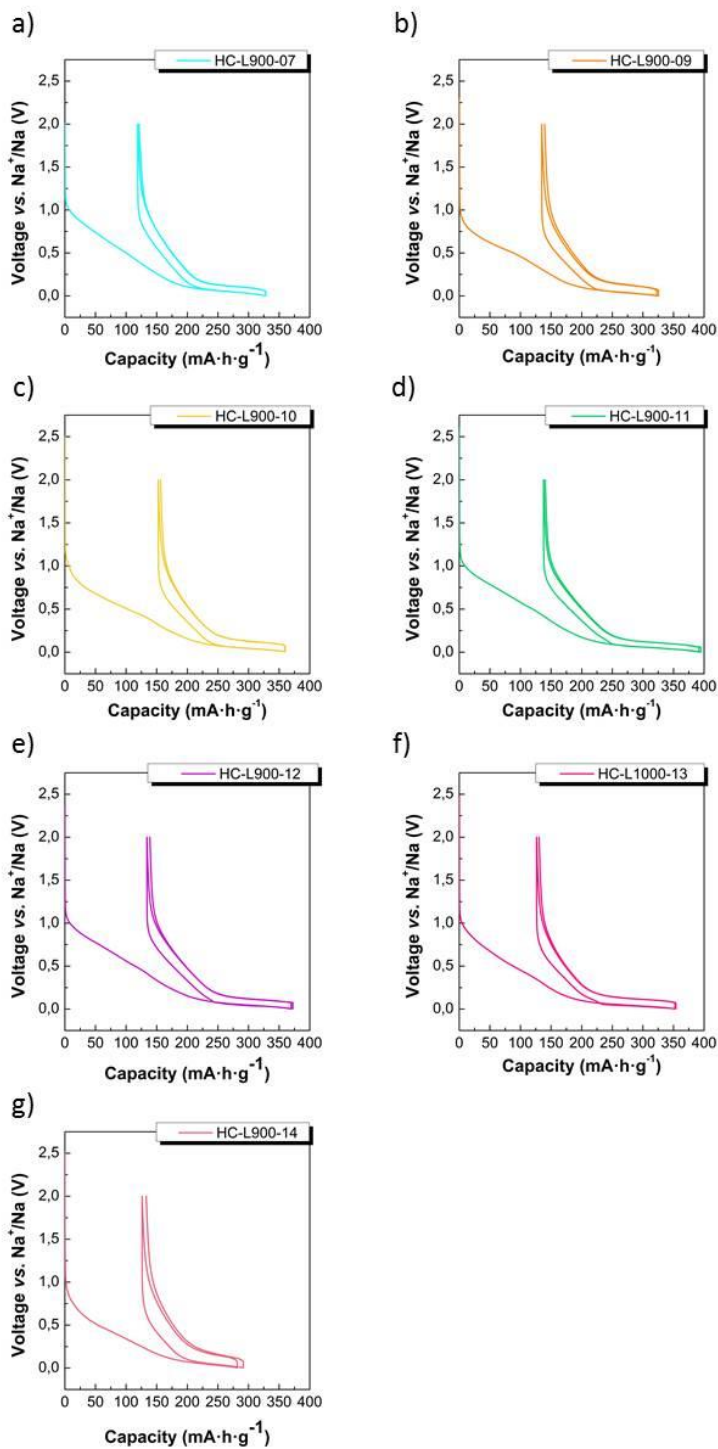


**Figure 2.27** Voltage profile of the first and second cycle (C/15 rate) and of lignin derived hard carbons synthesized with different conditions.

**Reproducibility.** Prior to the synthesis conditions optimization, a synthesis was carried out to ensure the reproducibility of the procedure after replacing the tube, the furnace and the boat. The replacement of the stainless steel tube and the Inconel boat by the quartz and alumina ones respectively, did not affect much the electrochemical performance although larger capacity was observed in the former. The difference in terms of reversible capacity between the optimal sample obtained in the stainless steel tube (HC-L900-07, Figure 2.27 a ) and that obtained in the new quartz tube under the same conditions (HC-L900-09, Figure 2.27 b) was of about  $20 \text{ mA}\cdot\text{h}\cdot\text{g}^{-1}$ . Despite the same batch of lignin precursor was used for both pyrolysis, the fact that the HC-L900-07 sample was produced as of freshly isolated lignin whereas some months had passed since the lignin extraction and the pyrolysis yielding HC-L900-09, it was necessary to confirm the effect that the ageing of the precursor might have on the electrochemical performance.

**Lignin ageing.** The degradation of the lignin structures due to ageing by photo and/or thermal oxidation has been reported in the literature.<sup>80</sup> Lignin, as an organic compound, is sensitive to oxidation so mere exposure to air during a prolonged period of time would cause structural changes. Two different syntheses were carried out with fresh and old lignin in the new quartz tube under the maximum Ar flow rate allowed by the gas line settings ( $180 \text{ mL}/\text{min}$ ). The use of recently extracted lignin for pyrolysis (HC-L900-11, Figure 2.27 d) provided larger reversible capacity ( $254 \text{ mA}\cdot\text{h}\cdot\text{g}^{-1}$ ) than old lignin (HC-L900-10, Figure 2.27c) which provided  $207 \text{ mA}\cdot\text{h}\cdot\text{g}^{-1}$ . This suggests that, actually, lignin degradation upon time might be detrimental for the performance of the lignin derived carbons.

**Ar flow rate.** The use of the new tubular furnace allowed a faster Ar flow rate ( $180 \text{ mL}\cdot\text{min}^{-1}$ ) than the previous tubular furnace, which was  $100 \text{ mL}\cdot\text{min}^{-1}$  at most. In Figure 2.27 b and c, synthesis performed with  $100$  and  $180 \text{ mL}\cdot\text{min}^{-1}$ , respectively are shown. Despite little differences in terms of reversible capacity are observed when the synthesis is performed under faster (HC-L900-10,  $207$

---

<sup>80</sup> Borgin, K., Faix, O. and Schweers, W., Effect of aging on lignins of wood, *Wood Sci. Technol.*, **1975**, 9, 3, 207-211.

$\text{mA}\cdot\text{h}\cdot\text{g}^{-1}$ ) or slower Ar flow rate (HC-L900-09,  $188 \text{ mA}\cdot\text{h}\cdot\text{g}^{-1}$ ), some authors<sup>59</sup> have demonstrated that high gas flow rates can suppress the carbon burnoff which has a dramatic effect on the cell performance. Carbon burnoff causes an opening of the nanopores so that the electrolyte can enter them and react with  $\text{Na}^+$  increasing the irreversible capacity and decreasing the pore surface available for  $\text{Na}^+$  adsorption and, as a consequence, the reversible capacity. An increase of the Ar flow would help to flush the released  $\text{CO}_2$  gases away and reduce substantially the carbon burnoff.

**Lignin grinding.** The effect of grinding the precursor prior to pyrolysis was studied (Figure 2.27 d and e). After extraction in aqueous media, lignin was dried in order to remove water. The drying process leads to lignin chunks of different sizes that are manually ground in an agate mortar. In an attempt to decrease the surface area of the resulting carbon, which can be closely related to the irreversible capacity, lignin chunks were used for pyrolysis and the electrochemical performance was compared to that of ground lignin (powder). However, lignin grinding (HC-L900-11) led to larger reversible capacity ( $254 \text{ mA}\cdot\text{h}\cdot\text{g}^{-1}$ ) and first cycle coulombic efficiency (65 %) than its counterpart (HC-L900-12), which showed a capacity of  $238 \text{ mA}\cdot\text{h}\cdot\text{g}^{-1}$  and a first cycle coulombic efficiency of 50 %. This improvement when the precursor has been powdered can be explained as a consequence of a better release of the pyrolysis gases. The easy escape of the gases reduces not only the chance to produce carbon burnoff but might also lead to purer carbons.

**Dwell time.** The increase of the dwell time at the highest temperature from 2 (Figure 2.27 d) to 4 hours (Figure 2.27 g) led to a substantial decrease of the reversible capacity. After 4 hours at the maximum temperature,  $155 \text{ mA}\cdot\text{h}\cdot\text{g}^{-1}$  of reversible capacity were obtained (HC-L900-14) whereas  $254 \text{ mA}\cdot\text{h}\cdot\text{g}^{-1}$  were observed when pyrolyzing for 2 hours in the same conditions (HC-L900-11). The decrease of capacity is related to an increase in the hysteresis involving that the low voltage plateau is severely diminished.

**Effect of temperature of pyrolysis.** Taking into account that in the previous series of synthesis larger capacities were observed when increasing the



temperature except for the sample pyrolyzed at 1000 °C due to the high impurities content, a new synthesis at that temperature was performed according to the optimum conditions (Figure 2.27 f). Although higher capacities could be expected from the fact that carbonizing at high temperatures usually lead to purer carbons, lower reversible capacity was still obtained at 1000 °C (226 mA·h·g<sup>-1</sup>) than at 900 °C, although the capacity is clearly improved to synthetic method B.

One possible explanation to this fact might be the closure of the micropores of lignin derived hard carbons at temperatures above 900 °C in a similar way to what Buiel *et al.* reported for sucrose derived hard carbons for lithium ion batteries. They observed closure of the micropores at temperatures greater than 1200 °C. As a consequence, they are not accessible for lithium insertion and the capacity is reduced above that critical temperature.<sup>81</sup> A similar trend was reported to happen to sugar derived hard carbons for sodium ion batteries being 1100 °C the critical temperature.<sup>60</sup>

In Table 2.12 the reversible and irreversible capacities of the first cycle are summarized.

**Table 2.12** Reversible and irreversible capacity values of lignin derived hard carbon during the first cycle.

Sample	Q <sub>rev</sub> (mA·h·g <sup>-1</sup> )			Q <sub>irr</sub> (mA·h·g <sup>-1</sup> )
	Q <sub>s</sub>	Q <sub>p</sub>	Q <sub>t</sub>	Q <sub>irr</sub>
HC-L900-07	121	88	209	119
HC-L900-09	128	60	188	135
HC-L900-10	129	78	207	153
HC-L900-11	157	97	254	137
HC-L900-12	143	95	238	134
HC-L1000-13	112	114	226	126
HC-L900-14	111	44	155	126

<sup>81</sup> Buiel, E. R.; George, A. E. and Dahn, J. R., Model of micropore closure in hard carbon prepared from sucrose, *Carbon*, **1999**, 37, 1399-1407.

The rate capability of the third series of samples cycled at different C rates is shown in Figure 2.28 and the capacity values are summarized in Table 2.13.

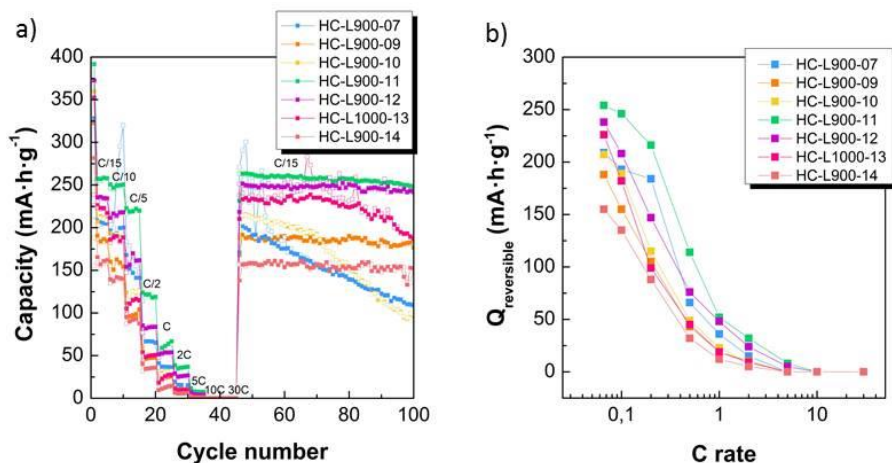


**Figure 2.28** a) Capacity vs. cycle of lignin derived hard carbons synthesized under different conditions (Table 2.11) at different c rates. b) Reversible capacity vs. c rate.

**Table 2.13** Capacity values of lignin derived hard carbons cycled at different rates

	C/15	C/10	C/5	C/2	C	2C	5C	10C	30C	C/15
L900-07	209	193	184	66	36	15	0	0	0	271*
L900-09	188	155	105	43	19	10	0	0	0	190
L900-10	207	189	115	49	23	9	0	0	0	215
<b>L900-11</b>	<b>254</b>	<b>246</b>	<b>216</b>	<b>114</b>	<b>52</b>	<b>32</b>	<b>8</b>	<b>0</b>	<b>0</b>	<b>263</b>
L900-12	238	208	147	76	48	24	5	0	0	251
L1000-13	226	182	99	45	19	9	0	0	0	237
L900-14	155	135	88	32	12	5	0	0	0	157

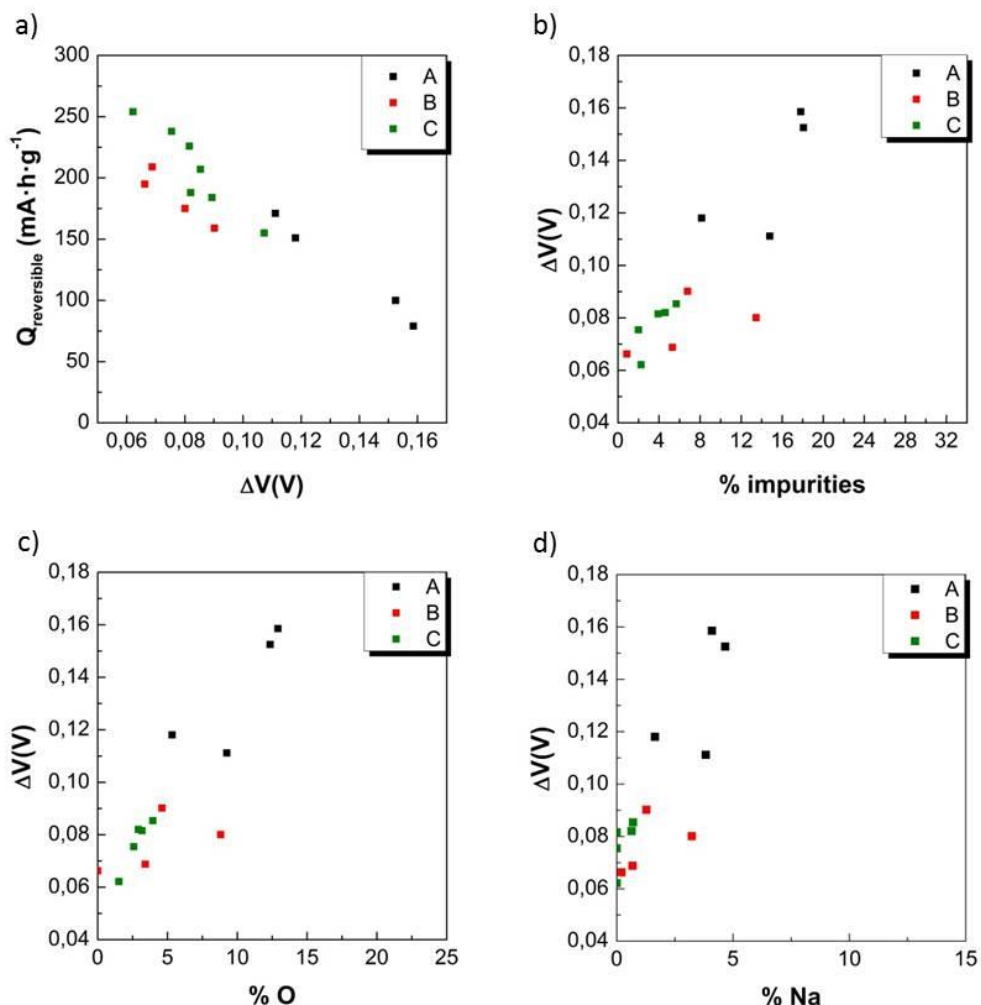
The sample HC-L900-11, apart from being the one exhibiting largest reversible capacity over all the synthesized samples, provides the best rate capability followed by the HC-L900-12, which has been synthesized under the same conditions except for the lignin precursor that was not ground. It is noteworthy that samples HC-L900-07 and HC-L900-10 show extremely fast capacity decay after having cycled 45 times at different C rates leading to poor capacity retentions (52 and 44 %, respectively after 100 cycles at different C rates).

## Analysis and understanding of electrochemical performance

From the representation of the electrochemical parameters of the samples prepared through different synthetic methods altogether, some conclusions can be drawn.

As it was previously mentioned, the loss of capacity at high rates can be related to the disappearance of the low voltage plateau due to an increase of the polarization or hysteresis between charge and discharge. Indeed, since the plateau, which appears at voltage below 0.2 V vs.  $\text{Na}^+/\text{Na}$ , it tends to disappear when the polarization approaches this value. In Figure 2.29 a, a correlation between the reversible capacity and the polarization is shown evidencing that lower polarization of the cell (lower than 80 mV) leads to larger capacity values.

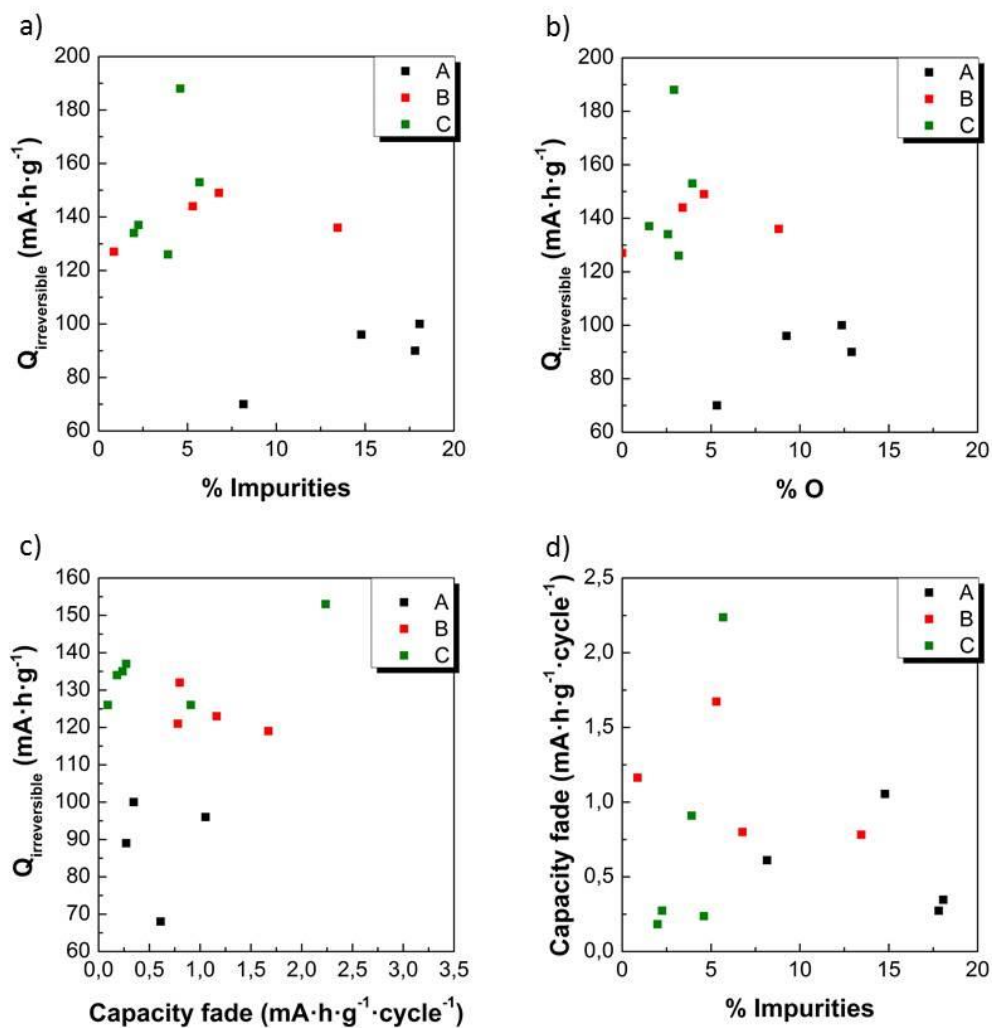
As it happened for hydrogen containing hard carbons tested in lithium ion batteries<sup>29</sup>, whose residual hydrogen content was reported to be responsible for the increase of the hysteresis, the polarization of the cell was enlarged with the increase of total amount of impurities in the material (Figure 2.29 b). The hysteresis caused by hydrogen between discharge and charge in sodium ion batteries has been reported to be significantly lower than that of their lithium counterparts.<sup>29</sup> Being most of the impurities oxygen, it was correlated the increase of the polarization with the increase of its content. (Figure 2.29c) No clear correlation was found for sodium content. (Figure 2.29 d)



**Figure 2.29** a) Correlation for the three series of synthesis (A, B and C) between a) first cycle reversible capacity ( $Q_{\text{irreversible}}$ ) and polarization ( $\Delta V$ ), b) Polarization ( $\Delta V$ ) and percentage of total impurities (O, Na and S) present in the samples, c) polarization ( $\Delta V$ ) and percentage of oxygen and, d) polarization ( $\Delta V$ ) and percentage of Na present in the samples.

As discussed in section 2.3.5, on the one hand, the presence of surface functional groups could also lead to irreversible capacity by increasing the reactivity of the carbon surface. On the other hand, the stability of the material upon cycling might be influenced by the extent of SEI formation, which is related to the irreversible capacity. Therefore, in an attempt to identify the source of the irreversible capacity, first cycle irreversible capacity was represented against the total impurities content, the oxygen content and the loss of capacity per cycle. In

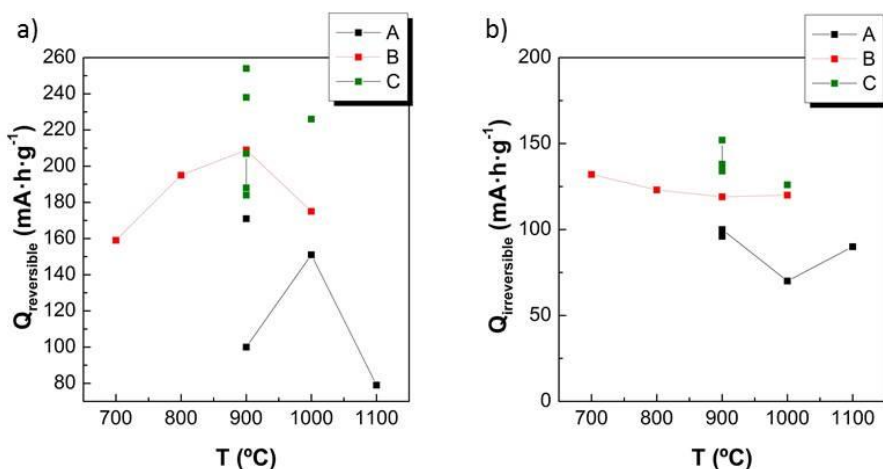
order to find the origin of the capacity fade, the capacity loss per cycle was also plotted against the total percentage of impurities (Figure 2.30)



**Figure 2.30** Representation for the three series of synthesis (A, B and C) of the a) first cycle irreversible capacity ( $Q_{\text{irreversible}}$ ) vs. percentage of impurities in the samples (O, Na and S) and, b) first cycle irreversible capacity ( $Q_{\text{irreversible}}$ ) vs. percentage of O in the samples, c) first cycle irreversible capacity ( $Q_{\text{irreversible}}$ ) vs. loss of capacity per cycle and d) loss of capacity per cycle vs. percentage of total impurities (O, Na, S).

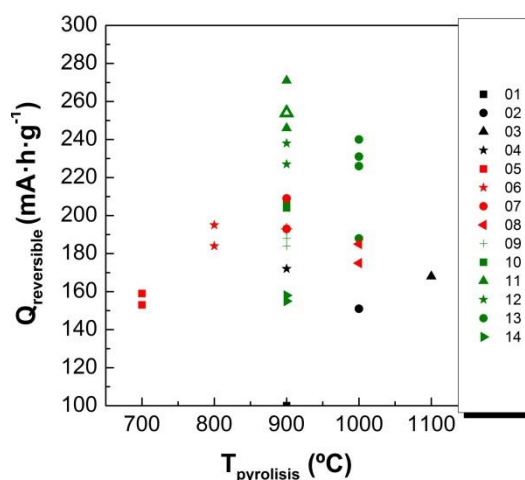
However, no correlation was found between the presence of impurities and the capacity fade upon cycling and the irreversible capacity. This fact could be indicative that the source of first cycle irreversibility might be ascribed to other cell components such as electrolyte, carbon additive, binder or even the sodium used as counterelectrode.

Figure 2.31 shows a summary of the reversible (a) and irreversible capacities (b) presented for the three different synthetic conditions at a given temperature of synthesis.



**Figure 2.31** Summary of the reversible and irreversible capacities observed for natural lignin derived hard carbons synthesized according to different synthesis conditions.

In Figure 2.32 the scattering of the reversible capacity values observed for analogous cells of the same material is shown. In the first methodology, only one cell was run for each experiment because the aim was just to confirm that the synthetic method was useful to provide hard carbons. For the second methodology, two cells were run for each experiment providing a maximum difference of capacity between cells of 16 mA·h·g<sup>-1</sup>. This difference corresponds to a 10 % of the lowest capacity observed in this series, which can be considered an acceptable error. For the third methodology several cells were run leading to a maximum difference in capacity between cells of 14 mA·h·g<sup>-1</sup> which corresponds to an acceptable value of 9 % of difference with respect to the lowest capacity observed for the series. Regarding the optimized sample (HC-L900-11) a maximum capacity of 271 mA·h·g<sup>-1</sup> was observed. However, as it was not reproducible it was discarded. The cell providing 254 mA·g·h<sup>-1</sup> was presented instead because it was found to be reproducible as it can be observed in Figure 2.32 (symbol 11).



**Figure 2.32** Reversible capacity values scattering observed for different cells of the same hard carbon material. Black symbols represent samples of the A methodology, whereas red and green represent B and C synthetic conditions, respectively. The number represents the sample number in Table 2.3.

### Comparison between the best lignin derived hard carbon with other carbons

In order to compare the electrochemical performance of the lignin derived hard carbons with those reported in the literature, the performance of sucrose derived hard carbons and PVC derived soft carbons and acetylene black was also studied. The formation of hard carbon upon pyrolysis of sucrose ( $C_6H_{12}O_6$ ) is favored by the presence of oxygen, whose quick release combined with H in order to produce water leads to a crosslinked low density carbon network, therefore a hard carbon. However, pyrolysis of a hydrocarbon like PVC, which is H rich, leads to the formation of a viscous liquid during a large temperature range promoting a progressive densification of the char structure until all hydrogen is released, leading to a soft carbon.<sup>5</sup>

The optimized lignin derived hard carbon (HC-L900-11) led to a reversible capacity of  $254 \text{ mA}\cdot\text{h}\cdot\text{g}^{-1}$  at C/15 with a capacity retention of 97 % after 100 cycles being the first 45 at different C rates (from C/15 to 30C with increasing rate) and the last 55 at C/15. It showed improved rate capability with respect to

the analogous samples synthesized in different conditions at C rates up to C/2. At C rates faster than C/2 (C, 2C, 5C, 10C and 30C) the performance is similar to other samples showing less capacity at slower C rates.

Figure 2.33 compares the electrochemical performance (first and second cycle) of the optimized lignin derived hard carbon (HC-L900-11), hard carbon derived from commercial lignin, sugar derived hard carbons synthesized via acid wash (HC-SAW) or by heating in air (HC-SA), commercial acetylene black (carbon black) and PVC-derived soft carbon. Three different types of PVC-derived hard carbons were synthesized: as of commercial PVC of low molecular weight (SC-PVCLM), of high molecular weight (SC-PVC-HM) and from recycled PVC (SC-PVCR). In Table 2.14 a summary of the numerical values of reversible and irreversible capacities is shown.

From the voltage profile of the different hard carbons it can be concluded that hard carbon produced as of natural lignin (HC-L900-11) leads to larger reversible capacity ( $254 \text{ mA}\cdot\text{h}\cdot\text{g}^{-1}$ ) than commercial lignin ( $171 \text{ mA}\cdot\text{h}\cdot\text{g}^{-1}$ ) and sugar ( $212$  and  $177 \text{ mA}\cdot\text{h}\cdot\text{g}^{-1}$  for SA and SAW, respectively). This improved capacity for natural lignin derived hard carbon is related to the enlargement of the low voltage plateau due to low hysteresis between charge and discharge. However, this materials provides large irreversible capacity ( $137 \text{ mA}\cdot\text{h}\cdot\text{g}^{-1}$ ) compared to sugar or commercial lignin.



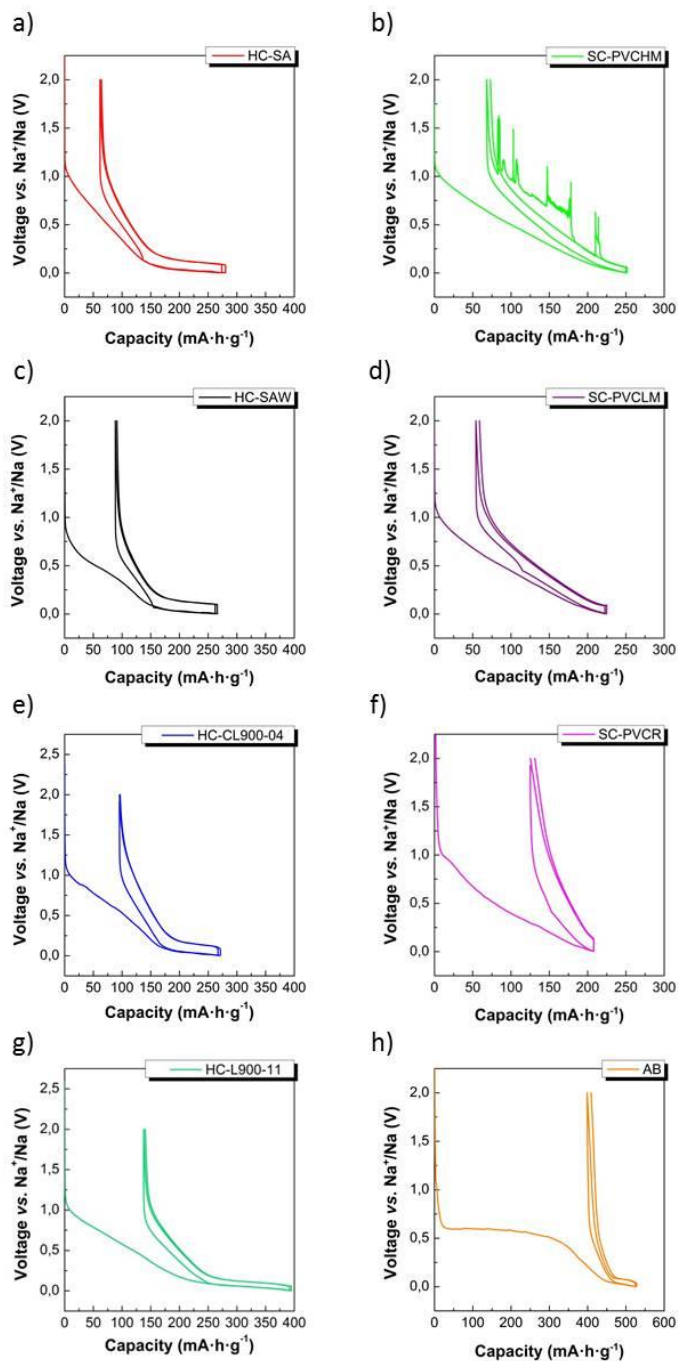


**Figure 2.33** Voltage profile of the first and second cycle of sugar derived hard carbon heated in air (a), acid washed sugar derived hard carbon (c), commercial lignin derived hard carbon (e), natural lignin derived hard carbon (g), high molecular weight PVC derived soft carbon (b), low molecular weight derived soft carbon (d), recycled PVC derived soft carbon (f) and acetylene black (h).

As expected, soft carbons provided less capacity than natural lignin derived hard carbon (HC-L900-11) due to the absence of the low voltage plateau, which has been proven to contribute notably to the overall capacity.<sup>29</sup> Both soft carbons derived from low or high molecular weight PVC provided comparable reversible capacities (178 and 168 mA·h·g<sup>-1</sup>, respectively) which are also similar to those capacities observed for acid-washed sugar derived hard carbon (177 mA·h·g<sup>-1</sup>) and commercial lignin derived hard carbon (171 mA·h·g<sup>-1</sup>). However, it should be pointed out that the first cycle reversible capacity attributed to SC-PVCHM (Figure 2.33 b) is not fully reliable due to the presence of the so-called trailing plateau which increases artificially the first charge capacity. In this regard, SC-PVCLM can be considered a better material as it provided comparable reversible capacity but slightly lower irreversible capacity (55 mA·h·g<sup>-1</sup>) than its high molecular weight counterpart (67 mA·h·g<sup>-1</sup>). The use of recycled PVC as soft carbon precursor is undesirable as it led to the lowest reversible capacity observed for any carbonaceous material studied in this chapter (83 mA·h·g<sup>-1</sup>) and large hysteresis between charge and discharge. Besides, on the one hand, depending on its application, recycled PVC contains different additives (plasticizers, minerals, metals, etc) which could make necessary to introduce a purification step prior to pyrolysis in order to avoid environmental issues. On the other hand, for mechanically recycled PVC, for instance, different kinds of PVC waste are fed to a mechanical recycler, thus the resulting product's composition which could affect the final electrochemical performance is difficult to predict.<sup>82</sup>

Commercial acetylene black provides relatively high reversible capacity (126 mA·h·g<sup>-1</sup>) but extremely high irreversible capacity (399 mA·h·g<sup>-1</sup>). This large irreversible capacity has been also observed for another type of carbon black (Super P) pointing out the need to decrease as much as possible the carbon black content in the electrode.<sup>83,84</sup>

---

<sup>82</sup> Sadat-Shojai, M. and Bakhshandeh, G. R., Recycling of PVC wastes, *Polym. Degrad. Stab.*, **2011**, 96, 404-415.

<sup>83</sup> Senguttuvan, P.; Rousse, G.; Seznec, V.; Tarascon, J. M. and Palacín, M. R., Na<sub>2</sub>Ti<sub>3</sub>O<sub>7</sub>: Lowest voltage ever reported oxide insertion electrode for sodium ion batteries, *Chem. Mater.*, **2011**, 23, 4109-4111.

<sup>84</sup> Bommier, C.; Luo, W.; Gao, W. Y.; Greaney, A.; Ma, S. and Ji, X., Predicting capacity of hard carbon anodes in sodium-ion batteries using porosity measurements, *Carbon*, **2014**, 76, 165-174.

**Table 2.14** Reversible and irreversible capacities of the first cycle of different carbon anodes.

Sample	$Q_{rev} (mA \cdot h \cdot g^{-1})$			$Q_{irr} (mA \cdot h \cdot g^{-1})$
	$Q_s$	$Q_p$	$Q_t$	$Q_{irr}$
HC-SA	142	70	212	62
HC-SAW	98	79	177	89
HC-CL900-04	111	60	171	96
HC-L900-11	157	97	254	137
SC-PVCHM	178	-	178	67
SC-PVCLM	168	-	168	55
SCPVC-R	83	-	83	125
AB	67	59	126	399

In Figure 2.34, the rate capability of the different carbonaceous anodes is represented. Numerical values of the capacity at different C rates are summarized in Table 2.15.

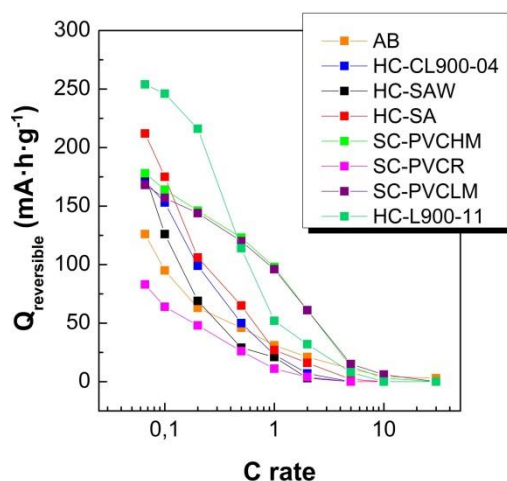


**Figure 2.34** Rate capability of sugar and lignin (natural and commercial) derived hard carbon, acetylene black and PVC derived soft-carbon (recycled and commercial of low and high molecular weight).

Natural lignin derived hard carbon (HC-L900-11 shows the largest reversible capacity at C/15 among all prepared carbons. At high rates (from C/15 to C/5) however, PVC-based soft carbons (SC-PVCHM and SC-PVCLM) show lower

reversible capacities at low rates but at high rates (C/2 and faster) they are able to maintain larger capacities. This is related to the fact that, in absence of the low voltage plateau, the sloping region is larger. Apart from showing poor capacity at low C rates, the rate capability of the recycled PVC based soft carbon is very poor and almost no capacity is delivered at C rates faster than C/5.

Among hard carbons, natural lignin derived hard carbon, although is not competitive at high rates (faster than C/2), shows better rate capability than sugar based hard carbons, retaining 216 mA·h·g<sup>-1</sup> at C/15. HC-SA and HC-SAW retain, at the same C rate 106 and 69 mA·h·g<sup>-1</sup>, respectively.

The sharp decrease of hard carbon's capacity can be explained by the high sensitivity of the low voltage plateau towards slight increases on the cell polarization. In this regard, at fast rates, more polarization between charge and discharge is produced and as a consequence, loss of capacity in terms of increase decrease of the low voltage plateau is observed.

**Table 2.15** Capacity values of sugar and lignin (natural and commercial) derived hard carbon, acetylene black and PVC derived soft-carbon (recycled and commercial of low and high molecular weight).

	C/15	C/10	C/5	C/2	C	2C	5C	10C	30C	C/15
HC-SA	212	175	106	65	27	16	2	0	0	222
HC-SAW	177	126	69	29	21	3	0	0	0	206
HC-CL900-04	171	153	99	50	23	7	0	0	0	171
HC-L900-11	254	246	216	114	52	32	8	0	0	263
SC-PVCHM	178	164	146	123	98	61	13	3	0	181
SC-PVCLM	168	157	144	120	96	61	15	6	0	118
SCPVC-R	83	64	48	26	11	4	0	0	0	80
AB	126	95	63	46	31	21	11	4	3	115

Figure 2.35 shows a comparison of the electrochemical performance of biomass derived hard carbon reported in the literature and the optimum lignin derived hard carbon developed in this thesis (HC-L900-11) at comparable cycling rates.

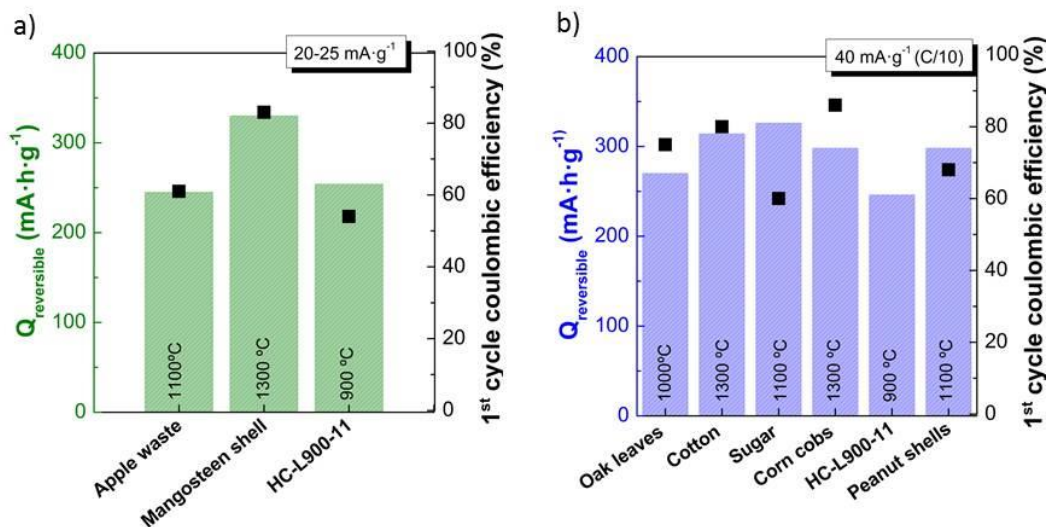


**Figure 2.35** Comparison of the reversible capacity ( $Q_{\text{reversible}}$ ) and first cycle coulombic efficiency of the lignin derived hard carbon sample exhibiting best performance (HC-L900-11) and hard carbons reported in the literature that have been synthesized from other biomass precursors and cycled at comparable current densities a) 20  $\text{mA}\cdot\text{g}^{-1}$  for apple waste and mangosteen sheel and 25  $\text{mA}\cdot\text{g}^{-1}$  for HC-L900-11. b) 40  $\text{mA}\cdot\text{g}^{-1}$  for all the samples. Note that the caption in each bar corresponds to the temperature of pyrolysis.

HC-L900-11 shows comparable capacity to other biomass derived hard carbons at low rates (Figure 2.35a) or faster C rates (Figure 2.35b). The use of lignin as hard carbon precursor leads to larger capacity than apple waste although smaller first cycle coulombic efficiency is obtained. Despite lower reversible capacity is observed for lignin than for oak leaves, cotton, sugar, corn cobs or peanut shells, higher temperatures of pyrolysis were used for synthesizing them. The fact that better capacity values and first cycle coulombic efficiencies are observed for hard carbons synthesized at high temperatures (exceeding 1000 °C) regardless of the precursor could indicate that reaching higher temperatures of pyrolysis is crucial to the improvement of the electrochemical performance. Therefore, an improvement of the reversible capacity and the first cycle coulombic efficiency could be expected from the use of temperatures of pyrolysis higher than 1000 °C.

## 2.4 Conclusions

Hard carbons can be obtained through direct pyrolysis of lignin extracted from black liquor, a byproduct of paper industry. The electrochemical performance of lignin derived hard carbons is affected by synthetic parameters such as the temperature of pyrolysis, grinding of the precursor, Argon flow rate and time at the maximum temperature. SAXS measurements demonstrate that the increase of the temperature of pyrolysis leads to an enlargement of the micropore diameter. However no correlation between the micropore diameter and the electrochemical performance was found.

The reversible capacity delivered by these carbon anodes was linearly correlated with the impurities content, which affects the polarization of the cell by reducing the low voltage plateau. After synthesis optimization, a reversible capacity of  $254 \text{ mA}\cdot\text{h}\cdot\text{g}^{-1}$  (at C/15) with 65 % of first cycle coulombic efficiency was observed. This capacity value is comparable to that of other biomass derived hard carbons reported in the literature.

---

# Chapter 3. Poly Schiff bases-Poly Ethylene oxide copolymers as anodes for sodium ion batteries

---

In this chapter, the synthesis and physicochemical characterization of polymeric electrodes containing Schiff base active units copolymerized polyethylene oxide ionically conducting, binding units will be presented. Materials will be electrochemically characterized as binder free anodes of sodium ion batteries as well as binder of other electrode materials.

## 3.1 Introduction

So far, the battery field has been always linked to the organic chemistry. Among all the components of a cell, the separator, the electrolyte and binder are typically based on organic and polymeric compounds in many commercial batteries with electrochemically active organic electrodes being heavily investigated.

**Electrolytes.** Since high working voltage batteries are required in order to get higher energy density, organic solvents with a large electrochemical stability window are used instead of aqueous electrolytes. For example, cyclic carbonates such as ethylene carbonate (EC) and propylene carbonate (PC) are usually employed mixed with linear carbonates such as dimethyl carbonate (DMC) and diethyl carbonate (DEC). Besides, some organic additives such as vinylene carbonate (VC) or fluoroethylene carbonate (FEC) are usually added into the organic electrolyte to

facilitate reduction and improve SEI characteristics.<sup>1</sup> However, the utilization of flammable liquid electrolytes in sodium-ion batteries may raise safety concerns, especially in large-scale energy storage systems. For that reason, there is a trend to substitute liquid electrolytes by solid electrolytes, typically polymer or ceramic electrolytes. The brittle ceramic electrolytes have been proposed to address the safety issues, but the solid-solid electrode-electrolyte interfaces may not sustain a long cycle life. Therefore, polymer electrolytes, and specially gel-polymer electrolytes, stand out as they take advantages of the polymer flexibility and the high ionic conductivity of the liquid electrolytes.<sup>2</sup> Among them, poly(ethylene oxide) (PEO) is the most studied host polymer due to its good ionic conductivity when a suitable salt is added.<sup>3</sup>

**Separators.** For lithium ion batteries available on the market, thin polyolefin separators are used to facilitate the movement of ions. Triple layer separators commercialized by Celgard™ are composed by polypropylene and polyethylene (PP-PE-PP). Recent studies in the field of separators for sodium ion batteries, report on the use of another polymer (polyvinylidene fluoride, abbreviated as PVdF) to develop more sophisticated electroactive separators.<sup>4</sup>

**Binders.** This fluorinated polymer is also employed as a typical binder in the electrode manufacturing processes. However, a new trend is being developed to substitute the PVdF by other binders having better elasticity, especially for improving the performance of anodes suffering huge volume changes. So far, candidates are polymers such as sodium carboxymethyl cellulose (CMC), polyamide

---

<sup>1</sup> Darwiche, A.; Bodenes, L.; Madeca, L.; Monconduit, L.; Martinez, H., Impact of the salts and solvents on the SEI formation in Sb/Na batteries: An XPS analysis, *Electrochim. Acta*, **2016**, 207, 284-292.

<sup>2</sup> Gao, H.; Zhou, W.; Park, K. and Goodenough, J. B., A Sodium-ion battery with a low-cost cross-linked gel-polymer electrolyte, *Adv. Energy Mater.*, **2016**, 1600467.

<sup>3</sup> Serra Moreno, J.; Armand, M.; Berman, M. B.; Greenbaum, S.G.; Scrosati, B.; Panero, S., Composite PEO:NaTFSI polymer electrolyte: Preparation, thermal and electrochemical characterization, *J. Power Sources*, **2014**, 248, 695-702.

<sup>4</sup> Janakiraman, S.; Surendran, A.; Ghosh, S.; Anandhan, S.; Venimadhav A., Electroactive poly(vinylidene fluoride) fluoride separator for sodium ion battery with high coulombic efficiency, *Solid State Ionics*, **2016**, 292, 130-135.



imide (PAI), and polyacrylic acid (PAA), polyimide (PI) and styrene-butadiene rubber (SBR).<sup>5</sup>

Regarding the **electrochemically active components** of the cell, the cathode and anode active materials of conventional primary and secondary batteries are dominated by metal and metal oxides as stated in the introduction (except oxygen and carbon that are used for the air battery cathode and the lithium battery anode, respectively), many of which come from limited resources. Recent development of organic batteries aiming at increasing the energy density has promoted a transition from inorganic to organic materials. The advantage of organic battery in terms of sustainability also comes from the excellent recyclability and safety as the inherent virtue of the organic materials as well as the compatibility with the rest of the components of the cell which are organic.

In that sense, organic electrodes and specially polymers can provide higher mobility of Na<sup>+</sup> ions thanks to their more flexible structures.<sup>6</sup> Despite organics usually have much lower mass density than inorganics, because of its highly branched structure and large porosity, the use of organic electrodes can bring considerable advantages in terms of power density given the faster reaction kinetics they show compared to that of intercalation compounds. Besides, for organic compounds, the existence of such a vast range of possible structures enables the proper tuning of structure-related properties according to the different requirements.

**Importance of organic electrodes.** One of the strengths of organic materials is that they can be ideally directly extracted or eventually, synthesized from biomass.<sup>7,8</sup> Apart from the potential low cost synthesis, the absence of heavy metals enables a

---

<sup>5</sup> Zhang, W.; Dahbi, M. and Komaba, S., Polymer binder: a key component in negative electrodes for high-energy Na-ion batteries, *Curr. Opin. Chem. Eng.*, **2016**, 13:36-44.

<sup>6</sup> A. L. Goodwin, *Nat. Mater.*, **2010**, 9, 7-8.

<sup>7</sup> Chen, H.; Armand, M.; Demailly, G.; Dolhem, F.; Poizot, P. and Tarascon, J.-M., From biomass to a renewable Li<sub>x</sub>C<sub>6</sub>O<sub>6</sub> organic electrode for sustainable Li-ion batteries, *ChemSusChem*, **2008**, 1, 4, 348-355.

<sup>8</sup> Milczarek, G. and Ingänas, O., Renewable cathode materials from biopolymer/conjugated polymer interpenetrating networks, *Science*, **2012**, 335, 1468-1471.

more environmentally friendly recycling or disposal.<sup>9</sup> Furthermore, their characteristics of solubility, film forming-ability and sublimation-ability would allow the use of other electrode manufacturing methods different from the traditionally employed casting technique. For example, the use of printing or vapour deposition can lead to thinner and more flexible electrodes, which is consistent with the actual tendency of making small portable devices.

Dissolution in the organic electrolyte, especially for small molecules, is an important drawback.<sup>10</sup> As a consequence, poor cycling performance and even shuttle effect can take place making the cell non-rechargeable. Several strategies have been suggested to tackle the dissolution issue, such as non-covalent or covalent attachment of redox molecules to substrates, optimization of molecular structure, and the use of solid electrolytes. On the other hand, this problem can be easily solved by polymerization of the active compound, which is, very often, insoluble in the electrolyte.<sup>11</sup>

According to this dissolution problem, much research has been carried out in an attempt to decrease the solubility of small molecules by incorporating certain functional groups into them or by developing polymeric anodes. The state-of-the-art in organic electrode materials for sodium ion batteries will be hereafter presented and the materials will be classified attending to their size into small molecules (salts) and polymers.

---

<sup>9</sup> Poizot, P. and Dolhem, F., Clean energy new deal for a sustainable world: from non-CO<sub>2</sub> generating energy sources to greener electrochemical storage devices, *Energy Environ. Sci.*, **2011**, 4, 2003-2019.

<sup>10</sup> Song, Z. and Zhou, H.; Towards sustainable and versatile energy storage devices: an overview of organic electrode materials, *Energy Environ. Sci.*, **2013**, 2280- 2301.

<sup>11</sup> Kim, J.-K.; Kim, Y.; Park, S.; Ko, H. and Kim, Y., Encapsulation of organic active materials in carbon nanotubes for application to high-electrochemical-performance sodium batteries, *Energy Environ. Sci.*, **2016**, 9, 4, 1264-1269.

**Organic electrode materials for sodium ion batteries.** In organic electrodes, in contrast to inorganic materials where the redox processes are related to the valence charge of the metal, redox reactions are based on the change of the state of charge of a given electroactive group or moiety with conjugated structure and atoms with lone pair electrons, such as N, O and S (belonging to keto, carboxylate or anhydride functionalities). The enolates formed are stabilized by extended conjugation in the aromatic rings.

### 3.1.1 Small molecules (salts)

To date, most organic electrode materials reported for sodium ion batteries are active at high voltages so they can be used as positive electrode materials. In general, to achieve high-voltage electrode materials, electrochemical reduction reactions leading to stable aromatic or Hückel units should be involved whereas the breakage of a Hückel-stabilized structure results in a low-voltage reduction reaction.

Electrode materials formed by small organic molecules usually owe their electrochemical activity to the presence of carbonyl groups. Carbonyls can be present in quinone-type compounds in which the keto-enolization reaction promoted by conjugation is the responsible for the electrochemical activity. In Figure 3.1 an example of the keto-enolization reaction of 2,5-dihydroxy-1,4-benzoquinone is shown.

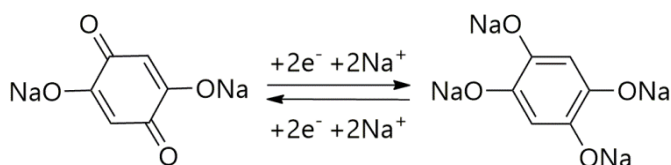


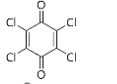
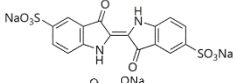
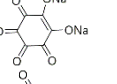
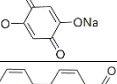
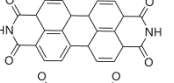
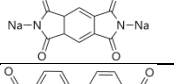
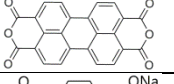
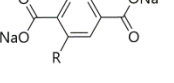
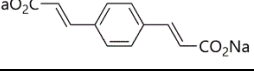
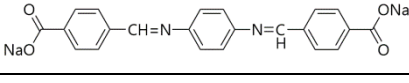
**Figure 3.1** Chemical structure and redox mechanism of disodium salt of 2,5-dihydroxy-1,4-benzoquinone.

As electrochemical reduction reactions lead to stable aromatic or Hückel units, quinones can be used as cathode materials whereas for aromatic systems the loss of resonance on the carboxylates and of aromaticity in the core molecule will bring this reaction to low potentials.

Table 3.1 summarizes the most important electrochemical parameters such as operating voltage and capacity, of organic salts such as 5-5'-indigosulfonic acid sodium salt<sup>12</sup>, 3,4,9,10-perylene-bis(dicarboximide)<sup>13</sup>, sodium pyromellitic diimide<sup>14</sup>, 3,4,9,10-perylene-tetracarboxylic acid dianhydride<sup>15</sup>, benzenediacylate<sup>16</sup> and disodium terephthalate<sup>17</sup>, which have been reported to be electrochemically active for sodium ion batteries.

- 
- <sup>12</sup> Yao, M.; Kuratani, K.; Kojima, T.; Takeichi, N.; Senoh, H. and Kiyobayashi, T., Indigo carmine: An organic crystal as a positive-electrode material for rechargeable sodium batteries, *Sci. Rep.*, **2014**, 4, 3650.
- <sup>13</sup> Deng, W.; Shen, Y.; Qian, J.; Cao, Y. and Yang, H., A perylene diimide crystal with high capacity and stable cyclability for Na-ion batteries, *ACS Appl. Mater. Interfaces*, **2015**, 7 (38), 21095-21099.
- <sup>14</sup> Renault, S.; Mihali, V. A.; Edström, K. and Brandell, D., Stability of organic Na-ion battery electrode materials: The case of disodium pyromellitic diimide, *Electrochem. Commun.*, **2014**, 45, 52-55.
- <sup>15</sup> Luo, W.; Allen, M.; Raju, V.; Ji, X., An organic pigment as a high-performance cathode for sodium-ion batteries, *Adv. Energy Mater.*, **2014**, 4, 1400554.
- <sup>16</sup> Mihali, V. A.; Renault, S.; Nyholm, L.; Brandell, D., Benzenediacylates as organic battery electrode materials: Na versus Li, *RSC Advances*, **2014**, 4, 72, 38004-38011.
- <sup>17</sup> Zhao, L.; Zhao, J.; Hu, Y.-S.; Li, H.; Zhou, Z.; Armand, M. and Chen, L., Disodium Terephthalate (Na<sub>2</sub>C<sub>8</sub>H<sub>4</sub>O<sub>4</sub>) as High Performance Anode Material for Low-Cost Room-Temperature Sodium-Ion Battery, *Adv. Energy Mater.*, **2012**, 2, 962-965.

Table 3.1 Typical organic salts based electrodes and their electrochemical parameters.

Compounds	Formula	Name	Redox potential (V vs. Na <sup>+</sup> /Na)	Theor. cap. (mAh/g)	Pract (mAh/g)	Ref.
Quinone derivatives		Tetrachloro-1,4-benzoquinone	2.72	218	150 (C/22)	19
		5-5'-indigosulfonic acid sodium salt	1.8	115	106 (0.1C)	12
		Sodium rhodizonate	2.3	250	190 (0.1C)	18
		Sodium 1,4-benzoquinone	1.2	291	265 (0.1C)	19
Polyketones with N-cycles		3,4,9,10-perylene-bis(dicarboximide)	1.5	137	140 (C/6)	13
		Sodium pyromellitic diimidate	1.3	203	150 (C/40)	14
Dianhydrides		3,4,9,10perylene-tetracarboxylic acid dianhydride	2.3	137	145 (0.1C)	15
Dicarboxilates		Disodium terephthalate	0.4	255	250 (0.1C)	17
		Benzenediacyrilate	0.6	205	178 (C/40)	16
Conjugated imines		Oligomeric Schiff base	0.97/0.65	260	278	21

Due to the intrinsic insulating properties of most organic electrodes, the capacity of microbulk samples with large size and, therefore, larger transport resistance for Na ions and electrons leads to poor stability. The use of nanorods of sodium rhodizonate,  $\text{Na}_2\text{C}_6\text{O}_6$ , for example, results in much better cycling performance.<sup>18</sup> With the aim of increasing the average potential without increasing much their molecular weight, the modification of the quinone structure by halogen substitution leading to tetrachloro-1,4-benzoquinone was reported.<sup>19</sup> The dissolution issue of low molecular organic compounds can be also restrained by the utilization of ionic molecules such as the disodium salt of 2,5-dihydroxy-1,4-benzoquinone.<sup>20</sup> Oligomeric Schiff bases containing benzilideneaniline and terminated by carboxylate groups show electrochemical activity due to the  $\pi$  conjugation of the  $\text{N}=\text{HC}-\Phi-\text{CH}=\text{N}$  unit ( $\Phi$ =Phenyl). These compound delivers 250 mAh/g with good capacity retention thank to their high structural stability and low solubility in the electrolyte.<sup>21</sup>

In summary, for most carbonyl compounds with quinone-type redox center (dianhydrides and quinone derivatives) the average sodium storage voltage is about 1.2-2.7 V vs.  $\text{Na}^+/\text{Na}$  whereas conjugated carboxylates with carboxyl redox center (terephthalates, Schiff bases oligomers) have lower storage voltage (below 1.5V vs.  $\text{Na}^+/\text{Na}$ ) so that they can be used as anodes.

### 3.1.2 Polymeric electrode materials

Among all the strategies reported to solve the issue of electrode dissolution, polymerization of the active compound is particularly interesting owing to its

---

<sup>18</sup> Wang, Y.; Ding, Y.; Pan, L.; Shi, Y., Yue, Z.; Y. Shi and Yu, G., Understanding the size-dependent sodium storage properties of  $\text{Na}_2\text{C}_6\text{O}_6$ -based organic electrodes for sodium-ion batteries, *Nano Lett.*, **2016**, 16, 5, 3329-3334

<sup>19</sup> Kim, H.; Kwon, J. E., Lee, B.; Hong, J.; Lee, M.; Park, S. Y. and Kang, K., High energy organic cathode for sodium rechargeable batteries, *Chem. Mater.*, **2015**, 27, 21, 7258-7264.

<sup>20</sup> Wu, X.; Jin, S.; Zhang, Z.; Jiang, L.; Mu, L.; Hu, Y.-S.; Li, H.; Chen, X.; Armand, M.; Chen, L. and Huang, X., Unraveling the storage mechanism in organic carbonyl electrodes for sodium-ion batteries, *Sci. Adv.*, **2015**, 1, e1500330

<sup>21</sup> López-Herraiz, M.; Castillo-Martínez, E.; Carretero-González, J.; Carrasco, J.; Rojo, T. and Armand, M.; Oligomeric-Schiff bases as negative electrodes for sodium ion batteries: unveiling the nature of their active redox centers, *Energy Environ. Sci.*, **2015**, 8, 3233-241.

versatility and the added advantages of improved thermal stability and increased kinetics of electron transfer through polymer chains. In Table 3.2, the typical polymeric electrodes reported for sodium ion batteries and their most important electrochemical parameters such as operating voltage and capacity are summarized. Like the small organic molecules, polymeric electrodes can be classified attending to their functional groups.

In humic acid, the existence of abundant quinone and ketone groups entails a reversible capacity of 220 mAh/g with good capacity retention after more than 200 cycles (80%).<sup>22</sup> Among polyimides, poly-1,4,5,8 naphthalene tetracarboxylic dianhydride imide show reduction and oxidation processes due to the ketone reduction into an alkoxide and viceversa accompanied by the association and disassociation of Na<sup>+</sup>.<sup>23</sup> The two-electron transfer of each monomer unit results in a discharge capacity of 140 mAh/g between 1.7 and 2.4 V vs. Na<sup>+</sup>/Na. Amines are also electrochemically active. For example, poly(triphenyl amine) is a p-dopable polymer that despite not being a Na host material, it can still serve as an effective cathode for Na ion batteries by hosting concomitant PF<sub>6</sub><sup>-</sup> anions along with Na<sup>+</sup> insertion into the anode.<sup>24</sup> The electrochemical performance of other polymeric anodes such as poly(benzoquinonyl sulphide)<sup>25</sup>, humic acid<sup>26</sup>,

---

<sup>22</sup> Zhu, H.; Yin, J.; Zhao, X.; Wang, C. and Yang, X., Humic acid as promising organic anodes for lithium/sodium ion batteries, *Chem. Commun.*, **2015**, 51, 14708-14711.

<sup>23</sup> Chen, L.; Li, W.; Wang, Y.; Wang, C. and Xia, Y., Polyimide as anode electrode material for rechargeable sodium batteries, *RSC Adv.*, **2014**, 4, 25369.

<sup>24</sup> Deng, W.; Liang, X.; Wu, X.; Qian, J.; Cao, Y.; Ai, X.; Feng, J. and Hanxi Y., Low cost, all-organic Na-ion battery based on polymeric cathode and anode, *Sci. Rep.*, **2013**, 3:2671.

<sup>25</sup> Song, Z.; Qian, Y.; Zhang, T.; Otani, M. and Zhou, H., Poly(benzoquinonyl sulfide) as a high-energy organic cathode for Rechargeable Li and Na batteries, *Adv. Sci.*, **2015**, 2, 1500124.

<sup>26</sup> Zhu, H.; Yin, J.; Zhao, X.; Wang, C. and Yang, X., Humic acid as promising organic anodes for lithium/sodium ion batteries, *Chem. Commun.*, **2015**, 51, 14708-14711.

poly(1,4,5,8-naphthalenetetracarboxylic dianhydride) imide<sup>27</sup>, N,N'-diamino-3,4,9,10 Perylenetetracarboxylic polyimide<sup>28</sup> and PolySchiff bases<sup>29</sup> are summarized in Table 3.2.

---

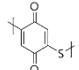
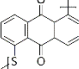
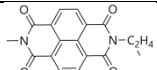
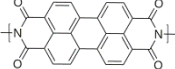
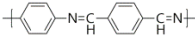
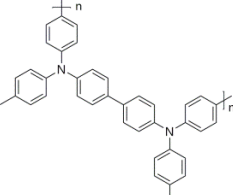
<sup>27</sup> Chen, L.; Li, W.; Wang, Y.; Wang, C. and Xia, Y., Polyimide as anode electrode material for rechargeable sodium batteries, *RSC Adv.*, **2014**, 4, 25369-25373.

<sup>28</sup> Banda, H.; Damien, D.; Nagarajan, K.; Hariharan, M. and Shaijumon, M. M, A polyimide based all-organic sodium ion battery, *J. Mater. Chem. A.*, **2015**, 3, 19, 10453-10458.

<sup>29</sup> Castillo Martínez, E.; Carretero-González, J. and Armand, M. Polymeric Schiff bases as low voltage redox centers for sodium ion batteries, *Angew. Chem. Int. Ed.*, **2014**, 53, 5341-5345.



Table 3.2 Typical polymeric electrodes and their electrochemical parameters.

	Formula (Monomer)	Name	Redox potential (V vs. Na <sup>+</sup> /Na)	Theor. cap. (mAh/g)	Pract. (mAh/g)	Ref.
Quinone		Poly(benzoquinonyl sulphide)	2.1	388	268	25
		Poly(antraquinonyl sulphide)	1.5	225	220 (1C)	24
	C <sub>67</sub> H <sub>37</sub> N <sub>4</sub> O <sub>30</sub>	Humic acid	1.0	-	220 (20 mA/g)	26
Polyketone with N cycles		Poly(1,4,5,8-naphthalenetetracarboxylic dianhydride) imide	2.0	279	140(1C)	27
		N,N'-diamino-3,4,9,10 perylenetetracarboxylic polyimide	1.5/3.5	257	126 (C/25)	28
Schiff bases		poly-[N,N'-p-(benzylidene)-p-phenylenediamine]	0.59 /1.04	-	350	29
Amines		Poly(triphenyl amine)	3.6	109	98 (1C)	24

### 3.1.2.1 PolySchiff bases

Schiff bases, known as azomethines is a family of compounds that have imine functional group and are represented by the general formula  $R_3R_2C=NR_1$  where  $R_1$ ,  $R_2$  and  $R_3$  may be alkyl, aryl, heteroaryl or hydrogen. They received their name from Hugo (Ugo) Joseph Schiff, who synthesized them for the first time.<sup>30</sup> Among all the synthesis methods of Schiff bases, the simple condensation reaction from aldehydes and amines is the most valuable methodology from the environmental point of view, as the only byproduct is water.<sup>31</sup>

Castillo-Martínez *et al.*<sup>29</sup> reported the synthesis of a series of Hückel stabilized polymeric Schiff bases that showed redox activity at low voltages vs.  $Na^+/Na$ . The redox voltage can be shifted by the addition of the proper substituents in the benzyl ring. Among all the polymers, which were prepared as of aromatic and nonaromatic diamine blocks and terephthalaldehyde or non-aromatic dialdehyde monomer units, the polymers showing best electrochemical performance contains the  $-N=CH-\Phi-HC=N-$  electroactive unit with enhanced cycle life for those with the  $-N=CH-\Phi-HC=N-\Phi$  repeating unit. It delivers a stable capacity of 180 mAh/g, which can be attributed to the presence of phenyl groups, which confer more structural stability thanks to  $\pi$ - $\pi$  interaction. The reduction and oxidation takes place in two processes (0.59 and 1.04 V during reduction and 0.76 and 1.16 V vs.  $Na^+/Na$  during oxidation) that may correspond to two one-electron processes. Further optimization of the electrode, leads to a reversible capacity of 350 mAh/g, which corresponds to an insertion of 1.4  $Na^+$ /azomethine moiety.

### 3.1.3 Smart binders in lithium Ion batteries

In a conventional electrode laminate, polymer binders are inactive but indispensable components. Polymer binders, such as, poly(acrylic acid) (PAA), poly(vinylalcohol) (PVA), sodium carboxymethyl cellulose (CMCNa) and conventional polyvinylidene

<sup>30</sup> Schiff, H.; *Mitteilungen aus dem universitatlaboratorium in Pisa: Eineneue reihe organischer basen, Justus Liebigs Ann. Chem.*, **1864**, 131, 118-119.

<sup>31</sup> D'alelio, G. F.; Crivello, J. V.; Schoenig, R. K. and Huemmer, T. F., *J. Macromol. Sci. Chem. A*, **1967**,1, 1299-1320.

fluoride (PVdF), hold the active materials and conductive additives mechanically together in the electrode laminate.<sup>32</sup> Electronic conductive additives, such as acetylene black (AB) or Carbon SuperC65 are used to allow electrical conductivity throughout the electrode. The combined polymer binder and conductive additives maintain the mechanical and electronic integrity of the entire electrode. In addition, polymer binders coat the active material surfaces, so the polymer swells in the electrolyte to provide ionic conductivity. The mechanical failure at the electrode interfaces (laminate/current collector and binder/particle interfaces) leads to particle isolation and delamination, which has been regarded as one of the main reasons for capacity decay and cell failure.

For some applications such as high capacity anodes in sodium or lithium ion batteries, the role of the binder in the electrode is especially important. Of those, silicon for example, has a high theoretical capacity of 4200 mAh/g<sup>33</sup> and a practical capacity of 3579 mAh/g in the fully lithiated phase<sup>34</sup>, which is almost 10 times higher than that of the current graphite anode (370 mAh/g). In sodium ion batteries it also shows a high theoretical capacity of 954 mAh/g for the NaSi phase.<sup>35</sup> However, the practical applications of Si as an anode material have been hindered due to severe volume changes (up to 300%) during ion insertion (sodiation/lithiation) and deinsertion (desodiation/delithiation) leading to loss of interparticle contact, pulverization of the electrode and fast capacity fade. Despite the fact that many strategies have been reported to alleviate volume changes (such as minimizing the size of the particles<sup>36,37</sup>, using multiphase alloys<sup>38,39</sup>, composites of

---

<sup>32</sup> Komaba, S.; Shimonura, K.; Yabuuchi, N.; Ozeki, T.; Yui, H. and Konno, K., Study on polymer binders for high-capacity SiO negative electrode of Li ion batteries, *J. Phys. Chem. C*, **2011**, 115, 13487-13495.

<sup>33</sup> Boukamp, B. A., Lesh, G. C. & Huggins, R. A., All-solid lithium electrodes with mixed-conductor matrix., *J. Electrochem. Soc.*, **1981**, 128, 725-729.

<sup>34</sup> Obrovac, M.-N. and Christensen, L., Structural changes in silicon anodes during lithium insertion/extraction, *Electrochem. Solid-State Lett.*, **2004**, 7, A93-A96.

<sup>35</sup> Chevrier, V. L.; Ceder, G. Challenges for Na-ion negative electrodes., *J. Electrochem. Soc.*, **2011**, 158, A1011-A1014.

<sup>36</sup> Chan, C.- K.; Peng, H.; Liu, G.; Mcllwraith, K., Zhang, X.-F.; Huggins R.-A and Cui, Y., High performance lithium battery anodes using silicon nanowires, *Nat. Nanotechnol.*, **2008**, 3, 31-35.

<sup>37</sup> Wu, H.; Chan, G.; Choi, J.-W.; Ryu, I.; Yao, Y.; McDowell, M.-T.; Lee, S.-W.; Jackson, A.; Yang, Y.; Hu, L.; Cui, Y., Stable cycling of double-walled silicon nanotube battery anodes through solidelectrolyte interphase control, *Nat. Nanotechnol.*, **2012**, 7, 310-315.

lithium reactive/non-reactive metals<sup>40,41</sup> or metal/carbon composites<sup>42</sup>), the employment of an efficient binder stand out as the ultimate solution. An optimized design of polymer binders should be capable of avoiding crack generation in the electrode.

Nanosizing has been widely employed as a useful strategy to avoid drastic volume changes. However, nanosized materials require high volume of conductive additives and therefore, the volumetric and gravimetric capacity is severely diminished. Moreover, as conductive additives have no binding force, it tends to be pushed away from particles by volume expansion leading to broken connections. Several authors, and specially the group of Gao Liu, have developed the so-called "smart binders" that merge several features to overcome this volume expansion issue. The main strategy is focused on the development of double-rolled binders that show both electronic conductivity and binding force. For example, the copolymerization of methacrylic acid (MAA) and 1-pyrenemethylmethacrylate yields a pyrene-based side chain conductive polymer binder (PPyMAA) that combines the electric-conducting pyrene moiety and the acid units for better adhesion.<sup>43</sup> The use of this polymeric binder with commercial Si nanoparticles leads to a good stability of the electrode when tested in lithium ion batteries, delivering 2200 mAh/g for over 180 cycles in absence of conductive carbon additive. In an attempt to improve processability, another pyrene-based polymer that incorporates flexible moieties

---

<sup>38</sup> Wang, Y.; Zhang, P.; Wang, J.; Li, Y.; Ren, X.; Lithium storage characteristics and electrochemical performance of Si-Sb-Ag composite anode materials, *Int. J. Electrochem. Sci.*, **2015**, 10, 9652-9665.

<sup>39</sup> Li, Y.; Huang, L.; Zhang, P.; Ren, X. and Deng, L., Synthesis of Si-Sb-ZnO composites as high performance anodes for lithium-ion batteries, *Nanoscale Res. Lett.*, **2015**, 10: 414.

<sup>40</sup> Polat, B. D.; Keles, O.; Chen, Z. H., and Amine, K., Si-Cu alloy nanowires grown by oblique angle deposition as a stable negative electrode for Li-ion batteries, *J. Mater. Sci.*, **2016**, 51: 6207.

<sup>41</sup> Huang, X.H.; Wu, J.B.; Cao, Y.Q.; Zhang, P.; Lin, Y.; Guo, R.Q., Cobalt nanosheet arrays supported silicon film as anode materials for lithium ion batteries, *Electrochim. Acta*, **2016**, 203, 213-220.

<sup>42</sup> Magasinski, A.; Dixon, P.; Hertzberg, B.; Kvit, A., Ayala, J. and Yushin, G., High-performance lithium-ion anodes using a hierarchical bottom-up approach, *Nat. Mater.*, **2010**, 9, 353-358.

<sup>43</sup> Zhao, H.; Wei, Y.; Qiao, R.; Zhu, C.; Zheng, Z.; Ling, M.; Jia, Z.; Bai, Y.; Fu, Y.; Lei, J.; Song, X.; Battaglia, V. S.; Yang, W.; Messersmith, P. B and Liu G., Conductive polymer binder for high-tap-density nanosilicon material for lithium-ion battery negative electrode application, *Nano Lett.*, **2015**, 15, 7927-7932.

has been reported (PPyE). The elasticity of polymers can be systematically manipulated by introducing polar ether moieties.<sup>44</sup> For example, the incorporation of flexible triethylene glycol units (TEG) into the poly(1-pyrenemethyl methacrylate) facilitates the interaction between the pyrene units, which are highly conductive due to  $\pi$ - $\pi$  stacking, and the Si particles. In addition, it increases solubility in polar solvents and, therefore makes easier its processability. The Si/PPyE electrode shows stable cycling performance and high capacity against Li (2300 mAh/g after 180 cycles).<sup>45</sup> The incorporation of TEG into poly(methacrylic acid) (PMAA) has been also reported to decrease the rigidity and brittleness of the PAA based electrodes, which are responsible for delamination during roll-to-roll electrode handling in industry. Therefore, enhanced cell cycling performance can be also obtained for graphite bound with PMMA-TEG in lithium ion half-cell, which provides a larger reversible capacity (270 mAh/g) than the unmodified PMMA binder (190 mAh/g).<sup>46</sup>

Polyfluorene, is another conductive polymer that can be catodically doped under the reducing lithium environment improving the overall electric conductivity. Based on this capability, the group of Gao Liu has modified the poly(9,9-dioctylfluorene)-co-fluorenone backbone in order to maintain high electronic conductivity while improving mechanical adhesion.<sup>47</sup> In this regard, the copolymerization with methyl benzoic ester leads to the formation of poly(9,9-dioctylfluorene)-co-fluorenone-co-methylbenzoic ester (PFM) which shows improved chain flexibility and stronger mechanical adhesion force between the active materials and the polymer binder. This binding force arises from to the transesterification reaction between the ester functional group of the binder and the SiOH surface group of the SiO particles that

---

<sup>44</sup> Wu, M.; Song, X.; Liu, X.; Battaglia, V.; Yang, W. and Liu, G., Manipulating the polarity of conductive polymer binders for Si-based anodes in lithium ion batteries, *J. Mater. Chem. A*, **2015**, 3, 3651.

<sup>45</sup> Park, S.-J.; Zhao, H.; Ai, G.; Wang, C.; Song, X.; Yuca, N.; Battaglia, V. S.; Yang, W.; Liu, Gao, Side-chain conducting and phase-separated polymeric binders for high performance silicon anodes in lithium-ion batteries, *J. Am. Chem. Soc.*, **2015**, 137, 7, 2565-2571.

<sup>46</sup> Yuca, N.; Zhao, H.; Song, X.; Dogdu, M. F.; Yuan, W.; Fu, Y.; Battaglia, V. S.; Xiao, X. and Liu, G., A systematic investigation of polymer binder flexibility on the electrode performance of lithium ion batteries, *ACS Appl. Mater. Interfaces*, **2014**, 6, 17111-17118.

<sup>47</sup> Dai, K.; Zhao, H.; Wang, Z.; Song, X.; Battaglia, V. and Liu, G., Toward high specific capacity and high cycling stability of pure tin nanoparticles with conductive polymer binder for sodium ion batteries, *J. Power Sources*, **2014**, 263, 276-279.

are employed as active material.<sup>48</sup> The main strength of this material is that with only 2 % by weight of binder in absence of carbon additives, the SiO anode material demonstrates stable high gravimetric capacity in lithium ion batteries (more than 1000 mAh/g for 500 cycles, with 90 % of capacity retention. This binder has been also successfully employed with Sn anodes in lithium ion batteries, leading to 510 mAh/g for 60 cycles.<sup>49</sup> The further partial replacement of octyl side chains with triethyleneoxide monomethyl ether moieties of the fluorine units constitutes a step forward in this strategic approach. The aim is the increase of polarity of the polymer and as a consequence, the enhancement of the electrolyte uptake.<sup>50</sup> In that sense, Wu *et al.* demonstrated that the polarity of PEFM polymer can be tuned by adjusting the molar ratio of polar triethylene oxide chain, changing the electrolyte up-taking properties of conductive polyfluorene-based polymers.<sup>51</sup> The use of PEFM as binder of commercial Si nanoparticles in lithium ion batteries, leads to an improvement of the capacity (3000 mAh/g after 50 cycles) with respect to the use of bare PFM (2500 mAh/g after 50 cycles).

The chemical structures of the above described polymeric binders are depicted in Figure 3.2.

---

<sup>48</sup> Zhao, H.; Wang, Z.; Lu, P.; Jiang, M.; Shi, F.; Song, X.; Zheng, Z.; Zhou, X.; Fu, Y.; Afdelbast, G.; conductive polymer binder for a high energy lithium ion battery design, *Nano lett.*, **2014**, 14, 6704-6710.

<sup>49</sup> Xun, S.; Song, X.; Battaglia, V. and Liu, G., Conductive polymer binder-enabled cycling of pure tin nanoparticle composite anode electrodes for a lithium ion battery, *J. Electrochem. Soc.*, **2013**, 160 (6), A849-A855.

<sup>50</sup> Wu, M.; Xiao, X.; Vukmirovic, N.; Xun, S.; Das, P. K.; Song, X.; Olalde-Velasco, P.; Wang, D.; Weber, A. Z.; Wang, L.-W. Battaglia, V. S.; Yang, W. and Liu, G., Toward an ideal polymer binder design for high-capacity battery anodes, *J. Am. Chem. Soc.*, **2013**, 135, 12048-12056.

<sup>51</sup> Wu, M.; Song, X.; Liu, X.; Battaglia, V.; Yang, W. and Liu, G., Manipulating the polarity of conductive polymer binders for Si-based anodes in lithium ion batteries, *J. Mater. Chem. A*, **2015**, 3, 3651-3658.

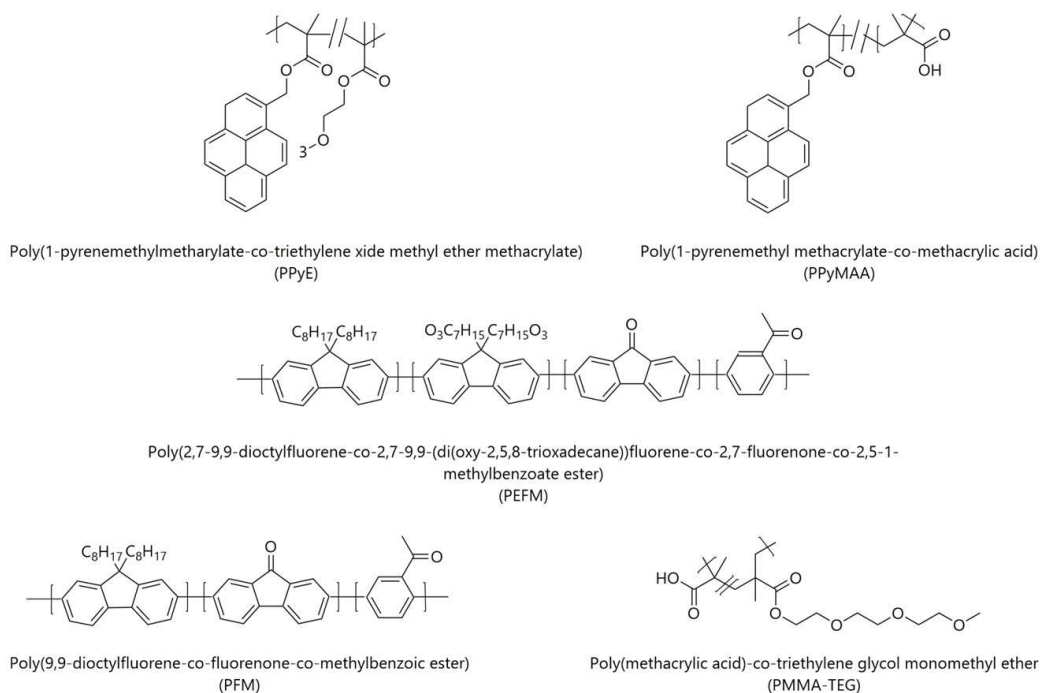


**Figure 3.2** Chemical structures of several double-rolled polymer binders.

### 3.1.4 Aim of the present work

The establishment of an affordable sodium ion technology for secondary batteries makes necessary the search for new electrode materials. Organic electrode materials are promising due to their potential low cost, environmental friendliness and ease of recycling or disposal. Despite there exists many examples of organic electrodes in the literature, there are a few materials that are active at low voltages vs. sodium. Recently, a family of compounds based on the Schiff base active unit has been reported to be active at low voltages vs. sodium ion batteries leading to high capacity values of about 350 mAh/g. One of the main strengths of these compounds is that they can be easily synthesized by a simple polycondensation reaction producing water as byproduct. In addition to the low cost and environmental friendliness of polySchiff bases, these kind of rigid chain structures containing aromatic rings stabilized by resonance and intermolecular interactions, entail good properties such as thermal stability, mechanical stress and fiber-forming ability. However, these structural features which endow desirable physicochemical

properties involve low solubility in organic solvents and extremely high glass transition or melting temperatures. These features, involving poor processability, limit strongly their applicability as electrode materials in real devices. In this regard: the objective of this work is:

1. The improvement of the processability of the PolySchiff bases as anodes, in order to obtain flexible polymers that can be manufactured by employing conventional laminating methods and, ultimately, by means of roll-to-roll industrial techniques. Besides, any improvement in the processing of the material is expected to be accompanied by an enhancement of the electrochemical performance. To this end, the synthesis of copolymers of poly-Schiff bases and different types of commercial polyethylene oxide polymers (Jeffamine ED®) which has been reported to be a useful tool in order to improve polymer flexibility as well as solubility, given the polar properties of the ethylene oxide branches and are available in a broad range of molecular weights is targeted.
2. Obtention of binder-free electrodes with good mechanical properties that can endure cycling. Inspired by the approach of the “so-called” smart binders, showing dual functionality (electronic conductivity and binding properties), the ultimate objective is the use of polySchiff-PEO copolymer as another kind of double-roled polymeric binder showing both redox activity and binding properties. This way, apart from avoiding the deadweight effect imposed by the use of an inactive binder, it should be possible to take advantage of the redox activity of the PolySchiff bases, when used as binder of anode materials. Besides, the presence of PEO in the polymeric backbone should facilitate the electrolyte uptake and, as a consequence, the ionic conductivity which might be translated into a better electrochemical performance.



## 3.2 Experimental

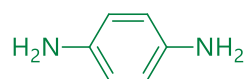
The bare PolySchiff bases synthesized by our group are the starting point for the synthesis optimization. A comparison of the characterization of polySchiff – polyethylene oxide copolymers with the previously reported bare polySchiff bases will be established. Hereafter, the electrochemical performance will be shown and related to the properties of the polymer. Finally, on the search of the double-rolled polymer that combines redox activity with binding properties, the optimized polymer will be employed as a binder of other active materials with higher energy density.

### 3.2.1 Synthesis of PolySchiff-PEO copolymers

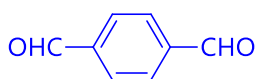
A modified synthesis of polymeric Schiff base (abbreviated as PSB) was performed based on the procedure reported by Castillo-Martínez et al.<sup>29</sup> Synthesis was carried out by mixing 4.8 mmol of terephthalaldehyde (99%, Sigma Aldrich) and 4.8 mmol of *p*-phenylenediamine (98%, Sigma-Aldrich) in 60 mL of dimethylformamide (DMF) at 150°C under vigorous stirring. After 24 hours of reaction, a yellow-orange suspension was formed and filtered while warm.

Synthesis of polymeric Schiff bases containing polyethylene-ethylene oxide blocks (abbreviated as PSB-PEO) was carried out by polycondensation of a dialdehyde (terephthalaldehyde) with two diamines: *p*-phenylenediamine and Jeffamine (PEO). In

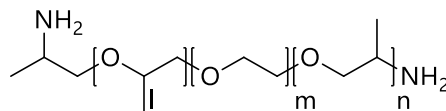
Scheme 3.1, the chemical structures of the monomers and the PSB-PEO are shown.



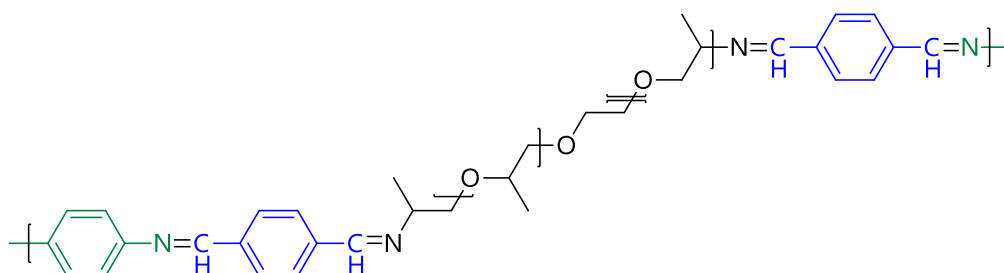
p-phenylenediamine



terephthalaldehyde



Jeffamine ED (PEO block)



PolySchiff-Jeffamine copolymer (PS-PEO)

**Scheme 3.1** Starting materials (*p*-phenylenediamine, terephthalaldehyde and O,O'-Bis(2-aminopropyl) polypropylene glycol-block-polyethyleneglycol-block-polypropylene glycol and the expected structure of the terpolymer (PSB-PEO). Note that *l*, *m* and *l* (the ratio between monomers present in the PEO block) are variable and depend on the molecular weight of the Jeffamine (see Table 3.4).

The first reaction step involved the reaction between the dialdehyde and the PEO block. Terephthalaldehyde (99%, Sigma Aldrich, 4.8 mmol, 0.65 g) was dissolved in 60 mL of solvent. Ethanol (EtOH, Sigma-Aldrich) toluene (TOL, Acros Organics) or *N,N*-dimethylformamide (DM, Fisher Scientific) were deployed in order to get P1, P2 and P3-P8, respectively (Table 3.3). The corresponding amino terminated PEO block (Jeffamine ED®, Sigma-Aldrich, 4 mmol for P4 and 0.8 mmol for the rest) was then added and the solution was vigorously stirred at a temperature close to the boiling point (78 °C, 105 °C and 150 °C for EtOH, TOL and DMF respectively). O,O'-Bis(2-aminopropyl) polypropylene glycol-block-polyethylene glycol-block-polypropylene glycol (PEO block) of 600 g·mol<sup>-1</sup> of molecular weight was used in order to get P1-P4 and P7-P8, while PEO of 900 g·mol<sup>-1</sup> and 2000 g·mol<sup>-1</sup> were deployed to obtain P5 and P6 respectively. After variable hours of reaction (Table 3.3) the second step involved the addition of *p*-phenylenediamine (Sigma-Aldrich) to the dialdehyde/PEO mixture. When a yellow-orange suspension was formed the reaction was considered complete.

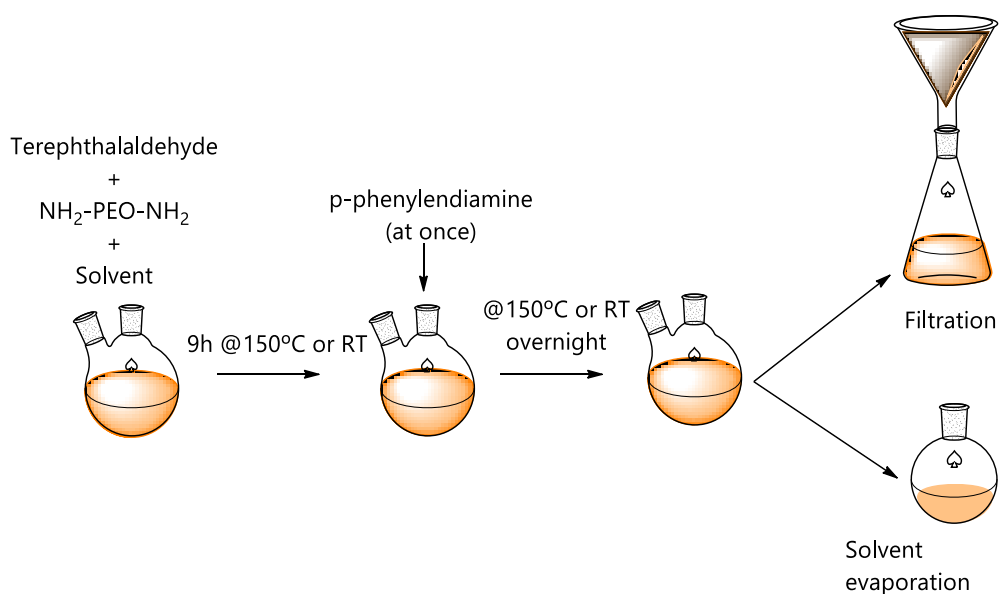
**Table 3.3** Summary of the reaction conditions for the bare PSB (PS0) and for the PSB-PEO terpolymers (P1-P8). A: *p*-phenylenediamine, B: terephthalaldehyde and C: O,O'-Bis(2-aminopropyl) polypropylene glycol-block-polyethylene glycol-block polypropylene glycol (PEO).

Studied effect	Name	Molar ratio A:B:C	Solvent	MW. PEO (g·mol <sup>-1</sup> )	1 <sup>st</sup> step		2 <sup>nd</sup> step		Isolation method
					T (°C)	t (h)	T (°C)	t (h)	
	PS0 (PSB)	6:6:0	DMF	-	150	9	78	14	Warm filtration
Solvent @ T <sub>boiling</sub>	P1	5:6:1	EtOH	600	78	9	78	14	Warm filtration
	P2	5:6:1	TOL	600	105	9	105	14	Warm filtration
	P3	5:6:1	DMF	600	150	9	150	14	Warm filtration
	P4	3:6:3	DMF	600	150	9	150	14	Warm filtration
M.W. PEO	P3	5:6:1	DMF	600	150	9	150	14	Warm filtration
	P5	5:6:1	DMF	900	150	9	150	14	Warm filtration
	P6	5:6:1	DMF	2000	150	9	150	14	Warm filtration
Time of reaction	P3	5:6:1	DMF	600	150	9	150	14	
	P7	5:6:1	DMF	600	150	24	25	4	
	P8	5:6:1	DMF	600	25	24	25	4	

In order to isolate the polymer, solvent evaporation and filtration while warm were employed to get rid of low molecular weight chains that might precipitate at low temperature.

The obtained precipitate was dried under vacuum at 120 °C for 24 hours to ensure solvent removal and, finally it was hand ground with an agate mortar and stored at ambient conditions.

The general synthesis procedure of PS-PEO is depicted in the Scheme 3.2.



**Scheme 3.2** Scheme of the synthesis of PSB-PEO terpolymer.

The synthesis was optimized by varying several synthetic parameters summarized in Table 3.3 and checking its influence of the electrochemical performance

First, the use of different solvents at a temperature of synthesis close to their boiling point (P1-P3) was evaluated. Then, a modification of the molar ratio between the three reactants/blocks in the synthesis performed in DMF led to the formation of P4. In order to carry out this synthesis optimization, a PEO of 600 g·mol<sup>-1</sup> was arbitrarily chosen. Further optimization of the molecular weight of the PEO block entailed the use of PEO 900 and 2000 g·mol<sup>-1</sup> providing P5 and P6 respectively. All the Jeffamines ED<sup>®</sup> that were used in this study share the same chemical structure, being the ratio between repeating units (see Scheme 3.2) and the molecular weight of the resulting block, the only difference. That ratio is summarized in Table 3.4.

**Table 3.4** Ratio between repeating units and molecular weight of polyetheramines (Jeffamine ED<sup>®</sup>). Note that l, m and n (the ratio between monomers present in the PEO block) are variable and depend on the molecular weight of the Jeffamine (Scheme 3.1)

Jeffamine <sup>®</sup>	m	l+n	M.W. (g/mol)
ED600	9	3.6	600
ED900	12.5	6	900
ED2003	39	6	2000

Finally, P7 and P8 were evaluated so as to evaluate the effect of varying the time at a given temperature of each reaction step.

### 3.2.2 Electrochemical characterization

With the aim of developing a double-rolled material, polymers were electrochemically characterized by galvanostatic cycling versus metallic sodium both as active material so as to observe their activity, and as binder of other active materials (such as carbons and metal carbodiimides) in order to assess the activity along with the binding ability upon cycling.

Prior to cell assembly and further electrochemical testing, electrode and electrolyte preparation was carried out.

### 3.2.2.1 Electrode preparation

The preparation of the electrode for further cycling is crucial for a good cell performance as properties of the electrode are strongly affected by processing of the material. Electrode is composed by electrochemically active material, conductive additives and binder. In general, any components other than active materials should be reduced as much as possible because the greater amounts of active materials filling up the volume, the more power can be obtained. However, in every case, the adhesion provided by the binder and electrical conductivity provided by carbon additive has to be guaranteed. For that reason, in an attempt to optimize the electrochemical performance of the material several ratios between electrode components were tried.

For PSB-PEO binder-free powder electrodes typically a 80 : 20 or 90 : 10 wt. % ratio of active and conductive agent (carbon material) were tried. C-Nergy Super C65 (Timcal) was used as conductive additive thanks to its low surface area ( $62 \text{ m}^2/\text{g}$ ) in order to prevent an increase in the irreversible capacity due to extensive SEI formation. Although it shows much larger surface area and less dispersibility, with the purpose of increasing the percolation paths for electronic conductivity when required, Ketjen Black (EC-600JD) carbon was also deployed.

According to the experiment specificities, different methods of preparing powder or laminate electrodes containing PS-PEO as binder or active material were implemented. The conditions for powder electrodes and for laminate electrodes are summarized in Table 3.5 and Table 3.6.

**Table 3.5** Composition of the powder electrodes tested as anodes in sodium half cells.

<b>Study</b>	<b>Active material</b>	<b>Additive</b>	<b>Ratio</b>	<b>Electrolyte</b>	<b>Voltage range (V)</b>
Ratio reactants and solvent	P1-P4	C65	80-20-0	1M NaFSI MeTHF	0.005-1.6
Size peo linker	P3, P5,P6	C66	80-20	1M NaFSI MeTHF	0.005-1.6
Effect temeprature	P7,P8	C67	80-20	1M NaFSI MeTHF	0.005-1.6
Electrode processing	P3	KB	50-50	1M NaFSI MeTHF	0.005-1.6
	P3	C65	50-50	1M NaFSI MeTHF	0.005-1.6
	P3	C65	90-10	1M NaFSI MeTHF	0.005-1.6
	P3	C66	80-20	1M NaFSI MeTHF	0.005-1.6

**Table 3.6** Composition of the laminate electrodes tested as anodes in sodium half cells.

Study	Foil	Active material	Additive	Binder	Ratio	Electrolyte	Voltage range (V)
Binder free	cu	P3,P5,P6,P7;P8	C65	-	80:20:0	1M NaFSI MeTHF	0.005-1.6
Powder vs. laminate	cu	P3	C65	-	80:20:0	1M NaFSI MeTHF	0.005-1.6
	cu	P3	C65	-	90:10.0	1M NaFSI MeTHF	0.005-1.6
	al	P3	C65	-	80:20:0	1M NaFSI MeTHF	0.005-1.6
	al	P3	C65	-	90:10.0	1M NaFSI MeTHF	0.005-1.6
P3 as binder of Sn	cu	Sn	C65	PVdF	80:10:10	1M NaFSI MeTHF	0.005-1.6
	cu	Sn	C65	PAA/SA	80:10:10	1M NaFSI MeTHF	0.005-1.6
	cu	Sn	C65	P3	10:10:80	1M NaFSI MeTHF	0.005-1.6
P3 as binder of hard carbon	cu	hard carbon	C65	P3	80:10:10	1M NaFSI MeTHF	0.005-1.6
	cu	hard carbon	C65	P3	80:10:10	1M NaClO <sub>4</sub> EC:PC	0.005-2
	cu	hard carbon	C65	PVdF	80:10:10	1 M NaFSI MeTHF	0.005-1.6
	cu	hard carbon	C65	PVdF	80:10:10	1M NaClO <sub>4</sub> EC:PC	0.005-2
Hard carbon electrode composition	cu	hard carbon	C65	PVdF /P3	80:20:0	1M NaClO <sub>4</sub> EC:PC	0.005-2
	cu	hard carbon	C65	PVdF/P3	80:10:10	1M NaClO <sub>4</sub> EC:PC	0.005-2
	cu	hard carbon	C65	PVdF/P3	80:18:02	1M NaClO <sub>4</sub> EC:PC	0.005-2
	cu	hard carbon	C65	PVdF/P3	50:40:10	1M NaClO <sub>4</sub> EC:PC	0.005-2
P3 as binder of soft carbon	cu	PVC	C65	P3/ PVdF	90:05:05	1M NaClO <sub>4</sub> EC:PC	0.005-2
	cu	PVC	C65	P3/ PVdF	80:10:10	1M NaClO <sub>4</sub> EC:PC	0.005-2
P3 as binder of ZnNCN	cu	ZnNCN	50/50 KB:C65	P3/PVdF	80:10:10	1M NaFSI MeTHF	0.005-2.5
	cu	ZnNCN	50/50 KB:C65	P3/ PVdF	70:10:20	1M NaFSI MeTHF	0.005-2.5
	cu	ZnNCN	50/50 KB:C65	P3	80:20:0	1M NaFSI MeTHF	0.005-2.5
	cu	ZnNCN	50/50 KB:C65	P3	40:40:20	1M NaFSI MeTHF	0.005-2.5



For laminate preparation polymer dissolved in the reaction media (DMF) is used. The amount of polymer was estimated in each case by evaporating solvent (DMF) and weighting dry residue of a given volume of reaction media.

Slurries were prepared by dispersing active material and C65 onto the polymer dissolved in DMF for 1 hour. Then, slurries were cast onto the Cu or Al foil and evaporated under vacuum at 120 °C. In order to avoid damage coming from further punching of the laminate, alternatively some electrodes were obtained by putting some droplets of slurry onto already punched Cu foil.

### 3.2.2.2 Electrolyte preparation

In this study two different home-made electrolytes were used. When testing PSB-PEO as active material 1M Sodium(I) bis(fluorosulfonyl)imide 99.7% (NaFSI, Solvionic, 99.7 %) in 2-methyltetrahydrofuran (99%, Sigma-Aldrich) 1M Sodium(I) bis(fluorosulfonyl)imide in 2-methyltetrahydrofuran (1M NaFSI in MeTHF).

Prior to dissolution in MeTHF, NaFSI was dried in a Büchi oven under vacuum at 120°C for 24 hours. Magnetic stirring overnight was required prior to utilization. A 1M Sodium(I) bis(fluorosulfonyl)imide (NaFSI, Solvionic, 99.7 %) in 2-methyltetrahydrofuran (99%, Sigma-Aldrich) solution was prepared in a glass bottle and stored in an aluminium bottle inside the glove box to avoid exposure to water and reactivity with the glass.

In order to prepare 1M sodium perchlorate in ethylene carbonate : propylenecarbonate (1M NaClO<sub>4</sub> EC:PC), Sodium perchlorate (NaClO<sub>4</sub>, Sigma-Aldrich, 98 %) was dissolved by magnetic stirring in a solution containing 50 wt. % ethylene carbonate (EC, Sigma-Aldrich, 99%, anhydrous) in propylene carbonate (PC, Sigma-Aldrich, 99%, anhydrous). The electrolyte was prepared and stored in an aluminium bottle inside the glove box to avoid exposure to water.

### 3.2.2.3 Cell assembly and galvanostatic cycling parametres

#### 3.2.2.3.1 Theoretical capacity values calculation

The aim of calculating the theoretical capacity of the anodic materials is to set the current that has to be applied so as to get a certain charge/discharge rate (C rate). In general, the current was calculated for a rate of discharge of 10, 5 and 1 hour (C/10, C/5 and 1C rates respectively). The applied current density ( $\text{mA}\cdot\text{g}^{-1}$ ) varied depending on the nature of the active material employed. The applied currents were calculated by multiplying the current density by the active mass. The capacity of a material is given by Faraday's law in equation 2.1 where  $F$  is the Faraday constant ( $96500 \text{ C}\cdot\text{mol}^{-1}$ );  $n_e$  is the number of exchanged electrons and  $M_w$ , the molecular weight of the active material in  $\text{g}\cdot\text{mol}^{-1}$ .

$$Q_{\text{theoretical}} = \frac{n_e F}{MW} \left[ \frac{\text{C}}{\text{g}} \right] \quad \text{Eq. 3.1}$$

In order to get the value in  $\text{mA}\cdot\text{h}\cdot\text{g}^{-1}$  the value in has to be multiplied by 1000 mA and divided by 3600 s.

As an active material, PSB-PEO was tested taking into account its theoretical capacity value. However, even though PSB-PEO might show activity, when tested as binder the applied current was calculated considering the theoretical capacity expected for the active material.

The largest value of  $\text{Na}^+$  inserted into the bare PS polymer was reported to be 1.4  $\text{Na}^+$  ions per azomethine unit when using a 50 wt. % of Ketjen Black.<sup>29</sup> Taking into account that more than one electron is accessible per  $\text{C}=\text{N}$  group, the current applied to the material was calculated for a discharge rate of 10, 5 and 1 hour considering the insertion of two  $\text{Na}^+$  ions per monomeric unit, ( $-\text{N}=\text{C}-\text{Ph}-\text{C}=\text{N}-$ ).

Assuming a nominal ratio 5 : 6 : 1 among reactants (*p*-phenylenediamine, terephthalaldehyde and Jeffamine) named A : B : C respectively takes part on the reaction in that stoichiometric relationship, the polymer formed would be of a A-B-A-B-A-B-A-B-A-C type. This configuration would lead to active segments of a

certain molecular weight depending on the molecular weight of the PEO used (600, 900 or 2000 g·mol<sup>-1</sup>). The scheme of the proposed structure of the resulting polymer with the same stoichiometry as the starting materials is represented In Figure 3.3

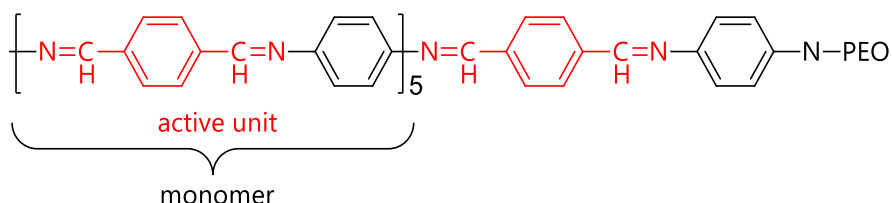


**Figure 3.3** Example of the chemical structure of a PSB-PEO containing a ratio between reactants of 5:6:1 moles of phenylenediamine, terephthalaldehyde and Jeffamine respectively.

Attending to the assumption that a maximum of 2 Na<sup>+</sup> ions can be inserted into each active unit, a total of 12 electrons are involved in the electrochemical reaction. In the equation 2.2, as an example, the theoretical capacity of the polymer containing a PEO block of 600 g/mol, therefore, a total molecular weight of 1732 g/mol, is calculated.

$$Q_{\text{theoretical}} = \frac{12 \cdot 96500 \text{ A} \cdot \text{s} \cdot \text{mol}^{-1} \cdot 1 \text{ h} \cdot 1000 \text{ mA}}{3600 \text{ s} \cdot 1 \text{ A} \cdot 540.31 \text{ g mol}^{-1}} = 186 \text{ mAh/g} \quad \text{Eq. 3.2}$$

The theoretical capacities along with the current densities applied for the PSB-PEO samples as a function of the molecular weight of the PEO block as well as the carbonaceous materials and metal carbodiimides are summarized in Table 3.7.

**Table 3.7** Theoretical capacities and current densities applied for C/10, C/5 and 1C charge rates of PSB-PEO synthesized as of PEO of different molecular weights.

	Theoretical capacity (mA·h·g <sup>-1</sup> )	Theoretical composition (sodiated)	Current density (mA·g <sup>-1</sup> )	Current density (mA·g <sup>-1</sup> )	Current density (mA·g <sup>-1</sup> )
<b>C rate (hours)</b>			<b>C/10</b>	<b>C/5</b>	<b>1C</b>
PSB-PEO600	186	1Na/C=N	18.6	37.2	186
PSB-PEO900	158	1Na/C=N	15.8	31.6	158
PSB-PEO2000	103	1Na/C=N	10.3	20.6	103
Carbons	372	NaC <sub>6</sub>	37.2	74.4	372
ZnNCN	508	Zn <sup>+</sup> Na <sub>2</sub> NCN	50.8	101.6	508

### 3.3 Results and discussion

In this section the structural, morphological and electrochemical characterization of the polymers will be shown.

#### 3.3.1 Structural and morphological characterization

##### 3.3.1.1 Attenuated total reflectance-Fourier Transform Infrared Spectroscopy (ATR-FTIR)

Formation of PSB-PEO as a result of the polycondensation reaction was verified by Attenuated total reflectance-Fourier Transform Infrared Spectroscopy (ATR-FTIR).

In Figure 3.4 a, the ATR-FTIR spectra of a PSB-PEO polymer (P3) is shown and compared to those of PSB and reactants (terephthalaldehyde, *p*-phenylenediamine and PEO). The presence of strong imine  $\nu\text{C}=\text{N}$  stretching band at frequencies between 1620 and 1690  $\text{cm}^{-1}$  confirmed the condensation between dialdehyde and amines (PEO or *p*-phenylenediamine).<sup>52</sup> The carbonyl  $\nu\text{C}=\text{O}$  stretching peak at 1690  $\text{cm}^{-1}$  is faintly visible in the PSB and PSB-PEO and corresponds probably to end groups whereas amine stretching band  $\nu\text{NH}_2$  from the starting materials in the 3300-3500  $\text{cm}^{-1}$  range becomes almost negligible in the products evidencing the consumption of the reactant. The incorporation of the PEO segment into the PSB-PEO polymer was corroborated by the presence of the vibrational band  $\nu\text{C}-\text{H}$  in the

<sup>52</sup> Clougherty, L.; Sousa, J. and Wyman, G.; *J. Org. Chem.*, **1957**, 22, 4, 462-462.

range 3000-2840  $\text{cm}^{-1}$  corresponding to aliphatic methyl or  $-\text{CH}_2-$  groups monomers of the PEO block as well as a strong signal at 1091  $\text{cm}^{-1}$  related to the symmetrical  $\text{CH}_2\text{-O-CH}_2$  stretching.

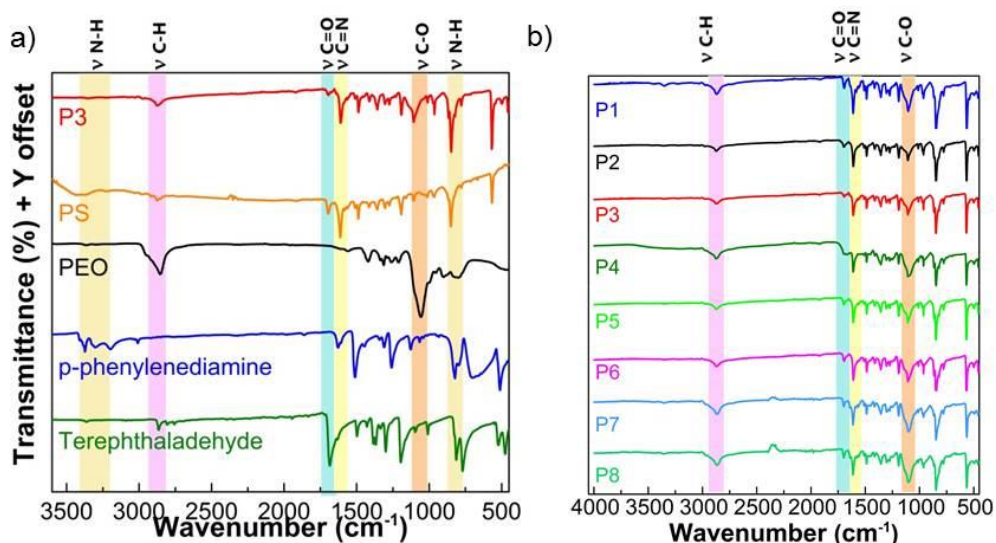


**Figure 3.4** a) Comparison of the FTIR spectra of PSB-PEO (P3) and bare PS with the reactants. b) Comparison of the different PSB-PEO polymers synthesized.

In Figure 3.4b, the FTIR of all the synthesized polymers is shown. The FTIR spectra of the polymers synthesized with different solvents (EtOH, TOL and DMF for P1, P2 and P3, respectively) as well as with a larger ratio of PEO (P4) showed almost no differences among them. They all showed the characteristic band of the azomethine  $\text{C}=\text{N}$  and  $\text{CH}_2\text{-O-CH}_2$  stretching evidencing the fulfilment of the reaction, although with different relative intensities of the absorptions. The fulfilment of the reaction in two steps was also confirmed, regardless of the temperature at which the reaction is carried out: 150 °C or room temperature for either steps (P3, P8) or a first step at 150 °C and a second at room temperature (P7).

### 3.3.1.2 Powder X-Ray diffraction (XRD)

The crystallinity of the polymers is a feature that affects the mechanical, thermal and chemical properties of the polymers as well as its electrochemical performance as it

will be shown later. The formation of a crystalline phase in all the samples synthesized under different conditions was qualitatively studied by XRD (Figure 3.5).

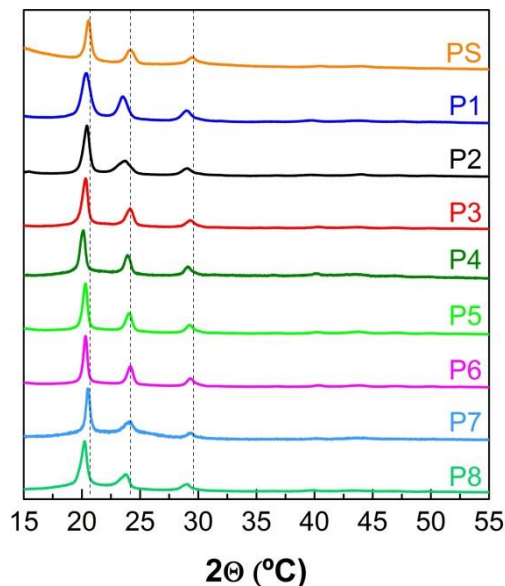


**Figure 3.5** XRD patterns of PSB and PSB-PEO samples synthesized with different conditions.

Both PSB and PSB-PEO showed broad diffraction peaks confirming that polymers were semicrystalline, meaning that highly ordered domains coexist with regions containing randomly coiled chains. This fact, which is related to partial alignment of the molecular chains and is strongly favored by regularity and the presence of  $\pi$ - $\pi$  interactions between aromatic rings, constitutes the reason for the great mechanical strength of the Schiff bases. The incorporation of PEO into the polymer backbone of the PSB does not produce loss of crystallinity which was reported to be necessary to ensure good electrochemical performance.<sup>29</sup> However, a decrease in the  $2\theta$  value of the reflections centered at  $20.3^\circ$  and  $29.2^\circ$  was observed for all the PSB-PEO terpolymers compared to those of the bare PSB. This decrease of the  $2\theta$  value in PSB-PEO is a consequence of the insertion of voluminous PEO blocks in the polymer chain that produces an expansion of the interplanar distance, even if the PEO blocks are part of the crystalline domain.

The use of different solvents (EtOH, TOL and DMF for P1, P2 and P3, respectively) for a given ratio among reactants led to subtle differences in the position of the main reflection peaks. They were slightly displaced to lower theta angles when using EtOH and TOL. Moreover, EtOH led to wider peaks evidencing smaller crystal size. Changes in the interplanar spacing of the crystalline regions of the polymer seem to be crucial for the electrochemical performance and will be further discussed in the electrochemical performance section. When comparing the samples synthesized in DMF at 150°C, the sample containing a molar ratio between *p*-phenylenediamine, terephthalaldehyde and PEO of 3:6:3 (P4), showed the three main reflections centered at 20.13 °, 23.88 ° and 29.09 ° at lower 2θ angles than the sample containing lower amount of PEO (P3). This is consistent with the fact that a larger amount of PEO would produce a bigger expansion of the crystal structure. It was also observed that the position of the diffraction peaks were kept when using PEO blocks of different molecular weights (P3, P4 and P5). This confirmed that crystalline domains were not disturbed by the insertion of bulkier or tinier PEO branches. Regarding the effect of the temperature, it was observed that there were no discrepancies between the peak positions of samples synthesized in two steps either at 150 °C /room temperature (P7) or when performing the whole process at room temperature (P8).

After synthesis optimization and despite the presence of few reflections and the peak broadening as a consequence of the partial crystallinity and likely small crystal size of the polymer, Dicvol was used to look for possible unit cells and symmetries of the sample providing best electrochemical performance (P3). Le Bail profile matching method was used in order to refine unit cell parameters, and among the 5 possible unit cells for the same *P 2/m* monoclinic symmetry, the solution showing best reliability factors ( $\chi^2=6.34$ ,  $R_p=3.73$ ) turned out to be the fourth model, (Figure 3.6) with unit cell parameters 12.51, 9.79, 9.21, 91.80° (summarized in Table 3.8).

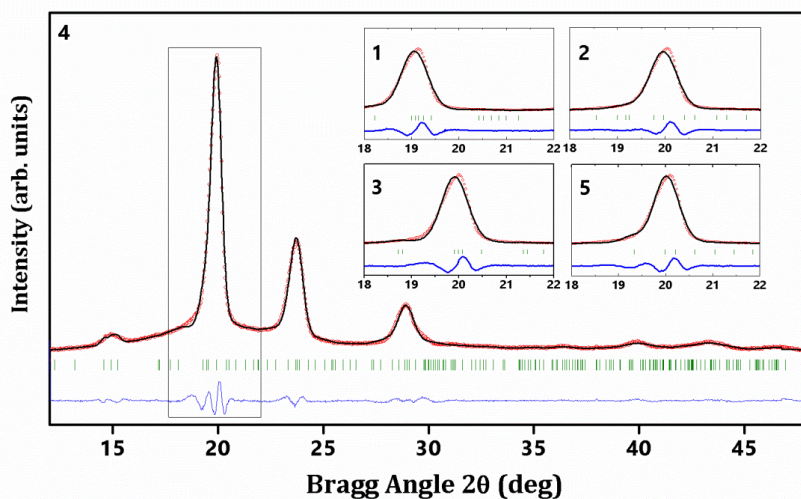


Figure 3.6 Dicvol and profile matching results of P3.

Table 3.8 Symmetries, space groups, refined unit cell parameters and reliability factors of the five solutions obtained from Dicvol for the P3.

	Model 1	Model 2	Model 3	Model 4	Model 5
Space group	<i>P 2/m</i>	<i>P 2/m</i>	<i>P 2/m</i>	<i>P 2/m</i>	<i>P 2/m</i>
a	10.56(2)	10.14(5)	12.01(3)	12.51(1)	12.95
b	12.52(2)	12.07(2)	8.67(3)	9.79(2)	9.18
c	9.23(3)	9.58(2)	12.28(2)	9.21(1)	8.80
α	90	90	90	90	90
β	90	93.99	90.37	91.80	106.43
γ	90	90	90	90	90
Chi <sup>2</sup>	9.51	8.90	11.2	6.34	9.02
Rp	4.46	4.25	4.71	3.73	4.28
Rwp	5.85	5.67	6.35	4.78	5.72
Rexp	1.90	1.90	1.90	1.90	1.90



### 3.3.1.3 Liquid $^1\text{H}$ -NMR

The completion of the reaction was studied by liquid NMR using DMSO- $d_6$  as solvent. Figure 3.7 displays the  $^1\text{H}$  NMR of the PSB (P3) and the PSB-PEO compared to the reactants. In Figure 3.8, the  $^1\text{H}$  NMR spectra of all the synthesized polymers are shown.

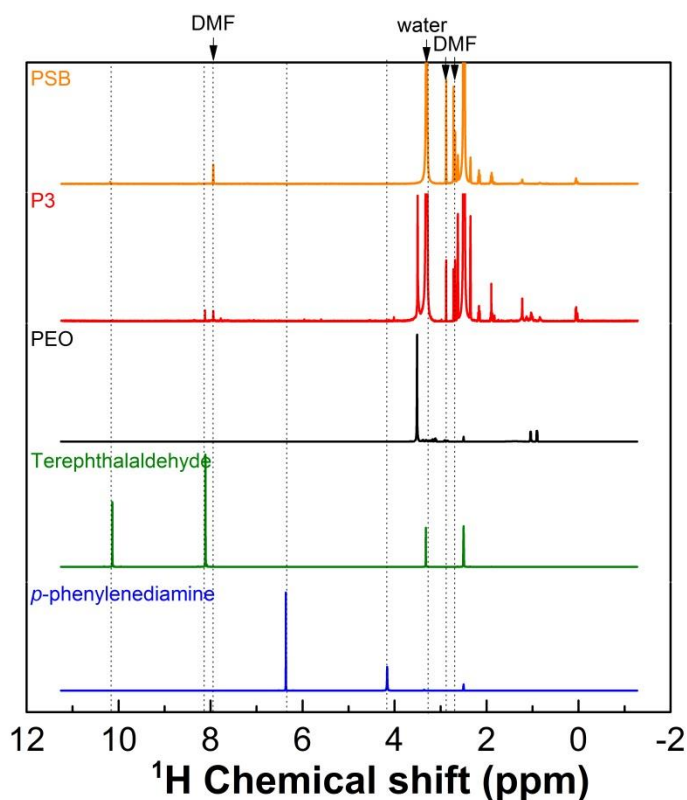


**Figure 3.7**  $^1\text{H}$ -NMR spectra of PSB (P3), PSB-PEO and reactants (terephthalaldehyde, PEO and *p*-phenylenediamine) Note that the signals of polymers have been zoomed in as the low solubility of the in DMSO did not give rise to high intensity and well resolved signals.

Peaks of the solvent (DMSO- $d_6$ ) and remnant water appear at 2.51 and 3.33 ppm respectively.<sup>53</sup> Likewise, signals of the solvent used for the synthesis (DMF) at  $\delta(\text{ppm})=7.96$  (s, CH), 2.89 (s,  $\text{CH}_3$ ), 2.73 (s,  $\text{CH}_3$ ) were observed in PSB, P3, P4, P5, P6 and P7. Signals of *p*-phenylenediamine at  $\delta(\text{ppm})=6.36$  (s, 4H), 4.16 (s, 4H) are not

<sup>53</sup> Gottlieb, H. E.; Kotlyar, V. and Nudelman, A., NMR chemical shifts of common laboratory solvents as trace impurities, *J. Org. Chem.*, **1997**, 62, 7512-7515.

present in the products whereas almost negligible amounts of unreacted terephthalaldehyde  $\delta(\text{ppm}) = 10.14$  (s, 2H), 8.11 (d,  $J = 0.8$  Hz, 8H, 4H) can be observed only in PSB and P5 evidencing the completion of the reaction. Noteworthy is the resonance at 3.53 ppm of the (-CH<sub>2</sub>-) of PEO, that is present in all the PSB-PEO samples (P1-P8) confirming the insertion of the polyetheramine in the polymeric backbone of the PolySchiff.<sup>54</sup> The fact that PEO signals can be observed in all the samples whereas the signals corresponding to azomethinic and aromatic protons are faintly visible, suggested that the polymer is partially solubilized by PEO segments. This is consistent with the fact that the aromatic region (6-8.5 ppm) showed better resolved signals for the sample containing PEO of largest molecular weight (P6). The presence of PEO might be helping to partially solubilize rigid regions containing Ph-CH=N-Ph- that give rise to the appearance of signals in the aromatics region. Despite the assignment of the signals is inconclusive because of the fact that only the low molecular weight fractions or oligomers might be soluble, according to the literature in the sample showing better spectrum (P6) which has PEO chains with largest molecular weight, signals located around 10.17 ppm might correspond to the azomethine proton<sup>55</sup> whereas signals at higher fields might be related to benzilidene units (8.02-8.26)<sup>56</sup> and phenylene units (7.64-7.16-6.92).

---

<sup>54</sup> Dust, J. M.; Fang, Z.-H. and Harris, J. M., Proton NMR characterization of poly(ethylene glycols) and derivatives, *Macromolecules*, **1990**, 23, 3742-3746.

<sup>55</sup> Yang, C. J. and Jenekhe, S. A.; Conjugated aromatic poly(azomethines). 1. Characterization of structure, electronic spectra, and processing of thin films from soluble complexes, *Chem. Mater.*, **1991**, 3 (5), 878-887.

<sup>56</sup> Kinney, Z. J. and Hartley, C. S.; Twisted macrocycles with folded ortho-phenylene subunits, *J. Am. Chem. Soc.*, **2017**, 139 (13), 4821-4827.

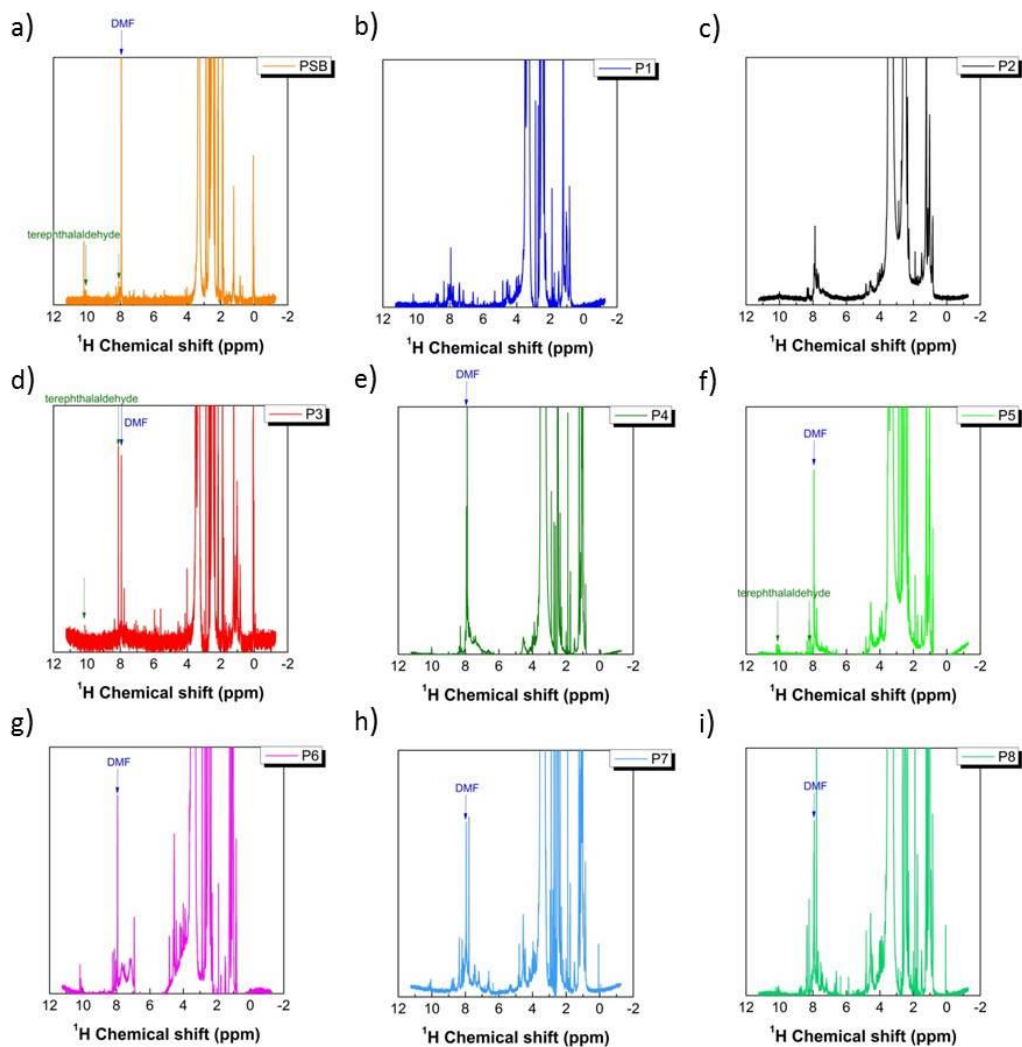


**Figure 3.8**  $^1\text{H}$ -NMR spectra of PSB, PSB-PEO and reactants (terephthalaldehyde, PEO and *p*-phenylenediamine) Note that the signals have been zoomed in.

### 3.3.1.4 Solid state NMR (ss-NMR)

In view of the poor solubility of PSB-PEO samples, ss-NMR was performed. In Figure 3.9, the  $^{13}\text{C}$  NMR of the bare PSB is shown.

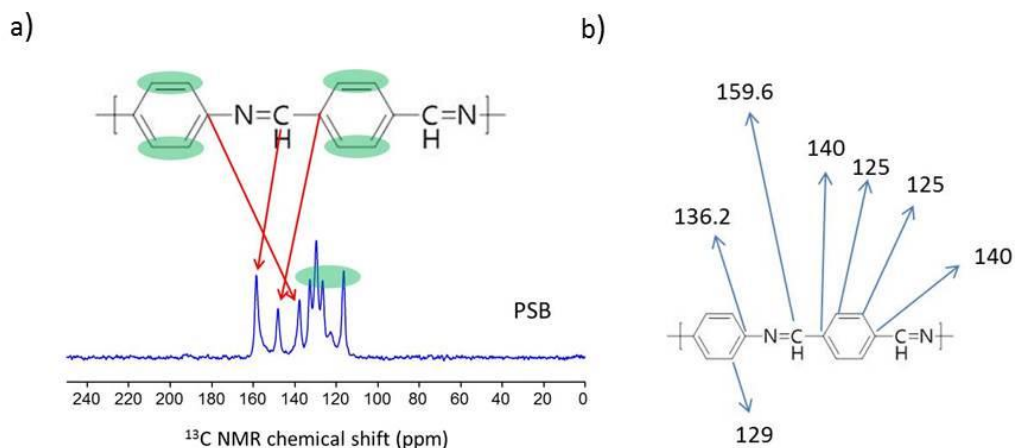


**Figure 3.9** a)  $^{13}\text{C}$  ss-NMR of PSB b) assignment of the chemical shifts of the spectrum of PSB.

The spectrum shows eight signals located in the zone of aromatics (110-160 ppm). The carbon next to the nitrogen is the one that shows up furthest downfield (159.6 ppm) due to the inductive effect promoted by the electronegativity of N. The rest of the protons can be assigned as shown in Figure 3.9. In Figure 3.10 a comparison between the spectrum of PSB and PSB-PEO (P3) is shown. It is observed that except for the signal centered at 69 ppm, which can be ascribed to the PEO block, the rest of the signals remain the same. This signal related to the carbon atoms of PEO in P3 was confirmed to be coupled to protons by means of an HETCOR experiment, as shown in Figure 3.10. The signal at 140 ppm attributed to the carbon atom bound to the N and to the C showed no coupling to protons in the HETCOR experiment, confirming its assignment.

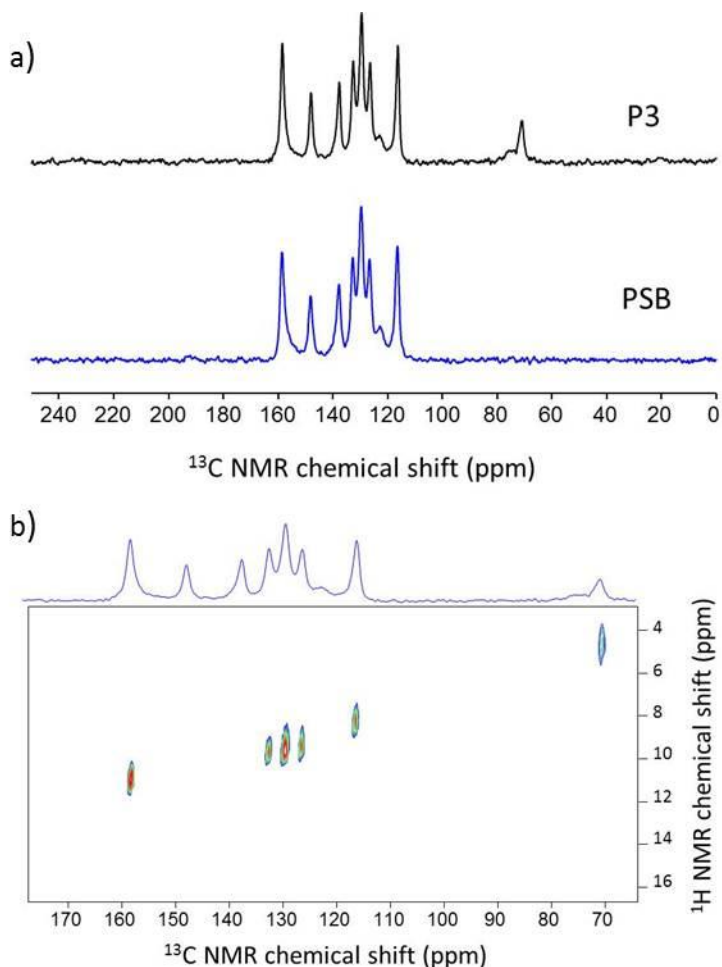


**Figure 3.10** a) Comparison of the  $^{13}\text{C}$  ss-NMR spectra of PSB and PSB-PEO (P3) and b) HETCOR experiment on P3.

### 3.3.1.5 Scanning electron microscopy (SEM)

The effect of the PEO insertion on the morphology was determined by scanning electron microscopy (SEM) in secondary electron mode (SE). In Figure 3.11, the micrographs of both bare PSB and PSB polymers are shown. Due to poor electronic conductivity, so as to avoid charging effects, both kind of samples were gold-coated. Flake-shape particles were observed regardless of the presence of PEO so it was concluded that polymer morphology was not affected by the incorporation of PEO blocks. On the one hand, the flake geometry allows large surface area flakes to easily come in contact with other flakes providing high particle-to-particle

interactions and facilitating the electron conduction between the polymer and any additive like carbon black.<sup>57</sup> But, on the other hand, a minimally porous, highly compact material would be much more desirable in order to increase the volumetric capacity and in order to diminish large irreversible capacity due to the electrolyte decomposition and SEI formation that might arise from a large surface area.

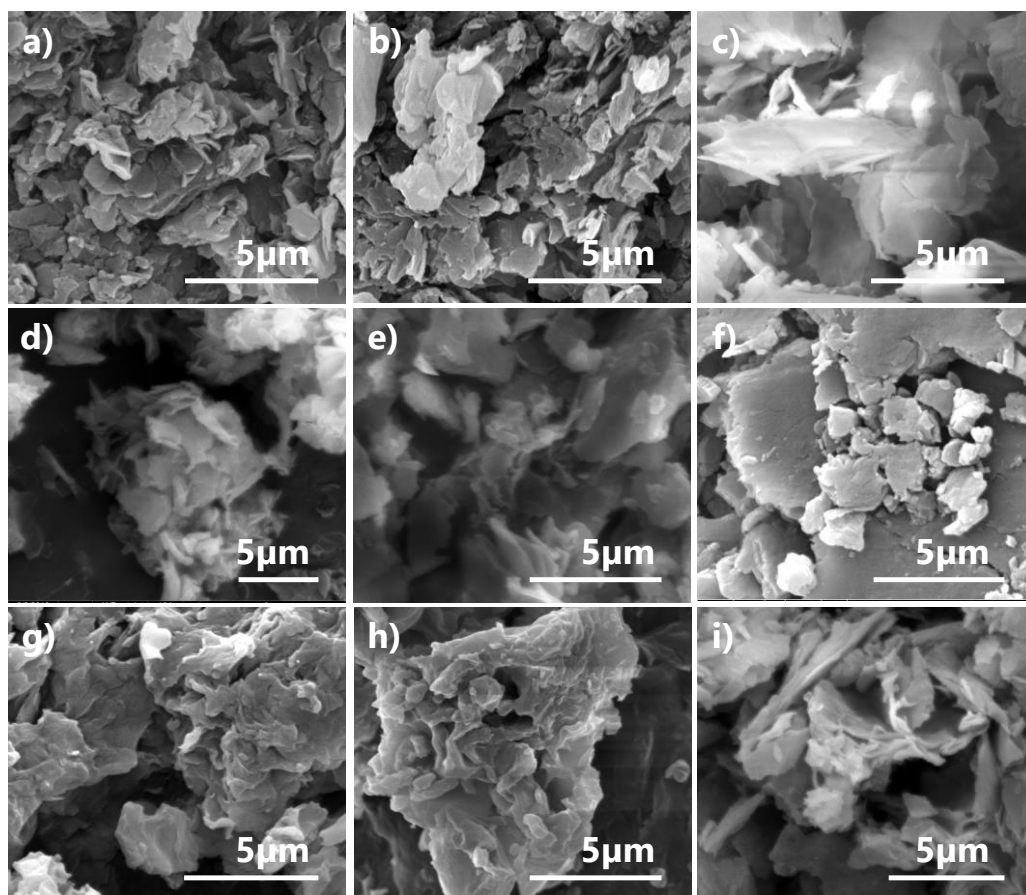


**Figure 3.11** SEM micrographs (secondary electron mode) of a) PSB, b) P1, c) P2, d) P3, e) P4, f) P5, g) P6, h) P7 and i) P8.

<sup>57</sup> Michler, G. H., *Electron Microscopy of Polymers*, 2008, Springer-Verlag Berlin Heidelberg, 295-296.

### 3.3.1.6 Thermogravimetric analysis analysis (TGA)

Thermal analysis was carried out to determine the behavior of the material when it is subjected to thermal treatments so as to evaluate their potential use or electrode processing at high temperature. Thermogravimetric Analysis (TGA) measures the amount and rate of change in the weight of a material as a function of temperature in a controlled argon atmosphere. A starting mass larger than 100% was observed for PSB-PEO due to a measurement artifact. Thermal decomposition of polymers may proceed by oxidative processes or simply by the action of heat but, in order to avoid the corrosion of the thermo-balance, the analysis was performed under Ar atmosphere. This way, the thermal decomposition is minimized due to the absence of oxidants such as air or oxygen, being the reported decomposition temperatures lower than those that could be observed in the presence of air atmosphere.

In Figure 3.12 the thermograms of the PSB-PEO copolymers synthesized in different conditions and bare PSB are compared.

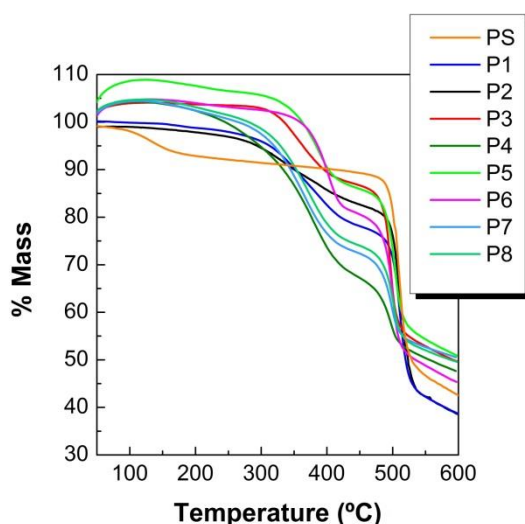


**Figure 3.12** TGA thermograms performed at a heating rate of  $10^{\circ}\text{C min}^{-1}$  under Ar atmosphere of PSB and PSB-PEO synthesized in different conditions.

Both PSB and PSB-PEO show good thermal stability as it was expected from the fact that they have regular structures and due to the strong  $\pi$ - $\pi$  interactions. Regarding bare PSB, the weight loss could be differentiated in two parts, being the first one

between 60-130 °C related to solvent evaporation which involved at least 6 wt. % of the mass of the polymer and a second one, starting at 460 °C, due to thermal degradation (monomer scission). This thermal behavior is consistent with the one observed by Yang, *et al.* in analogous polyazomethines.<sup>58</sup> However, as it was expected, given the presence of bulky and flexible polyether linkages that disturb the regularity of the polymer, PSB-PEO showed lower thermal stability, with degradation of the polymer starting at a lower temperature (300 °C) than bare PSB (400 °C). A second mass loss started at 500 °C. This two-step degradation profile might be related to the presence of two kind of polymeric segments: those containing bare azomethine units, which are rigid and, therefore, more thermally stable, which would correspond to the slope above 450 °C, and those containing PEO units, which are flexible and less stable, related to the slope centered at 350 °C. This is consistent with the half decomposition temperature ( $T_{1/2}$ ) of PEO, meaning the temperature at which the polymer loses a 50 % of its weight, being 350 °C.<sup>59</sup>

### 3.3.1.7 Solubility tests

The insertion of flexible comonomer units (“spacers”) like PEO chains has been one of the most reported strategies in order to reduce the rigidity of macromolecules and increase their solubility.<sup>60</sup> However, in the case of PSB this approach has been unsuccessful so far and no noticeable improvement of the solubility of the PSB-PEO with respect to the PSB has been observed. A summary of the results obtained when trying to dissolve the bare PSB and the PSB-PEO in common solvents is shown in Table 3.9 As expected, both are totally insoluble in non-polar solvents like hexane and toluene. The presence of polar bonds like -C=N- and C-O enables partial solubility of the compounds in polar aprotic solvents like DMSO, DMF and acetone.

---

<sup>58</sup> Yang, C.-J. and Jenekhe, S. A. Conjugated aromatic poly(azomethine). Characterization of structure, electronic spectra and processing of thin film from soluble complexes. *Chem. Mater.*, **1991**, 3, 878-887.

<sup>59</sup> Mark, J. E., Physical Properties of Polymers Handbook, **2007**, Springer-Verlag New York, 932.

<sup>60</sup> Ballauff, M. Stiff-chain polymers-structure, phase behavior and properties, *Angew. Chem.* **1989**, 3, 28, 253-267.



**Table 3.9** Solubility tests performed for PSB and PSB-PEO.

Solvent		PS	PSB-PEO (P3)
Non polar	HEX	-	-
	TOL	-	-
	Et <sub>2</sub> O	-	-
"Polar" aprotic	THF	-	-
	DCM	±	±
Polar aprotic	ACTN	±	±
	NMP	±	±
	ACN	-	±
	DMF	±	±
	DMSO	±	±
Polar protic	EtOH	-	-
	WATER	-	-

Soluble (+), partially soluble (±), insoluble (-), HEX= hexane, TOL= toluene, Et<sub>2</sub>O= diethyl ether, THF= tetrahydrofuran, DCM= dichloromethane, ACTN= acetone, NMP= *N*-methyl-2-pyrrolidone, ACN= acetonitrile, DMF= dimethylformamide, DMSO= dimethyl sulfoxide, EtOH= ethanol.

Characterization of Schiff bases along with processability has always been limited by the poor solubility in common solvents. Insolubility of the aromatic polyesterazomethines has been attributed to the rigid –CH=N– linkages or to the high molecular weight of the resulting macromolecules.<sup>61</sup> However, it is not simply due to the latter since even their low molecular weight structural Schiff base analogue compounds are equally insoluble in common organic solvents. Many attempts of solubilizing Schiff bases included dissolution in sulfuric or hydrofluoric acid involving hydrolyzation of the azomethine bond or electron donor-acceptor complexes of polymers with metal halide Lewis acids.<sup>62,63</sup> However these routes are

<sup>61</sup> Banerjee, S. and Saxena, C., Poly-Schiff bases. III. Synthesis and characterization of polyesterazomethines, *J. Polym. Sci. A Polym. Chem.*, **1996**, 34, 3565-3572.

<sup>62</sup> Jenekhe, S. A. and Johnson, P. O. Complexation mediated solubilization and processing of rigid chain and ladder polymers in aprotic organic solvents., *Macromolecules*, **1990**, 23, 4419-4429.

unsuitable as the breakage of the azomethine entity might lead to the disappearance of the redox activity and the Lewis acid-base complexation might interfere with the electrochemical performance.

From the point of view of an organic electrode material, being one of the main drawbacks of these kinds of materials the high solubility in organic solvents, which is responsible for the poor cycling performance and capacity fade, the intrinsic insolubility of the PSB could be considered an advantage rather than a drawback. However, the ultimate goal of the project, being the development of a redox active binder requires dissolving the polymer into a given solvent in order to get electrodes by conventional techniques while keeping poor solubility into the electrolyte.

### **3.3.2 Electrochemical performance**

The synthesis of PSB-PEO copolymers was optimized according to their electrochemical performance. For that reason, the products were tested as anode materials initially in powder electrodes only mixed with carbon. Later, on the search for a polymer capable of combining redox activity and binding properties, materials were tested as metal supported binder free anodes as detailed in the experimental section. Finally, the PSB-PEO copolymer was used as binder of other anode materials that exhibit higher capacities.

#### **3.3.2.1 Electrochemical performance of the PSB-PEO as active material**

##### **Optimization of the ratio between reactants and type of solvent**

The electrochemical performance of the PSB-PEO polymers prepared with different ratios of reactants and different solvents at a temperature close to their boiling point is shown in Figure 3.13. All samples showed a large first cycle irreversible capacity that can be attributed to electrolyte decomposition, SEI layer formation

---

<sup>63</sup> Yang, C.-J. and Jenekhe, S. A., Conjugated aromatic poly(azomethine). Characterization of structure, electronic spectra and processing of thin film from soluble complexes., *Chem. Mater.* **1991**, 3, 878-887.

and the intrinsic irreversible capacity corresponding to the conducting carbon additive. The use of a protic solvent like EtOH (P1) might, in principle, promote the condensation reaction shifting the electric charge of the carbonyl group resulting in larger capacity. However, when a non-polar solvent like TOL at 105 °C was employed, the reversible capacity of the resulting polymer (P2) was actually larger ( $158 \text{ mA}\cdot\text{h}\cdot\text{g}^{-1}$ ) than when using EtOH ( $116 \text{ mA}\cdot\text{h}\cdot\text{g}^{-1}$ ) and lower than when using DMF as solvent (P3), which provided  $178 \text{ mA}\cdot\text{h}\cdot\text{g}^{-1}$ . This, along with the stronger polarity of DMF compared to TOL and the fact that both lead to similar capacities, suggested that a high temperature is the key factor to force the completion of the reaction, which is responsible for better capacity values. Although TOL led to lower irreversible capacity than DMF (190 and  $256 \text{ mA}\cdot\text{h}\cdot\text{g}^{-1}$ , respectively) and despite showing less irreversible capacity is an important feature of an anode material in order to prevent the consumption of the  $\text{Na}^+$  from the cathode in a full-cell, the sample synthesized using DMF provided slightly larger and more stable reversible capacity in the subsequent cycles (Figure 3.13 b) For that reason, a 5:6:1 ratio of *p*-phenylenediamine, terephthalaldehyde and PEO in DMF at 150 °C (P3) was considered to be the optimal conditions since it achieved largest reversible capacity of  $256 \text{ mA}\cdot\text{h}\cdot\text{g}^{-1}$  with a 95 % of capacity retention after 25 cycles (C/15) and 89 % after 25 more cycles (C/10).

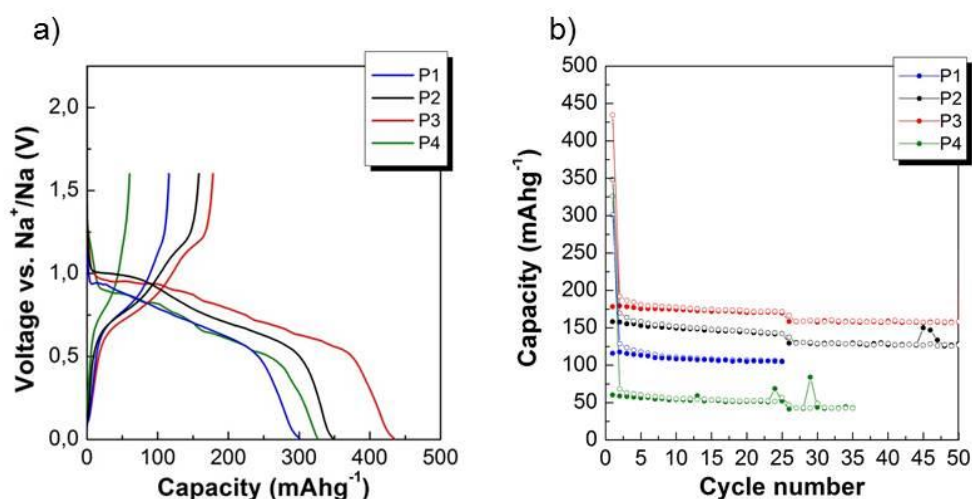


**Figure 3.13** Electrochemical performance of PSB-PEO600 polymers synthesized with different conditions of solvent, temperature and ratio between reactants for powder electrodes containing 80 wt. % PSB-PEO600 and 20 wt. % C65 and using 1M NaFSI MeTHF as electrolyte. a) Voltage profile of

the first charge and discharge at a current density of 19 mA/g and b) Rate capability at current densities of 19 mA·g<sup>-1</sup> equivalent to a C/10 rate (first 25 cycles) and 38 mA·g<sup>-1</sup> equivalent to a C/5 rate (next cycles).

In an attempt to further increase the processability of the polymer, the amount of PEO was increased up to a 25 % of the total moles (P4). However, the increase of the ratio between PEO and *p*-phenylenediamine came at the expense of lower reversible capacity: Capacities ranging from 115-178 mA·h·g<sup>-1</sup> were observed for those polymers prepared with less than 8 % of PEO (P1-P3) whereas a capacity of 67 mA·h·g<sup>-1</sup> was observed for P4. This suggests that the use of different solvents did not affect the reversible capacity as much as the amount of PEO inserted in the chain. This can be explained as the PEO block is non-active but contributes to the overall weight of the active material. Besides, the C=N bond formed by the condensation of the aldehyde with the amine group of the aliphatic PEO block might be less active than the azometine unit derived from the reaction between *p*-phenylene diamine and terephthalaldehyde.

Analogously to what happens to oligomeric Schiff bases<sup>21</sup> when the non-active central phenyl ring (-CH=N-Ph-N=CH-) is substituted by an ethylene unit (-CH=N-CH<sub>2</sub>-CH<sub>2</sub>-N=CH-), the insertion of PEO block might lead to the formation of several units (-CH=N-PEO-N=CH-) that, apart from being inactive, prevents the stabilizing effect derived from the  $\pi$ - $\pi$  interactions between phenyl groups. Therefore, even if an improved processability might be expected from the fact that P4 contains larger amount of PEO than P3, the better capacity of the latter makes it more promising in terms of electrochemical performance.

The differences in the capacity values (Table 3.10) observed might occur as a consequence of changes in the crystalline structures of the samples because crystallinity is known to play an important role on the volume changes suffered during sodiation and de-sodiation processes upon cycling.<sup>64</sup>

---

<sup>64</sup> Zhang, W.; Dahbi, M. and Komaba, S., Polymer binder: a key component in negative electrodes for high-energy Na-ion batteries, *Curr. Opin. Chem. Eng.*, **2016**, 13, 36-44.

**Table 3.10** Electrochemical parameters of PSB-PEO600 synthesized under different conditions of solvent and ratio between reactants

Electrochemical parameters							
	Ratio*	Solvent	Q <sub>r</sub>	Q <sub>i</sub>	C <sub>r25</sub>	1 <sup>st</sup> C <sub>e</sub>	C <sub>e</sub>
P1	4:4.8:0.8	EtOH	116	210	90	18	-
P2	4:4.8:0.8	TOL	158	190	89	45	12
P3	4:4.8:0.8	DMF	178	256	95	41	14
P4	2:4:2	DMF	60	240	87	38	15

\*Ratio among *p*-phenylenediamine, terephthalaldehyde and Jeffamine ED600®, Q<sub>r</sub> (1<sup>st</sup> cycle reversible capacity, mAh/g), Q<sub>i</sub> (irreversible capacity, mAh/g), C<sub>r</sub> (Capacity retention after 25 and 50 cycles, mAh/g), 1<sup>st</sup> C<sub>e</sub> (1<sup>st</sup> cycle coulombic efficiency, %), C<sub>e</sub> (cycle in which a 99% coulombic efficiency is reached).

As said above, the reflections of the PSB-PEO terpolymers showed small shifts to lower  $2\theta$  angles and slightly broader peaks than in PSB-PEO. This suggests that the insertion of PEO block produces an increase of the interplanar spacing in order to accommodate the voluminous chains. Among them, the sample containing the largest amount of PEO (P4) is also the one exhibiting smallest  $2\theta$  spacing probably due to greater expansion of the crystal structure in order to accommodate such a large amount of PEO (25 wt. %). However, no clear correlation was found between the crystalline features and the electrochemical performance since the sample showing largest  $2\theta$  spacing (P4) provides lowest capacity and the one providing largest capacity (P3) shows an intermediate  $2\theta$  spacing between that of P4 and those of P1 and P2. Even though the crystalline domains remain similar, different reaction conditions might be playing an important role on the electrochemical performance of the material as it might produce changes in the conjugation pathway leading to differences in the capacity.

All samples presented a remarkable cycling stability and coulombic efficiency after the first 5 cycles except for P4, the polymer containing largest amount of PEO. The coulombic efficiency is improved after a few cycles due to the so-called activation of the polymer by improving the wettability of the PSB-PEO on the electrolyte upon cycling.<sup>65</sup>

<sup>65</sup> Song, Z. and Zhou, H., *Energy Environ. Sci.*, **2013**, 6, 2280-2301.

In Figure 3.14, the  $\delta Q/\delta V$  vs. voltage curves of the PSB-PEO polymers are shown and compared to that of bare PSB. The  $\delta Q/\delta V$  or differential capacity plot is a measure of the relative change in capacity as a function of the voltage. The presence of a peak indicates that a redox process occurs at a given voltage. It can be observed that two different redox processes occur during the insertion and de-insertion of Na ions.

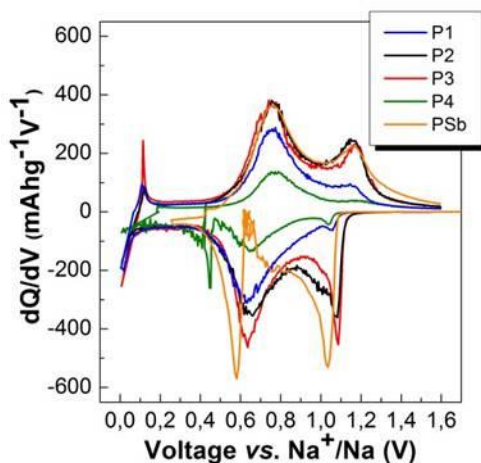
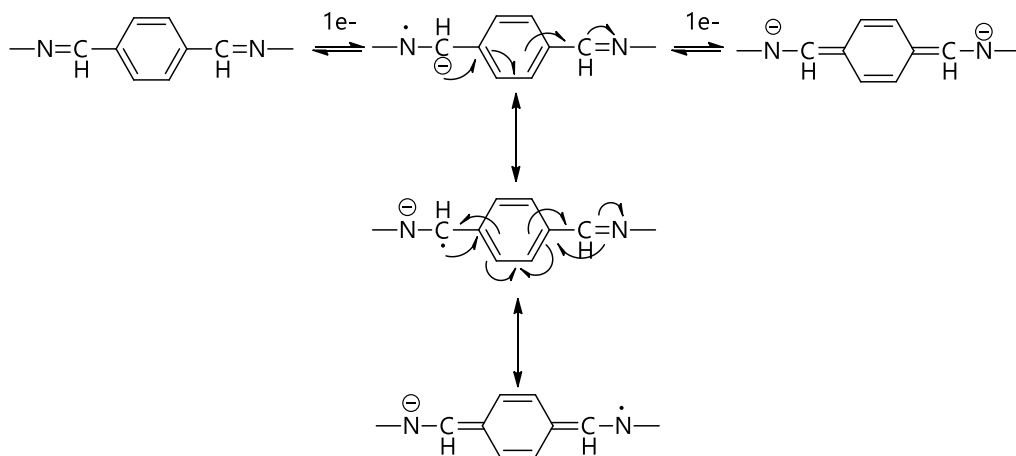


**Figure 3.14**  $\delta Q/\delta V$  vs. voltage curves of the second cycle of powder electrodes at a current density of  $19.7 \text{ mA}\cdot\text{g}^{-1}$  (C/10).

The redox peaks can be assigned to two successive one-electron reactions, as described by Martinet *et al.* for benzylideneaniline in DMF solution.<sup>66</sup> According to the mechanism proposed by them in which the first electron forms a radical anion in resonance between the azo and carbo radical and the second electron yields the dianion, the proposed mechanism of the PS base electrochemical reduction is depicted in Scheme 3.3.

<sup>66</sup> Martinet, P.; Simonet, J. and Tendil, J., Courbes intensité-potential de quelques bases de Schiff dans le diméthylformamide anhydre, *Comp. Rend. Sci. Chem. Serie C*, **1969**, T269, 303–305.



**Scheme 3.3** Mechanism of electrochemical reduction of the PSB.

During oxidation, the redox processes take place at the same voltage (0.76 and 1.16 V vs.  $\text{Na}^+/\text{Na}$ ) as those observed for the fully aromatic PSB prepared without PEO (PSB). However, during reduction PSB-PEO samples showed redox peaks (0.63 and 1.09 V vs.  $\text{Na}^+/\text{Na}$ ) centered at higher voltage than PSB (0.59 and 1.04 V vs.  $\text{Na}^+/\text{Na}$ ), which implies lower hysteresis

In principle, the insertion of PEO into the polymeric chain should result in a decrease of the voltage due to a decrease of the conjugation. The decrease of the conjugation might be expected from the fact that the insertion of PEO might change the spatial conformation of the C=N bond. Castillo-Martínez *et al.* demonstrated that the (-N=CH-Ph-HC=N-) active unit in polySchiff bases is electrochemically active whereas the reverse unit, although isoelectronic (-CH=N-Ar-N=CH) is not. This difference arises from the change of the spatial conformation of the C=N double bond. In the active (-N=CH-Ph-HC=N-) unit, the aniline ring is twisted out of the C-N=C-C plane and the benzylidene ring also lies out of the plane with a smaller and opposite twist.<sup>67</sup> This conformation in which the Ph-CH=N lays in the same plane allows the interaction between the two nonbonding electrons on N atoms with  $\text{sp}^2$  hybridization and the  $\pi$  electrons of the benzene ring improving the conjugation. Later, López-Herraiz *et al.*<sup>21</sup> also confirmed the importance of the co-planarity of the analogous 10- $\pi$  electrons Hückel units of

oligomeric Schiff bases. They proved by DFT calculations Ph-N=C units are non-planar and no-conjugated whereas the Ph-CH=N units are planar and  $\pi$ -conjugated. However, although the aniline ring is not conjugated in the Ph-C=N plane, it was also reported that when two electron-donor methyl groups are introduced on the aniline ring of a PS, the voltage shifts down by 0.1–0.2 V meaning that it plays, somehow, a role. For that reason, the substitution of the aniline ring by PEO might with affect the redox voltage. On the other hand, the shift of the redox peaks of the PSB-PEO might be indicative of a gain in stability of the intercalates due to the strong solvation of Na<sup>+</sup> in the presence of PEO blocks. Alternatively, the expanded  $\pi$  spacing could also favor the intercalation of Na<sup>+</sup> ions leading to a higher reduction voltage. In any case, the increase of the reduction voltage implies less hysteresis in the PSB-PEO than in the PS and is beneficial in the event of using the material in a full-cell because it would provide higher energy density. The reason why the oxidation peak is kept at the same voltage for both PSB and PSB-PEO remains unclear.

Apart from the voltage of reduction there are also changes in the relative intensities of both redox peaks. The redox peak at 1.09 V vs. Na<sup>+</sup>/Na during reduction decreases enormously when the polymer was prepared using EtOH as solvent (P1) whereas the low voltage reduction (0.6 V vs. Na<sup>+</sup>/Na) remains the same. When the synthesis is performed in DMF with a large ratio of PEO (P4) the intensities of both redox peaks during reduction decreased with respect to those of P3 indicating that the sodium insertion is hindered. On the other hand, the intensities of the signals during oxidation are comparable for the polymers prepared in TOL (P2) or DMF (P3) despite larger insertion is observed for the latter. In view of the electrochemical results, synthesis conditions deployed for P3 (reacting in DMF at 150 °C and containing 8 mol % of PEO) are the optimal ones.

### **Choice of the size of the PEO linker**

The evolution of the capacity vs. cycle number for PSB-PEO synthesized with PEO blocks of different molecular weight is shown in Figure 3. 15 a. Despite the XRD

---

<sup>67</sup> Traetteberg, M. and Hilmo, I., The molecular structure of N-benzilidene aniline, *J. Mol. Struct.*, **1978**, 48, 395–405.



patterns showed no differences between them, confirming that they have similar crystalline domains, the weight of PEO clearly influences the electrochemical performance of the polymers. This suggests that the synthesis conditions, which do influence the peak positions on the XRD pattern, have a greater impact on the polymer structure than the size of the PEO block. As expected, the use of PEO block with increasing molecular weights (600, 900, 2000 g·mol<sup>-1</sup> leading to P3, P5 and P6 respectively) translated into lower reversible capacities (175, 125 and 100 mA·h·g<sup>-1</sup> respectively). Apart from showing the best capacity retention (95 % after 25 cycles), the sample containing PEO of 600 g·mol<sup>-1</sup> (P3) was the only one that reached coulombic efficiency values close to 99% (in the 14<sup>th</sup> cycle). The coulombic efficiencies of P5 and P6 were found to be always below 98%.

In Figure 3. 15 b, the  $\delta Q/\delta V$  curves for the second reduction and oxidation of P3, P5 and P6 are compared. As happened for P1-P4, PSB and PS showed redox peaks at the same voltage during oxidation (0.76 and 1.17 V vs. Na<sup>+</sup>/Na), whereas during reduction redox activity takes place at higher voltages for PSB-PEO (1.09 and 0.63 V vs. Na<sup>+</sup>/Na) than for PS (1.04 and 0.59 V vs. Na<sup>+</sup>/Na). On the other hand, it was observed that an increase of molecular weight of the PEO block produced a noticeable decrease of the intensity in the  $\delta Q/\delta V$  peaks during reduction and oxidation, especially for those peaks corresponding to the redox process at 1.09 V. This indicated that increasing the molecular weight of the PEO did not only decrease the specific capacity due to the increase of deadweight with no contribution to the capacity, but it also modified the mechanism of the reduction reaction, since two different one-electron processes are not observed anymore.

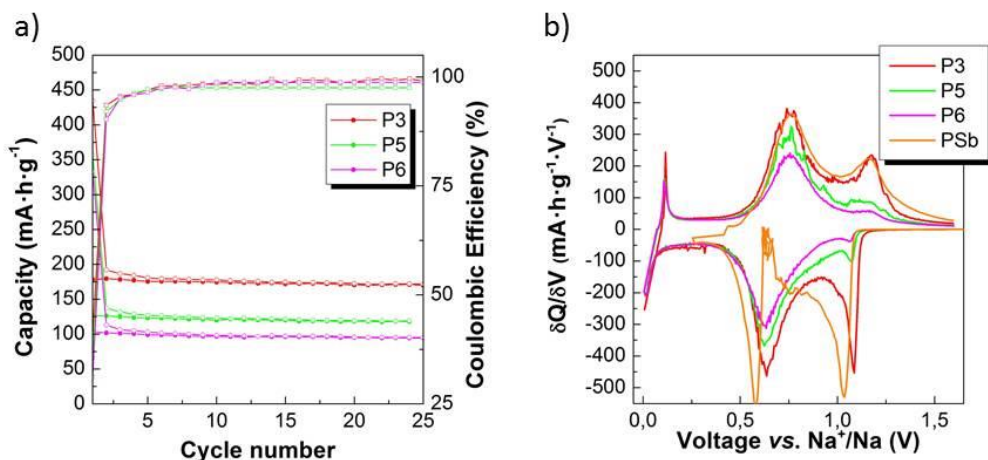


**Figure 3.15** a) Cycle life of powder electrodes containing 20 wt. % C65 and 80 wt. % PSB-PEO. b) Differential capacities of the samples synthesized with PEO blocks of different molecular weights.

The electrochemical properties are summarized in Table 3.11

**Table 3.11** Electrochemical properties of PSB-PEO synthesized with Jeffamines (PEO blocks) of different molecular weight.

Sample	PEO M.W. (g·mol <sup>-1</sup> )	Electrochemical parameters				
		Q <sub>r</sub>	Q <sub>i</sub>	C <sub>r,25</sub>	1 <sup>st</sup> C <sub>e</sub>	C <sub>e</sub>
P3	600	178	257	95	41	14
P5	900	128	229	82	35	-
P6	2003	103	230	91	31	-

Q<sub>r</sub> (1<sup>st</sup> cycle reversible capacity, mAh/g), Q<sub>i</sub> (irreversible capacity, mAh/g), C<sub>r</sub> (Capacity retention after 25 and 75 cycles, mAh/g), 1<sup>st</sup> C<sub>e</sub> (1<sup>st</sup> cycle coulombic efficiency, %), C<sub>e</sub> (cycle in which a 99% coulombic efficiency is reached).

### Effect of the temperature of synthesis

Given the good electrochemical performance of PSB-PEO600, the effect of the temperature of synthesis was further studied with the aim of controlling the tendency of PEO block to be inserted in the polymeric chain. Due to huge steric hindrance, PEO block may react much slower with terephthalaldehyde than *p*-phenylenediamine so, in order to boost reaction between the PEO block and the aldehyde, the reaction between them was carried out at high temperature whereas then the addition of the *p*-phenylenediamine was performed at room temperature

to avoid reequilibration of the Schiff-Base bond and the exclusion of the PEO groups from the copolymer

In Figure 3.16 a, the capacity vs. cycle number of powder electrodes of the polymers synthesized in two steps at different temperatures is shown.

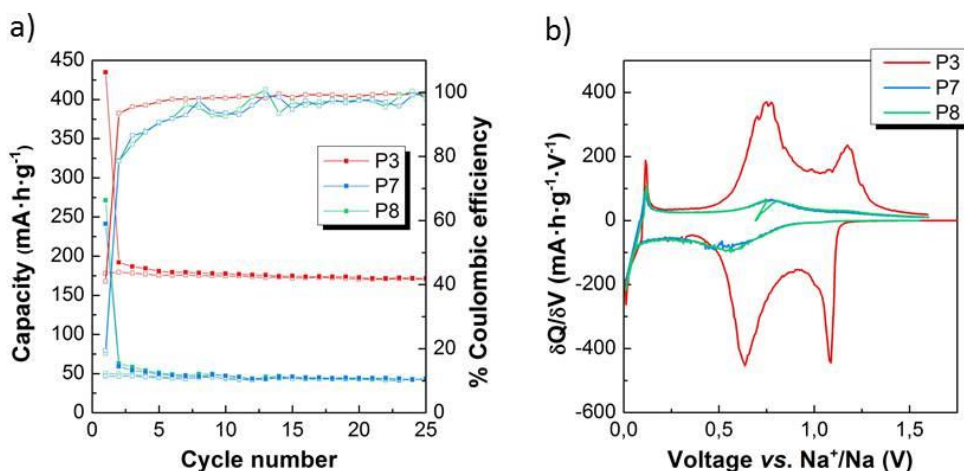


**Figure 3.16** a) Capacity vs. cycle of samples synthesized at different temperatures. (Capacities referred to the active mass for an 80:20 PSB-PEO600: C65 ratio for powder electrodes). b) Differential capacity vs. voltage of samples synthesized at different temperatures.

When the synthesis is performed in two steps being the first one (reaction between PEO and terephthalaldehyde) at 150 °C and the second (addition of *p*-phenylenediamine) at room temperature (P7), the capacity observed (50 mA·h·g<sup>-1</sup>) is the same to that of the synthesis performed in two steps at room temperature (P8). The capacity of these two polymers (P7 and P8) was much smaller than that of the polymer synthesized at 150 °C. In Figure 3.16 b, the  $\delta Q/\delta V$  plots of the three samples are depicted. The poor capacity provided by P7 and P8 can be ascribed to the lack of activity of the resulting polymers and might be provided by the C65, which can insert Na<sup>+</sup> ions at a voltage below 0.8 V and close to 0 V vs. Na<sup>+</sup>/Na in the cycling conditions. (Figure 3.17)

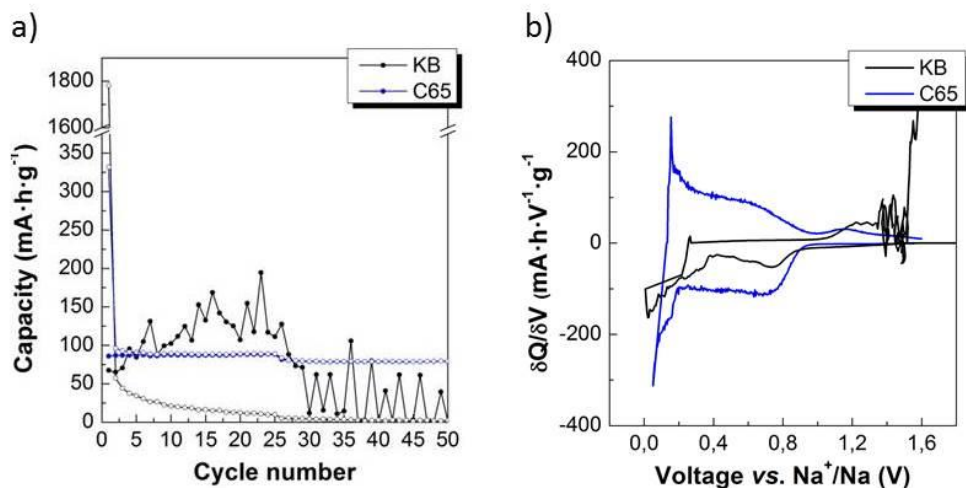


**Figure 3.17** a) Galvanostatic cycling of C65 and KB conductive carbons in powder electrodes of KB and C65 conductive carbons (at C/10 rate calculated on the basis of a theoretical capacity of  $372 \text{ mA}\cdot\text{h}\cdot\text{g}^{-1}$ ). b) Differential capacity vs. voltage of C65 and KB in the same conditions.

The redox peak at 1.09 V during reduction is not even expressed whereas the one at 0.65 V vs.  $\text{Na}^+/\text{Na}$  is observed with extremely low intensity. This suggests that although the XRD and FTIR of P7 and P8 showed no differences with respect to P3, and considering that when solvents that reached lower boiling temperatures than DMF (150 °C) led to lower capacities, performing both steps or the second step of the synthesis at room temperature might not provide enough Schiff bases entities so as to get acceptable capacity values.

In the table below the above described electrochemical parameters are summarized.

**Table 3.12** Electrochemical parameters of PSB-PEO synthesized with Jeffamine ED600 in two steps at different temperature when cycling powder electrodes.

Electrochemical parameters							
Entry	T(°C)		Q <sub>r</sub>	Q <sub>i</sub>	C <sub>r25</sub>	1 <sup>st</sup> C <sub>e</sub>	C <sub>e</sub>
	1 <sup>st</sup> step	2 <sup>nd</sup> step					
1	150	150	178	257	89	41	14
2	150	25	48	193	71	19	13
3	25	25	50	221	60	18	13

$Q_r$  (1<sup>st</sup> cycle reversible capacity, mAh/g),  $Q_i$  (irreversible capacity, mAh/g),  $C_r$  (Capacity retention after 25 and 75 cycles, %), 1<sup>st</sup>  $C_e$  (1<sup>st</sup> cycle coulombic efficiency, %),  $C_e$  (cycle in which a 99% coulombic efficiency is reached).

### Optimization of the electrode processing

After an initial screening of the best synthesis conditions, powder electrode composition was optimized for P3, the polymer exhibiting best electrochemical performance.

In Figure 3.18, the voltage profiles of the first cycle of P3 powder electrodes processed with different ratios of two different types of conductive carbon (KB and C65) are shown.

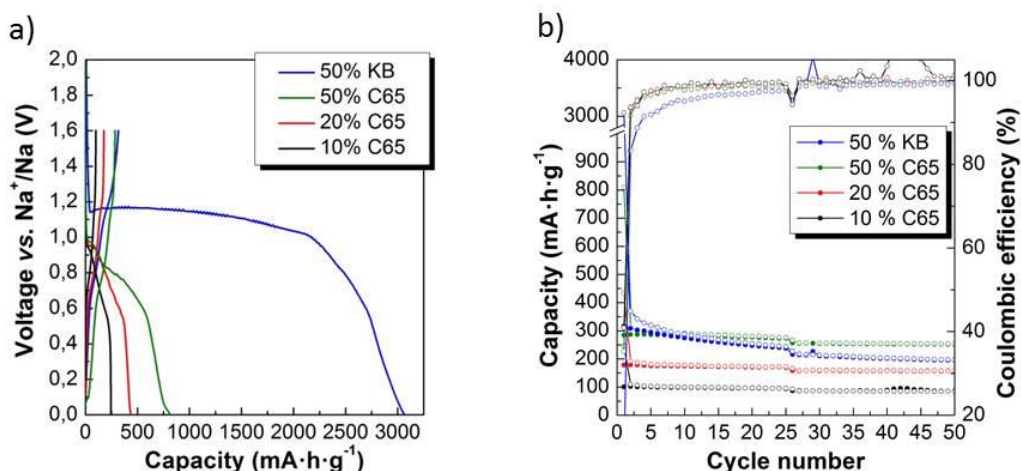


**Figure 3.18** a) Voltage-capacity profile of the first cycle of powder electrodes of P3 (19.7 mA·g<sup>-1</sup>) with different percentages of conductive carbon. b) Capacity vs. cycle number of powder electrodes of P3 at a cycling rate of 19.1 mA·g<sup>-1</sup> for the first 25 cycles and 39 mA·g<sup>-1</sup> for the next 25 cycles.

As expected, given the electronically insulating nature of the PSB-PEO as well as the Na insertion of the conductive carbon itself, the presence of a larger amount of carbon on the electrode led to larger reversible capacity. The largest reversible capacity was observed when a 50 wt. % of KB and C65 were employed. They yielded 316 mA·h·g<sup>-1</sup> and 285 mA·h·g<sup>-1</sup> respectively. Likewise, the use of 20 wt. % of C65 provided larger capacity (178 mA·h·g<sup>-1</sup>) than the use of 10 wt. % of C65 (100 mA·h·g<sup>-1</sup>). Despite providing larger reversible capacity, the use of high surface area KB was

discarded due to the enlargement of the first cycle irreversible capacity and poor cycling stability (Figure 3.17).

The electrochemical performance of the polymers was next evaluated in laminate form. Taking into account that the use of C65 provided the best trade-off between a large reversible capacity and low the irreversible capacity, laminate electrodes containing 20 % wt. of that conductive carbon were prepared. Thanks to the incorporation of PEO groups into the polymer, their processability in terms of solubility and flexibility was improved, so it was possible to cast the polymer onto a foil without the need of any extra binder. Slurries were prepared with 80 : 20 wt. % ratio between PSB-PEO and C65.

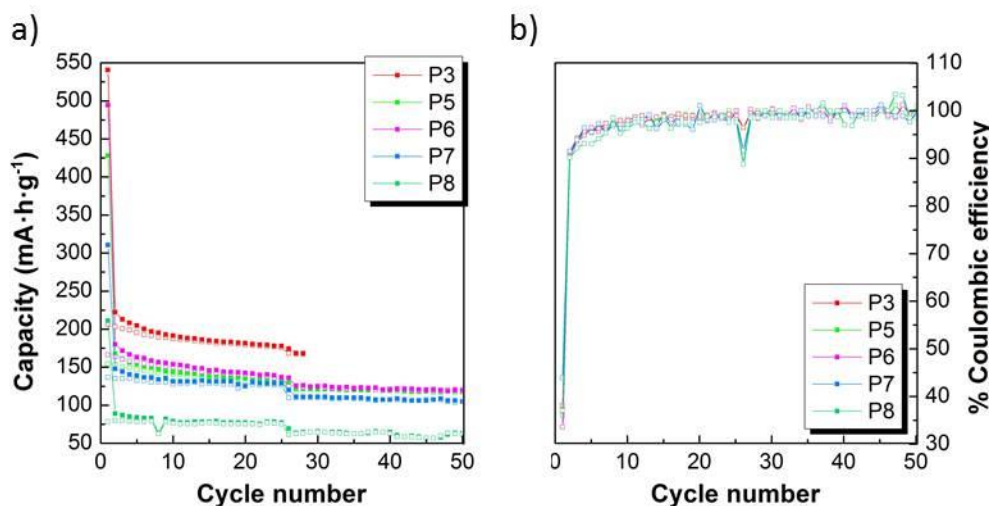


**Figure 3.19** Comparison of the electrochemical performance of binder-free laminated electrodes of PSB-PEO in Cu foil containing 20 wt. % of C65 at a C/10 rate (first 25 cycles) and at C/5 (next 25 cycles). a) Capacity vs. cycle and, b) coulombic efficiency vs. cycle.

According to the reversible capacity, performing the two steps of the synthesis at 150°C (P3) provided the largest capacity value (205 mA·h·g<sup>-1</sup>), as it happened when testing the performance in powder electrodes. When the second step is carried out at room temperature (P7) much less capacity was observed (137 mA·h·g<sup>-1</sup>) whereas performing both steps at room temperature (P8) provided only 78 mA·h·g<sup>-1</sup>. The fact that the electrochemical performance of the three polymers synthesized at different temperatures differs from that observed for powder electrodes of the same composition (178 mA·h·g<sup>-1</sup>, 48 mA·h·g<sup>-1</sup> and 50 mA·h·g<sup>-1</sup> of reversible capacity for P3,

P7 and P8 respectively) might be indicative of an improvement of the interparticle contact in laminated electrodes. Contrary to what was observed for powder electrodes, in which the increase of the molecular weight of the PEO translates into a decreased capacity, for laminate electrodes P6 (PEO 2000  $\text{g}\cdot\text{mol}^{-1}$ ) showed an improved capacity ( $166 \text{ mA}\cdot\text{h}\cdot\text{g}^{-1}$ ) over P5 (PEO 900  $\text{g}\cdot\text{mol}^{-1}$ ), which provided  $155 \text{ mA}\cdot\text{h}\cdot\text{g}^{-1}$  of reversible capacity. This unexpected feature will be further discussed.

### Powder vs laminate electrode performance

Apart from reversible capacity, other important electrochemical parameters when designing an electrode material are coulombic efficiency, capacity retention and first cycle coulombic efficiency. The comparison between the performance in powder and laminate electrodes is shown in Figure 3.20 and the values are summarized in Table 3.13.

**Table 3.13** Comparison of the electrochemical properties of powder (P) and laminated (L) electrodes containing 20 wt. % of C65: first cycle reversible capacity ( $Q_{\text{rev}}$ ), first cycle irreversible capacity ( $Q_{\text{irr}}$ ), % capacity retention after 25 cycles ( $Cr_{25}$ ) and first cycle coulombic efficiency (C. E.)

Sample	$Q_{\text{rev}}$ (P) $\text{mAh}\cdot\text{g}^{-1}$	$Q_{\text{rev}}$ (L) $\text{mAh}\cdot\text{g}^{-1}$	$Q_{\text{irr}}$ (P) $\text{mAh}\cdot\text{g}^{-1}$	$Q_{\text{irr}}$ (L) $\text{mAh}\cdot\text{g}^{-1}$	$Cr_{25}$ (P) $\text{mAh}\cdot\text{g}^{-1}$	$Cr_{25}$ (L) $\text{mAh}\cdot\text{g}^{-1}$	C.E. (P) $\text{mAh}\cdot\text{g}^{-1}$	C.E. (L) $\text{mAh}\cdot\text{g}^{-1}$
P3	178	206	257	335	95	85	41	38
P5	128	154	229	274	82	78	35	36
P6	103	166	230	357	91	75	31	34
P7	48	137	193	310	71	93	19	44
P8	50	78	221	132	60	96	18	37

For every sample, laminated electrodes provided larger reversible capacities than their powder counterparts. The irreversible capacity, which translates into an over-expenditure of  $\text{Na}^+$  ions of the cathode in an eventual full cell, is also increased when using laminated electrodes (except for P8). However, the first cycle coulombic efficiency, which represents a ratio between the first cycle reversible and irreversible capacity is maintained at the same value for either laminate or powder or even improved for laminates because of the fact that the increase of the irreversible capacity is accompanied by an increase of the reversible capacity. The capacity retention is affected by lamination evidencing that the mechanical properties of the laminates are still far from being good enough to endure cycling.

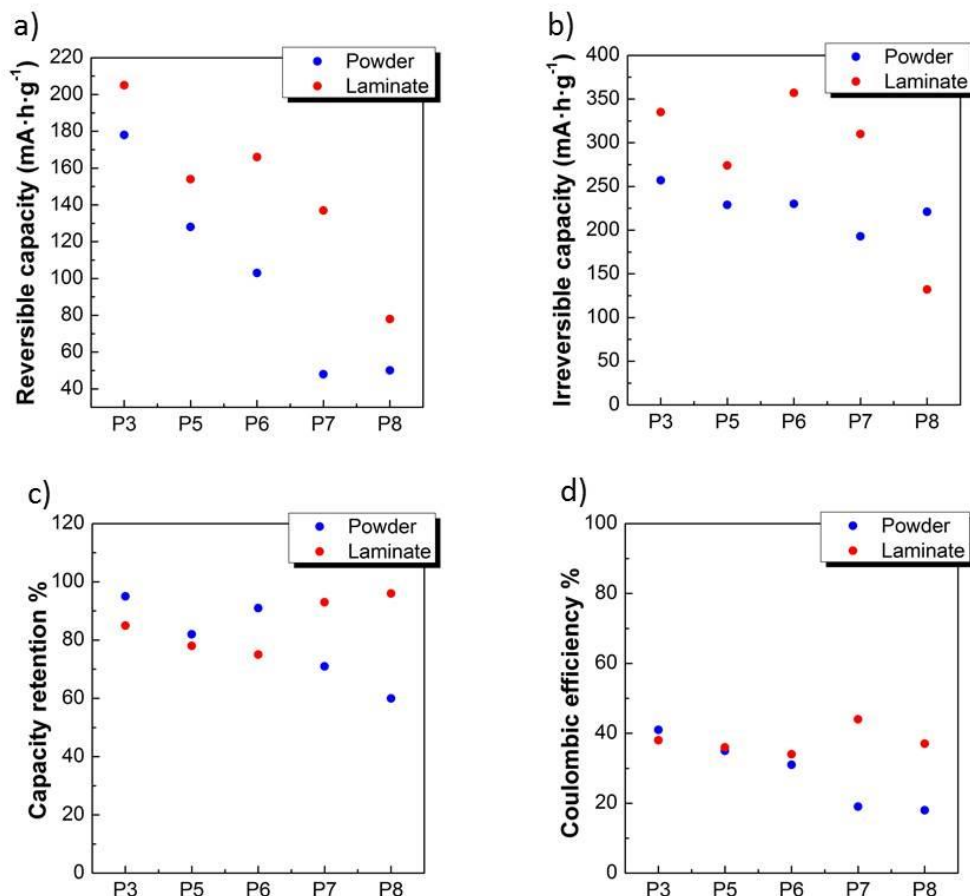


**Figure 3.20** Electrochemical properties of powder and laminated electrodes containing 20 wt. % of C65. a) First cycle reversible capacity, b) First cycle irreversible capacity, c) % Capacity retention after 25 cycles and, d) First cycle coulombic efficiency.

The fact that P6, which has a PEO block of higher molecular weight than P5, led to larger reversible capacity can be explained in view of the differential capacity vs. voltage plot (Figure 3.21 a) which shows an increased redox activity due to C65 in P6 electrodes with respect to P5. Despite P5 and P6 showed comparable intensities of the redox peaks related to the PSB-PEO activity (at 0.63 and 1.09 V vs. Na<sup>+</sup>/Na) in the second cycle, the low voltage peak close to 0 V vs. Na<sup>+</sup>/Na, related to the Na<sup>+</sup> insertion into the C65, is more intense for P6. This suggests that the larger amount of PEO allows faster Na<sup>+</sup> diffusion and therefore more activity at low voltages (C-65) before plating. Therefore, as the total activity can be built as the sum of the activity



coming from the PSB-PEO and from the C65, the reversible capacity was found to be larger if the activity of C-65 improved.

The activity of C-65 also explains the fact that the laminate electrodes provide larger capacity than powder electrodes. As observed in Figure 3.21 a and c, where differential capacities of the second cycle of laminate and powder electrodes respectively are shown, the redox peaks concerning  $\text{Na}^+$  insertion into the C65 are much more intense in laminates than in powder electrodes. This might be attributed to a better interparticle contact achieved when the electrode is casted onto a metallic foil, which seems to be critically important when there are redox processes at voltages close to the voltage cutoff as discussed in previous chapter.

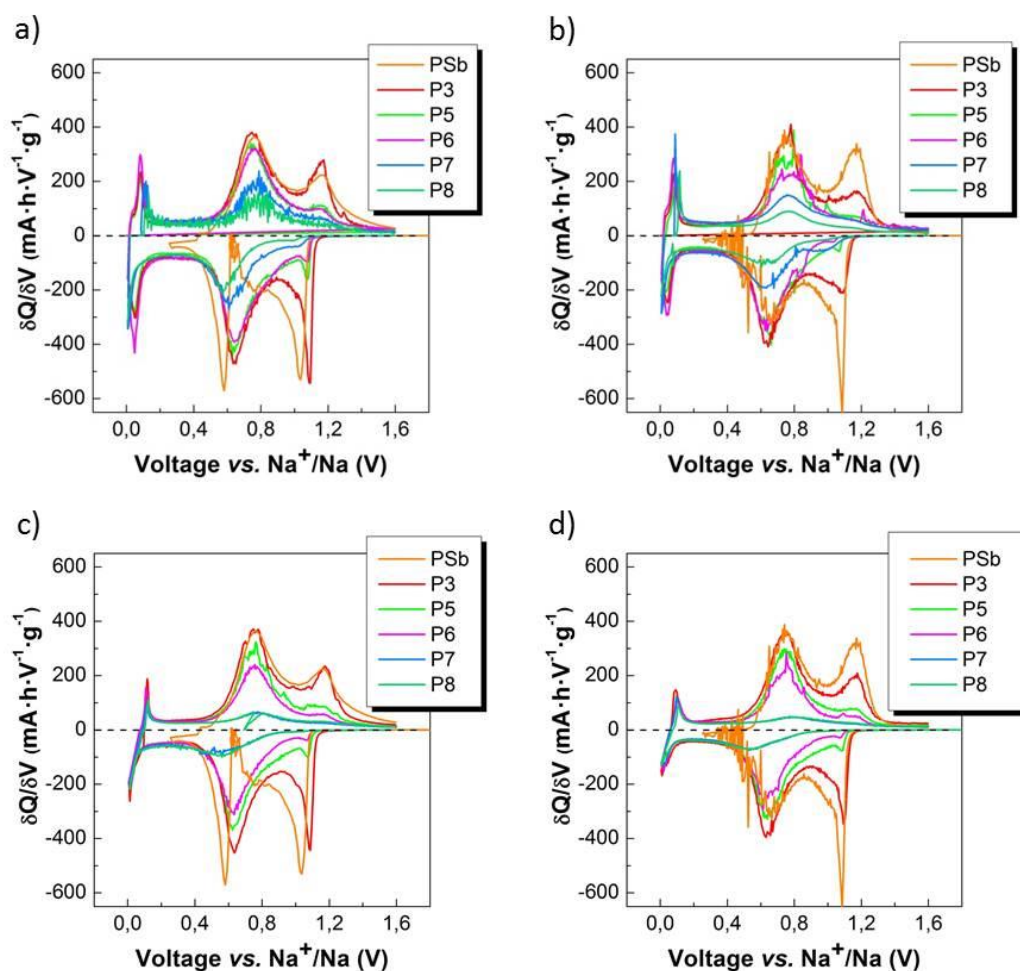


**Figure 3.21** Differential capacity vs. voltage of PSB-PEO polymers and of PSb (powder electrode) at C/10 rate in the a) 2<sup>nd</sup> cycle in binder-free laminate electrodes and b) 25<sup>th</sup> cycle in binder-free laminate electrodes, c) 2<sup>nd</sup> cycle in powder electrodes and d) 25<sup>th</sup> cycle in powder electrodes.

In P3, P5 and P6 the capacity retention was poorer in laminate than in powder electrodes. It seems to be related to the decrease in intensity of the redox peak at 1.09 V vs. Na<sup>+</sup>/Na during reduction in laminate electrodes because despite the peak at 0.63 V remained more or less the same intensity after 25 cycles, the peak at 1.09 V was drastically reduced in P3 and P5 and it even disappeared in P6. (Figure 3.21) The intensity ratio between the peaks at 0.63 and 1.09 V vs. Na<sup>+</sup>/Na during reduction in powder electrodes is kept more or less constant after 25 cycles. For that reason, the capacity retention is better in powder electrodes. For P7 and P8, on the contrary, showing much less redox activity, the intensity of both peaks is kept after cycling and, therefore, the capacity retention value is close to 100 %. This improvement in the capacity retention is crucial in order to extend the cycle life of the battery; however, it is useless as long unless it is accompanied by a moderate reversible capacity. In view of the general properties of all the polymers, P3 was set as optimum material because it showed largest reversible capacity along with better capacity retention and first cycle coulombic efficiency.

Next step was the optimization of the composition of the binder-free electrodes for P3. To do so, two different carbon contents were tried (10 and 20 wt. %) in two different metallic foils (Cu and Al). Figure 3.22 shows the galvanostatic cycling of P3 electrodes of different compositions and Table 3.14 summarizes the electrochemical parameters.

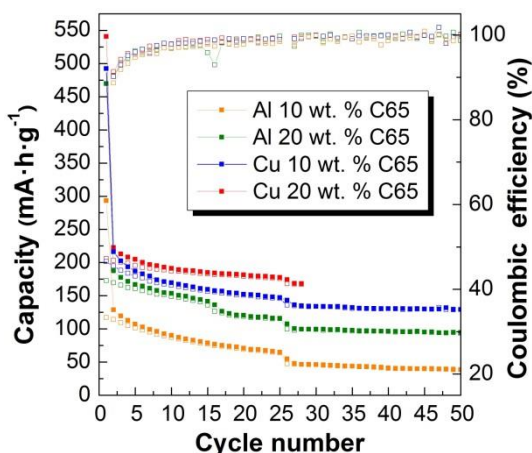


**Figure 3.22** Galvanostatic cycling of P3 binder-free laminated electrodes onto Cu or Al foil containing variable amounts of C65 (10–20 wt. %) First 25 cycles were cycled at a C/10 rate and next 25 cycles at C/5.

**Table 3.14** Summary of the electrochemical parameters of binder free laminated electrodes of P3 onto Cu or Al foil

<b>C65</b> (wt.%)	<b>Foil</b>	<b>Q<sub>rev</sub></b> mAh·g <sup>-1</sup>	<b>Q<sub>irr</sub></b> mAh·g <sup>-1</sup>	<b>Cr<sub>25</sub>(P)</b> mAh·g <sup>-1</sup>	<b>C.E. (P)</b> mAh·g <sup>-1</sup>
10	Al	117	176	55	40
20	Al	173	297	67	37
10	Cu	201	291	72	41
20	Cu	<b>206</b>	335	<b>85</b>	38

Despite the use of Al foil as current collector for Na ion batteries is desirable in terms of cost savings and reduction of the weight, smaller capacities were observed compared to Cu foil. This fact might be ascribed to a better adhesion of the polymer to Cu foil rather than to the Al. In principle, larger reversible capacity should be expected for those electrodes containing larger content of active material. However, the fact that those electrodes containing 20 wt. % C65 (173 and 206 mA·h·g<sup>-1</sup> for Al and Cu respectively) provide larger capacity than their analogues containing 10 wt. % (117 and 201 mA·h·g<sup>-1</sup> for Al and Cu respectively) may be indicative that the presence of conductive C65 is crucial to get the most out of the PSB-PEO's performance. The electrochemical performance of the polymer, being electronically insulating, might specially benefit from the presence of a larger amount of conductive additive that helps with electron conduction. On the other hand, as previously explained, the ability of the C65 to insert sodium at the cycling conditions provides extra capacity. This can be corroborated by Figure 3.23, where  $\delta Q/\delta V$  curves of the 2<sup>nd</sup> and 25<sup>th</sup> cycles of binder-free electrodes are shown.

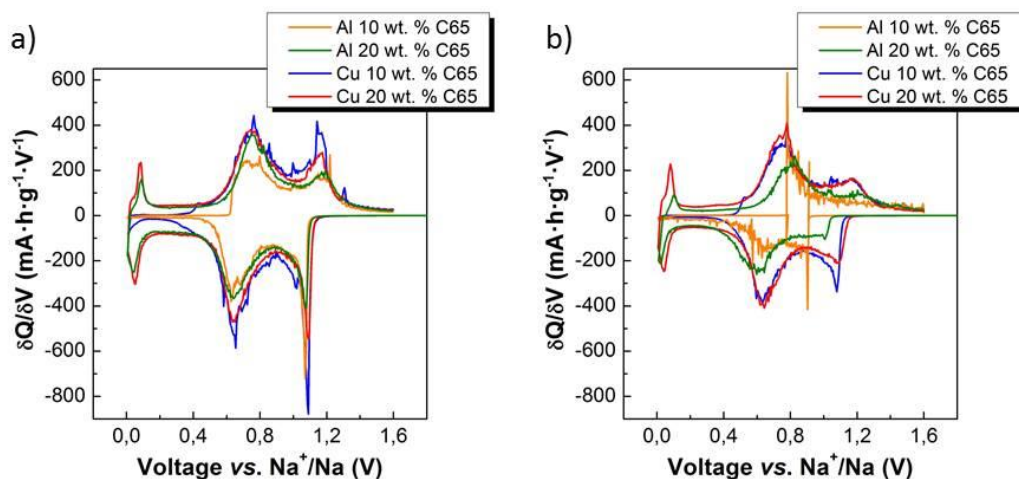


**Figure 3.23** Differential capacity vs. voltage of the second cycle (a) and 25<sup>th</sup> cycle (b) binder free electrodes laminated onto Cu or Al foil with different amounts of C65 (10-20 wt. %)

Actually the Cu supported electrode containing 10 wt. C65 shows more intense redox peaks related to PSB-PEO (at 0.63 and 1.09 V vs. Na<sup>+</sup>/Na) than the one containing twice the amount of C65, but the capacity of the latter is larger because of the contribution of the carbon to the capacity. This contribution can be confirmed in view of the intense redox peak close to 0 V vs. Na<sup>+</sup>/Na related to Na<sup>+</sup> ion insertion into the carbon. Analogously, and considering that the PSB-PEO redox peaks appear to be similar, the electrode that had been casted in Al containing 20 wt. % of C65 showed improved capacity (173 mA·h·g<sup>-1</sup>) with respect to the one containing half of the C65 (117 mA·h·g<sup>-1</sup>) due to contribution of the carbon. After 25 cycles, the PSB-PEO redox peaks of all the electrodes are downsized and as a result, the electrodes suffer capacity fade. It is also noteworthy that the oxidation redox peaks of the sample that was casted onto Al and contains 20 wt. % were shifted to larger voltage whereas reduction peaks were shifted to smaller values increasing the hysteresis between charge and discharge. The fact that the C65 is able to reversibly insert C65 after 25 cycles providing capacity, cushions the impact that might have on the reversible capacity the decrease of the redox activity of the PSB-PEO. After the optimization, P3 as a binder-free electrode provided 206 mA·h·g<sup>-1</sup> of reversible capacity, 335 mA·h·g<sup>-1</sup> of first cycle irreversible capacity with an 85 % of capacity retention after 25 cycles at C/10.

*Postmortem* analysis was carried out to analyse the integrity of the laminated electrodes after repeated cycling. The SEM micrographs of electrodes of P3 (pristine and after being galvanostatically cycled 25 times) revealed that the tested electrodes maintained their original shape without observing any cracking nor pulverization. (Figure 3.24) Wrinkles were formed as a consequence of the electrode manipulation but the polymer particles remain attached forming a film. The absence of delamination is indicative of the apparent good binding properties of the polymer.

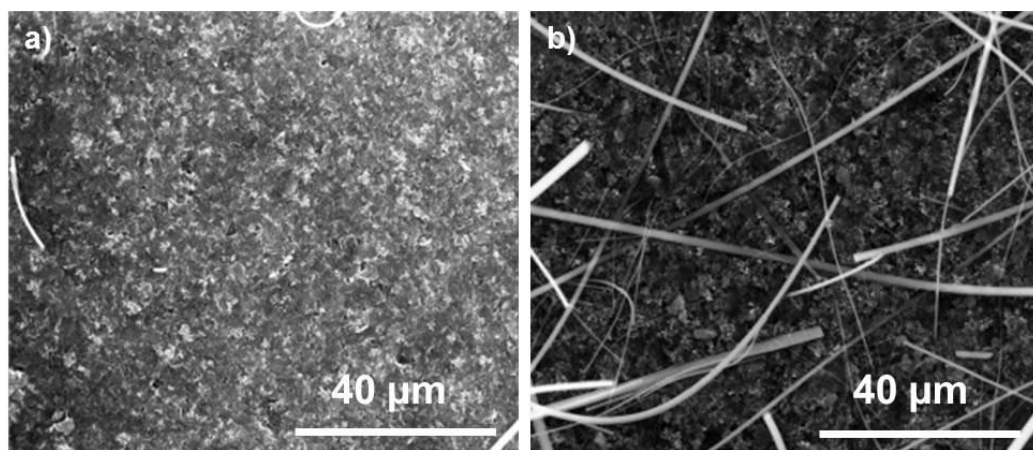


**Figure 3.24** Electrodes containing P3 and 20 wt. % of C65, pristine (a) and after 25 cycles (b) Note that fibers in the already cycled electrodes are due to glass fiber separator.

### 3.3.2.2 Electrochemical performance of PSB-PEO as binder

The use of a polymer like PSB-PEO that can provide binding properties along with reversible electrochemical activity might help to improve the capacity of the electrode. The polymer exhibiting best electrochemical performance in binder-free electrodes was chosen in order to be tested as binder of several active materials such as high capacity commercial Sn nanoparticles, low cost carbons (PVC derived soft carbon and sugar derived hard carbon), and electrolyte compatible novel metal carbodiimides (Zn carbodiimides). Despite there are many binders with specific features like CMC, PAA or PVA, the resulting electrochemical performance of the PSB-PEO as binder will be compared to that of PVdF, one of the most widespread used commercial binder as well as to PAA in the case of Sn.

### PSB-PEO and commercial Sn nanoparticles composites

Sn was selected for being one of the materials reported showing largest gravimetric theoretical capacity ( $847 \text{ mA}\cdot\text{h}\cdot\text{g}^{-1}$  for the most sodiated  $\text{Na}_{15}\text{Sn}_{14}$  phase). Therefore, it was expected that the use of a small fraction of Sn in a PSB-PEO electrode, would increase the overall capacity of the electrode and, at the same time, PSB-PEO as a flexible polymer matrix, would inhibit the huge volume changes that Sn based electrodes suffer during alloying and dealloying. In Figure 3.25, the electrochemical performance of commercial Sn nanoparticles bound with a 10 wt. % PVdF or PAA/sodium alginate (50:50 wt.) in the presence of 10 wt. % of C65 is represented. None of the two binders prevents the electrode from showing huge capacity decay due to repeated expansion and contraction of the material in order to accommodate and release sodium ions during reduction and oxidation. The mechanical stress leads to pulverization of the material (loss of interparticle contact and detachment from the Cu foil).

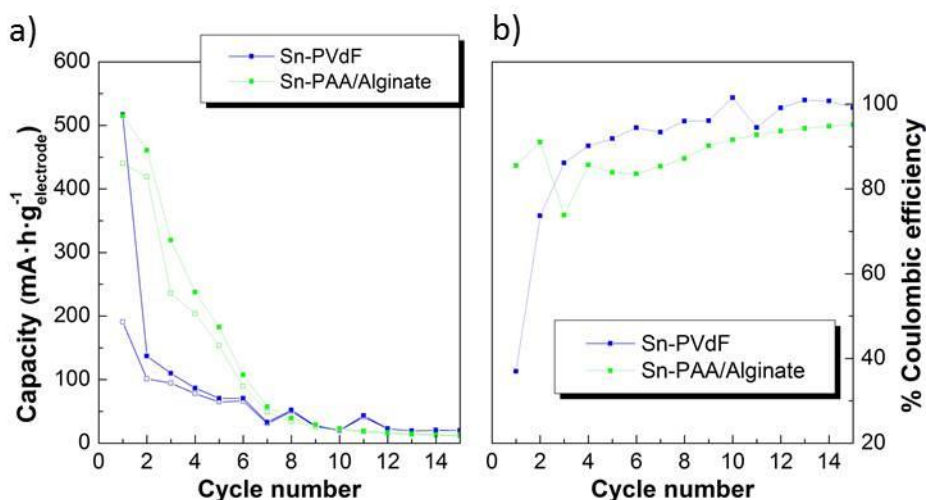


**Figure 3.25** a) Galvanostatic cycling of commercial Sn nanoparticles bound with PVdF or a mixture (50:50 wt.) of PAA and alginate at a cycling rate of  $C/10$ . b) Coulombic efficiency of the same measurement.

Despite relatively large reversible capacities can be observed in the very first cycles ( $440 \text{ mA}\cdot\text{h}\cdot\text{g}^{-1}$  and  $190 \text{ mA}\cdot\text{h}\cdot\text{g}^{-1}$  for PVdF and PAA/Alginate binders respectively), they are still far from the theoretical value ( $847 \text{ mA}\cdot\text{h}\cdot\text{g}^{-1}$ ). Besides, poor coulombic efficiency and capacity retention values were observed (7 % and 2% of capacity

retention after 25 cycles respectively). This demonstrates that the electrode processing is crucial to take the full advantage of the capacity of the material. The poor coulombic efficiency observed for Sn/PSB-PEO600 composites and Sn nanoparticles bound with PAA-Alginate suggested that sodiation/desodiation transitions are kinetically limited. Lower charge rates (C/50) should have been used to provide enough time for reactions to be complete. In Figure 3.26, the  $dQ/dV$  curves of the second cycle two measurements are shown.

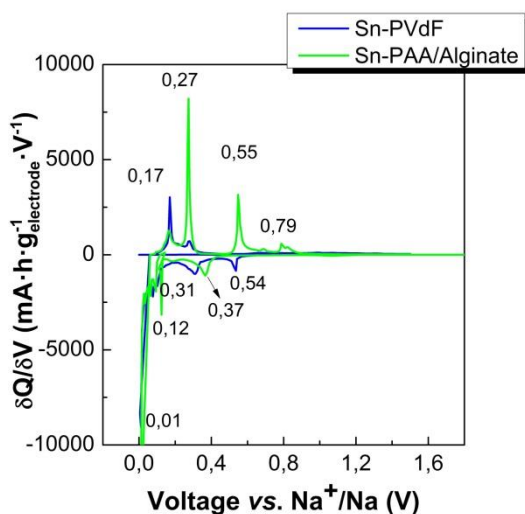


**Figure 3.26** Comparison of the differential capacity vs. voltage curves of Sn nanoparticles bound with PVdF and PAA/Alginate at a cycling rate of C/10.

The fact that PAA/Alginate provided larger capacity is related to a better expression of the redox activity of the Sn particles. According to the literature<sup>68</sup>, sodiation of Sn progressed in a series of steps starting from the bare Sn evolving towards more sodiated phases ( $\text{NaSn}_5$ ,  $\text{NaSn}$ ,  $\text{Na}_9\text{Sn}_4$ ,  $\text{Na}_{15}\text{Sn}_4$ ). Redox peaks appearing at certain voltages (during oxidation) correspond to four Na-Sn two-phase reactions:

<sup>68</sup> Ellis, L. D.; Hatchard, T. D. and Obrovac, M. N., Reversible insertion of sodium in tin, *J. Electrochem. Soc.*, **2012**, 159, 11, A1801-A1805.

Plateau 1	$\text{Na} + \text{Sn} \rightarrow \text{NaSn}_3$	0.6 V vs. $\text{Na}^+/\text{Na}$
Plateau 2	$\text{Na} + \text{NaSn}_3 \rightarrow \text{a-NaSn}$	0.5 V vs. $\text{Na}^+/\text{Na}$
Plateau 3	$5\text{Na} + 4(\text{a-NaSn}) \rightarrow \text{Na}_9\text{Sn}_4$	0.25 V vs. $\text{Na}^+/\text{Na}$
Plateau 4	$6\text{Na} + \text{Na}_9\text{Sn}_4 \rightarrow \text{Na}_{15}\text{Sn}_4$	0.15 V vs. $\text{Na}^+/\text{Na}$

The observed redox peaks are identified and summarized in Table 3.15.

**Table 3.15** Voltages vs.  $\text{Na}^+/\text{Na}$  at which redox reduction and oxidation peaks appear in the  $\delta Q/\delta V$  plot of electrodes containing Sn nanoparticles bound with PAA-Alginate or PVdF.

Plateau*	Sn/PVdF	Sn/PAA-Alg
Reduction voltage (V vs. $\text{Na}^+/\text{Na}$ )		
Sn (4)	0.07	-
Sn (3)	-	0.18
Sn (2)	0.31	0.37
Sn (1)	0.53	-
	-	1.08
Oxidation voltage (V vs. $\text{Na}^+/\text{Na}$ )		
Sn(4)	0.17	0.17
Sn(3)	0.27	0.27
Sn(2)	-	0.56
Sn(1)	-	0.69

\* Number of voltage plateau.

In order to test the electrochemical properties of PSB-PEO in the presence of Sn nanoparticles, a laminated electrode containing 80 wt. % of P3, 10 wt. % of C65 and 10 wt. % of commercial Sn nanoparticles was galvanostatically cycled and compared to the performance of P3 in absence of Sn (Figure 3.27). As that the reversible capacity is referred to the overall weight of the electrode and Sn shows much higher theoretical reversible capacity than C65 it should be expected that the capacity of the electrode containing Sn nanoparticles would be larger. However, larger reversible capacity ( $163 \text{ mA}\cdot\text{h}\cdot\text{g}^{-1}_{\text{electrode}}$ ) and better coulombic efficiency was observed in the absence of Sn than in the presence of it ( $53 \text{ mA}\cdot\text{h}\cdot\text{g}^{-1}_{\text{electrode}}$ ). In the  $\delta Q/\delta V$  plot (Figure 3.27b) it was observed that the redox activity of the polyazomethines, which show redox peaks at 0.63 and 1.09 V vs.  $\text{Na}^+/\text{Na}$  during reduction, was not visible in the P3/Sn composites. The obtained capacity can be therefore ascribed to the formation of  $\text{Na}_x\text{Sn}$  phases and to the sodium insertion into the C65. The poor coulombic efficiency along with the



capacity fade after a few cycles (28 % of capacity retention after 10 cycles) suggested that apart from avoiding the expression of the redox activity of the PSB-PEO itself, the polymer matrix did not be properly buffer the volume changes of the particles during cycling.

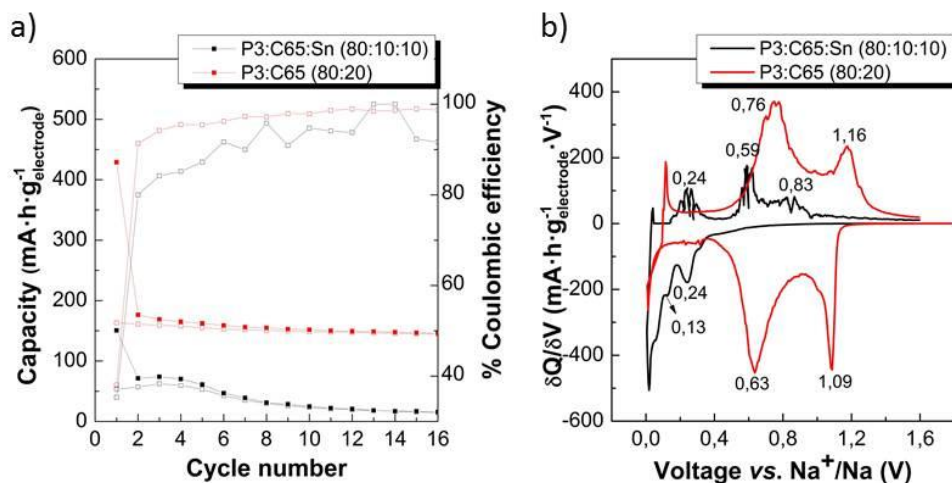


**Figure 3.27** Comparison of the galvanostatic cycling (a) and differential capacity vs. voltage of the second cycle (b) of laminate electrodes containing P3/Sn nanoparticles and bare P3. b) The gravimetric capacity is referred to the whole electrode mass and a current density of 19.8 mA/g equivalent to a C/10 rate based on PSB-PEO was used.

The low capacity observed in the P3/Sn electrode can be also explained as a consequence of the lack of homogeneity of the laminate and poor presence of Sn particles in the electrode. In Figure 3.28, SEM micrographs of pristine electrodes are shown.

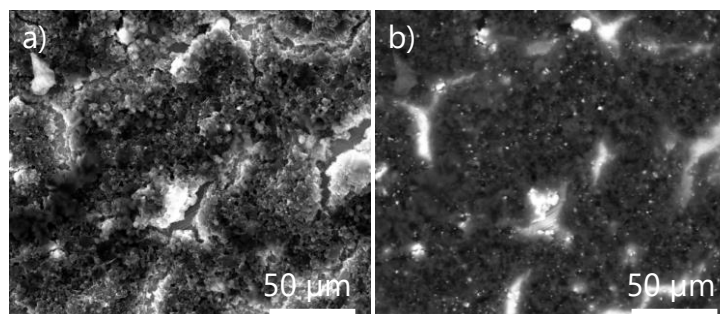


**Figure 3.28** SEM micrographs of electrodes containing 80 : 10 : 10 P3 : Sn nanoparticles : C65 synthesized a) secondary electron image b) backscattering electron image.

Sn particles appear as shiny zones in the back scattering images as the heavier the atom, the brighter the resulting image. As a consequence of a bad dispersion of Sn nanoparticles in the slurry, which was prepared by sonication, Sn nanoparticles formed micron-sized agglomerates. The use of nano-sized materials is a commonly used strategy to overcome the pulverization as they can effectively withstand the stress induced by volume changes. For that reason, the existence of a poor dispersion of the particles that leads to the formation of micron-sized agglomerates of Sn particles is responsible for the huge capacity fade upon cycling. The reason why the redox activity of the PSB-PEO disappeared in the presence of Sn remains unclear. Contrary to what happened when cycling PAA-Alginate based electrodes, a high voltage irreversible capacity (AHVIC) was not observed for P3/Sn, even though the upper voltage cutoff necessary to observe redox activity of the P3 (1.6 V vs. Na<sup>+</sup>/Na) surpassed the voltage at which decomposition of electrolyte occurs according to the literature (0.8 V vs. Na<sup>+</sup>/Na).<sup>68</sup> This electrolyte decomposition catalyzed by Sn surface containing negligible amounts of sodium is related to the formation of a thick layer of decomposed electrolyte that inhibit the diffusion of the ions, decreasing the overall capacity in subsequent cycles..

In Table 3.16, the summary of the electrochemical properties of the P3/Sn composites and the Sn nanoparticles is compared to that of pVdF and PAA binders experimentally measured.

**Table 3.16** Electrochemical parametres of bare P3, P3/Sn and of electrodes containing commercial Sn nanoparticles (80% wt.), PAA-Alginate or PVdF as binder (10% wt.) and C65 (10% wt.).

	<b>Q<sub>r</sub></b>	<b>Q<sub>i</sub></b>	<b>C<sub>r25</sub></b>	<b>1<sup>st</sup> C<sub>e</sub></b>	<b>C<sub>e</sub></b>
P3	163	266	85	38	17
P3/Sn	53	98	23	35	13
Sn/PVdF	191	325	7	37	12
Sn/PAA-Alg	440	75	2	85	-

Q<sub>r</sub> (1<sup>st</sup> cycle reversible capacity, mAh/g), Q<sub>i</sub> (irreversible capacity, mAh/g), C<sub>r</sub> (Capacity retention after 25 and 75 cycles, %), 1<sup>st</sup> C<sub>e</sub> (1<sup>st</sup> cycle coulombic efficiency, %), C<sub>e</sub> (cycle in which a 99% coulombic efficiency is reached).

### PSB-PEO as binder of commercial hard carbon

Binding properties of the PSPEO600 were tried using commercial hard carbon as active material.

In Figure 3.29 SEM pictures of the laminates prepared with PVdF or PSB-PEO600 are shown. Likewise PVdF, PSB-PEO was able to bind hard carbon particles creating polymeric pathways among particles. Moreover, no presence of wrinkles or delamination were observed, confirming that the polymer provided homogeneous electrodes with good mechanical properties.

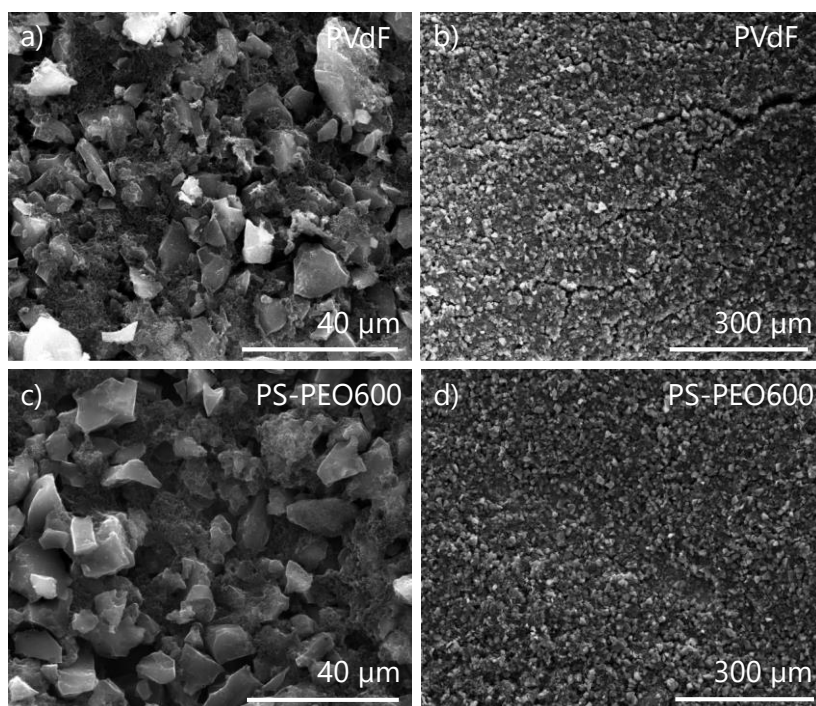


**Figure 3.29** SEM micrographs of electrodes prepared by dispersing components in NMP and containing 10 % wt. of hard carbon, 10% wt. of C65 and a and c) PVdF as binder, b and d) PSB-PEO600 as binder.

### Choice of cycling conditions

Cells were assembled and cycled vs.  $\text{Na}^+/\text{Na}$  using two different electrolytes and voltage windows. Optimum conditions for bare PSB involved the use of 1M NaFSI in

MeTHF as electrolyte in the 0.005V-1.6V voltage range whereas for hard carbons carbonate based solvents are commonly used in a 0.005- 2V range as in the previous chapter.<sup>69</sup>

In (Figure 3.30 a), the electrochemical performance of hard carbon cycled under the above described conditions is shown. As all the components (except for PVdF) are electrochemically active, results were referred to the electrode mass instead of active mass. The electrochemical properties of the HC cycled with PSEPEO and PVdF binders in different electrolytes are summarized In Table 3.15.

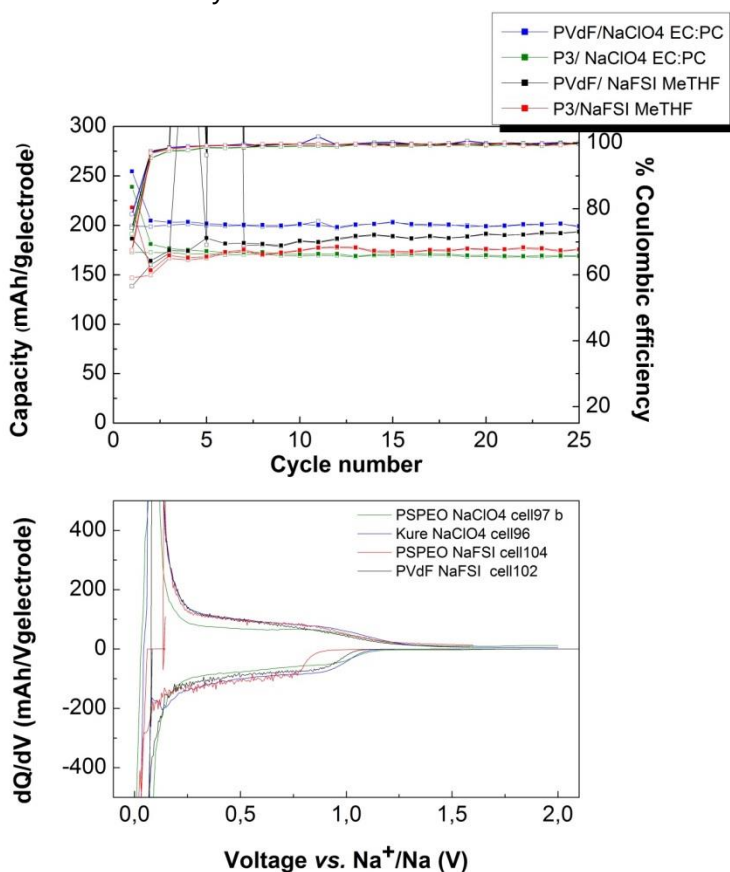


**Figure 3.30 a)** Capacity vs. cycle electrodes containing hard carbon as active material (80% wt.), PVdF or PSB-PEO (P3) as binder (10 % wt.) and C65 as additive (10% wt.) using 1 M NaClO<sub>4</sub> in EC:PC in the

<sup>69</sup> Zhao, J.; Zhao, L.; Chihara, K.; Okada, S.; Yamaki, J.; Matsumoto, S.; Kuze, S.; Nakane, K., Electrochemical and thermal properties of hard carbon-type anodes for Na-ion batteries, *J. Power Sources*, **2013**, 244, 752-757.

0.005-2V voltage window or 1M NaFSI in MeTHF in the 0.005-1.6V range. Cycling was performed at a rate of C/15 (24.8 mA/g<sub>hard carbon</sub>). b) Zoom of the differential capacity of the first and second cycle of the same samples.

**Table 3.17.** Electrochemical parameters of the hard carbon bound with PSB-PEO600 and PVdF with different electrolytes and voltage windows.

Electrochemical parameters									
Binder	Electrolyte/Voltage window	Q <sub>r</sub>	Q <sub>s</sub>	Q <sub>p</sub>	Q <sub>i</sub>	C <sub>r25</sub>	1 <sup>st</sup> C <sub>e</sub>	C <sub>e</sub>	
PSB-PEO600	1M NaClO <sub>4</sub> EC:PC	173	91	82	66	98	72	10	
PVdF	0.005-2V	199	77	122	55	99	78	5	
PSB-PEO600	1M NaFSI MeTHF	146	65	81	71	120	67	5	
PVdF	0.005-1.6V	139	69	70	49	139	74	8	

Q<sub>r</sub> (1<sup>st</sup> cycle reversible capacity, mAh/g), Q<sub>s</sub> (1<sup>st</sup> cycle reversible capacity of the sloping region), Q<sub>p</sub> (1<sup>st</sup> cycle reversible capacity of the sloping region), Q<sub>i</sub> (irreversible capacity, mAh/g), C<sub>r</sub> (Capacity retention after 25 and 75 cycles, mAh/g), C<sub>e</sub> (cycle in which a 99% coulombic efficiency is reached).

The use of appropriate conditions for hard carbons did make a difference in terms of reversible capacity and cycling stability in the first 25 cycles, which are comparable for a C/15 rate (28.4 mA/g<sub>hard carbon</sub>). Largest first cycle reversible capacity was obtained for the 1M NaClO<sub>4</sub> in EC : PC- PVdF couple (199 mAh/g<sub>electrode</sub>) which was maintained through cycling whereas initial capacity when using 1M NaFSI in MeTHF – PVdF was much smaller (139 mAh/g<sub>electrode</sub> ) but increased during cycling reaching a capacity of 190 mAh/g<sub>electrode</sub> after 15 cycles. The same behavior was observed for the PSB-PEO600, which showed a stable capacity of 173 mAh/g<sub>electrode</sub> when 1M NaClO<sub>4</sub> EC : PC was used, but an initially lower but increasing capacity of 146 mAh/g<sub>electrode</sub> when 1MNaFSI in MeTHF was used. After 10 cycles, the electrodes containing PSB-PEO600 as binder reached the same capacity value of 174 mAh/g<sub>electrode</sub> regardless of the electrolyte. For those containing PVdF, almost the same capacity was observed after 25 cycles (199 mAh/g<sub>electrode</sub>). This steady capacity provided by NaClO<sub>4</sub> EC: PC might be due to a better wettability of the electrode material in that electrolyte, which is crucial in ensuring proper ion diffusion.

The fact that samples processed with PVdF led to larger reversible capacities than those prepared with PSPEO600 as binder suggests that the latter is not providing capacity. The absence of typical redox peaks of PSB-PEO (0.65 and 1.09 V vs. Na<sup>+</sup>/Na during reduction and 0.76 and 1.17 V vs. Na<sup>+</sup>/Na during oxidation) in the  $\delta Q/\delta V$  plot proves the lack of its redox activity in all cases. (Figure 3.30 b) The only observable peak is the one close to 0 V vs. Na<sup>+</sup>/Na that corresponds to the insertion of Na ions in the carbon materials. In spite of showing less capacity than PVdF based electrodes, PSB-PEO600 based electrodes still showed good cycling stability leading to a 98 % of capacity retention when using 1M NaClO<sub>4</sub> EC:PC after 25 cycles showing that 10 or 20% wt. of PSB-PEO can be used as binder for a NIB replacing PVdF.

### **Effect of electrode composition**

In order to optimize the electrochemical performance of commercial hard carbon bound with different amounts of binder (P3 or PVdF) in the presence or absence of C65 electrodes were prepared and cycled with 1M NaClO<sub>4</sub> EC:PC. Their capacity v.s cycle number is shown in Figure 3.31. According to the best conditions observed in the previous experiments, 1M NaClO<sub>4</sub> EC : PC as electrolyte was used in the voltage range between 0.005-2V vs. Na<sup>+</sup>/Na. As all the materials that are present in the electrode show electrochemical activity (except for PVdF), results were reported per gram of electrode instead per gram of active material.

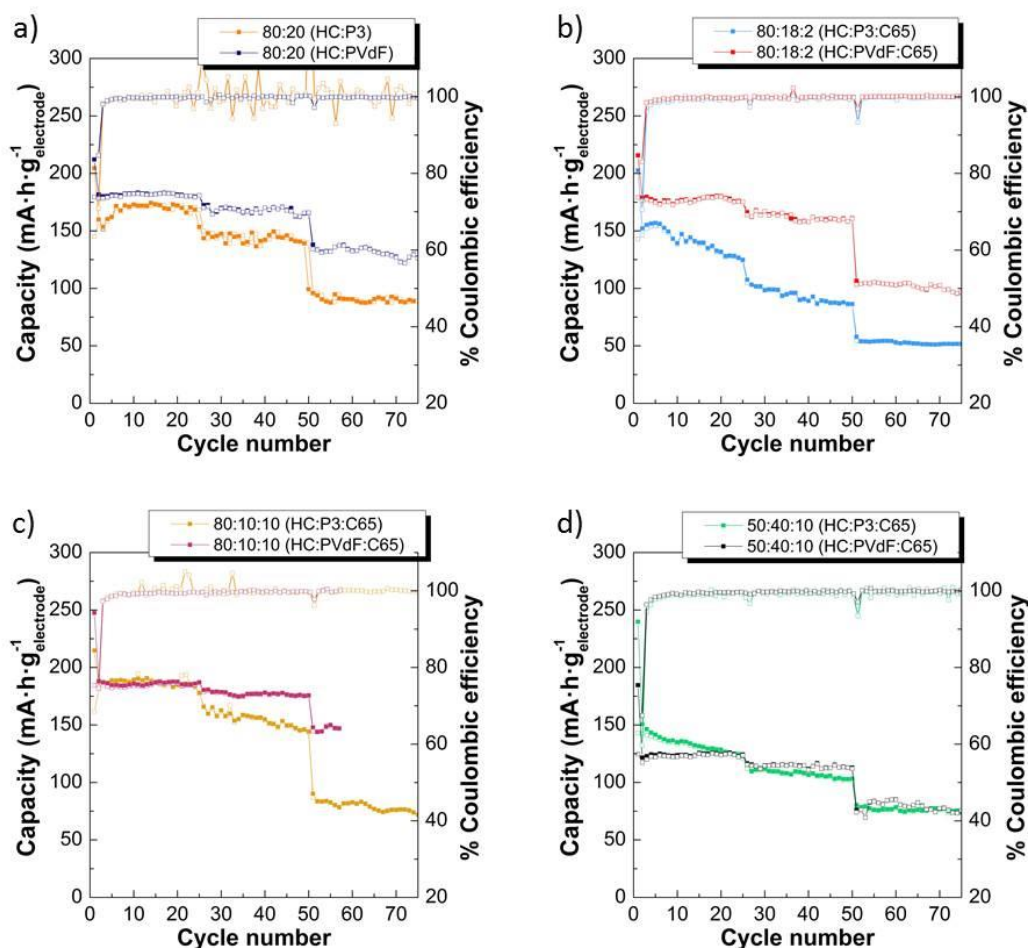


**Figure 3.31** Comparison of the capacity vs. cycle life of electrodes containing different ratios between hard carbon : binder : C65. Currents were calculated for C/15 (25 cycles), C/10 (25 cycles) and C/5 rate (25 cycles).

In electrodes composed of 80% wt. HC 20% wt. binder, or 80:10:10 it is observed that the capacity increases upon cycling when P3 is used as binder. It can be attributed to an insufficient contact between polymer and electrolyte which is gradually improved upon cycling (**¡Error! No se encuentra el origen de la referencia.**a). In absence of C65 wt. %, (Figure 3.31b), the reversible capacity observed for hard carbon is lower than when using PVdF as binder. However, when a 10 wt. % of C65 is employed, the reversible capacity at low rates (C/15) are similar

for P3 and PVdF. A reversible capacity of 162 mA·h·g<sup>-1</sup> were observed when P3 was used as binder and 184 mA·h·g<sup>-1</sup> were observed when PVdF was used. It is noteworthy that the difference in capacity between the two binders was more pronounced at high rates (C/5). This can be ascribed to an increase of the *IR* losses and polarization effects due to an increase of the current drain. As a consequence of the increase of polarization, the discharge plateau appears at a lower voltage, the slope of the discharge curve close to 0.1 V becomes more pronounced, and the delivered coulombic capacity of the PSB, is reduced as it is shown in Figure 3.32.

Besides, an important aspect of the performance is revealed when the voltage profile of both binders are compared (Figure 3.32b). All hard carbons exhibit two distinct regions: slope decay around 2-0.115 V and a plateau around 0.1 V. as discussed in detail in chapter 3. Sloping region corresponds to the Na insertion into defect sites, edges and the surface of graphene whereas the plateau, to Na adsorption into the voids.<sup>70</sup> This low voltage plateau related to sodium atoms interacting with nanoporosity in a process analogous to adsorption<sup>71</sup> or pore-filling is strongly affected by polarization. As a consequence, an increase in the polarization translates into a decrease on the “length” of the plateau and therefore, a decrease of the capacity is noticeable. In the voltage profile it can be observed than when PVdF is used, much lower polarization is obtained and the plateau region is enlarged and, therefore, the capacity is larger.

---

<sup>70</sup> Stevens, D. A. and Dahn, J. R., *J. Electrochem. Soc.*, **2000**, 147, 4428-4431.

<sup>71</sup> Bommier, C.; Surta, T.W.; Dolgos, M. and Ji, X.L., *Nano Lett.*, **2015**, 15, 5888–5892.



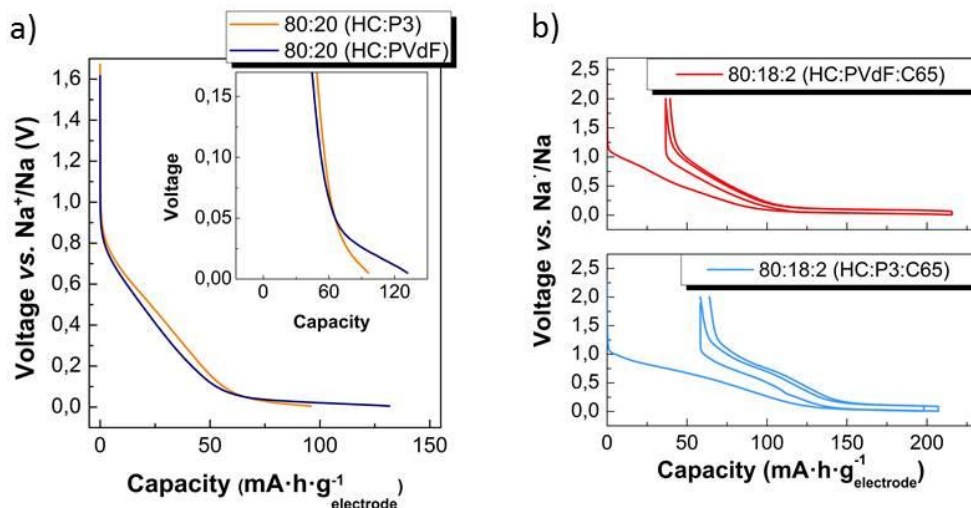


**Figure 3.32** a) Voltage vs. capacity (referred to the electrode mass) of Cu supported electrodes containing 80 % wt. of hard carbon and 20 % of binder (PVdF or P3) cycled at 24.8 mA/g in the 52<sup>nd</sup> cycle. b) Voltage profile of the first and second cycle of electrodes containing 80 : 18 : 02 hard carbon : binder : C65 at C/15.

When the ratio of P3 was large enough (40%), the polymer definitely provided additional capacity and, as a consequence, the observed reversible first cycle capacity (143 mAh/g) was larger than that obtained when using PVdF as binder (117 mAh/g). This proved that the polymer is capable of showing a double role as binder and active material and that it can insert sodium reversibly giving an extra capacity. Unfortunately, the use of P3 as binder gives rise to a larger irreversible capacity (96 mAh/g vs. 67 mAh/g for PVdF) and lower capacity retention (84 % after 25 cycles compared to a 100 % for PVdF). This irreversible capacity found in the first reduction is probably due to the electrochemical reaction between sodium and the conductive carbon additive<sup>72</sup>, electrolyte co-intercalation into the carbon<sup>73</sup>, as well

<sup>72</sup> Senguttuvan, P.; Rouse, G.; Seznec, V.; Tarascon, J. M. and Palacin, M. R., Na<sub>2</sub>Ti<sub>3</sub>O<sub>7</sub>: Lowest voltage ever reported oxide insertion electrode for sodium ion batteries, *Chem. Mater.*, **2011**, 23, 4109 – 4111.

<sup>73</sup> Abe, T.; Mizutani, T.; Tabuchi, K.; Ikeda, K.; Asano, M. Harada, T.; Inaba, M. and Ogumi, Z., Intercalation of lithium into natural graphite flakes and heat-treated polyimide films in ether-type solvents by chemical method, *J. Power Sources*, **1997**, 68, 216-220.

as SEI formation from trace water or below the electrochemical voltage stability of the electrolyte.<sup>74</sup>

The fact that the electrode containing a 40% of P3 showed larger capacity than the analogous electrode containing PVdF is a proof of the extra capacity coming from the P3. That, can be corroborated by the appearance of the reduction and oxidation redox peaks in the  $\delta Q/\delta V$  plot corresponding to the PSB-PEO600 at 0.65 and 1.09 V vs.  $\text{Na}^+/\text{Na}$  (upon reduction) and at 0.76 and 1.17 V vs.  $\text{Na}^+/\text{Na}$  (upon oxidation). (Figure 3.33)

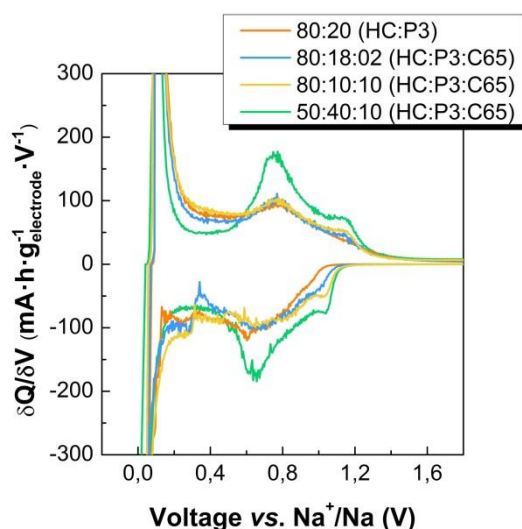


**Figure 3.33** Differential capacity vs. voltage of electrodes of different composition of hard carbon : P3 : C65. Note that the plot has been zoomed in so as to peaks of PSB-PEO600 are visible.

Although those redox peaks were more intense for the 50 : 40 : 10 than for the other ratios, the overall capacity of the electrode was smaller due to the lower activity of the polymer compared to that of the hard carbon, whose activity corresponds to the most intense peak at 0.1 V. Electrodes containing a larger ratio of active HC (80% wt.) provide larger capacities. The electrode giving the largest capacity is the 80 : 10 : 10, which showed the presence of small redox peaks of the P3, being the one at 0.6 V more intense. The laminate having 80 : 20 : 00 hard

<sup>74</sup> Ponrouch, A.; Marchante, E.; Courty, M.; Tarascon, J. M. and Palacin, M. R., *Energy Environ. Sci.*, **2012**, 5, 8572 – 8583.

carbon : P3 : C65 although has a larger amount of P3 than the previous one, had less intense peaks that are only visible during reduction but not during oxidation. So, as the P3 activity was not being expressed the capacity was lower. No presence of redox peaks at 0.6 or 1.1 V were observed for the 80 : 18 : 02 and, as a consequence, the capacity was lower but comparable to the one obtained with much less amount of active material (50%). This suggests that the conductivity provided by carbon is crucial for the PSB-PEO to be able to express its redox activity.

In Table 3.18 the electrochemical properties are summarized.

**Table 3.18** Electrochemical properties of the hard carbon bound with P3 or PVdF with different ratios of active : binder : C65.

Electrochemical properties						
Binder	Ratio	Q <sub>r</sub>	Q <sub>i</sub>	C <sub>r,25</sub>	C <sub>r,75</sub>	C <sub>e</sub>
P3	80:20	145	59	116	61	5
PVdF		180	36	100	70	6
P3	80:18:02	143	60	87	36	6
PVdF		179	37	98	42	4
P3	80:10:10	<b>162</b>	<b>53</b>	<b>110</b>	<b>44</b>	<b>6</b>
PVdF		<b>184</b>	<b>64</b>	<b>100</b>	-	<b>8</b>
P3	50:40:10	143	96	84	52	6
PVdF		117	67	100	64	8

Q<sub>r</sub> (1<sup>st</sup> cycle reversible capacity, mAh/g), Q<sub>i</sub> (irreversible capacity, mAh/g), C<sub>r</sub> (Capacity retention after 25 and 75 cycles, mAh/g), C<sub>e</sub> (cycle in which a 99% coulombic efficiency is reached)

In Figure 3.34 the reversible and irreversible capacity as well as the capacity retention after 25 cycles are plotted as a function of the percentage of active material, binder and C65. Logically, for electrodes containing PVdF, the reversible capacity increases when the percentage of active material (hard carbon) is increased. For PSB-PEO600 the decrease of the amount of active material from an 80% to a 50% does not produce a decrease in the capacity because a 50% of active is coupled with a 40% of PSB-PEO that provides additional capacity. A ratio among components of 80:10:10 (hard carbon: binder:C65) leads to better capacity values than 80:20:0 or 80:18:02 regardless of the use of PSB-PEO or PVdF as binder. This is consistent with the fact that C65 not only insert Na<sup>+</sup>, contributing to the capacity of

the electrode, but it also improves the electrical conductivity, facilitating the kinetics of the electrochemical reactions. For PVdF-based electrodes, an increase of the percentage of binder from 10-20 % to 40% is translated into a decrease of the reversible capacity because the capacity values are referred to the electrode mass and it does not contribute the overall capacity. Despite the fact that electrodes having 10, 18 or 20% of binder have the same amount of active material (80 %), a 10 % of binder is accompanied by a larger amount of C65 (10%) than the other two. For that reason, regardless of the type of binder, the electrode of composition 80:10:10 provides larger capacity.

As it was previously mentioned, an increase of the binder percentage from 18-20 to 40% does not produce a decrease in the reversible capacity of the PSB-PEO600 based electrodes thank to the intrinsic capacity of that component. When representing the reversible capacity against the percentage of carbon, it is noticeable that even for a content of C65 of 0% wt. the capacity is still high thanks to the partial conductivity of the hard carbons which, although it is mainly disordered, still retains some graphitic domains that allow electrical conductivity.

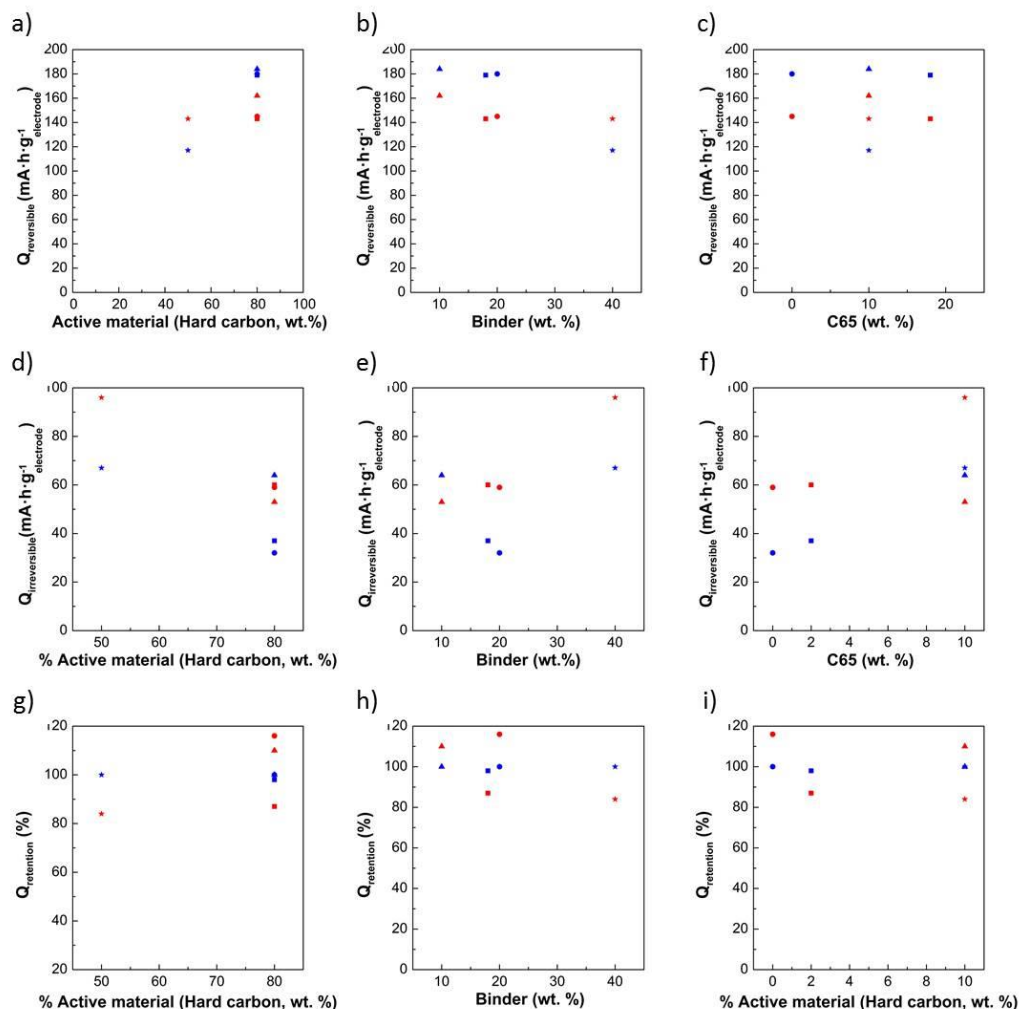


**Figure 3.34** Reversible and irreversible capacities and capacity retention after 25 cycles as a function of the percentage of hard carbon, binder (PSB-PEO600 and PVdF) and C65 content of the electrodes.

During the first electrochemical insertion of sodium into the hard carbon, some sodium is irreversibly consumed forming a solid electrolyte interface (SEI) due to electrolyte decomposition. This passivating layer is crucial for the electrode stability as it prevents uncontrolled consumption of the electrolyte but it also results in a loss of capacity, namely, irreversible capacity. For PVdF containing electrodes a linear correlation between the percentage of C65 and the irreversible capacity was found. (Figure 3.34 f) As the SEI is consequence of superficial reactions, a larger surface area is usually the cause for a larger irreversible capacity. Although C65 has relatively low BET surface area, ( $62 \text{ m}^2/\text{g}$ ) it is much larger than that of the hard

carbon ( $5.6 \text{ m}^2/\text{g}$ ). As it was previously shown in (Figure 3.17), C65 is capable of inserting  $\text{Na}^+$  at low voltages vs.  $\text{Na}^+/\text{Na}$  contributing to, both irreversible and reversible capacity. For the PSB-PEO600, the irreversible capacity does not depend on the carbon content. However, when comparing electrodes with the same carbon content (10% wt. of C65), the irreversible capacity appeared to be much higher for those electrodes having a 40% of PSB-PEO600 rather than those with 18-20 %wt. This suggests that PSB-PEO600 is the main source of irreversibility due to unknown secondary reactions or because of the destruction of the crystallinity or because of structural changes. For PVdF, an increase of the binder content from 10 to 20 % produces a decrease of the irreversible capacity but although dehydrofluorination of the PVdF<sup>75</sup> might also contribute to the irreversible capacity, in this case it is mainly related to the amount of carbon, which is also reduced. Actually, when increasing the PVdF content up to 40% wt., the irreversible capacity is similar to that of the electrode having 80% wt. of active and the same content of C65 (10% wt.)

The capacity retention after 25 cycles is not clearly affected by the hard carbon, C65 or binder content for PVdF based electrodes. The good cycling stability of hard carbon bound with PVdF is a consequence of the absence of volume changes on the structure of the hard carbon during sodium intercalation/deintercalation, which usually constitutes the main reason for anode pulverization. This lack of volume change is enabled by fact that the electrochemical reduction of the hard carbon is mostly based on the adsorption of sodium ions on the surface of the carbon graphene sheets and micropores.<sup>76</sup> For PSB-PEO600 containing electrodes, the same behaviour is observed. However, the electrodes prepared with ratios of 80:20 (hard carbon : PSB-PEO600) and 80:10:10 (hard carbon:PSB-PEO600:C65) show capacity retention values larger than 100% because of the increase of reversible capacity after a few cycles due to the so-called "activation of the polymeric binder".

---

<sup>75</sup> Muñoz-Márquez, M. A.; Zarrabeitia, M.; Castillo-Martínez, E.; Eguía-Barrio, A.; Rojo, T. and Casas-Cabanas, M., Composition and evolution of the solid-electrolyte interphase in  $\text{Na}_2\text{Ti}_3\text{O}_7$  electrodes for Na-ion batteries: XPS and Auger parameter analysis, *ACS Appl. Mater. Interfaces*, **2015**, 7, 14, 7801–7808.

<sup>76</sup> Park, J.-K., Principles and applications of lithium secondary batteries, **2012**, Wiley-VCH Verlag, Weinheim, Germany, 108-109.

This phenomenon is attributed to insufficient contact between the polymer and the electrolyte, which is gradually improved during the charge/discharge process.<sup>77</sup>

As it was previously mentioned, the polarization of the electrode affects the capacity. In an ideal device, all the stored energy could be converted to useful electric energy. However, losses occur due to polarization effects that consume part of the energy which is given off as waste heat and therefore, not all the theoretically available energy is converted into useful electrical energy. Apart from polarization, internal impedance of the cell (the sum of electronic resistances of active mass, current collectors, electrical tabs of both electrodes and contact resistance between active mass and current collector) causes a voltage drop (also known as ohmic polarization or IR drop).<sup>78</sup> In practice it is difficult to estimate the polarization components because of the complicated physical structure of the electrode but an easy estimation of the overall polarization was performed by calculating the polarization as the difference in volts between the discharge voltage and the voltage at a certain point (arbitrarily chosen) during charge (established at 0.04 mAh for all the cells). The methodology used to calculate the polarization for each battery is shown in Figure 3.35.

---

<sup>77</sup> Song, Z. and Zhou, H.; Towards sustainable and versatile energy storage devices: an overview of organic electrode materials, *Energy Environ. Sci.*, **2013**, 2280- 2301.

<sup>78</sup> Linden, D. and Reddy, T. B.; Handbook of batteries, McGrawHill, 3<sup>rd</sup> edition, **2002**, New York, 2.1-2.5.

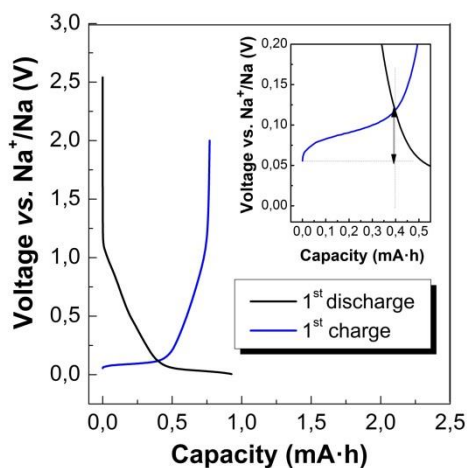


**Figure 3.35** Example of polarization calculation as of the first cycle voltage vs. capacity plot of an 80 : 18 : 02 hard carbon : PVdF : C65 laminate.

In Figure 3.36 the capacity per gram of electrode prepared as of HC with PSB-PEO600 and PVdF and the polarization are represented and an almost linear correlation between the capacity and the polarization found for each laminate composition with 80% wt. in hard carbon. When 50% hard carbon was used with 40% binder, a different linear relationship was observed since the polarization was calculated in for the low voltage process of insertion into the HC and other components have similar weights %. In general, larger capacities were observed for smaller polarization values. Since the electrodes having PVdF showed less polarization, that fact would explain the higher capacity with respect to the PSB-PEO600, especially in a material with such a large capacity at close to sodium plating voltages.



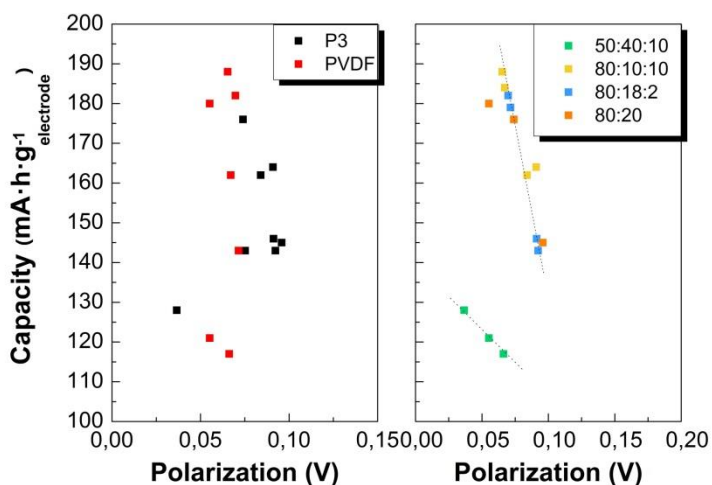


**Figure 3.36** Correlation between the capacity and the polarization for laminates containing PSB-PEO and PVdF as binder and with different ratios of active material : binder : C65.

The digital pictures of the electrodes containing P3 as binder are shown in Figure 3.37. The mechanical properties of the laminates were quite poor so it was necessary to press the electrodes for 10 minutes to increase the adhesion of the mixture to the copper foil. Despite compression of the foil can result in a decrease of the porosity, which has to be large enough to allow for a good contact between the particles and the electrolyte providing a large effective surface area available for the electrochemical reactions; pressing was necessary to ensure the electrical contact between the active particles and the current collector.

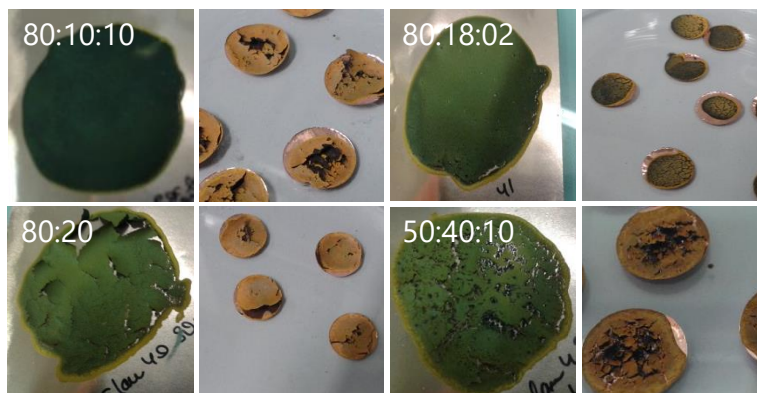


**Figure 3.37** Dry laminates and electrodes (before pressing) of hard carbon with PSB-PEO as binder and C65, when required as additive.

Except for the laminate containing a ratio of 80:10:10, The polymer segregates leading to two differenced phases in the electrode. P3 remains on the surface of the electrode whereas the hard carbon/C65 stay at the bottom. This is detrimental for the electrochemical performance as the aim of the binder is to keep the integrity of the electrode during cycling by maintaining the binding among the components. SEM of the pristine electrodes revealed the surface morphology of the electrodes containing PVdF and P3. (Figure 3.38). In general, all the laminates containing PVdF as binder showed the same characteristics: polymer is forming a pathway that keeps the hard carbon particles uniformly attached to each other. In the electrodes containing P3 as binder, the degree of homogeneity is poor and there are some regions fully covered by polymer and others where hard carbon particles are isolated and exposed on the surface (o, p). A P3 content of 10% does not lead to an observable polymeric pathway. However, laminates containing 20 % wt. and 40 % wt. (g, h, o, p) evidences the presence of the polymer binding hard carbon particles, especially in the latter, as the amount of polymer is much higher.

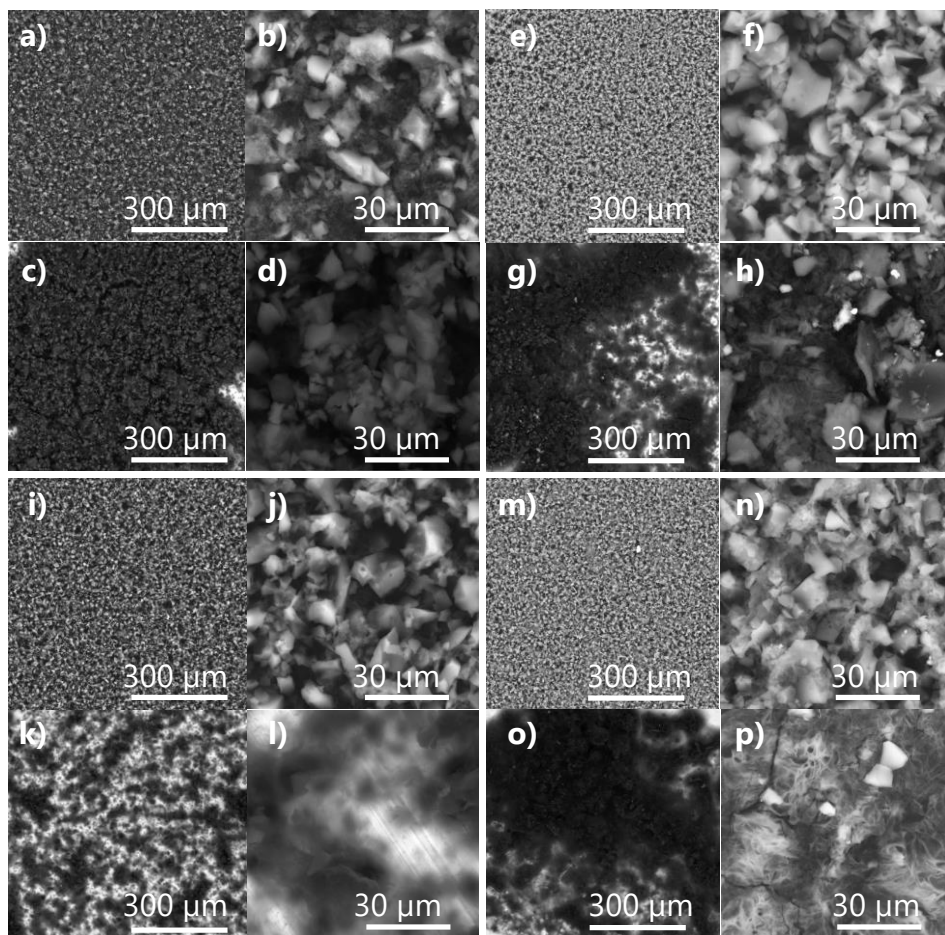


**Figure 3.38** SEM micrographs of Cu supported electrodes containing hard carbon and a) PVdF as binder (10% wt.), C65(10% wt.), b) PVdF as binder (10% wt.), C65(10% wt.), c) P3 as binder (10% wt.), C65(10% wt.), d) P3 as binder (10% wt.), C65 (10% wt.), e) PVdF as binder (20% wt.), f) PVdF as binder (20% wt.), g) P3 as binder (20% wt.), h) PS-PE060 as binder (20% wt.), i) PVdF as binder (18% wt.), C65 (2 % wt.), j) PVdF as binder (18% wt.), C65 (2 % wt.), k) P3 as binder (18% wt.), C65 (2% wt.), l) P3 as binder (18% wt.), C65 (2% wt.), m) PVdF as binder (40% wt.), C65(10% wt.), n) PVdF as binder (40% wt.), C65(10% wt.) o) P3 as binder (40% wt.), C65(10% wt.), p) P3 as binder (40% wt.), C65(10% wt.)

However, the most remarkable feature is that as it was previously observed visually, the PSB-PEO remained on the surface leading to charging effects due to its bad electronic conductivity. Although PVdF is also an insulating polymer, no charging effects due a poor dissipation of the electron beam are observed meaning that the PVdF is intimately connecting hard carbon and C65 which are conducting. The segregation between polymer and carbon in the electrodes containing PSB-PEO as

binder can be responsible for the poorer electrochemical performance. If P3, hard carbon and C65 were perfectly mixed leading to a homogeneous electrode, all the particles would be forced to be equipotential with their neighbouring particles because they are in electrical contact. As a consequence, the overall electrode polarization would increase but the higher conductivity of the C65 and hard carbon would still combat that polarization increase to some extent by providing a conductive pathway through the thickness of the electrode. However, the layered electrodes in which the PSB-PEO is on top of the electrode and the hard carbon and C65 at the bottom, makes that the current is forced to pass through the P3 before reaching the conducting components and therefore, due to the insulating nature of the polymer, the electrode is strongly polarized.<sup>79</sup>

The fact that a substantial part of the capacity comes from the low voltage plateau and thus it is strongly affected by the increase of polarization makes hard carbon a complicated active material when trying to evaluate the contribution to the capacity coming from the P3 as binder. For that reason, it was decided to explore other active materials.

### **PSB-PEO as binder of PVC derived soft carbon**

PVC (poly vinylene chloride) derived soft carbon synthesized at CIC Energigune was chosen as the disordered and graphitizable nature of this material gives rise to a voltage profile with just a sloping region and no low voltage plateau. Besides, the synthesis and electrochemical performance was proven to be highly reproducible (chapter 2).

Electrodes, which were prepared dispersing PVC derived soft carbon onto the reaction media of the P3, showed good mechanical properties. Contrary to what happened when preparing electrodes as of hard carbon, no segregation of the components was observed with wt. % of binder as low as 5%. (Figure 3.39)

---

<sup>79</sup> Julien, C.; Mauger, A.; Vihj, A.; Zhagib, K., Lithium batteries, Springer, Switzerland, **2016**, 590-592.

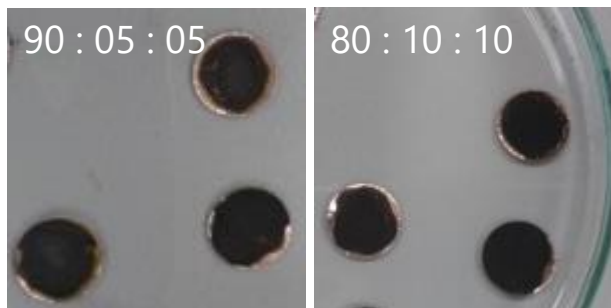


**Figure 3.39** Electrodes of PVC derived soft carbon with PSB-PEO600 as binder and C65, as additive.

Being the PVC derived soft carbon the majoritary component of the electrode, the electrochemical performance of PVC-derived soft carbons bound with PVdF or P3 was carried out using 1M NaClO<sub>4</sub> EC : PC as electrolyte, which is particularly suitable for carbonaceous anodes. Voltage profiles of the first and second cycles of PVC derived hard carbons with PSB-PEO binder and PVdF binder are depicted in Figure 3.40. Soft carbons contain small crystallite domains of roughly 10-12 graphene layers stacked approximately parallel to each other. The layers are randomly rotated and shifted relative to each other, producing turbostratic disorder. This disorder creates interlayer sodium insertion sites with a range of chemical environment. Since sodium is distributed into various locations, the capacity develops over a wide range of potentials, giving a characteristic “sloping voltage” electrochemical profile.<sup>80</sup>

It is noteworthy the appearance of a noisy signal during the first and second charge of the electrode bound with P3. This noise is related to the presence of a large plateau during charge whose source remains unclear. The so-called “trailing plateau” was also reported to happen for the bare PolySchiff<sup>29</sup> but it was also randomly observed when hard carbon bound with PVdF was cycled in the 0.005-1.6 V vs. Na<sup>+</sup>/Na using NaFSI MeTHF as electrolyte (see section 2.3.2.2.2 in this thesis) and when lignin derived hard-carbon was cycled with NaClO<sub>4</sub> in EC : PC in the 0.002-2 V vs. Na<sup>+</sup>/Na voltage range. This suggests that the process is related to reaching very low voltages during the reduction process (such as 0.002-0.005V vs. Na<sup>+</sup>/Na) because of sodium plating leading to micro short-circuits.

<sup>80</sup> Zheng, T.; Reimers, J. N. and Dahn, J. R., Effect of turbostratic disorder in graphitic carbon hosts on the intercalation of lithium, *Phys. Rev. B*, **1995**, 51, 734-741.

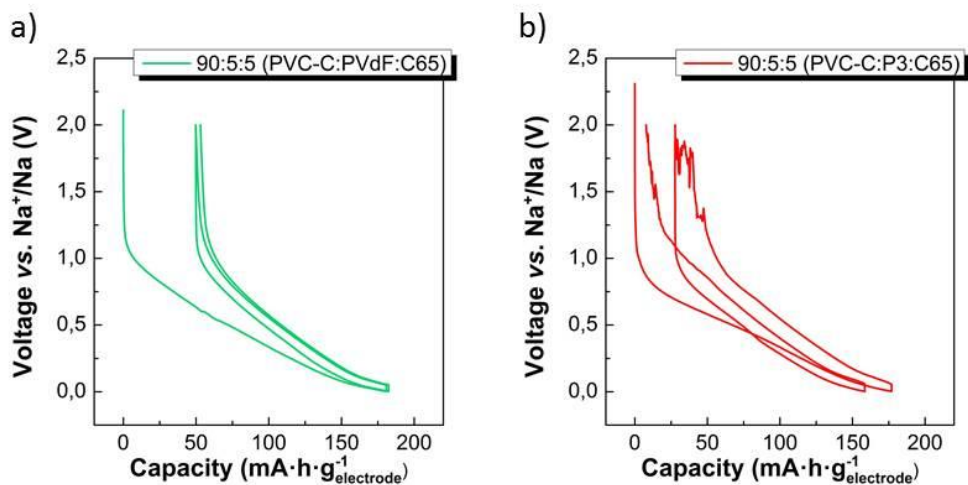


**Figure 3.40** Voltage profile of the first and second cycle of electrodes containing 90 : 05 : 05 PVC soft carbon :binder : C65 at C/15.

In the  $\delta Q/\delta V$  plot (Figure 3.40 a), differential capacity per gram of electrode of the second cycle of electrodes containing PVdF and P3 is shown. There is a small peak centered at 0.65 V during reduction that might correspond to the  $\text{Na}^+$  insertion in the PSB-PEO, the low intensity along with the absence of the other typical redox peak of PSB-PEO at 1.09 V vs.  $\text{Na}^+/\text{Na}$  suggested that the extra capacity coming from PSB-PEO is almost negligible in agreement with the low loading.

The rate capability of the PVC derived soft carbon bound with PVdF or P3 for a 90:5:5 wt. % ratio among active: binder and C65 is shown in Figure 3.41 b. In the second cycle (when a current of  $24.8 \text{ mA}\cdot\text{g}^{-1}$  equivalent to C/15 based on a theoretical capacity of  $372 \text{ mA}\cdot\text{h}\cdot\text{g}^{-1}$  for  $\text{NaC}_6$  formation), electrodes prepared with P3 led to similar discharge capacity values than those with PVdF ( $160 \text{ mA}\cdot\text{h}\cdot\text{g}^{-1}_{\text{electrode}}$ ). Reversible capacities cannot be compared though, because of the presence of the trailing plateau during oxidation that contributes to the capacity. Therefore the capacity observed for P3 ( $178 \text{ mA}\cdot\text{h}\cdot\text{g}^{-1}_{\text{electrode}}$ ) is not a real value due only to sodium extraction from carbon. Both binders provide similar first discharge capacity values ( $211$  and  $218 \text{ mA}\cdot\text{h}\cdot\text{g}^{-1}_{\text{electrode}}$  for PSB-PEO and PVdF, respectively)

The fact that the components of the electrode are intimately mixed instead of having the PSB-PEO on top of the electrode might reduce considerably the overall irreversible capacity, which arises from surface reactions. Irreversible capacity might

be therefore, consequence of the soft carbon surface defects.<sup>76</sup> At low C rates (C/15, C/10) the discharge capacity of the PVC derived soft carbon electrodes containing PSB-PEO and PVdF is comparable. However, at higher currents, the difference between using PVdF and PSB-PEO becomes increasingly larger.

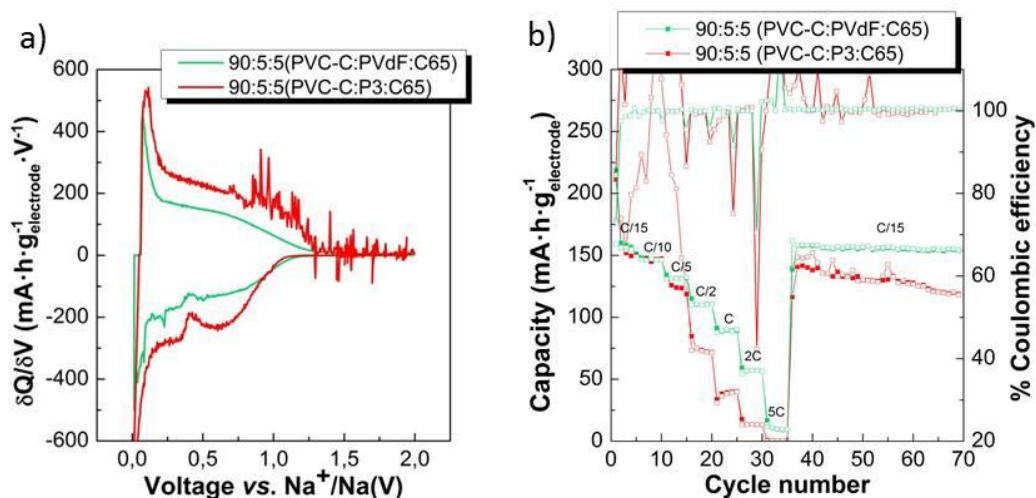


**Figure 3.41** a) Differential capacity vs. voltage of second cycle (at C/15 rate) of electrodes containing 90 : 05 : 05 PVC soft carbon : binder : C65 at C/15 and b) Comparison of the capacity vs. cycle number of the second cycle of electrodes containing 90 : 05 : 05 PVC soft carbon : binder (PVdF or PSB-PEO) : C65.

Initially, as it can be observed in the  $\delta Q/\delta V$  plot, P3 shows larger polarization (the redox peak close to 0 V vs. Na<sup>+</sup>/Na upon oxidation occurs at higher voltage values than for PVdF based electrodes). Considering that P3 contains PEO groups that increase the ionic conductivity, it is unlikely that the increase on the polarization is related to the concentration polarization due to higher diffusion rates of the Na ions in PVdF than in PSB-PEO. The increase of the polarization when using PSB-PEO might be a consequence of the electrodes showing less porosity than their PVdF counterparts and therefore, an increased charge-transfer polarization due to worse electrolyte uptake.

PVdF based electrodes also retained better the capacity after cycling 60 times at different C rates. They retained a 99% of the initial capacity whereas PSB-PEO maintained only 73%. However, it should be emphasized that cycling at high currents (C/2, C, 2C, 5C) did not provide much capacity with none of the binders,

meaning that the electrochemical reaction was far from being complete. Therefore, the capacity retention after 50 cycles being 20 of them at relatively high currents might be larger than if cycled at low currents, since long cycling at low currents can also lead to electrode deterioration. The fact that electrodes containing PSB-PEO suffers faster capacity decay than those having PVdF can be a consequence of the poorer mechanical properties of the laminates prepared with PSB-PEO.

In an attempt to observe the redox activity of the PSB-PEO, the amount of binder was increased up to 10 %. In Figure 3.42 the voltage profile of the electrodes containing 80 wt. % of soft carbon, 10 wt. % of C65 and 10 wt. % of binder are shown. By decreasing the content of soft carbon down to 80 wt. % in the electrode containing both PVdF or PSB-PEO, larger capacity values are observed probably due to the contribution of the C65 additive. Besides, the lower mass loading of the electrodes containing PVdF (2.6 mg compared to 5.7 mg for PSB-PEO) would facilitate the diffusion of electrons as well as that of ions through the electrode providing better performance. P3 provides less reversible capacity ( $146 \text{ mA}\cdot\text{h}\cdot\text{g}^{-1}$ ) than PVdF ( $188 \text{ mA}\cdot\text{h}\cdot\text{g}^{-1}$ ) but less irreversible capacity (62 and  $106 \text{ mA}\cdot\text{h}\cdot\text{g}^{-1}$ ) as well.

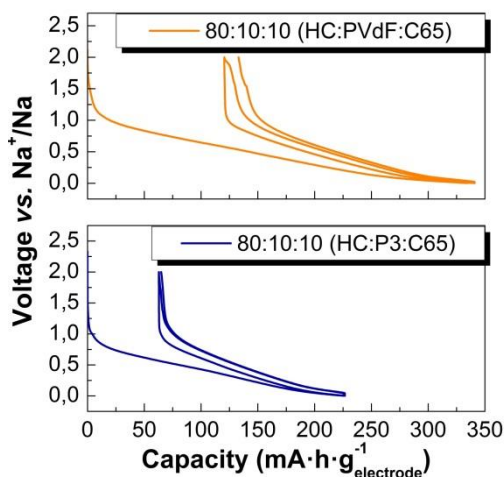


**Figure 3.42** Voltage profile of the first and second cycle of electrodes containing 80 : 10 : 10 PVC soft carbon :binder : C65 at C/15.



The lack of activity of PSB-PEO can be noticed in the  $\delta Q/\delta V$  plot (Figure 3.43 a) where no presence of the redox peaks at 0.65 and 1.09 V vs.  $\text{Na}^+/\text{Na}$  during reduction is observed. Probably, as it happened for hard carbon based electrodes in order to observe the activity of the PSB-PEO much larger binder content is required. The rate capability of the two types of electrodes is shown in Figure 3.43 b. Despite larger capacities are observed for electrodes containing PVdF, P3 shows better capacity retention (90 % compared to 85 % for PVdF) after 50 cycles at different rates.

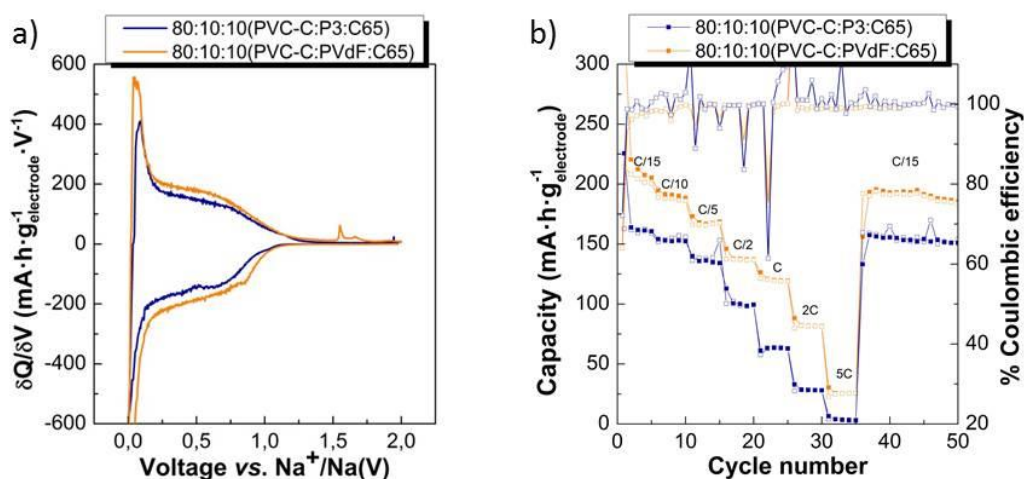


**Figure 3.43** (Above) Comparison of the capacity vs. cycle number of electrodes containing 80 : 10 : 10 PVC soft carbon : binder (PVdF or PSB-PEO) : C65. (Below) Differential capacity vs. voltage of second cycle (at C/15 rate) of electrodes containing 80 : 10 : 10 PVC soft carbon : binder : C65 at C/15.

In the Table 3.19 the most relevant electrochemical properties of electrodes prepared with soft carbons and P3 are summarized and compared to electrodes prepared with PvDF.

**Table 3.19** Electrochemical properties of the PVC soft carbon bound with PSB-PEO600 and PVdF with different ratios of active : binder : C65.

Electrochemical properties						
Binder	Ratio	$Q_r$	$Q_i$	$C_{r60}$	1 <sup>st</sup> ce	$C_e$
PSB-PEO600	90:5:5	178	33	73	84	-
PVdF		160	58	99	73	5
PSB-PEO600	80:10:10	163	62	89	72	4
PVdF		214	121	73	64	13

$Q_r$  (1<sup>st</sup> cycle reversible capacity, mAh/g),  $Q_i$  (irreversible capacity, mAh/g),  $C_r$  (Capacity retention after 25 and 75 cycles, mAh/g),  $C_e$  (cycle in which a 99% coulombic efficiency is reached).

### PSB-PEO as binder of metal carbodiimides

Next experiments with transition metal carbodiimides were designed based on the premise that both the active material and the PSB-PEO binder showed good electrochemical performance in similar conditions (1 M NaFSI-MeTHF as electrolyte) and this would help the PSB-PEO600 to show its activity as double-rolled binder. The use of an appropriate electrolyte has an impact on the electrochemical performance as it can provide an SEI layer of different composition or thickness leading to different irreversible capacity values as well as distinct ionic diffusion rates through the electrode.

Among all the home-made carbodiimides proven to be electrochemically active as anodes in Na-ion batteries by Eguía-Barrio *et al.*<sup>81</sup> (MNCN with  $M = \text{Cu, Zn, Mn, Fe, Co, and Ni}$ ), Zinc carbodiimides were chosen. The reason is that ZnNCN can be easily synthesized in aqueous media, and that although they have smaller reversible capacity compared to Ni and Co carbodiimides, it has also much smaller irreversible capacity in the first cycle. ZnNCN, which has a reversible capacity of  $250 \text{ mA}\cdot\text{h}\cdot\text{g}^{-1}$ , has one plateau centered at 0.5 V vs.  $\text{Na}^+/\text{Na}$ . This allows proper monitoring of the activity of the PSB-PEO, which shows its activity at higher voltage.

The electrochemical performance of electrodes prepared as of different ratios among ZnNCN, binder (P3 or PVdF) and C65 (80:10:10, 80:20:0, 70:10:20 and 40:40:10) is shown in Figure 3.44.

---

<sup>81</sup> Eguía-Barrio, A.; Castillo-Martínez, E.; Liu, X., Dronskowski, R., Armand, M. and Rojo, T., Carbodiimides: new materials applied as anode electrodes for sodium and lithium ion batteries, *J. Mater. Chem., A*, **2016**, 4, 1608-161.

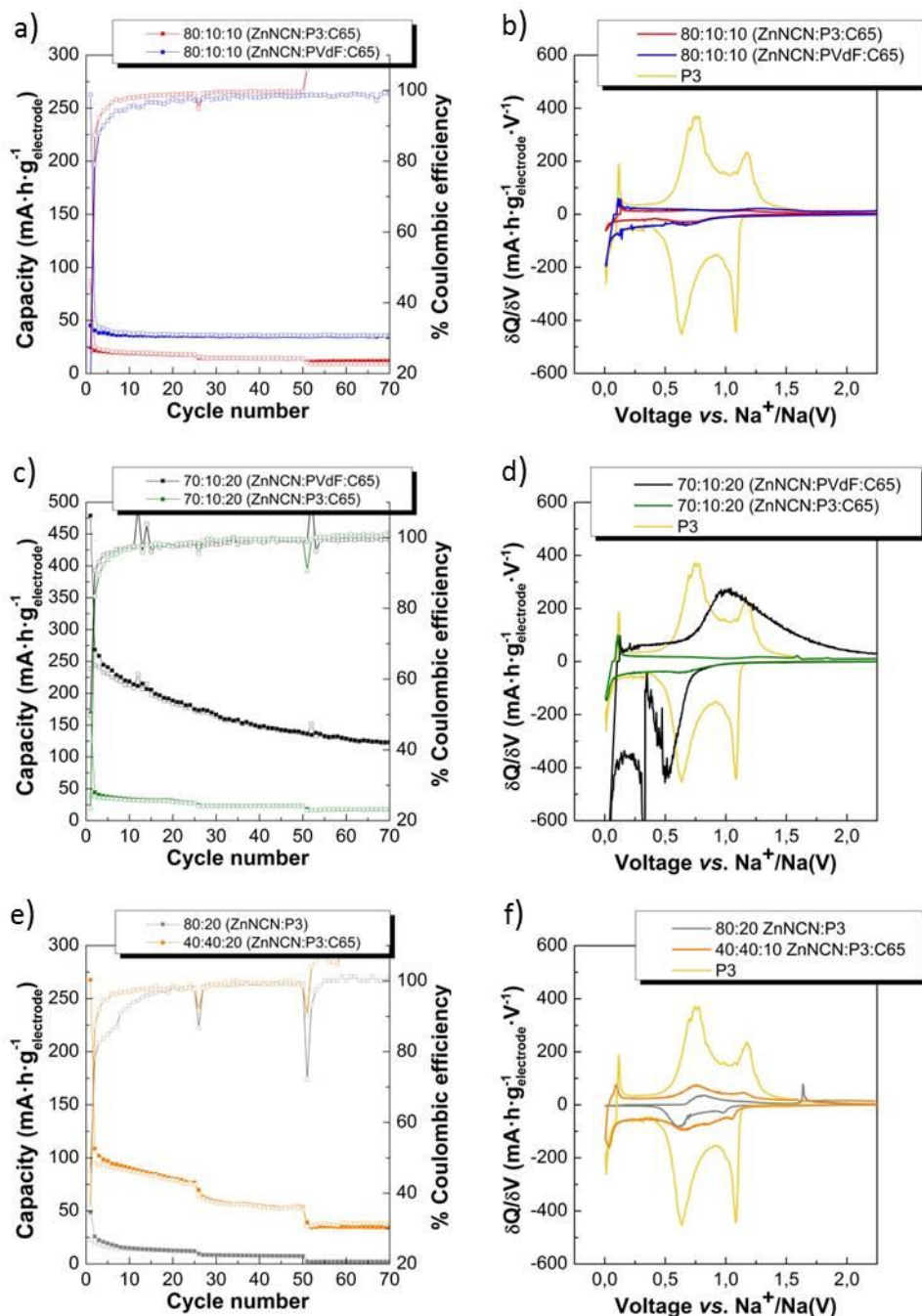


**Figure 3.44** Comparison of the performance of PVdF and PSB-PEO (P3) as binders on the capacity vs. cycle number of electrodes containing a ratio among ZnNCN, binder and C65 of 80:10:10, 80:20:0, 70:10:20 and 40:40:10. Currents were calculated for a C/10 rate based on the capacity of the active material (50.8 mA/g ZnNCN).

Electrodes containing 80 wt. % of ZnNCN, 10 wt. % of conductive additive (mixture of C65:KB 50:50 wt. %) and 10 wt. % of binder, the capacity referred to the total electrode mass is very low with both binders, but it is lower when P3 is used is ( $23 \text{ mA}\cdot\text{h}\cdot\text{g}^{-1}_{\text{electrode}}$ ) than when using PVdF ( $45 \text{ mA}\cdot\text{h}\cdot\text{g}^{-1}_{\text{electrode}}$ ). (Figure 3.44 a) In the  $\delta Q/\delta V$  plot, (Figure 3.44 b) the absence of redox peaks of the ZnNCN (at 0.5 V vs.  $\text{Na}^+/\text{Na}$  upon reduction and 1V vs.  $\text{Na}^+/\text{Na}$  upon oxidation), of PSB-PEO (0.65 V and 1.09 V vs.  $\text{Na}^+/\text{Na}$  upon reduction and 0.76 and 1.16 V vs.  $\text{Na}^+/\text{Na}$ ) and the presence of a redox peak close to 0 V vs.  $\text{Na}^+/\text{Na}$  upon reduction suggests that the observed capacity is related to the insertion of Na ions into the conductive additive only. Taking into account the poor conductivity of ZnNCN, a larger amount of conducting carbon might be required to deliver the capacity from the active material.

When the amount of conductive additive was increased up to 20 wt. % (70:10:20 ratio), an intense peak of ZnNCN reduction at 0.5 V vs.  $\text{Na}^+/\text{Na}$  was observed in the  $\delta Q/\delta V$  plot (Figure 3.44 d) when PVdF is used. However, no activity coming from the  $\text{Na}_2\text{NCN}$  formation or from the  $\text{Na}^+$  insertion into the azomethine bonds of the P3 was observed. Accordingly, electrodes containing PVdF reached a capacity of  $239 \text{ mA}\cdot\text{h}\cdot\text{g}^{-1}_{\text{electrode}}$  for the first cycle whereas  $40 \text{ mA}\cdot\text{h}\cdot\text{g}^{-1}_{\text{electrode}}$  were delivered by conductive carbon in electrodes containing P3 as binder. (Figure 3.44 c)

In order to demonstrate whether it was possible to get any capacity of the PSB-PEO, the amount of polymer was increased up to 40 wt. %. (Figure 3.44 e) In the  $\delta Q/\delta V$  plot (Figure 3.44 f) where the comparison of the differential capacity of the second cycle of the bare PSB-PEO, bare ZnNCN and two different ratios between ZnNCN, PSB-PEO and carbon is depicted. It can be confirmed that the capacity ( $96 \text{ mA}\cdot\text{h}\cdot\text{g}^{-1}_{\text{electrode}}$ ) is derived from the activity of PSB-PEO and from the conductive carbon. Redox peaks corresponding to the PSB-PEO and conductive carbon were observed at 1.09 V and 0.65 V vs.  $\text{Na}^+/\text{Na}$  and close to 0 V vs.  $\text{Na}^+/\text{Na}$ , respectively. Surprisingly no electroactivity of ZnNCN is observed for any PSB-PEO ratio. This might be due to the segregation or detachment of the active material in the electrode avoiding the proper electric contact.

As it was expected, the absence of conductive additive led to very poor capacity ( $22 \text{ mA}\cdot\text{h}\cdot\text{g}^{-1}_{\text{electrode}}$ ) arising from the PSB-PEO. No activity of the ZnNCN was observed evidencing that the proper electronic conductivity is crucial for the good performance of the carbodiimide.

The electrochemical properties above discussed are summarized in Table 3.20

**Table 3.20** Electrochemical properties of the ZnNCN bound with P3 and PVdF with different ratios of active : binder : C65.

Electrochemical properties						
Binder	Ratio	$Q_r$	$Q_i$	$C_{r25}$	$1^{\text{st}} C_e$	$C_e$
P3	70: 10 : 20	40	128	70	23	-
PVdF		239	240	72	50	-
P3	80 : 10 : 10	23	64	74	26	23
PVdF		45	218	78	17	-
P3	80 : 20	22	27	54	46	36
	40 : 40 : 20	96	172	78	36	32

In summary, the use of P3 is detrimental for the electrochemical performance of ZnNCN. The polymer is not just unable to express its capacity but the activity of ZnNCN is also almost negligible and most of the redox properties observed are derived from the use of KB and C65 as additives. A good binder should guarantee the homogeneous dispersion of active materials and conductive carbon together with stable bonding to the metallic collector but PSB is not appropriate for binding ZnNCN.

### 3.4 Conclusions

Copolymers of PolySchiff bases and Jeffamines ED® (polyetheramines) have been developed and optimized as electroactive anodes for sodium ion batteries exhibiting reversible capacities of 175 mAh/g.

The copolymer showed a typical behaviour of the polyethylene oxide products, which typically impart increased flexibility. The TG measurements showed lower thermal stability compared to the bare polymer that showed extremely high glass transition temperatures (400 °C). Thanks to the presence of polar ethylene oxide groups distributed in the polymer chain, the reinforced intermolecular interactions between polymer and metal collector resulted in an increased electrochemical performance of the polymer when it was directly casted with no need of extra binder leading to a reversible capacity of 205 mAh/g with an 86% of capacity retention after 25 cycles.

No observable improvement was achieved in terms of solubility of the PolySchiff-PEO600 with respect to the bare PolySchiff. Nevertheless, it was possible to disperse the polymer in NMP and use it as binder to prepare slurries of other active materials, which was not possible with bare PolySchiff.

No improved electrochemical performance was observed when using PSB-PEO vs PVdF as binder with Sn nanoparticles as active material due to agglomeration of the nanoparticles and lack of homogeneity of the electrode.

The intrinsic voltage profile of hard carbons entailed that the larger polarization of PSB-PEO compared to that of the PVdF was translated into a lower capacity. For small ratios of binder no activity coming from the PSB-PEO. However, for an 40%wt. of polymer content, PSB-PEO exhibited a double role as active binder contributing to the overall capacity of hard carbon and leading to a reversible capacity of 143 mAh/g<sub>electrode</sub> or 272 mAh/g<sub>active</sub>, larger than that obtained when using PVdF.

Due to the low conductivity of Zn carbodiimide, the insulating nature of the PSB-PEO was not appropriate for getting the electrochemical response of the material

but on the other hand, soft carbons exhibited comparable capacities at low rates proving the good binding properties of the polymer.

In summary PSB-PEO can be successfully casted in laminate form without the addition of any extra binder and maintaining an electrochemical performance comparable to that of bare PS. On the other hand while only 5-10% wt of PSB-PEO can be used to bind other anodic electroactive materials in Na-ion batteries, in overall its performance does not improve that of benchmark PVdF binder mostly due to poorer mechanical properties which in turn affect the electrochemical performance.





---

## Chapter 4. Development of Na-ion full-cells based on polySchiff-PEO and soft carbon anodes.

---

### 4.1 Introduction

Sodium metal anodes are commonly used on the laboratory scale to evaluate the electrochemical performance of electrode materials in a half-cell. The use of metallic Na as the counter electrode and reference electrode facilitates the measurement of the electrochemical properties at the working voltage, which is especially important in order to understand the basic properties of each electrode material. However, the reliability of the half-cell characterization has been called into question after evidencing differences with respect to lithium in the SEI stability formed on the surface of sodium metal anodes as a result of electrolyte degradation reactions.<sup>1,2</sup> According to these studies, since much higher impedance values are recorded for Na than for Li metal anodes, a significantly higher IR drop is expected in Na half-cell when compared with a full-cell configuration. Besides, poorer cyclability for electrode tested in sodium half-cell when compared with full-cell configuration is expected as well as unstable potential measurement when using Na metal as a reference electrode.

---

<sup>1</sup> Iermakova, D. I.; Dugas, R.; Palacín, M. R. and Ponrouch, A., On the comparative stability of Li and Na metal anode interfaces in conventional alkyl carbonate electrolytes, *J. Electrochem. Soc.*, **2015**, 162 (13) A7060-A7066.

<sup>2</sup> Zarrabeitia, M.; Muñoz-Márquez, M. M.; Nobili, F.; Rojo, T. and Casas-Cabanas, M.; Influence of using metallic Na on the interfacial and transport properties of Na-Ion Batteries, *Batteries*, **2017**, 3, 16.

The analysis of full-cells, which take on the complete form of a battery, goes a step further in the understanding of the electrochemical reactions occurring at both the cathode and the anode by allowing a direct measurement of battery characteristics and performance. However, electrode balancing can severely affect performance because the absence of an unlimited source of sodium ions, like when metallic sodium is used as counter-electrode, can lead to lack of sodium after its consumption due to SEI formation on the anode.

The safety issues related to sodium metal currently prevent its use as a negative electrode for commercial applications. The low melting point of Na (98 °C) presents a significant safety hazard in devices designed for use at ambient temperatures using a Na metal electrode.<sup>3</sup> Besides, metallic Na shows high reactivity with organic electrolyte solvents and dendrite formation during Na metal deposition.<sup>4,5</sup> Therefore, there is a need for searching for a rechargeable battery based on an anode material that fulfils all the safety and efficiency requirements. From the point of view of the state-of-the-art of the anode materials for sodium ion batteries, carbon anodes seems to be the most promising material due to its relatively high first cycle coulombic efficiency, low voltage plateau and good electrochemical stability along with environmental friendliness.<sup>6</sup> Moreover, carbon anodes have been reported to exhibit very good electrochemical performance in combination with many cathode materials in sodium-ion cells.<sup>7,8,9</sup> In that sense, the study of a carbonaceous material developed in this thesis as anode in a full-cell would be a window of opportunity to compare the electrochemical properties under realistic conditions. Furthermore, while many studies based on full-cell for carbon anodes have been performed, fewer attempts have been carried out regarding organic electrodes. From a perspective of materials resource sustainability, organic electrodes provide a better option regarding energy consumption and recycling. For that reason, it is also worth studying the performance of polySchiff bases-PEO copolymers as anodes in true battery systems.

---

<sup>3</sup> Palomares, V.; Serras, P.; Villaluenga, I.; Hueso, K. B.; Carretero-González, J. and Rojo, T., Na-ion batteries, recent advances and present challenges to become low cost energy storage systems, *Energy Environ. Sci.*, **2012**, 5, 5884-5901.

<sup>4</sup> Stevens, D. A. and Dahn, J. R., High capacity anode materials for rechargeable sodium-ion batteries, *J. Electrochem. Soc.*, **2000**, 147 (4), 1271-1273.

<sup>5</sup> Kundu, D.; Talaie, E.; Duffort, V. and Nazar, L. F., The emerging chemistry of sodium ion batteries for electrochemical energy storage, *Angew. Chem. Int. Ed.*, **2015**, 54, 3431-3448.

<sup>6</sup> Hou, H.; Qiu, X.; Wei, W.; Zhang, Y. and Ji, X., Carbon anode materials for advanced sodium-ion batteries, *Adv. Energy Mater.*, **2017**, 1602898.

<sup>7</sup> Dugas, R.; Zhang, B.; Rozier, P. and Tarascon, J. M., Optimization of Na-ion battery systems based on polyanionic or layered positive electrodes and carbon anodes, *J. Electrochem. Soc.*, **2016**, 163 (6) A867-A874.

<sup>8</sup> Song, J.; Wang, L.; Lu, Y.; Liu, J.; Guo, B.; Xiao, P.; Lee, J.-J.; Yang, X.-Q.; Henkelman, G. and Goodenough, J. B.; Removal of Interstitial H<sub>2</sub>O in hexacyanometallates for a superior cathode of a sodium-ion battery, *J. Am. Chem. Soc.*, **2015**, 137, 2658-2664.

<sup>9</sup> Alcántara, R.; Jiménez-Mateos, J. M.; Lavela, P. and Tirado, J. L., Carbon black: a promising electrode material for sodium ion batteries, *Electrochem. Commun.*, **2001**, 3, 639-642.

On the cathode side, polyanionic compounds such as sodium transition metal phosphates, fluorophosphates and pyrophosphates are currently under investigation.<sup>10</sup> These materials typically reveal high operating voltages with rather flat profiles, and this makes them interesting for full-cell applications. However, their high molecular weights result in moderate specific capacities.<sup>11</sup> Alternatively, sodium transition metal-based layered oxides (NaMO<sub>2</sub>) with different structures (mostly O3- or P2-type) have been considered to be a promising cathode system for Na-ion batteries due to their high capacity, material cost, and safety.<sup>12,13,14</sup> Moreover, this family of compounds stands out over Prussian Blue analogues because of their better thermal and electrochemical stabilities along with high tap density, which leads to better packing of the material in the device and improved volumetric capacity.

In this chapter, polySchiff-PEO and PVC derived soft carbon anodes are presented in a full cell. A P2-Na<sub>0.67</sub>Fe<sub>0.5</sub>Mn<sub>0.5</sub>O<sub>2</sub> layered sodium oxide was selected as cathode as it provided very good results in sodium half cells.<sup>15</sup> Among all sodium layered oxide candidates, Fe and Mn containing layered oxide was chosen because of advantages including environmental benignity, inexpensiveness, and large reversible capacity.

Because in a full battery a unique electrolyte is used for both electrodes, the electrochemical performance of the materials with the selected electrolyte will be first presented separately as sodium half-cell electrodes. Next, the electrochemical properties of the polymer and the carbon will be shown in the full-cell system and the results will be compared to those of other full-cell systems. 3-electrode measurements are used in the polymer- Na<sub>0.67</sub>Fe<sub>0.5</sub>Mn<sub>0.5</sub>O<sub>2</sub> full-cell to understand the origin of performance, whereas a precycling strategy was followed in the case of SC- Na<sub>0.67</sub>Fe<sub>0.5</sub>Mn<sub>0.5</sub>O<sub>2</sub> full-cell.

One of the most meaningful electrochemical parameters that will be determined is the specific energy. This parameter is useful for comparing the energy content of batteries of different voltage. The specific energy (also called gravimetric energy density) represents the stored energy per unit mass, expressed as watt-hours per kilogram (of

---

<sup>10</sup> Kim, H.; Kim, H.; Ding, Z.; Lee, M. H.; Lim, K.; Yoon, G. and Kang, K., Recent progress in electrode materials for sodium-ion batteries, *Adv. Energy Mat.*, **2016**, 6, 19, 1600943.

<sup>11</sup> Palomares, V.; Casas-Cabanas, M.; Castillo-Martínez, E.; Han, M. H. and Rojo, T. *Energy Environ. Sci.*, **2013**, 6, 2312 – 2337.

<sup>12</sup> Keller, M.; Vaalma, C.; Buchholz, D. and Passerini, S., Development and characterization of high performance sodium-ion cells based on layered oxide and hard carbon, *ChemElectroChem*, **2016**, 3, 1-10.

<sup>13</sup> Han, M. H.; Gonzalo, E.; Sharma, N.; Lopez del Amo, J. M.; Armand, M.; Avdeev, M.; Saiz Garitaonandia, J. J. and Rojo, T.; High-Performance P2-Phase Na<sub>2/3</sub>Mn<sub>0.8</sub>Fe<sub>0.1</sub>Ti<sub>0.1</sub>O<sub>2</sub>, cathode material for ambient temperature sodium-ion batteries, *Chem. Mater.*, **2016**, 28, 106-116.

<sup>14</sup> Han, M. H.; Gonzalo, E.; Singh, G. and T. Rojo, A comprehensive review of sodium layered oxides: powerful cathodes for Na-ion batteries, *Energy Environ. Sci.*, **2015**, 8, 81-102.

<sup>15</sup> Park, K.; Han, D.; Kim, H.; Chang, W.-S.; Choi, B.; Anass, B. and Lee, S., Characterization of a P2-type chelating-agent assisted Na<sub>2/3</sub>Fe<sub>1/2</sub>Mn<sub>1/2</sub>O<sub>2</sub> cathode material for sodium-ion batteries, *RSC Adv.*, **2014**, 4, 22798-22802.

active material in lab scale studies) and is determined by the specific capacities and operating voltages of the anode and the cathode.

The energy obtained from the full cell can be calculated according to Eq. 4.1.

$$\text{Specific energy (W} \cdot \text{h} \cdot \text{kg}^{-1}) = \int_{t_0}^t \text{Capacity (A} \cdot \text{h} \cdot \text{kg}^{-1}) \cdot \text{Voltage (V)} dt \quad (4.1)$$

Where voltage represents the voltage difference between the cathode and the anode at any given point of the charge/discharge curve of the battery. Graphically, specific energy can be calculated as the area under the voltage vs. specific capacity curve resultant of the charge or discharge of the cell. (Figure 4.1)

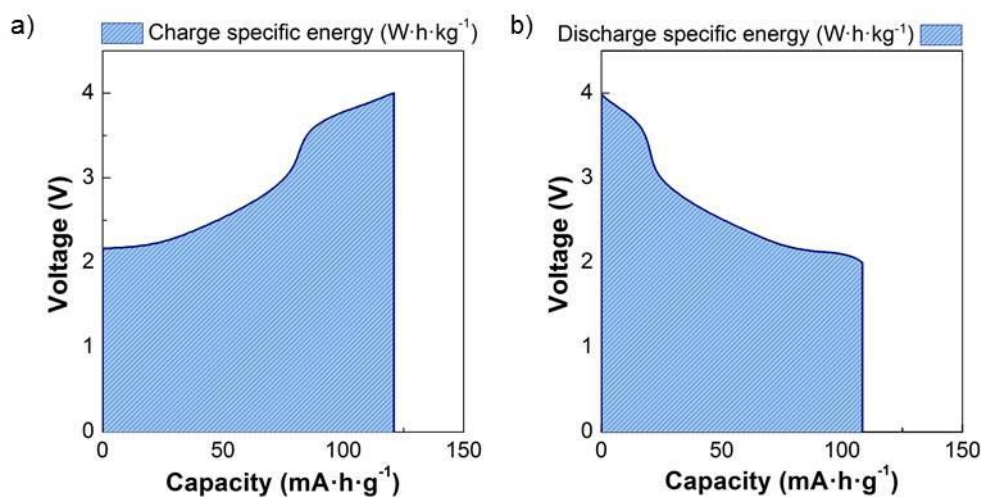


**Figure 4.1** Graphical calculation of the specific energy or gravimetric energy density by means of the calculation of the integral of the electrochemical charge (a) and discharge (b) curves of a sodium ion battery.

Nevertheless, reporting the energy and power densities per weight of active material alone may not give a realistic picture of the performance that the assembled device could reach because the weight of the other device components also needs to be taken into account. Usually, a factor of 3 to 4 is frequently used to extrapolate the energy of the device from the performance of the material.<sup>16</sup> Thus, an energy density value of 200 W·h·kg<sup>-1</sup> of active material could translate into about 50 W·h·kg<sup>-1</sup> of packaged cell. For that reason, the proper choice of the electrode materials is crucial.

<sup>16</sup> Gogotsi, Y. and Simon, P., True performance metrics in electrochemical energy storage, *Science*, **2011**, 334, 917-918.

## 4.2 Experimental

### 4.2.1 Synthesis of sodium layered oxide: P2-Na<sub>0.67</sub>Fe<sub>0.5</sub>Mn<sub>0.5</sub>O<sub>2</sub>

The synthesis of P2-Na<sub>0.67</sub>Fe<sub>0.5</sub>Mn<sub>0.5</sub>O<sub>2</sub> phase was carried out following the co-precipitation method reported by Han *et al.*<sup>17</sup> A mixture of Fe(NO<sub>3</sub>)<sub>3</sub> (8.08 g) and Mn(NO<sub>3</sub>)<sub>2</sub> (5.74 g) was prepared in 100 mL distilled water under vigorous stirring. The pH of nitrates solution was at 1.0. On a separate container, a solution of 4.0 g NaOH in 50 mL of distilled water was prepared. The pH of NaOH solution was measured to be 13. Two solutions were mixed together dropwise and stirred for 6 hours. The final pH was adjusted to be 10. The precipitate was then washed 3 times with distilled water using a centrifuge. The precipitates were mixed with stoichiometric amounts of NaNO<sub>3</sub> (2.27 g) because the use of this nitrate as sodium precursor leads to the crystallization of only the P2-phase without undergoing formation of O3-phase. The pelletized powder (D: 20 mm, T: 2.0 mm) was then annealed at 900 °C (5 °C·min<sup>-1</sup>) for 6 hours under a normal atmospheric conditions. Upon cooling, the pellet was immediately transferred to Ar-filled glove box in order to avoid moisture contact.

### 4.2.2 Electrode preparation of sodium layered oxide: P2-Na<sub>0.67</sub>Fe<sub>0.5</sub>Mn<sub>0.5</sub>O<sub>2</sub>

Due to the air-sensitivity of the material, electrode preparation was carried out in an Ar-filled glove box. The slurry of electrode was prepared by mixing the active material, super carbon C65, and PVdF in a mass ratio of 80:10:10 in NMP (*N*-methyl-2-pyrrolidone) followed by vigorous stirring for 2 hours. The slurry was then casted onto an Al current collector sheet using the mini coater and dried in the vacuum oven at 120 °C for 12 hours. Electrodes were punched out and pressed at 5 tons prior to battery assembly.

### 4.2.3 Electrode preparation of PVC derived soft carbon and PSB-PEO

The PVC-derived soft carbon was synthesized according to the procedure described in chapter 2. The soft carbon laminate electrode contained 90 wt. % of active material, 5 wt. % of Super C65 carbon and 5% wt. of PVdF, while electrodes composed of P2-Na<sub>0.67</sub>Fe<sub>0.5</sub>Mn<sub>0.5</sub>O<sub>2</sub> contained 80 wt. % of active, 10 wt. % of Super C65 and 10 wt. % of PVdF.

<sup>17</sup> Huon Han, M.; Acebedo, B.; Gonzalo, E.; Sánchez-Fontecoba, P.; Clarke, S.; Saurel, D.; Rojo, T, Synthesis and Electrochemistry Study of P2- and O3-phase Na<sub>2/3</sub>Fe<sub>1/2</sub>Mn<sub>1/2</sub>O<sub>2</sub>, *Electrochim. Acta*, **2015**, 182, 1029-1036.

PSB-PEO (P3) electrodes were cast as binder-free electrodes as explained in chapter 3. Therefore, they did not contain any binder and were composed of a 79 wt. % of active material and 21 wt. % of C65.

## 4.3 Results and discussion

### 4.3.1 Structural characterization of P2- $\text{Na}_{0.67}\text{Fe}_{0.5}\text{Mn}_{0.5}\text{O}_2$

The synthesized P2- $\text{Na}_{0.67}\text{Fe}_{0.5}\text{Mn}_{0.5}\text{O}_2$  phase was characterized by powder X-Ray diffraction through Pattern Matching method included in the FullProf program.<sup>18</sup> (Figure 4.2) P2-phase is characterized by oxide layer stacking of  $A_{\text{Na}}AB_{\text{Na}}BA_{\text{Na}}A$  where the  $\text{Na}^+$  cations occupy trigonal prismatic sites and share either all edges or entirely a face with a  $\text{MO}_6$  octahedra in adjacent oxide layers, the iron and manganese being disordered.

The PXRD pattern is in good agreement with simulated patterns without any apparent impurity. P2-phase  $\text{Na}_{2/3}\text{Fe}_{1/2}\text{Mn}_{1/2}\text{O}_2$  crystallizes as hexagonal lattice ( $P6_3/mmc$ ), and the lattice parameters are calculated to be  $a = 2.9309(2) \text{ \AA}$  and  $c = 11.219(2) \text{ \AA}$

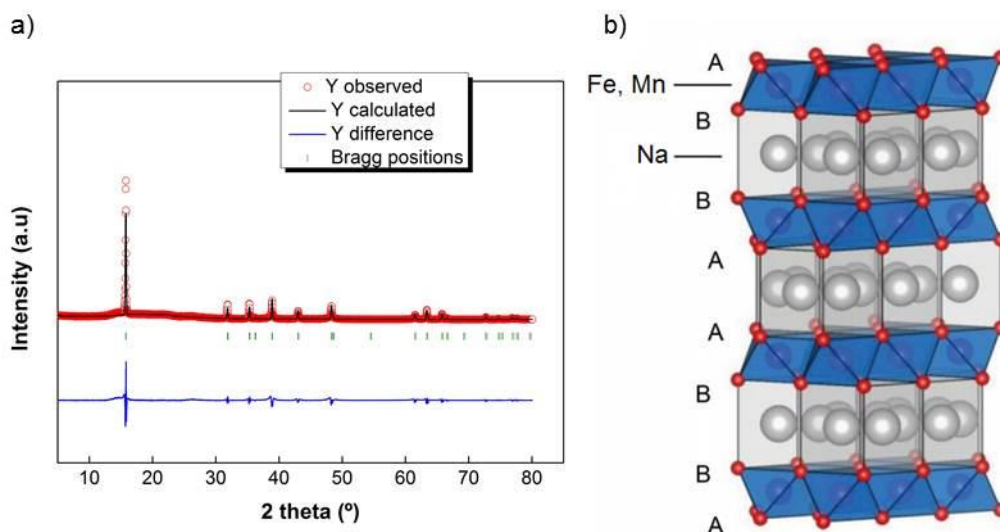


**Figure 4.2** a) Pattern matching of the layered oxide P2-  $\text{Na}_{2/3}\text{Fe}_{1/2}\text{Mn}_{1/2}\text{O}_2$  where red dots are the experimental pattern, black line is the calculated pattern, blue line is the difference between observed and calculated patterns and green ticks are the Bragg positions. b) Structure of the P2- $\text{Na}_{2/3}\text{Fe}_{1/2}\text{Mn}_{1/2}\text{O}_2$  where red balls represent oxygen atoms, grey balls are the two different sodium ions and the octahedral centers are Fe and Mn atoms. Reproduced from ref<sup>19</sup>

<sup>18</sup> Rodríguez Carvajal, J.; *Physica B*, **1993**; 19, 55.

<sup>19</sup> Yabuuchi, N.; Hara, R.; Kajiyama, M.; Kubota, K.; Ishigaki, T.; Hoshikawa, A and Komaba, S., New O2/P2-type Li-excess layered manganese oxides as promising multi-functional electrode materials for rechargeable Li/Na batteries, *Adv. Energy Mater.*, **2014**, 1301453.

### 4.3.2 Electrochemical characterization of P2- $\text{Na}_{2/3}\text{Fe}_{1/2}\text{Mn}_{1/2}\text{O}_2$ in half cell.

To do a proper mass balance in a sodium-ion full-cell it is important to study the performance of the two electrode materials separately by their individual characterization in sodium-metal half cells. Therefore, prior to performing the electrochemical test in full-cell, the P2-  $\text{Na}_{0.67}\text{Fe}_{0.5}\text{Mn}_{0.5}\text{O}_2$  cathode material was potentiostatically and galvanostatically cycled in a sodium half-cell with the same electrolyte that was used for soft carbon (Section 2.3.7) Half-cells were constructed with laminate electrode using 2032 coin cells and 1.0 M  $\text{NaClO}_4$  in EC (ethylene carbonate): PC (propylene carbonate) as electrolyte. The currents were calculated on the basis of a theoretical capacity of  $243 \text{ mA}\cdot\text{h}\cdot\text{g}^{-1}$ . The electrochemical tests were performed within the voltage range of 2.0–4.0 V vs.  $\text{Na}^+/\text{Na}$ .

Figure 4.3 a shows cyclic voltammetry (CV) of the compound. The CV curve shows an oxidation peak at approximately 3.9 V and a reduction peak at 3.8 V, corresponding to the redox couples of  $\text{Mn}^{3+/4+}$  and  $\text{Fe}^{3+/4+}$ . Accordingly, Figure 4.3b shows non-defined *plateaus* or *pseudo-plateaus* at the same voltage values in the voltage profile for the typical discharge-charge cycles from 2.0 to 4.0 V vs.  $\text{Na}^+/\text{Na}$ . In that voltage range, the electrode delivered a charge capacity of  $78 \text{ mA}\cdot\text{h}\cdot\text{g}^{-1}$  after the first charge corresponding to a final Na content of 0.35. After the first discharge,  $114 \text{ mA}\cdot\text{h}\cdot\text{g}^{-1}$  were obtained corresponding to a final Na content of 0.77 (P2-  $\text{Na}_{0.77}\text{Fe}_{0.5}\text{Mn}_{0.5}\text{O}_2$ ). In the second charge and discharge capacities of 119 and  $114 \text{ mA}\cdot\text{h}\cdot\text{g}^{-1}$ , respectively were observed corresponding to approximately 0.46 reversible Na ions and to a final Na content of 0.80 (P2-  $\text{Na}_{0.80}\text{Fe}_{0.5}\text{Mn}_{0.5}\text{O}_2$ ) after the second discharge. The cycle life of the material is shown in Figure 4.3 c . It is observed that the P2 phase exhibited gradual capacity loss during cycling being the discharge capacity retention of 82 % after 25 cycles at C/10 rate.

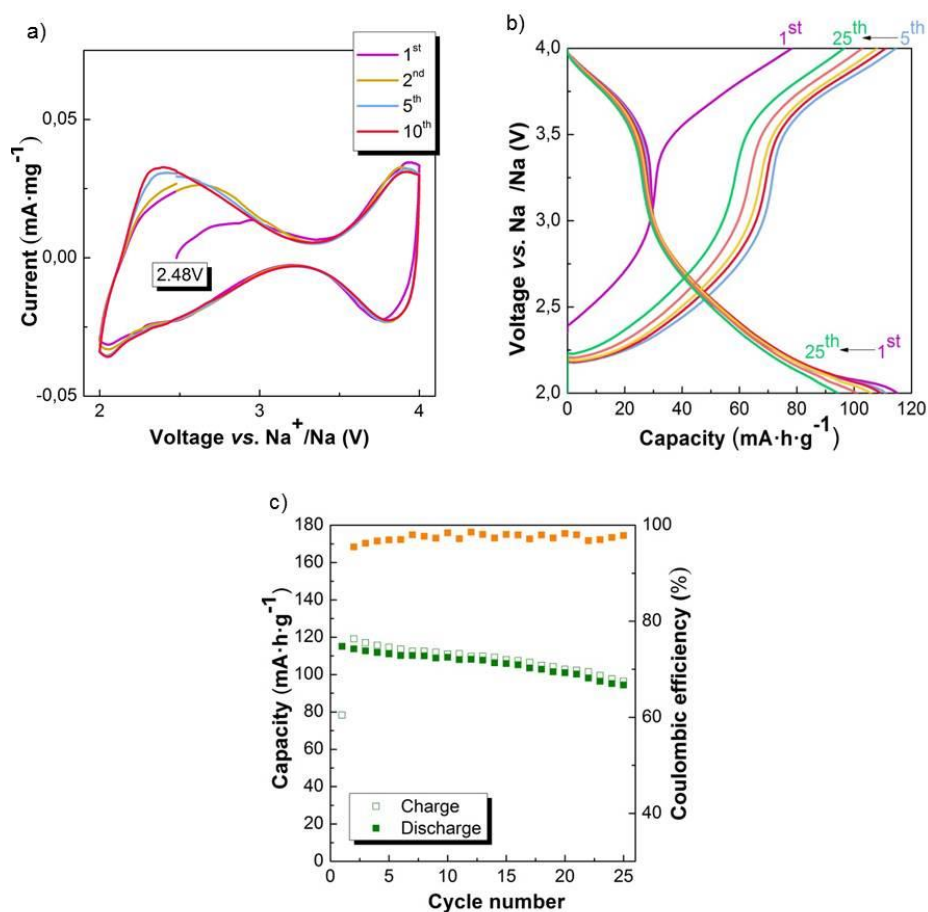


**Figure 4.3** a) Cyclic voltammograms (scan rate of 0.1 mV·s<sup>-1</sup> within the potential range of 2.0–4.0 V), b) voltage vs. capacity profile and c) cycle life at C/10 rate of P2-Na<sub>0.67</sub>Fe<sub>0.5</sub>Mn<sub>0.5</sub>O<sub>2</sub> phase.

### 4.3.3 Electrochemical performance of PSB-PEO in a full-cell

Both cathode (P2-Na<sub>0.67</sub>Fe<sub>0.5</sub>Mn<sub>0.5</sub>O<sub>2</sub>) and anode (PSB-PEO) were used in laminate form. P2-Na<sub>0.67</sub>Fe<sub>0.5</sub>Mn<sub>0.5</sub>O<sub>2</sub> electrode was prepared as in the previous section. Even though 1M NaTFSI in MeTHF was proven to provide better electrochemical performance for PS in sodium half-cell, 1.0 M NaClO<sub>4</sub> in EC (ethylene carbonate) : PC (propylene carbonate) was used as electrolyte. The reason is to avoid electrolyte decomposition at high voltages because NaClO<sub>4</sub> in EC : PC has been reported to be one of the electrolytes showing largest electrochemical potential window stability.<sup>20</sup>

<sup>20</sup> Ponrouch, A.; Marchante, E.; Courty, M.; Tarascon, J.-M. and Palacín, M. R.; In search of an optimized electrolyte for Na-ion batteries, *Energy Environ. Sci.*, **2012**, 5, 8572–8583.



## 2-electrode full-cell

Initially, electrochemical tests in full-cells were performed in CR2032 coin cells in the 0.005-1.6 V voltage range (based on the anode). The current (20  $\mu\text{A}$ ) was calculated on the basis of a C/10 rate for a mass loading of active material of 0,98 mg of PSB-PEO and a theoretical capacity observed for the anode of approximately  $200 \text{ mA}\cdot\text{h}\cdot\text{g}^{-1}$  in a half-cell. Considering the specific reversible and first cycle irreversible capacities of  $\text{Na}_{0.67}\text{Fe}_{0.5}\text{Mn}_{0.5}\text{O}_2$  ( $Q_{\text{rev}}=114 \text{ mA}\cdot\text{h}\cdot\text{g}^{-1}$ ,  $Q_{\text{irrev}}=36 \text{ mA}\cdot\text{h}\cdot\text{g}^{-1}$ , Figure 4.3 b) and Schiff Bases carbon ( $Q_{\text{rev}}=206 \text{ mA}\cdot\text{h}\cdot\text{g}^{-1}$  and  $Q_{\text{irrev}}=334 \text{ mA}\cdot\text{h}\cdot\text{g}^{-1}$ ) the cathode was put in excess (a ratio of 3.09 mg of cathode for 1 mg of anode). Figure 4.4 shows the electrochemical performance of the full-cell.

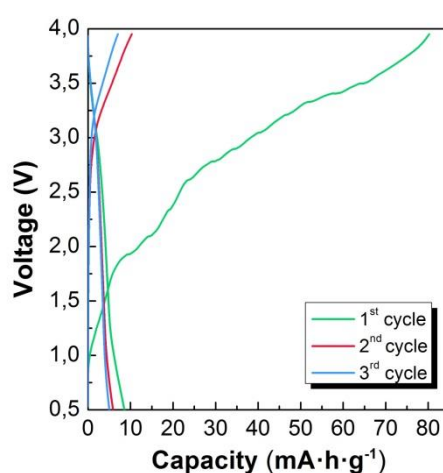


**Figure 4.4** Voltage profile vs. capacity of the full cell composed of P2-  $\text{Na}_{0.67}\text{Fe}_{0.5}\text{Mn}_{0.5}\text{O}_2$  phase and PSB-PEO as cathode and anode respectively at a current of 200  $\mu\text{A}$  the potential range of 1.6-0.005 V based on the anode load.

The open circuit voltage of the full cell was around 0.6 V. Initially, the cathode is oxidized so sodium ions are deintercalated from the P2-  $\text{Na}_{0.67}\text{Fe}_{0.5}\text{Mn}_{0.5}\text{O}_2$  phase causing the oxidation of the transition metals and the reduction of the polyazomethine anode. As consequence, the full-cell is charged up to 3.8 V reaching a capacity of  $80 \text{ mA}\cdot\text{h}\cdot\text{g}^{-1}$ . During the discharge of the full-cell, the voltage reaches 0.5 V very fast, providing a very small capacity of just  $5 \text{ mA}\cdot\text{h}\cdot\text{g}^{-1}$ .

This lack of reversibility of the redox processes might be ascribed to the existence of a huge  $\text{Na}^+$  ions consumption on the anode side during the first charge of the full-cell due to SEI formation. This sodium consumption is particularly problematic considering that sodium deficiency of P2-  $\text{Na}_{0.67}\text{Fe}_{0.5}\text{Mn}_{0.5}\text{O}_2$  gives a significant reduction in the delivered capacity when using non-sodium containing anode material like PSB-PEO.

On the other hand, 1M NaFSI MeTHF electrolyte was the optimum electrolyte for polySchiff bases materials.<sup>21</sup> Therefore, the choice of 1.0 M NaClO<sub>4</sub> in EC (ethylene carbonate) : PC (propylene carbonate) for comparative purposes, might be detrimental for the performance of the PSB-PEO anode as it might be causing the dissolution of the material or providing insufficient electrolyte uptake.

### **3-electrode full cell**

The fact that the electrochemical measurements in two-electrode full-cells allowed no distinction of the contribution of the cathode and the anode to the capacity separately, the assembly of three-electrode full-cells turned out to be necessary because with additional use of a reference electrode, the full-cell is able to reflect the electric potential difference between the two electrodes through individual measurements at the cathode and anode.

For the three-electrode full-cell assembly (Figure 4.5 a), laminate electrodes of P2-Na<sub>0.67</sub>Fe<sub>0.5</sub>Mn<sub>0.5</sub>O<sub>2</sub> phase and PSB-PEO were employed being the masses of the active materials 3.03 mg and 0.98 mg, respectively. The excess of cathode material (3.09 times the amount of mass of the anode) compensated the higher capacity of the anode electrode compared to the cathode leading to an upper voltage of almost 4 V during charge.

---

<sup>21</sup> Castillo Martínez, E.; Carretero-González, J. and Armand, M. Polymeric Schiff bases as low voltage redox centers for sodium ion batteries, *Angew. Chem. Int. Ed.*, **2014**, 53, 5341-5345.

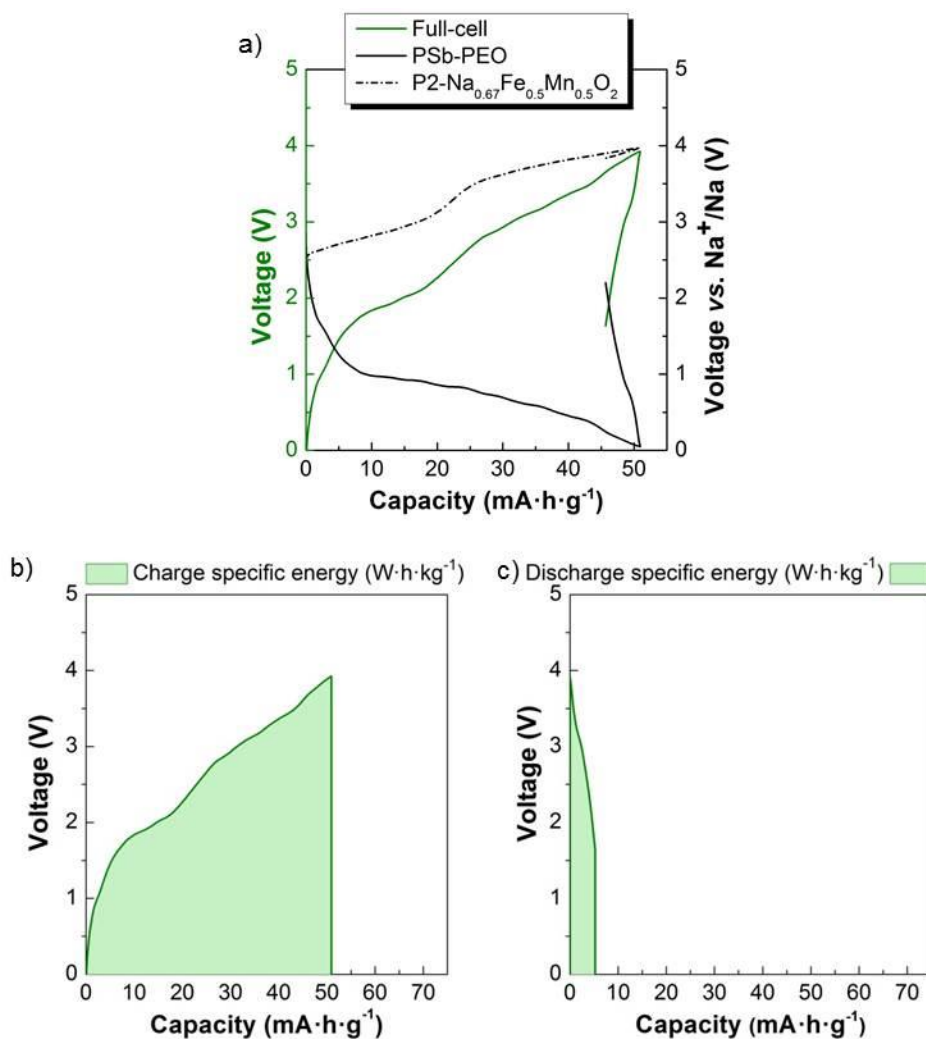


**Figure 4.5** a) Electrochemical behavior of the anode (black line), cathode (black dash/dotted line) and full-cell (green line) of P2- Na<sub>0.67</sub>Fe<sub>0.5</sub>Mn<sub>0.5</sub>O<sub>2</sub> /PSB-PEO full-cell. b) Calculation of the energy density by integration of the curve in the first charge and c) calculation of the energy density by integration of the curve in the first discharge.

Initially, the full-cell was charged and the oxidation of the cathode led to a *pseudo*-plateau around 3.8 V vs. Na<sup>+</sup>/Na which is consistent with that observed in the sodium half-cell related to the Mn<sup>3+</sup> and Fe<sup>3+</sup> oxidation. At the same time, the reduction of the PSB-PEO proceeded through a *pseudo*-plateau below 1 V vs. Na<sup>+</sup>/Na, which is attributed to the polyazomethine reduction. However, the typical pseudo-plateau of the PSB-PEO centered at 0.6 V vs. Na<sup>+</sup>/Na during reduction is not observed when cycling in the full-cell. In Figure 4.6 the  $\delta Q/\delta V$  curves of the first cycle of the PSB anode in the 3-electrode full-cell is represented and compared to that of the PSB anode in a sodium half-cell.

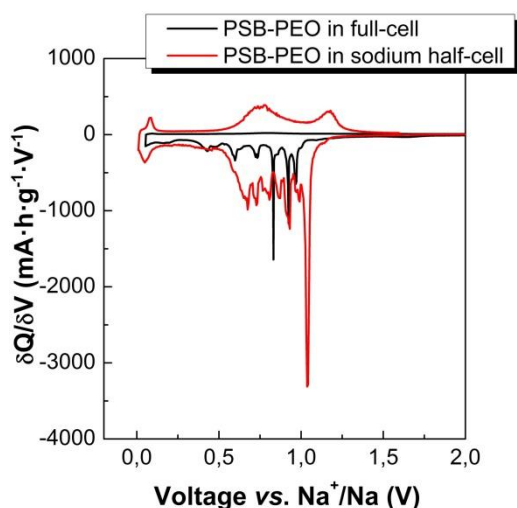


**Figure 4.6** First cycle differential capacity curves of PSB-PEO in sodium half-cell and in the 3-electrode full cells based on P2-  $\text{Na}_{0.67}\text{Fe}_{0.5}\text{Mn}_{0.5}\text{O}_2$  as cathode and PSb-PEO as anode.

It is observed that during the first reduction, the peaks at 1.09 V vs.  $\text{Na}^+/\text{Na}$ , which are responsible for the PSB-PEO redox activity along with the peak at 0.63 V is not present in the PSB-PEO cycled in the full-cell but only when cycled in the half-cell. The absence of that peak might be related to the lack of reversibility of the redox processes in the next charge. Except for that peak, the same redox processes seem to occur in both cells with subtle differences in their intensity and potential.

The lack of reversibility of the anode was confirmed in view of the voltage profile of the curve relating to the PSB-PEO which is unable to provide reasonable capacity when oxidizing it after reduction. As a consequence, only  $5 \text{ mA}\cdot\text{h}\cdot\text{g}^{-1}$  were reversibly obtained after the first discharge in the full-cell indicating that, although showing good electrochemical performance when tested in half-cell, the applications of PSB-PEO in full-battery systems are severely hindered by the lack of reversibility of the redox processes. Again, the lack of reversibility can be explained as a consequence of huge sodium consumption in the first cycle due to the inherent irreversible capacity of the PSB-PEO, which reaches a 163 % of the reversible capacity in a sodium half-cell. In order to overcome the irreversibility of the anode, it would be necessary to pre-cycle the polymer anode in a sodium half-cell configuration so that the SEI can be formed at the expense of the metallic sodium instead of the P2- $\text{Na}_{2/3}\text{Fe}_{1/2}\text{Mn}_{1/2}\text{O}_2$  cathode. On the other hand, in view of the fact that PSB-PEO suffers from capacity decay after 25 cycles retaining 85 % of the initial reversible capacity in the sodium half-cell, degradation of the electrode by means of loss of interparticle contact and detachment from the Cu foil was thought to be a plausible reason for the lack of reversibility of the redox process in the anode. However, no visible delamination was observed and nor in the SEM pictures of the cycled electrodes rinsed with PC (Figure 4.7).

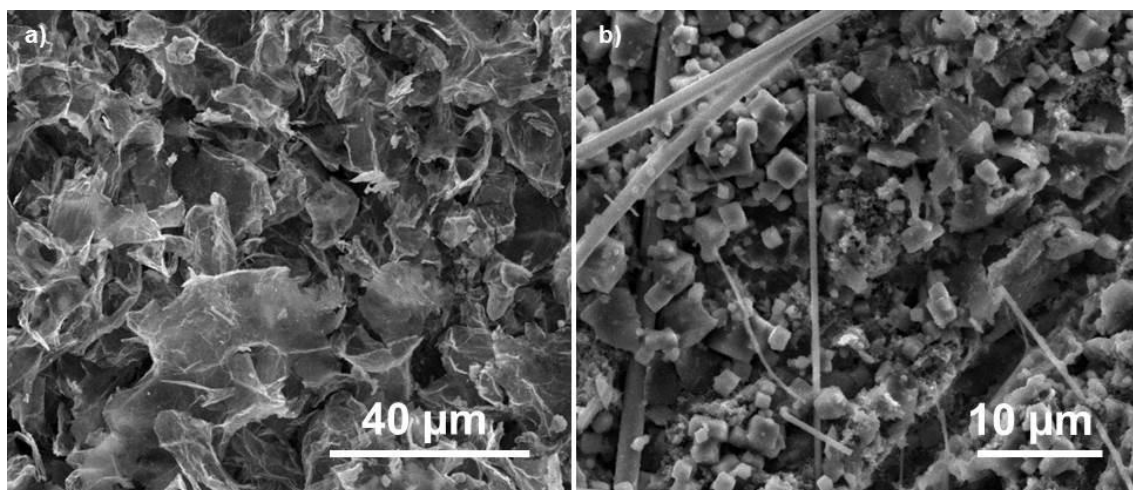


**Figure 4.7** a) SEM images (SE mode) of the cycled electrodes (5 cycles) in the three-electrode full-cell (2400x) and b) SEM image (SE mode) at higher magnification (12000x) on a different area of the electrode.

The flakes corresponding to the PSB-PEO are observed in Figure 4.7a. Additionally, many areas of the electrode (Figure 4.7 b) appeared fully covered with glass fiber residues from the separator, as well as with a cubic salt that is, arguably,  $\text{NaClO}_4$  salt from the electrolyte despite the electrode had been rinsed with a small fraction of PC (solvent of the electrolyte) with the purpose of washing it..

Although the energy density value does not represent the feasibility of the  $\text{P2-Na}_{0.67}\text{Fe}_{0.5}\text{Mn}_{0.5}\text{O}_2$  phase /PSB-PEO system, it was calculated for comparative purposes. Given the fact that the redox processes are not reversible after the first charge of the full-cell, the integration of the electrochemical curve so as to calculate the energy density was performed over the first charge and discharge. The integration provided a charge specific energy of  $131 \text{ W}\cdot\text{h}\cdot\text{kg}^{-1}$  and a discharge specific energy of  $15 \text{ W}\cdot\text{h}\cdot\text{kg}^{-1}$ . Considering the discharge specific energy, the average voltage can be calculated as 3V, which is a good voltage, but unfortunately meaningless given the very low round trip efficiency of approximately 12%

$$\text{Voltage} = \frac{15 \text{ W} \cdot \text{h} \cdot \text{kg}^{-1}}{5 \text{ A} \cdot \text{h} \cdot \text{kg}^{-1}} = 3.0 \text{ V} \quad (4.2)$$

In short, despite showing relatively high reversible capacity and acceptable cycling stability in sodium half-cells, an optimization of the PSB-PEO would be necessary to make the material appropriate as an anode of a full-cell. Considering that the poor reversibility is related to the huge sodium consumption during SEI formation, a decrease of the intrinsic irreversible capacity of the PSB-PEO would be required. To do so, it would be necessary to diminish the surface area of the material so as to get a minimally porous material.

#### 4.3.4 Electrochemical performance of PVC-derived hard carbon||P2- $\text{Na}_{0.67}\text{Fe}_{0.5}\text{Mn}_{0.5}\text{O}_2$ full cell

##### Precycling of the electrode in sodium half-cell.

The low sodium content of the cathode along with the sodium consumption during SEI formation on the anode would result in extremely low sodium content after the first cycle in the full-cell. Therefore both electrodes were precycled, using 1.0 M  $\text{NaClO}_4$  in EC (ethylene carbonate): PC (propylene carbonate) as electrolyte. This way, it is possible to induce the SEI formation on the anode in the presence of an unlimited source of sodium ions (the metallic sodium counter electrode of the half-cell). Both cathode (P2- $\text{Na}_{0.67}\text{Fe}_{0.5}\text{Mn}_{0.5}\text{O}_2$ ) and anode (PVC-derived soft carbon) laminate electrodes were cycled 2 times in a sodium half-cell prior to full-cell assembly at a current density equivalent to C/10 rate. Cathodes were cycled in the 2.0-4.0 V vs.  $\text{Na}^+/\text{Na}$  range so as to reach a fully sodiated state whereas the anode was cycled in the 0.002-2V vs.  $\text{Na}^+/\text{Na}$  range in order to obtain a SEI built Na free phase. After cycling, electrodes were rinsed with PC and dried in a vacuum oven at 120 °C for 12 hours.

In Figure 4.8, the voltage profiles of the first and second cycles of the pre-cycled electrodes are shown.

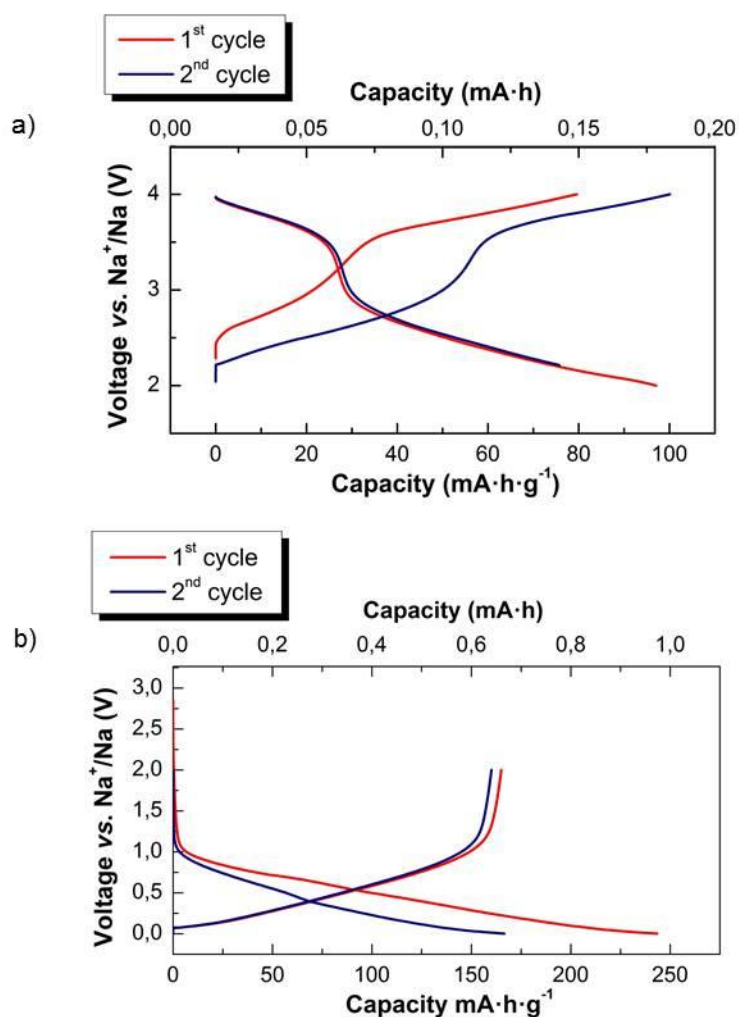


**Figure 4.8** Electrochemical performance (precycling) of the P2- Na<sub>0.67</sub>Fe<sub>0.5</sub>Mn<sub>0.5</sub>O<sub>2</sub> phase (a) and PVC-derived soft carbon (b) in sodium half-cells

It was observed that PVC led to a first cycle irreversible capacity of 78 mA·h·g<sup>-1</sup> and a reversible capacity of 165 mA·h·g<sup>-1</sup> whereas P2-Na<sub>0.67</sub>Fe<sub>0.5</sub>Mn<sub>0.5</sub>O<sub>2</sub> phase provided a charge and discharge capacity of 80 and 72 mA·h·g<sup>-1</sup> respectively. The fact that P2-Na<sub>0.67</sub>Fe<sub>0.5</sub>Mn<sub>0.5</sub>O<sub>2</sub> provided lower capacity after the second discharge (0.13 mA·h) than PVC-derived soft carbon after the second charge (0.63 mA·h) evidenced that the cathode was the limiting electrode. The anode was in excess with respect to the cathode in a ratio of 2.22 mg of anode for each gram of cathode.

### **Full cell performance**

The electrochemical tests in full-cells were performed in CR2032 coin cells using the same electrolyte as for half-cells in the 3.8-1.0 V voltage range at C/10 based on the cathode material loading. Figure 4.9 shows the electrochemical performance of the full-cell. The voltage profile of the full-cell is different from the performance of the electrodes in half cells because it is the difference in voltage between both electrodes and therefore reflects both cycling profile shapes: that of the anode and that of the

cathode. In the first cycle, sodium ions were deintercalated from the  $\text{P2-Na}_{0.67}\text{Fe}_{0.5}\text{Mn}_{0.5}\text{O}_2$  causing the oxidation of the Fe and Mn from 3+ to 4+, and inserted into the soft carbon, leading to its reduction. The full-cell reached a charge capacity of  $51 \text{ mA}\cdot\text{h}\cdot\text{g}_{(\text{cathode}+\text{anode})}^{-1}$  followed by subsequent discharge capacity of  $29 \text{ mA}\cdot\text{h}\cdot\text{g}_{(\text{cathode}+\text{anode})}^{-1}$ . The fact that the capacity provided by the full-cell is smaller than that of the half-cell might be a consequence of the existence of side reactions leading to inactive sodium ions. After 25 cycles, the discharge capacity retention was 76 % meaning that the degradation of the electrodes or the electrolyte might be taking place.

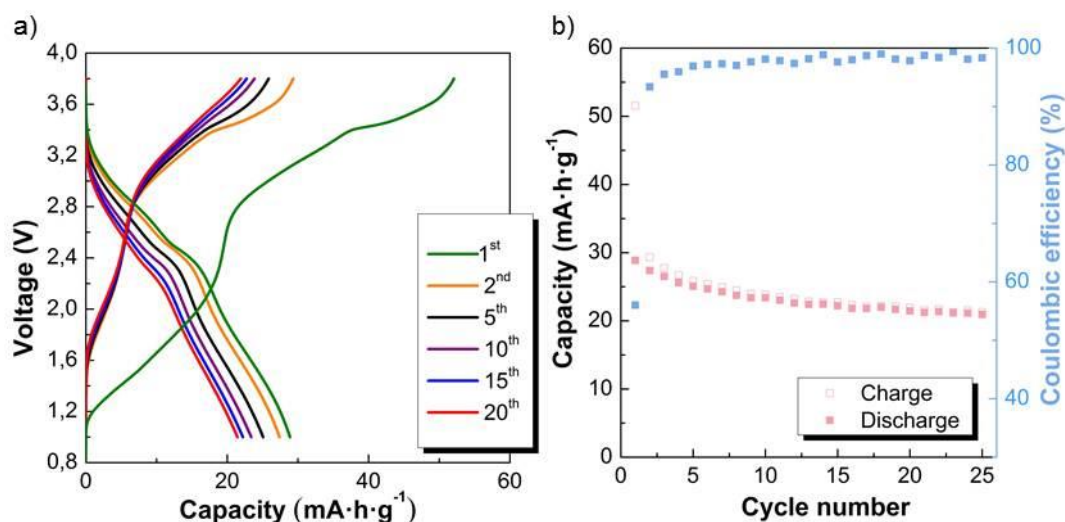


**Figure 4.9** a) Voltage profile vs. capacity of the full cell composed of P2-  $\text{Na}_{0.67}\text{Fe}_{0.5}\text{Mn}_{0.5}\text{O}_2$  phase and PVC-derived hard carbon and b) cycling performance of the full cell during 25 cycles at C/10 within the potential range of 3.8-1.0 V at C/10 based on the cathode load.

The integration of the charge and discharge curve provided an energy density of 90 and  $62 \text{ W}\cdot\text{h}\cdot\text{kg}^{-1}$  respectively as it can be seen in Figure 4.10. The ratio between the energy recovered in discharge and the energy spent on charge (energetic efficiency) was 69 %. This value is lower than those observed for analogous  $\text{Na}_{0.67}\text{Fe}_{0.5}\text{Mn}_{0.5}\text{O}_2$  / Hard carbon (Super P) system reported in the literature<sup>22</sup>, which provides as much as  $234 \text{ W}\cdot\text{h}\cdot\text{kg}^{-1}$  with an 88% of energetic efficiency.

<sup>22</sup> Dugas, R.; Zhang, B.; Rozier, P. and Tarascon, J. M. Optimization of Na-ion battery systems based on polyanionic or layered positive electrodes and carbon anode, *J. Electrochem. Soc.*, **2016**, 163 (6) A867-A874.



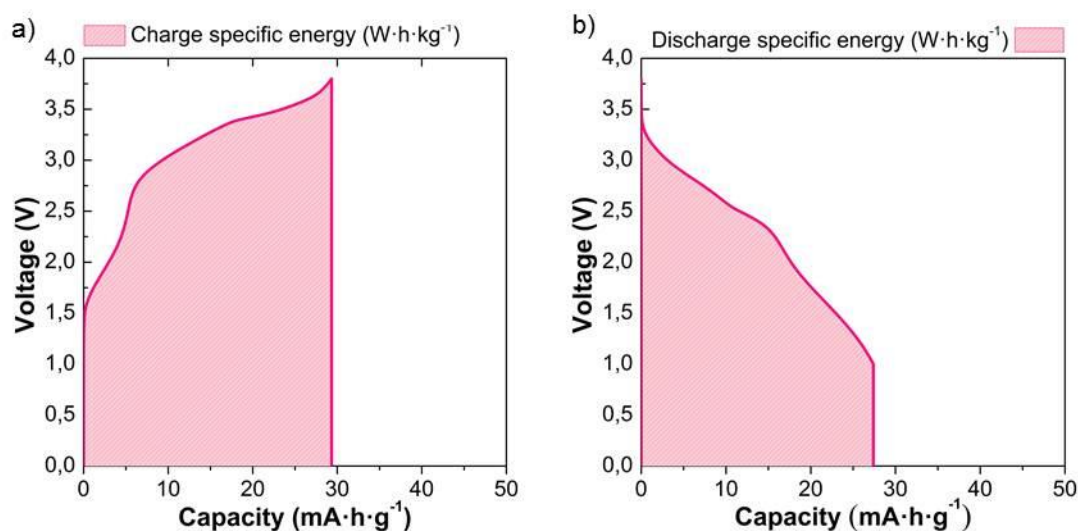


**Figure 4.10** Graphical calculation of energy density by the integration of the curve in the second charge and second discharge of the P2- Na<sub>0.67</sub>Fe<sub>0.5</sub>Mn<sub>0.5</sub>O<sub>2</sub> /Hard carbon system.

By knowing the energy and capacity of the discharge, the average voltage can be calculated from equation 5.2. The average voltage was calculated to be 2.26 V, which is moderate for real application. In order to increase the energy density of the cell and considering that up to now, layered oxides are the cathodes exhibiting largest reversible capacities in sodium ion batteries, it would be necessary to use another anode showing improved capacity retention upon cycling as well as larger potential difference.

$$\text{Voltage} = \frac{62 \text{ W} \cdot \text{h} \cdot \text{kg}^{-1}}{29 \text{ A} \cdot \text{h} \cdot \text{kg}^{-1}} = 2.14 \text{ V} \quad (5.3)$$

On the other hand, the optimization of other parameters such as the choice of electrolyte or additives, which can affect the overall capacity of the cell, is crucial to get a large energy density. For example, Komaba *et al.* demonstrated that the addition of a 0.5 % FEC to the NaPF<sub>6</sub> PC and PC : EC is optimal for higher capacity and better cyclability.<sup>23</sup> According to their study, fluorine compounds help to form an electronically-insulating, ionically-conducting, and insoluble surface layer to effectively passivate the electrode surface of hard carbon.

<sup>23</sup> Dahbi, M.; Nakano, T.; Yabuuchi, N.; Fujimura, S.; Chihara, K.; Kubota, K.; Son, J.-Y.; Cui, Y.-T.; Oji, H.; Komaba, S., Effect of hexafluorophosphate and fluoroethylene carbonate on electrochemical performance and the surface layer of hard carbon for sodium-ion batteries, *ChemElectroChem*, **2016**, 3 (11), 1856-1867.

### 4.3.5 Comparison of the electrochemical performance of PVC-derived hard carbon

In Table 4.1, the experimental values of voltage, capacity and energy density of the full-cells developed in this chapter are represented and compared to a full-cell developed in CIC Energigune consisting of the same P2-  $\text{Na}_{0.67}\text{Fe}_{0.5}\text{Mn}_{0.5}\text{O}_2$  cathode and commercial hard carbon (Kureha Corporation) as anode.

**Table 4.1** Experimental values of average voltage and energy density of the second discharge of the full-cells prepared with P2-  $\text{Na}_{0.67}\text{Fe}_{0.5}\text{Mn}_{0.5}\text{O}_2$  phase as cathode and carbon or PSB as anodes. The capacity calculation was referred to the sum of the masses of the anode and the cathode.

Cathode material	Anode material	Capacity ( $\text{A}\cdot\text{h}\cdot\text{kg}^{-1}$ )	$\Delta V$ (V)	Energy density ( $\text{W}\cdot\text{h}\cdot\text{kg}^{-1}$ )
P2- $\text{Na}_{0.67}\text{Fe}_{0.5}\text{Mn}_{0.5}\text{O}_2$	Kureha HC	48	2,9	139
P2- $\text{Na}_{0.67}\text{Fe}_{0.5}\text{Mn}_{0.5}\text{O}_2$	PVC SC	29	2,1	62
P2- $\text{Na}_{0.67}\text{Fe}_{0.5}\text{Mn}_{0.5}\text{O}_2$	PSB-PEO	5	3.0	15

The use of commercial hard carbon leads to better capacity, voltage and energy density than the use of PVC soft carbon. Contrary to hard carbons, which show two distinctive regions in the discharge voltage profile (sloping and plateau regions corresponding to insertion between graphene sheets and adsorption into the pores, respectively), soft carbons do only have the sloping region. Therefore, the capacity provided by soft carbons is expected to be smaller to that of hard carbons.<sup>24</sup> Despite lignin hard carbons developed in this work might have led to larger capacity and energy density values in full-cell given their larger capacity in sodium half-cell, the existence of a randomly observed trailing plateau during charge prevented their study in full-cell system. The electrochemical performance of PVC-soft carbons, although they showed lower capacity, was more consistently reproducible.

As previously mentioned, the P2- $\text{Na}_{0.67}\text{Fe}_{0.5}\text{Mn}_{0.5}\text{O}_2$ /PSB-PEO provides poor capacity. In order to increase the poor capacity value, which has been related to the excessive sodium consumption during the first cycle, it would be possible to use  $\text{NaN}_3$  as an additive. This compound can be used as an extra reservoir of sodium compensating the sodium depletion when it is decomposed during cycling to form  $\text{Na}^+$  and  $\text{N}_2$ .<sup>25</sup> However, this approach was discarded because in order to use the  $\text{NaN}_3$  salt, cycling conditions and separate compartment dimensions in which the gases generated during

<sup>24</sup> Stevens, D. A. and Dahn, J. R.; The mechanisms of lithium and sodium insertion in carbon materials, *J. Electrochem. Soc.*, **2001**, 148 (8), A803-A811.

<sup>25</sup> Martinez De Ilarduya, J. Otaegui, L.; López del Amo, J. M.; Armand, M. and G. Singh,  $\text{NaN}_3$  addition, a strategy to overcome the problem of sodium deficiency in P2  $\text{Na}_{0.67}[\text{Fe}_{0.5}\text{Mn}_{0.5}]\text{O}_2$  cathode for sodium-ion battery, *J. Power Sources*, **2017**, 337, 197-203.

formation can be stored have to be carefully selected in order to avoid overpressure entailing an extra cost and effort on optimization.

## **4.4 Conclusions**

An organic (PSB-PEO) and a carbonaceous (PVC derived hard carbon) material have been tested in a full cell using a layered oxide (P2-  $\text{Na}_{0.67}\text{Fe}_{0.5}\text{Mn}_{0.5}\text{O}_2$  phase) as cathode in order to compare the performance in complete form of a battery, in which electrochemical reactions occurring at both the cathode and the anode can induce a different behavior from that observed in a half-cell. Being the ratio between the masses of the anode and the cathode a key parameter so as to get the most out of the electrochemical performance, a proper balance was found in which the cathode was in larger proportion than the PSB-PEO (3 : 1 for cathode and anode). Despite PSB-PEO shows good cycling performance with a reversible capacity of  $206\text{mAh/g}_{\text{anode}}$  at  $19.2\text{mA/g}_{\text{anode}}$  in sodium half-cell, when tested in a full-cell, the lack of reversibility of the redox process after the first reduction of the anode makes the material inadequate for its use in a real device, with only  $5\text{mAh/g}_{\text{cathode+anode}}$  being reversibly extracted. PVC derived soft carbon, on the contrary, has shown good compatibility with the P2-  $\text{Na}_{0.67}\text{Fe}_{0.5}\text{Mn}_{0.5}\text{O}_2$  cathode in a full-cell leading to an energy density value of  $62\text{ W}\cdot\text{h}\cdot\text{kg}^{-1}$ . Nevertheless, the ratio between anode and cathode was not properly adjusted leading to a large excess of anode that result in a decrease of the energy density of the cell.



---

# Chapter 5: Conclusions and perspectives

---

## 5.1 Conclusions

After discussing the results of this work, several conclusions can be drawn:

1. Pyrolysis of both sugar and natural lignin isolated from black liquor lead to the formation of hard carbon while pyrolysis of PVC leads to soft carbon.
2. Lignin and sugar derived hard carbons show similar internal microporosity, low superficial area and degree of disorder.
3. The hard carbon obtained from the pyrolysis of lignin (isolated from a byproduct of the paper industry) shows good electrochemical properties as anode of sodium ion batteries.
4. Different parameters such as heating rate, argon flow rate, dwell time at the highest temperature, grinding of the precursor, age of lignin, and maximum temperature of pyrolysis have significant influence on the electrochemical behavior of the lignin based materials.

5. The optimized lignin derived hard carbon after pyrolysis at 900 °C exhibits better electrochemical performance than the hard carbon derived from sugar obtained at higher temperature of carbonization (1050 °C).
6. The reversible capacity of lignin derived hard carbons depends directly on the polarization between charge and discharge which is directly affected by the impurities content.
7. Lignin derived hard carbons show comparable electrochemical performance to that of other biomass derived hard carbons, like sugar, which is a debatable precursor because of being valuable food for people.
8. The incorporation of polyethylene oxide (PEO) in the polySchiff bases polymer (PSB) backbone allowed obtaining polySchiff base-PEO copolymers (PSB-PEO).
9. Insertion of PEO blocks into the PSB backbone increased the ionic conductivity together with the processability and adhesion properties of the material. However, the solubility of this material in different solvents (like NMP) was not good enough to be used as a conventional binder.
10. The PSB-PEO polymers can act as binder-free anode material showing good binding properties and exhibiting promising electrochemical properties with reversible capacities up to 205 mA·h·g<sup>-1</sup>, 98 % coulombic efficiency (25<sup>th</sup> cycle) and 86 % capacity retention after 25 cycles at low C rates (C/10).
11. PSB-PEO can be also used as smart redox active binder of hard carbon anodes providing comparable performance to PVdF based electrodes at low loadings and additional capacity to the electrode at high loadings.

12. The failure of the full-cell composed of PSB-PEO as anode and the P2- $\text{Na}_{0.67}\text{Fe}_{0.5}\text{Mn}_{0.5}\text{O}_2$  layered oxide as cathode is attributed to the lack of reversibility of the organic anode.
13. A full-cell prepared by using PVC-derived soft carbon as anode and the same layered oxide cathode has been successfully built delivering an energy density of  $62 \text{ W}\cdot\text{h}\cdot\text{kg}^{-1}$  (cathode + anode).

## 5.2 Future perspectives

Considering the actual scenario, recent progress during the development of this work and practical issues, the following future perspectives of sodium ion batteries can be devised:

**General requirements.** More efforts are needed directed towards the development of high capacity, non-toxic, easy-to-synthesize and scalable electrode materials such as the hard and soft carbons developed in this thesis. The choice of precursors should be oriented towards the use of low-cost compounds that does not conflict with other needs like feeding as it happens with sugar. Converting harmful or valueless local biomass wastes into high-value functional materials as for example wood chips, fruit pits, polymer waste should be considered. Alternatively, more organic electrodes designed through non-expensive and mild protocols as PSB polymers could provide a reasonable path to the cost reduction.

Strategies to increase the energy density by controlling the microstructure (degree of disorder and porosity) of the carbon anodes and thus, the capacity, should be carried out. In the case of hard carbons which show a very low voltage plateau, the use of these materials as anodes with a suitable cathode and proper balance among them, could give rise to an increase of the energy density of the cell. For organic electrodes, the insertion of appropriate substituents can shift the redox voltage of the insertion reaction. Therefore, synthetic strategies should

focus on tuning the redox voltage and decreasing the inactive weight of the active molecules or polymers in order to increase the gravimetric capacity. The use of additives that allow operating at higher voltages would be another reasonable way to increase energy density.

**Development of smart-binders.** In this work we have developed PSB-PEO polymers as active material that does not require any additional binder to be casted into an electrode but it still requires additional conducting additive. Development of smart-binders combining binder properties and electronic conductivity could increase the energy density by decreasing the amount of inactive components needed. The development of these smart binders for Na-ion batteries would be also an interesting approach avoiding also the loss of electrical contact during electrode expansion and contraction associated with materials that undergo alloying reactions.

**Understanding mechanisms on SEI formation.** It is crucial to understand more extensively the formation of SEI. In order to protect the electrolyte from continuous decomposition, it is important to select carefully the electrolyte/electrode combination that leads to the formation of a stable and robust SEI for each material. Besides, a deep knowledge about the SEI formation mechanisms would help to decrease the irreversible capacity which is one of the main issues for the practical utilization of hard carbons. This irreversible capacity translates in loss of available sodium and thus in a lower total battery capacity hence penalizing the maximum achievable energy density. This cannot be overcome by enhancing the mass loading of the positive electrode. An excess of negative active material should be used in order to avoid sodium deposition upon overcharge and safety hazards.

**Study on full-cell systems.** As it has been shown in this thesis good performance in half-cell does not always translate in good performance in full cell. Therefore, in order to fully understand the electrochemical behavior of materials, deep studies should be performed in full-cell systems. Interactions between the anode and cathode play a determinant role on the electrochemical properties of these full-cell systems.



---

# Appendix: Instrumental techniques

---

In this annex, the measurement conditions and a brief description of the experimental techniques used in this work will be presented.

## A1. X-Ray scattering techniques

X-ray scattering techniques are a family of non-destructive analytical techniques that reveal information about the crystallographic structure (atomic arrangement and unit cell dimensions), chemical composition, and physical properties of materials. These techniques are based on observing the scattered intensity of an X-ray beam hitting a sample as a function of incident and scattered angle and wavelength or energy.<sup>1</sup>

### A1.1 X-Ray powder diffraction (PXRD)

Diffraction of a beam of X-rays by a crystalline material is a process of scattering of the beam by electrons of the atoms in the crystal and interference of these scattered X-rays because of the periodic arrangement of the atoms and its symmetry. This process leads to the enhancement of the intensity of the scattered radiation in certain directions due to constructive interference controlled by the periodicity and destructive interferences in all other directions. The measurement of the directions of constructive beam allows determining the

---

<sup>1</sup> Jenkin, R., X-ray Techniques: Overview, Encyclopaedia of Analytical Chemistry, John Wiley & Sons Ltd, Chichester, **2000**.

fundamental properties of the unit cell of the crystal and its symmetry.<sup>2</sup> Each crystalline solid leads to a characteristic X-ray pattern so that they can be used as “fingerprint” for identification.

In a diffraction experiment, the incident waves have wavelengths comparable to the spacings between atoms. The interplanar spacing,  $d$ , sets the difference in path length for the ray scattered from the top plane and the ray scattered from the bottom plane. Figure A.1 shows that the difference in the path length is  $2d\sin\theta$ . Constructive wave interference occurs when the difference in path length for the top and bottom rays is equal to one wavelength ( $\lambda$ ) giving rise to the Bragg’s Law:<sup>3</sup>

$$2d_{hkl} \sin\theta = n\lambda \quad \text{Eq. A.1}$$

Where  $n$  is a positive integer,  $d$  is the distance between two consecutive planes defined by a vector of  $hkl$  components,  $\theta$  is the angle of incidence of two parallel rays and  $\lambda$  is the wavelength of incident wave.

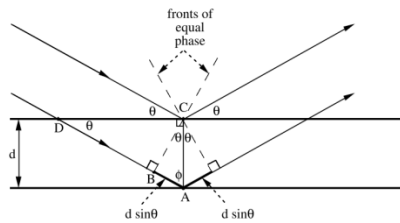


**Figure A.1** Geometry for interference of a wave scattered from two planes separated by a  $d$  spacing.

The intensity of the diffracted X-rays is continuously recorded as the source of the spinner and the detector rotate through their respective angles. When the crystal contains lattice planes with  $d_{hkl}$ -spacings appropriate to diffract X-rays at that value of  $\Theta$ , a peak in intensity appears. Resulting diffractograms represent the X-ray counts (intensity) along the  $y$  axis against peak position at  $2\Theta$  along  $x$  axis.

<sup>2</sup> Birkholz, M.; Thin film analysis by X-Ray scattering, Wiley, Weinheim, **2006**.

<sup>3</sup> Fultz, B. and Howe, J., Transmission electron microscopy and diffractometry of materials, Graduate Texts in Physics, Springer-Verlag, Berlin, Heidelberg, **2013**.

The PXRD patterns included in this work have been performed in a Bruker D8 Advanced emitting both  $K\alpha_1$  (1.5406 Å) and  $K\alpha_2$  (1.5444 Å) in CIC Energigune. Measurements were performed between 5 and 85° with a 0.02° step size for 1 hour.

### **A1.2 Small Angle X-ray Scattering (SAXS)**

SAXS is another analytical method to determine the structure of particle systems in terms of averaged particle sizes or shapes based on an X-ray beam hitting a sample. The difference with respect to PXRD is that the scattered beam after X-Ray irradiation is collected after transmission through the sample on a 2D detector centred in the incident beam axis allowing better resolution at low angle than the Bragg-Brentano geometry typically used in PXRD diffractometers. (Figure A.2 a) In addition to the diffraction peaks that can be observed in the 5-45° range as in a PXRD diffractometer, at low angle the scattering intensity gives information about differences in electron densities that may correspond to internal fluctuations of density of the sample or between the sample and the surrounding atmosphere.

When X-rays are scattered at atoms, every atom emits spherical waves emanating from the position of the respective atom. Because the outgoing light waves from Thomson-scattering processes are synchronized with the incoming plane waves, they produce interference patterns at the detector's position. The interferences can be constructive (in phase), destructive (out of phase) or somewhere in-between depending on the observation angle  $2\theta$ , the orientation and the distance of the light-emitting atoms from each other. (Figure A.2 b) In a constructive constellation the interference causes a bright spot at the detector and in a destructive constellation the waves extinguish each other, thus producing a dark spot at the detector. The result is a 2D interference pattern, where the intensity varies from position to position in the detection plane (usually measured in terms of scattering angle and azimuth angle). The interference pattern is characteristic to the internal structure of the material, i.e., to the orientation and distances of the atoms relative to each other.

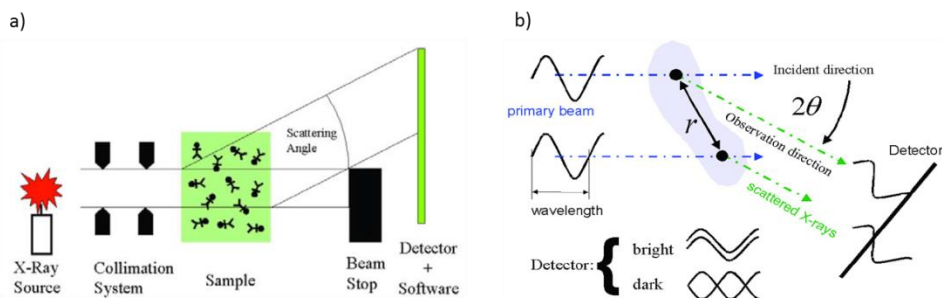


**Figure A.2** a) Scheme of the components of a SAXS instrument and, b) Explanation on how the intensity of interfering waves depends on the distance of the emitting atoms and on their orientations with respect to the directions of incidence and observation.

When analysing SAXS data a number of corrections have to be considered in order to get an accurate representation of the interaction between sample and the incident beam. These corrections include the sample holder scattering removal, transmission correction, angular and distance correction and absolute intensity corrections. After angular integration to get intensity profiles, the following equation has to be applied considering all the necessary corrections in order to lead to intensity in absolute units ( $\text{cm}^{-1}$ ).

$$I (\text{cm}^{-1}) = \frac{1}{I_0} \frac{1}{e (\text{cm})} \left[ \frac{I_{\text{sample+tape}} (\text{cps})}{t_{\text{sample+tape}}} - \frac{I_{\text{tape}} (\text{cps})}{t_{\text{tape}}} \right] \frac{D (\text{cm}^2)}{\text{pixel area} (\text{cm}^2) \times (\cos \theta)^3} \quad \text{Eq. A.2}$$

Where  $I_0$  is the intensity of the incident beam,  $e$  is the thickness of the sample holder,  $I_{\text{s+t}}$  is the measured intensity of the scattered beam,  $I_{\text{tape}}$  is the intensity of the beam scattered by the tape alone (blank),  $t$  is the transmission,  $D$  is the distance between the sample and the detector in the axis of the incident beam, and pixel area is the surface area of each pixel in the detector. In an attempt to become independent from the wavelength, scattering patterns are usually presented as functions of  $q$  (length of the scattering vector or momentum transfer).

$$q = \frac{4\pi}{\lambda} \sin \theta \quad [1/\text{nm}] \quad \text{Eq. A.3}$$

Once the  $I$  vs.  $Q$  plot is obtained, the data is ready for analysis.

Small Angle X-ray Scattering (SAXS) measurements were performed using a Nanostar U (Bruker, Germany) equipped with microfocus Cu source, evacuated beam path and Vantec 2000 detector, using 107 cm, 26 cm and 5 cm sample-detector distances. The incident beam has been carefully calibrated in order to obtain absolute intensities in  $\text{cm}^{-1}$  with a perfect overlap of the measurements made at the three distances. Intensities were then normalized in  $\text{cm}^2.\text{g}^{-1}$  by the macroscopic density of the powder samples.

### **A2. Scanning Electron Microscopy (SEM)**

Electron microscopy is a powerful tool for material characterization at a high magnification that supplies information regarding particle size, morphology, porosity and microstructure. A scanning electron microscope (SEM) consists of an electron optical column, a vacuum system and electronics (Figure A.3 a). The electron gun at the top of the column produces an electron beam by a thermal emission source, such as a heated tungsten filament, or by a field emission cathode when a difference between 5-30 KeV is applied. The beam is focused into a fine spot of less than 4 nm of diameter by a series of electromagnetic lenses in the SEM column. It is scanned in a rectangular raster over the specimen. As a consequence of the interaction of the electrons with the specimen, secondary electrons are produced and detected. The amplitude of the secondary electron signal varies with time according with the topography of the specimen surface. The signal is amplified and used to cause the brightness of the electron beam in a cathode ray tube (CRT). Both the beam in the microscope and the one in the CRT are scanned at the same rate and there is a one to one relationship between each point on the CRT screen and the corresponding point in the specimen. Thus, a picture is built. The ratio of the size of the screen of the viewing monitor (CRT) to the size of the area scanned is the magnification. Increasing the magnification is achieved by reducing the size of the area scanned on the specimen.

As a consequence of the interactions between the beam electrons and sample atoms, several phenomena can occur. They are represented in Figure A.3 b:

- The specimen itself emits secondary electrons (SE).

- Some of the primary electrons are reflected backscattered electrons (BSE). These backscattered electrons can also cause the emission of secondary electrons as they travel through the sample and exit the sample surface.
- The specimen emits X-rays.
- Electrons are absorbed by the specimen.
- The specimen sometimes emits photons of visible light (cathodoluminescence).
- If the sample is thin, the SEM may be operated in STEM mode with a detector located below the sample to collect transmitted electrons.

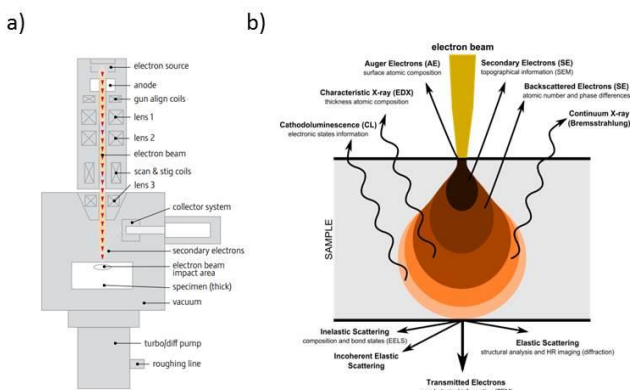


**Figure A.3** a) Scheme of a SEM and b) electron interactions with sample.

All these phenomena are interrelated and all of them depend to some extent on the topography, the atomic number and the chemical state of the specimen. The most commonly imaged signals in SEM are SE and BSE. SE, because of their very low energies, can escape the sample to be detected only if they originate very close to the sample surface. This gives SE images high spatial resolution and strong topographic contrast. The BSE signal is used primarily for its strong atomic number contrast. Qualitative and quantitative chemical microanalysis information can be also obtained using an energy dispersive x-ray spectrometer (EDX) thanks to the analysis of characteristic X-rays. <sup>4</sup>

<sup>4</sup> An Introduction to electron microscopy, *FEI*, July 2010.

Morphological characterization of Schiff bases and hard carbons was carried out by Scanning Electron Microscopy (SEM) in a field emission Quanta 200 FEG (FEI) scanning electron microscope equipped with an EDAX (Energy Dispersive X-ray Analysis).

### *SEM Sample preparation*

As the specimen must be able to withstand the vacuum of the chamber the PolySchiff samples were supported onto carbon tape. However, hard carbon samples were directly put onto Aluminium pin stub in order to avoid the overestimation of the C content by EDX by depositing some droplets of acetone, which does not damage the sample and helps sticking it onto the surface of the holder. Prior to the analysis, samples were dried to remove any volatile components such as water that can damage. As PolySchiff samples are non-conducting samples they tended to accumulate charge under electron bombardment so it was necessary to coat them with a conducting layer. Gold gives a fine grained coating and is easily applied in a sputter coater. It gives a good yield of secondary electrons, and consequently, a good quality image of the surface, for that reason, it was chosen as coater.

### **A3. Surface area analysis (BET method)**

The external porosity of the hard carbon materials was studied by gas adsorption technique in a Surface Area and Porosimetry Analyzer. Calculation of the surface area was based on the Brunauer, Emmet and Teller (BET) model<sup>5</sup>, according to the so called BET equation (Eq. A.4).<sup>6</sup> This equation allows the calculation of the adsorbed monolayer volume (the amount adsorbed per gram of solid that covers completely the surface with a layer of a unique molecule) and the value of superficial area as of the relative pressure and adsorbed volume values from the N<sub>2</sub> isotherm.

---

<sup>5</sup> Langmuir, I., The constitution and fundamental properties of solids and liquids, *J. Am. Chem. Soc.*, **1916**, 38, 2221.

<sup>6</sup> Brunauer, S.; Emmet, P. H. and Teller, E., Adsorption of gases in multimolecular layers, *J. Am. Chem. Soc.*, **1938**, 309-319.

$$\frac{X}{n^a(1-x)} = \frac{1}{n_m^a} + \frac{C_{BET-1}}{n_m^a} X \quad \text{Eq. A.4}$$

Where X represents the  $P/P^0$  relative pressure,  $n_a$  is the amount of adsorbed gas at the pressure P,  $n_m^a$  is the amount of gas required to form a monolayer on the surface of the adsorbent at the pressure P,  $P^0$  is the saturation pressure of the adsorbate at the adsorption temperature and  $C_{BET}$  is a parameter related to the adsorption heat of the first adsorbed layer. This is given by Eq. A.5.

$$C_{BET} = \exp\left(\frac{E_1 - E_L}{RT}\right) \quad \text{Eq. A.5}$$

Where  $E_1$  is the average enthalpy of adsorption of the first layer,  $E_L$  is the enthalpy of adsorbate liquefaction, R is the gases constant, T the temperature. The linear correlation range of the BET equation is usually limited to a pressure range between 0.05 and 0.3.

From the  $X/[n_a(1-X)]$  vs. X, for a given range of pressures, the monotonical relationship permits the calculation of the monolayer capacity. Known this value and the surface occupied by an adsorbed  $N_2$  molecule, the specific surface of the solid can be calculated using the following equation.

$$S_{BET} = n_m^a \sigma N_A \quad \text{Eq. A.6}$$

Where  $\sigma$  is the area of one adsorbate molecule on the surface of the solid at the adsorption temperature (0.162 nm<sup>2</sup> for  $N_2$  at 77 K) and  $N_A$  is the Avogadro number.

This model fails at lower relative pressures due to adsorbent surface heterogeneity and at  $P/P^0 > 0.35$  where neglect of lateral interactions between neighbouring adsorbate molecules and the process of capillary condensation produce deviations in the plot. The linear range, deemed to yield the "correct" surface area, varies widely from adsorbate–adsorbent pairs. Although this model is reasonable for external surface of a particle and the internal surface of the pore whose dimensions are large relative to the size of an adsorbate molecule,



its validity in small pores is disputed. For microporous materials, the actual surface area may be much larger than the surface area determined from a BET-based standard plot. This is due to the difference between the accessible surface, i.e. that not covered by filled pores, and the real surface area under the adsorbate. Again the assumption that the adsorbent surface is energetically homogeneous is very rarely applicable as most surfaces tend to be heterogeneous in this respect.<sup>7</sup>

Isotherm presents volume adsorbed as a function of the gas pressure and it was calculated by a volumetric method consisting of the calculation of the adsorbed gas at the equilibrium pressure as a difference between the volume of introduced gas and the required gas to fill the dead volume at a given pressure. By introducing several small gas amounts and waiting enough time to reach the equilibrium state, the isotherm is built point by point in the pressure range. The shape of the adsorption isotherms can give an idea of the size and porosity degree of the material.<sup>8</sup>

Microporous carbons usually lead to a type I isotherm in which the asymptotic approach to a limiting quantity indicates that all of the surface sites are occupied. In the case of physical adsorption, type I isotherms are related to microporous powders whose pore size does not exceed a few adsorbate molecular diameters. A gas molecule, when inside the pores of these small dimensions, encounters the overlapping potential from the pore walls which enhances the quantity adsorbed at low relative pressures. Mesoporous carbon is able to adsorb at all pressures. Initially, a monolayer is formed on the walls of the mesopores but in the intermediate pressure region the volume adsorbed increases continuously as a consequence of the multilayer adsorption within the pores formation. Finally, at pressure values close to gas saturation (e.g. 1), the volume adsorbed increases rapidly with small changes in pressure. This is attributed to condensation of the gas inside the pores and leads to a type II isotherm. Type III isotherms are characterized principally by heats of adsorption which are less than the

---

<sup>7</sup> Condon, James B. Surface area and porosity determinations by physisorption : measurements and theory, *Elsevier*, Amsterdam, The Netherlands, **2006**, 203-204.

<sup>8</sup> Brunauer, S.; Deming, L. S., Deming, W. S. and Teller, E., On a theory of the Van der Waals adsorption of gases, *J. Am. Chem. Soc.*, **1940**, 62, 1723.

adsorbate heat of liquefaction. Thus, as adsorption proceeds, additional adsorption is facilitated because the adsorbate interaction with an adsorbed layer is greater than the interaction with the adsorbent surface. Type IV isotherms occur on porous adsorbents possessing pores in the radius range of approximately 15-1000 Angstroms (Å). The slope increase at higher relative pressures indicates an increased uptake of adsorbate as the pores are being filled. As is true for the type II isotherms, the knee of the type IV isotherm generally occurs near the completion of the first monolayer. Type V isotherms result from small adsorbate-adsorbent interaction potentials similar to the type III isotherms. However, type V isotherms are also associated with pores in the same range as those of the type IV isotherms.<sup>9</sup>

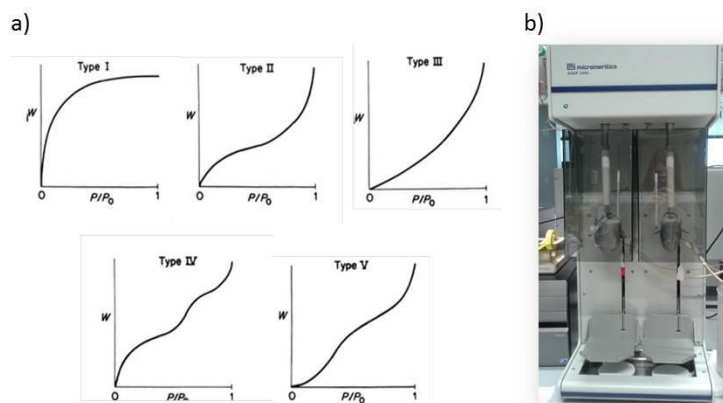


**Figure A.4** a) Five isotherm classification according to BDDT (Brunauer, S.; Deming, L. S., Deming, W. S. and Teller, E.). W, weight adsorbed; P, adsorbate equilibrium pressure;  $P^0$ , adsorbate saturated equilibrium vapour pressure;  $P/P^0$ , relative pressure. Condensation occurs at  $P/P^0 \sim 1$ . b) Micromeritics ASAP 2460 Surface area and pore analyser. Second degas mode in analysis port prior to analysis.

Determination of surface area was performed in a Micromeritics ASAP 2460 Surface area and Pore Analyzer. These analyses were carried out in CIC Energigune. In order to perform the analysis, an amount of approximately 50 mg of sample was weighted and placed in a dry glass bulb. Prior to analysis, it was degassed at 350 °C for 24 hours in the degas port so that the humidity and/or adsorbed species can be removed. Then the adsorbate, which is the probe gas, is

<sup>9</sup> Lowell, S. and Shields, J. E., *Powder surface area and porosity*, Springer Netherlands, **1984**, 11-13.

introduced into the sample tube. In this work N<sub>2</sub> adsorption at 77K was used because it is adequate for expected pore volume (micropores) of the samples. After degassing, the tube was filled with N<sub>2</sub> (99.9% Praxair) and weighted to determine the mass of clean sample. Then, it was placed in the analysis port and reevacuated at 350°C for 4 hours (2<sup>nd</sup> degassing). After degassing, the sample bulb was immersed in a constant temperature bath of N<sub>2</sub>. The adsorption was performed in a temperature and pressure range just below the condensation point of the gas to liquid transition. For that reason, in measuring the adsorption of nitrogen, liquid nitrogen was used to control the temperature of the sample. This is a convenient coolant, which assures a known vapour pressure over the sample.

The selection of data used for fitting B.E.T. surface area in a proper way was calculated according to MicroActive software from Micromeritics Instrument Corporation.<sup>10</sup> The process for data selection to yield the specific surface area of a material was carried out taking into consideration rules advocated by Prof. J. Rouquerol:

1. A linear fit to the (BET) transformed data should be obtained.
2. C<sub>BET</sub> constant must be positive (C > 0).
3. The Rouquerol transform  $n_{ads}(1-P/P^0)$  should be increasing with  $P/P^0$  for the data selected.
4. The monolayer capacity  $n_m$  should be within the limits of data that were used to fit the B.E.T. parameters.
5. The value of  $1/(\sqrt{C} + 1) \approx P/P^0$  at the monolayer capacity.

Rules 3, 4, and 5 have been contributed by Prof. Rouquerol and these rules allow for the selection of points to calculate the B.E.T. surface area. Using rule three,  $n_{ads}(1 - P/P^0)$  is monotonically increasing with  $P/P^0$ . This provides a clear basis for determining the maximum values of  $P/P^0$  and  $n_{ads}$  as the Rouquerol Transform plot has a peak maximum corresponding to the maximum values to be used in

---

<sup>10</sup> <http://www.micromeritics.com/Product-Showcase/MicroActive-Interactive-Data-Analysis-Software.aspx>

the BET transform. Rule four is used to confirm that the calculated value of the monolayer capacity  $n_m$  falls within the range of data used to calculate the BET parameters. This confirms that the monolayer capacity has not been extrapolated. Rule five ( $1/(\sqrt{C+1}) \approx P/P^0$ ) provides a check for consistency and may be used to further optimize the selection of points used to calculate the B.E.T. fit. The value of  $1/(\sqrt{C+1})$  should approach the relative pressure calculated from the B.E.T. transform at the monolayer capacity.

## **A4. Thermal analysis**

### **A4.1 Thermogravimetric analysis (TGA)**

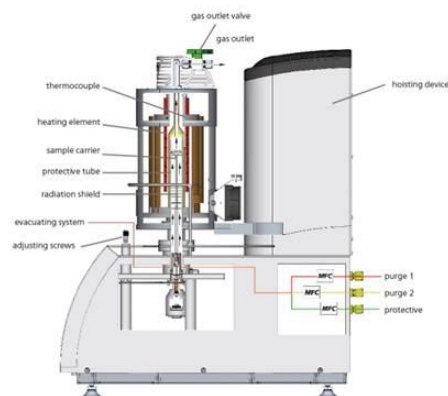
Thermogravimetric analysis (TGA) is the most widely used thermal method. In a thermogravimetric analysis (TGA) the mass loss of a sample in a controlled atmosphere is recorded continuously as a function of temperature or time as the temperature of the sample is increased (usually linearly with time). A plot of mass or mass percentage as a function of time is called a thermogram or a thermal decomposition curve. Thermogravimetric analysis is a useful tool to determine thermal stability over a given temperature range, composition of mixtures and moisture, volatile and ash.<sup>11</sup>

Commercial instruments for TGA consist of a sensitive microbalance with a pan loaded with the sample, called a thermobalance; a furnace; a purge-gas system for providing an inert, or sometimes reactive, atmosphere; and a computer system for instrument control, data acquisition, and data processing (Figure A.5).

---

<sup>11</sup> Brown, M. E., Thermal analysis techniques and applications, Kluwer Academic Publishers, New York, **2004**, 20.

a)



b)



**Figure A.5** a) NETZSCH Simultaneous Thermal Analyzer (STA) 449 F3 Jupiter® and b) Scheme of a thermobalance<sup>12</sup>.

Usually thermobalances are coupled to FTIR and mass spectrometers. As the temperature increases, the sample decomposes and several components are released. By means of mass spectrometers, the weight percentage of each resulting mass change can be measured, leading to the identification of the composition of the degradation products. TGA can be also performed along with DSC. This is known as Simultaneous Thermal Analysis (STA) and it refers to the application of thermogravimetry and differential Scanning Calorimetry to one and the same sample in a single instrument under the same conditions (gas flow rate, heating rate, etc) In DSC, the instrument measures the difference in the heat flow between the sample and the reference. Along with TGA, Differential thermal analysis (DTA) measurements can be carried out. In DTA the difference in temperature between a substance and a reference material is measured as a function of temperature while the substance and reference material are subjected to a controlled temperature program.

The thermogravimetric experiments were performed in a NETZSCH Simultaneous Thermal Analyzer (STA) 449 F3 Jupiter® under inert atmosphere (Ar, 60 mL min<sup>-1</sup>)

<sup>12</sup> <https://www.netzsch-thermal-analysis.com/us/products-solutions/simultaneous-thermogravimetry-differential-scanning-calorimetry/sta-449-f3-jupiter/>

heating from room temperature to 600 °C in the case of PolySchiff bases and up to 900°C for lignin, at a heating rate of 10 °C min<sup>-1</sup>.

#### A4.2 Differential Scanning Calorimetry (DSC)

Differential scanning calorimetry consists of a measuring system that measures simultaneously the sample and a reference sample. They are mounted in the same furnace and commonly subjected to a controlled temperature program (heating or cooling). (Figure A.6 a) DSC measures the amount of energy absorbed or released by a sample when it is heated or cooled, providing quantitative and qualitative data on endothermic (heat absorption) and exothermic (heat evolution) processes.<sup>13</sup> The result of a DSC experiment is a curve of heat flux versus temperature or versus time. There are two different conventions: exothermic reactions in the sample shown with a positive or negative peak, depending on the kind of technology used in the experiment.

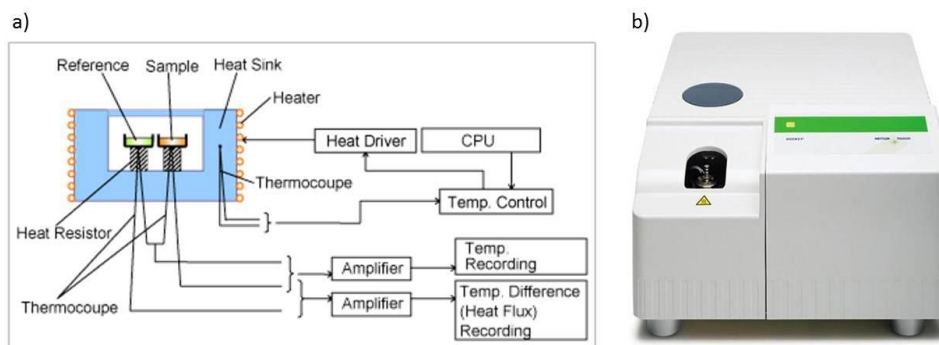


**Figure A.6** a) Scheme of a DSC apparatus and b) DSC822e Differential Scanning Calorimeter (Mettler Toledo) used in this work.

DSC can be used to measure melting temperature, heat of fusion, latent heat of melting, reaction energy and temperature, glass transition temperature, crystalline phase transition temperature and energy, precipitation energy and temperature, denaturation temperatures, oxidation induction times, and

<sup>13</sup> Czichos, H., Saito, T. and Smith, L. (Eds.), Handbook of Metrology and Testing 2<sup>nd</sup> edition, Springer-Verlag, Berlin, Heidelberg, 2011, 465.

specific heat or heat capacity. In this work it was used in order to know the melting or glass transition temperatures of PolySchiff base polymers.

Measurements were performed in a DSC822e Differential Scanning Calorimeter (Mettler Toledo) in UPV-EHU (Figure A.6b) DSC experiment begins by weighing an empty aluminium sample pan. A small portion of the sample (5-10 mg) is then transferred making sure that a uniform layer at the bottom of the pan is formed. The pan is hermetically sealed in Ar inside a glove box and then they are weighed again. Measurements were performed from -70 °C to 280 °C for PSB-PEO samples and from -70 °C to 380 °C for PSB at a heating and cooling rate of 10 K·min<sup>-1</sup> under inert atmosphere.

#### **A5. Attenuated Fourier Transform Infrared Spectroscopy (ATR-FTIR)**

Infrared (IR) Spectroscopy consists of the analysis of the interaction of IR radiation (generally from 4000 to 400 cm<sup>-1</sup>) with molecules inducing the vibration of the bonds. Therefore, this technique is very useful for the determination of functional groups. If the frequency of the radiation exactly matches a natural vibrational frequency of the molecule, absorption of the radiation takes place producing a change in the amplitude of the molecular vibration and leading to transitions of molecules from one vibrational or rotational energy state to another.<sup>14</sup>

In this work, attenuated total reflectance, or ATR-FTIR has been performed. Contrary to traditional transmission spectra, in which the IR light passes through the sample, in ATR-FTIR the beam penetrates a small distance into the less dense medium before reflection occurs. The penetrating radiation is called the evanescent wave. At wavelengths where the less dense medium absorbs the evanescent radiation, attenuation of the beam occurs, which is known as attenuated total reflectance, or ATR. (Figure A.7 a) The depth of penetration, which varies from a fraction of a wavelength up to several wavelengths, depends on the wavelength, the index of refraction of the two materials, and the angle of the beam with respect to the interface.

---

<sup>14</sup> Wade, Jr., L.G. Organic Chemistry, 5<sup>th</sup> ed. Pearson Education Inc., **2003**, 492-499.

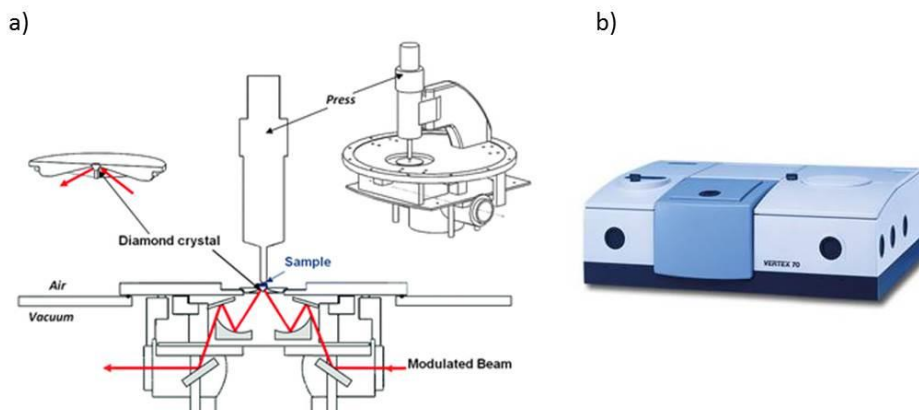


**Figure A.7** a) Scheme of an ATR-FTIR apparatus and, b) Vertex 70 spectrometer (Bruker) used in this work.

The resulting ATR spectrum resembles that of a conventional IR spectrum with some differences. It is usually represented in an analogous way with the % transmittance in the y axis and the wavenumber ( $\text{cm}^{-1}$ ) in the x axis. Transmittance can be calculated as the ratio between the intensity of the transmitted light after absorption by the sample and the intensity of the incident beam before sample absorption. However, the spectra obtained with ATR methods can differ from IR absorption spectra because of distortions that occur near strong absorption bands where the sample refractive index may change rapidly. Also, the orientation of the sample on the ATR crystal can influence band shapes and relative intensities. However, the ATR band intensity is usually proportional to concentration so that quantitative measurements can be made.<sup>15</sup>

In this work, Fourier Transform Infrared spectra coupled with attenuated total reflectance (ATR-FTIR) were recorded on Vertex 70 spectrometer (Bruker) in the range of  $\lambda = 4000\text{-}450 \text{ cm}^{-1}$ . (Figure A.7 b)

<sup>15</sup> Skoog, D. A.; Holler, F. J. and Crouch, S. R., Principles of instrumental analysis. 6th Edition, Thomson Brooks/Cole, Belmont, CA, USA, 2007, 430-439.



## A6. Nuclear Magnetic Resonance (<sup>1</sup>H-NMR)

### A6.1 Liquid state NMR

Nuclear magnetic resonance spectroscopy (NMR) is a non-destructive powerful tool available for organic structure determination. It is used to study a wide variety of nuclei, including <sup>31</sup>P, <sup>1</sup>H, <sup>13</sup>C, <sup>15</sup>N and <sup>19</sup>F.

A nucleus with an odd atomic number or an odd mass number has a nuclear spin that can be observed by the NMR spectrometer. When a proton is placed in an external magnetic field it twists to align itself with the field of the larger magnet either with the external field ( $\alpha$ -spin state) or against the field ( $\beta$ -spin state). In a strong magnetic field, the energy difference is proportional to the strength of the magnetic field, as expressed in the equation:

$$\Delta E = \gamma \frac{h}{2\pi} B_0 \quad \text{Eq.A7}$$

Where:

$\Delta E$  = energy difference between  $\alpha$  and  $\beta$  states

$h$  = Planck's constant

$B_0$  = strength of the external magnetic field

$\gamma$  = gyromagnetic ratio, 26,753 sec<sup>-1</sup> gauss<sup>-1</sup> for a proton.

When a proton interacts with a photon with just the right amount of electromagnetic energy, the proton's spin can flip from  $\alpha$  to  $\beta$  or from  $\beta$  to  $\alpha$ . A nucleus aligned with the field can absorb the energy needed to flip and become aligned against the field. When a nucleus is subjected to the right combination of magnetic field and electromagnetic radiation to flip its spin, it is said to be "in resonance", and its absorption of energy is detected by the NMR spectrometer. This is the origin of the term "nuclear magnetic resonance".

In a molecule, the electron cloud around each nucleus acts like a loop of wire, rotating in response to the external field. This induced rotation is a circular current whose magnetic field opposes the external field. The result is that the

magnetic field at the nucleus is weaker than the external field, and we say the nucleus is shielded. The effective magnetic field at the shielded proton is always weaker than the external field, so the applied field must be increased for resonance to occur at a given frequency. Because of the diverse structures of organic molecules, the shielding effects of electrons at various positions are generally different. The number of different absorptions (also called signals or peaks) implies how many different types of protons are present. On the other hand, the amount of shielding shown by these absorptions implies the electronic structure of the molecule close to each type of proton.

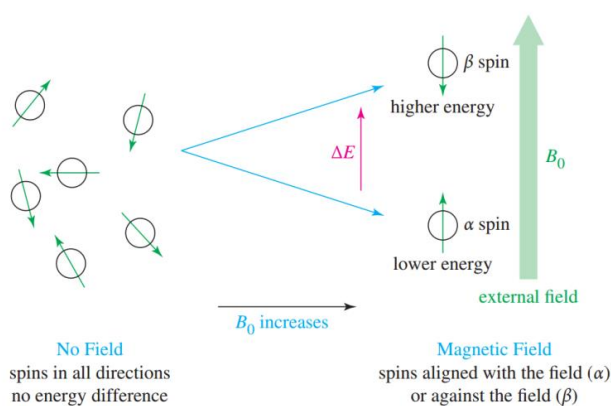


**Figure A.8** Effect of an external magnetic field on the nuclei.

Two other aspects of the NMR spectrum that have to be considered are the intensities of the signals and their splitting patterns: the intensities of the signals imply how many protons of each type are present whereas the splitting of the signals gives information about other nearby protons. Protons in a molecule are partially shielded from the magnetic field, and this shielding depends on each proton's environment. Thus, protons in different environments within a molecule exposed to a constant frequency absorb the radiation at different magnetic field strengths. The NMR spectrometer was originally developed to vary the magnetic field and plot a graph of energy absorption as a function of the magnetic field strength. Such a graph is called a nuclear magnetic resonance spectrum.

The variations in the positions of NMR absorptions, arising from electronic shielding and deshielding, are called chemical shifts. They are usually referred to a compound added to the sample. The difference in the magnetic field strength between the resonances of the sample protons and the reference protons can be measured very accurately. The most common NMR reference compound is tetramethylsilane abbreviated TMS. Chemical shifts are measured in parts per million (ppm), a dimensionless fraction of either the total applied field or the total radio frequency. A chemical shift in parts per million can be calculated by dividing the shift measured in hertz by the spectrometer frequency measured in millions of hertz (megahertz or MHz).

$$\text{Chemical shift (ppm)} = \frac{\text{shift downfield from TMS (Hz)}}{\text{total spectrometer frequency (MHz)}} \quad \text{Eq.A8}$$

The chemical shift (in ppm) of a given proton is the same regardless of the operating field and frequency of the spectrometer. The use of dimensionless chemical shifts to locate absorptions standardizes the values for all NMR spectrometers. The most common scale of chemical shifts is the  $\delta$  (delta) scale. The signal from tetramethylsilane (TMS) is defined as 0.00 ppm on the scale. Most protons are more deshielded than TMS, so the scale increases toward the left of the spectrum. The spectrum is calibrated in both frequency and ppm  $\delta$ .<sup>16</sup>

Liquid <sup>1</sup>H-NMR was performed at room temperature in a Bruker AVANCE 500 spectrometer (500 MHz) in UPV-EHU. d<sub>6</sub>-DMSO was used as solvent for PSB and PSB-PEO.

## A6.2 Solid state NMR

Liquid state NMR is usually employed to determine the structure and dynamics of organic compounds. However, there are many compounds which cannot be either placed into a solution, like PSB-PEO, which are not fully soluble, or need to be studied in the solid state. In NMR, magic-angle spinning (MAS) is a technique often used to perform experiments in solid-state NMR spectroscopy. By spinning

---

<sup>16</sup> Wade, Jr., L.G. Organic Chemistry, 5<sup>th</sup> ed. Pearson Education Inc., **2003**, 492-499.

the sample (usually at a frequency of 1 to 100 KHz) at the magic angle  $\Theta_m$  (ca.  $54.74^\circ$ , where  $\cos^2\Theta_m=1/3$ ) with respect to the direction of the magnetic field, the normally broad lines become narrow, increasing the resolution for better identification and analysis of the spectrum.

All Magic Angle Spinning Nuclear Magnetic Resonance (MAS-NMR) spectra were recorded with a Bruker Avance III 500 spectrometer working at a  $^1\text{H}$  frequency of 500.24 MHz. Samples were packed in standard 2.5 mm rotors and spun at the magic-angle at an MAS frequency of 20 kHz in all cases.  $^1\text{H}$  and  $^{13}\text{C}$  spectra were referenced to bulk water resonating at 4.7 ppm, and solid adamantane respectively.  $^{13}\text{C}$  spectra were obtained using the cross-polarization (CP) technique with a  $1.8\ \mu\text{s}$   $^1\text{H}$  pulse, and a contact time during CP of 0.6 ms. Hard proton SPINAL64 decoupling was used during  $^{13}\text{C}$  acquisition. The acquisition time was set to 25 ms and the recycling delay was set to 5s. The  $^{13}\text{C}$ - $^1\text{H}$  2D correlation was performed using the Frequency Switched Lee Goldberg Heteronuclear Correlation (FSLG HETCOR)<sup>17</sup>. Homonuclear decoupling in the  $^1\text{H}$  evolution period was achieved with an FSLG pulse train of  $6.3\ \mu\text{s}$  pulses.

### A7. Electrochemical testing

Except for the results presented in the chapter 4, the electrochemical characterization of the materials presented in this work has been performed on coin half cells. It consists of a positive electrode and a negative electrode located as close as possible to minimize the internal resistance. They are separated by a thin porous insulating material (glass fiber) that acts as separator preventing the two electrodes to touch each other and, thereby, shortcircuiting. The pores of the separator are filled with electrolyte which conducts ions between the two electrodes, but which is itself an electronic insulator to avoid internal short-circuit.

The chemical reactions that generate electricity take place at the two electrodes. They are made up of the chemicals that undergo electrochemical reactions (active material) and conducting additives that provide an improved pathway for

---

<sup>17</sup> Van Rossum, B.-J.; Foerster, H. and de Groot, H. J. M., *J. Magn. Reson.* **2003**, 124, 516-519.

electrons (carbon black) and stuck to a Cu foil (current collector) thanks to a binding agent or binder (usually, PVdF) . Each electrode undergoes a half-cell reaction. In a discharging battery, electrochemical oxidation of the electrode proceeds at the negative terminal. Electrons transferred from the negative terminal through the external circuit engage in reduction at the positive terminal, which is known as a cathode. Since batteries are generally considered to operate under discharge, the negative electrode is often known as the anode and the positive electrode as the cathode. The difference between the potentials of the anode and the cathode gives the so-called reversible or open-circuit voltage (OCV), that is, the voltage across the terminals of the cell when there is no current flow.<sup>18</sup>

### A.7.1 Electrode preparation

The preparation of the electrodes was carried out by different techniques according to the nature of the sample. Specific ratio among components has already been described for each material. In general, the electrode preparation involves the mixture by hand grinding in an agate mortar of the active material, conductive carbon and binder. Then, a few mL of NMP are added so as to obtain a homogeneous mixture. Hereafter, the slurry is cast onto Cu foil manually or with the help of a blade. The laminates are left so that they partially dry for 30 minutes on top of a flat surface and then they are placed in the vacuum oven. After an overnight vacuum drying at 120°C, electrodes of a given diameter (usually 11 mm) are obtained with a punchcutter.

### A.7.2 Cell assembly

All the electrochemical measurements have been performed on CR2032 (Hohsen) coin-type cells. The CR2032 is constituted by a case of 20 mm of diameter and 32 mm of thickness. In **¡Error! No se encuentra el origen de la referencia.**, a scheme of the coin cell assembly is shown. Firstly, the gasket is inserted in the bottom base and the electrode is placed on top of it with the metal side on top of the case. Then the separator (Whatman) is put on top of

---

<sup>18</sup> Dell, M. R. and Rand, D. A. J.; Understanding batteries, RSC Paperbacks. Cambridge, **2001**, 14-21.

the electrode and it is filled with some droplets of electrolyte. After that, metallic sodium attached to a stainless steel spacer is put with the surface of the sodium touching the separator. Finally, a spring is put on top of the spacer and the bottom case. The coin cell is hermetically closed with a Hoshen Corporation press.

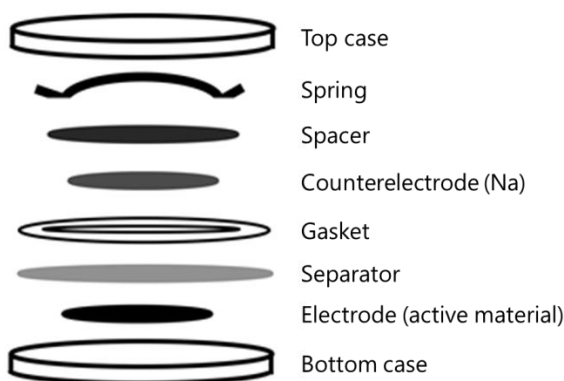


**Figure A.9** Scheme of coin cell assembly.

For the preparation of three electrode full cells, Swagelok cells were employed. They are assembled in an analogous way being the main difference, the existence of a third electrode (reference electrode). The reference electrode (metallic sodium) is in contact with the counter electrode (metallic sodium) and the working electrode by a glass fiber separator soaked with electrolyte. (Figure A.10)

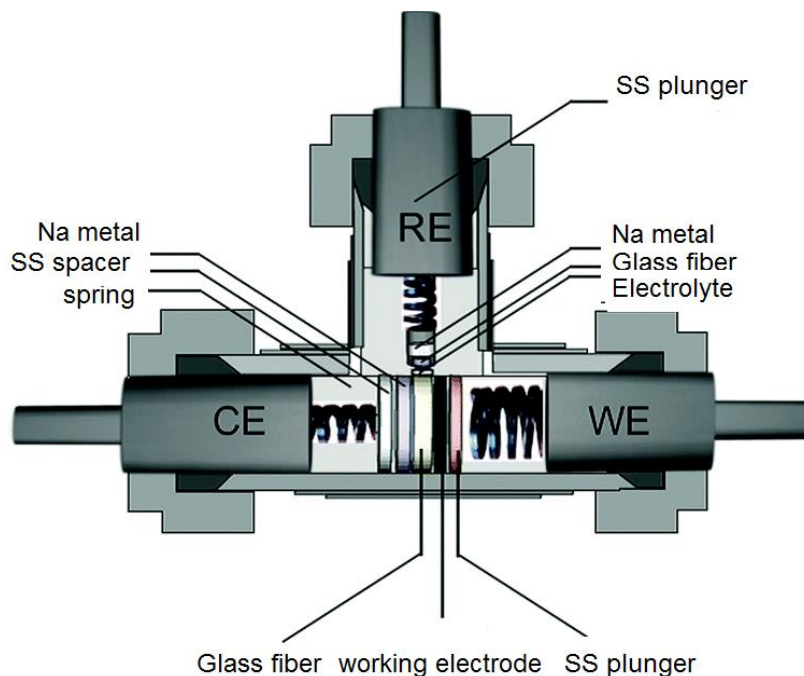


**Figure A.10** Scheme of a Swagelok cell assembly

### A.7.3 Galvanostatic cycling

The electrochemical characterization of the materials was performed using two different devices: a Maccor Battery Tester Series 4000 and a Biologic VMP3 Multi-channel potentiostat.

Galvanostatic cycling is a method that examines battery characteristics by measuring changes in voltage over time under a constant current. Continuous charging and discharging experiments are conducted to measure changes in voltage under a constant current for a given potential range. It is a method of electrochemical analysis that derives the quantity of electrical charge under continuous charging and discharging with varying voltage over time. The voltage can be represented as a function of the time, capacity or fraction of inserted ions and capacity, reversibility, resistance, and rate of diffusion are electrochemical properties that can be obtained from this method.

The capacity of a battery is the product of the total amount of charge, when completely discharged under given conditions, and time. It is the product of the current drawn from a battery, multiplied by the number of hours this current flows. The unit in which capacity is measured is the ampere-hour, equivalent to 3600 coulombs. The specific capacity is the capacity that the material provides by unit of active mass and it is expressed in mA·h·g<sup>-1</sup>. When a battery is measured on load (when drawing current) the measured voltage will be lower than the OCV because of the internal impedance of the battery created by polarization losses at the electrode and ohmic losses in the current collectors, electrolyte and active masses. If the discharge rate of the battery increases, the internal resistance and the polarization effects increases and the discharge is produced at a lower voltage leading to a decrease of the cycle life of the cell. Under low current density conditions, both voltage and discharge capacity of the working battery come close to the theoretical equilibrium although extremely long discharge time can lead to damage of the active material and subsequent capacity fade.<sup>19</sup>

Considering the capacity and the stored energy available from a battery, it is essential to define the discharge rate. The term C/t (where t is the discharge time in hours) is often used to define the rate at which the capacity is calculated. Thus, C/5 is the 5-hour discharge rate.

Apart from understanding the mechanisms of the electrochemical reactions, which are indicated by the shapes of the charge/discharge curves, galvanostatic cycling also provide information regarding the maintenance of the major properties of the electrode material over many discharge /charge cycles. Cycle life is the number of charge and discharge cycles that a battery can achieve before its capacity is depleted. A high-performance battery should be able to maintain its capacity even after numerous charge and discharge cycles. The cycle life of secondary batteries strongly depends on the structural stability of electrode active materials during the charging/discharging process. This is important as applications that involve many cycles of operation require cells to

---

<sup>19</sup> Linden, D.; Reddy, T.B. *Handbook of Batteries. Third Edition.* Mac Graw-Hill. New York, **2002**.



be designed and constructed such that the capacity loss per cycle is extremely low.<sup>20</sup>

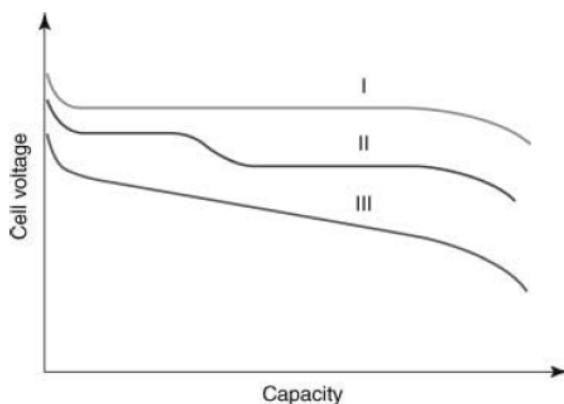


**Figure A.11** Types of discharge curves obtained from electrochemical reactions

#### A.7.4 Cyclic voltammetry

Cyclic voltammetry is an electrochemical analysis method that scans voltage with a constant scan rate of voltage for a given potential range of an electrochemical cell. Cyclic voltammetry observes changes in current by applying voltage under a constant scan rate. However, cyclic voltammetry repeats the same experiment for each cycle. It provides information on redox reactions occurring within the cell, including potential, quantity of electricity, reversibility, and continuity (sustainability of reversible electrochemical reaction). While the scan rate differs depending on the purpose of experiments, a low scan rate is recommended for detailed analysis of electrochemical reaction.

<sup>20</sup> Park, J.-K., Principles and applications of lithium secondary batteries, Wiley-VCH Verlag & Co. KGaA, Germany, **2012**, 17-20.

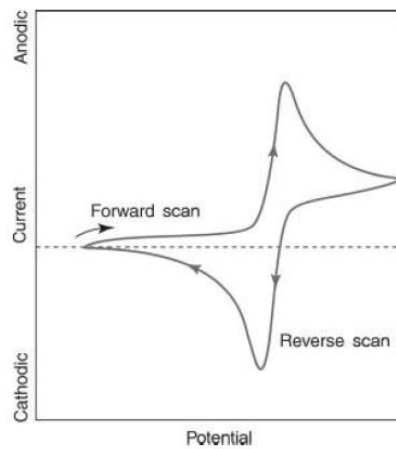


**Figure A.12** Current-voltage experiments in cyclic voltammetry